DISCHARGE PLASMA PROCESSES OF
RING-CUSP ION THRUSTERS

Thesis by

Richard E. Wirz

In Partial Fulfillment of the Requirements for the

Degree of

Doctor of Philosophy

CALIFORNIA INSTITUTE OF TECHNOLOGY

Pasadena, California

2005

(Defended April 13, 2005)

ACKNOWLEDGEMENTS

Since it is difficult to rank the importance of all the wonderful people that helped with this dissertation, I present my acknowledgements in chronological order. First and foremost, I thank my wife, Kristi Wirz, for her amazing support and patience through this process, and for being the best friend I have ever had. My JPL advisor and friend, Jay Polk, introduced me to the intoxicating world of advanced propulsion and my Caltech advisor, Fred Culick, gave me the freedom to follow an unbeaten path with my research. Juergen Mueller introduced me to micropropulsion and has been a great person to work with through these years and hopefully many to come. Colleen Marrese helped and supported me when I was fresh and ignorant and taught me the ins and outs of an electric propulsion laboratory. Al Owens taught me how to work in the metal machine shop to make vital parts for my research (without killing myself). John Ziemer has been a great friend and mentor and had the pleasure of helping me completely dismantle my vacuum system and develop computer controlled plume diagnostics. Rob Kolasinski has been in the trenches with me through the early days of the "wonderful" first year at Caltech and has helped me immensely in the lab. The Discharge Model would not exist without the brilliance and knowledge of Ira Katz, who guided me through the world of plasma modeling. Dan Goebel has helped in so many ways it is hard to keep track – he is an ion thruster discharge and cathode guru and his influence is found throughout my research. Another Caltech grad, Mike Gale, did an amazing job assembling and programming the automated data acquisition system in a single summer! My wonderful sister, Karen Wirz, has patiently proofread several of my technical papers and this dissertation. Yiangos Mikellides has given me indispensable advice on modeling. And lastly, I must thank the rest of my committee: Tony Leonard, Paul Bellan, and Oscar Bruno; who have taken time out of their schedules to read and critique my research. To all of you, "THANKS!"

ABSTRACT

This study has increased the viability of miniature ion thruster technology, advanced state-of-the-art discharge modeling, and revealed important aspects of discharge plasma processes. These extensions of existing ion thruster technology and understanding are necessary to fulfill the needs of future space missions. Miniature ion thrusters (<5cm diameter) are ideally suited for precision formation flying missions while future exploration missions require ion thruster power and life well beyond that of existing thruster technology. Experimental comparisons of the discharge performance of an array of miniature (3cm diameter) ion thruster discharge configurations were conducted. The tests included axial, divergent axial, line cusp, 3-ring cusp, and 2-ring cusp magnetic field configurations and anode length-to-diameter ratios of 1.0, 0.75, and 0.5. Of these configurations, a 3-ring configuration with length-to-diameter ratio of 1.0 exhibited the best performance. High magnetic field versions of the configurations typically exhibited very poor performance, which was contributed to discharge instabilities. A non-intrusive technique for measuring the discharge plasma density was developed and used to interrogate the 3-ring configuration. This technique extrapolates downstream beam profile data to the thruster exit plane, and then uses an ion extraction grid computational model to determine the plasma density immediately upstream of the grids. Analysis of the results from this technique led to the use of small accelerator grid holes, which yielded improvements in discharge loss ($\Delta \varepsilon_B \approx$ -100eV/ion) and propellant efficiency ($\Delta \eta_{ud} \approx$ 10%). A compact and lightweight version of the 3-ring configuration exhibited discharge losses of $\varepsilon_B \approx$ 250-550eV/ion and propellant efficiency of as much as 87%. This performance represents a significant advancement in miniature ion thruster efficiency and demonstrates that a miniature thruster of low magnet and thruster weight can yield desirable performance.

A multi-component hybrid 2-D computational "Discharge Model" was developed to help identify important ion thruster discharge processes and investigate miniaturization issues. The model is designed to integrate thruster component (cathode and grid) wear models to allow the determination of thruster life and long-term performance. The model accounts

for the five major chamber design parameters (chamber geometry, magnetic field, discharge cathode, propellant feed, ion extraction grid characteristics) and self-consistently tracks the effects of the four plasma species (neutral propellant atoms, secondary electrons, primary electrons, and ions). Run-time is minimized by treating the neutral propellant atoms with techniques similar to thermal transport view factors. High-energy primary electrons are tracked with a Boris-type predictor-corrector algorithm while secondary electrons are treated as a quasi-neutral component of the plasma with a depleted-tail Maxwellian distribution. An ion optics code is used to determine grid transparency to ions and neutrals. Ion diffusion is assumed ambipolar and a non-classical correction is used for the perpendicular diffusion of secondary electrons. A correction for double ions is used to approximate double ion content inside the chamber and in the beam. The non-uniform secondary electron temperature is determined by an electron thermal model that accounts for the transfer of primary electron energy to the secondary population.

Results from the model show good agreement with experimental data at two operating points for the 30cm NSTAR ion thruster. A thruster design sensitivity performed with the Discharge Model suggests that NSTAR thruster performance is greatly enhanced by increasing the strength of the middle magnet ring. The model analyses show that the peak observed in the NSTAR beam profile is due to double ions that are created by over-confinement of primary electrons on the thruster axis. Design sensitivity results show that, at the NSTAR thruster scale, efficient *confinement* of primary electrons is relatively easy to achieve; therefore, efforts to improve thruster performance should focus on effectively *utilizing* the primary electrons to minimize double ion production and maximize the number of single ions extracted to the beam. The model also shows good agreement with experimental data from the 3cm ion thruster developed in this study. The results suggest that the primary electrons are poorly utilized at this scale since over 50% are lost to the anode before having a collision with a propellant atom. Combining this observation with the discharge stability concerns at higher magnetic fields reveals that magnetic field optimization for a miniature ion thruster is bracketed by considerations of primary electron utilization and discharge stability. The Discharge Model results also show that non-classical effects are important for predicting the perpendicular mobility of secondary

electrons in ion thruster discharges. Good agreement with experimental data was found by weighting the influence of Bohm-type diffusion by considering the non-uniform levels of ionization in the discharge. It was found that ion thrusters operate in an intermediately ionized plasma regime that is between fully and weakly ionized approximations.

The observations from this study have furthered the understanding of discharge processes and should improve future ion thruster design and modeling efforts. The Discharge Model advances state-of-the-art ion thruster modeling and provides a framework for a complete thruster model that can be used for long-life performance assessment and life validation.

TABLE OF CONTENTS

Appendix A: Terrestrial Planet Finder (TPF) Thrust Requirements
Appendix B: Preliminary Miniature Ion Thruster Tests
Appendix C: Micro-Ion Thruster Performance Data
Appendix D: Non-Intrusive Discharge Diagnostics and Grid Performance Analysis
Appendix E: Development of Miniature Ion Thruster Cathode Technologies
Appendix F: Magnetostatic Theory and Results
Appendix G: Plasma and Computational Formulations
Appendix H: Additional Discharge Model Results

NOMENCLATURE

A = area

$\mathbf{B}$ = magnetic flux density

$\underline{\underline{\mathbf{D}}}$ = plasma diffusion tensor

$D_{//}$ = parallel plasma diffusion coefficient

$D_\perp$ = parallel plasma diffusion coefficient

$\mathbf{E}$ = electric field

e = electron charge

f_{inel} = secondary inelastic collision fraction

f_A = fraction of ion current to anode surfaces

f_B = fraction of ion current to the beam

f_C = fraction of ion current to cathode surfaces

F_B = beam flatness

F_T = thrust correction due to divergence of beam

$\hat{h}$ = unit direction vector

I_{sp} = specific impulse

j = current density

j_B^+ = beam current density due to singly charged ions

j_B^{++} = beam current density due to doubly charged ions

j_{screen}^+ = screen current density due to singly charged ions

j_{screen}^{++} = screen current density due to doubly charged ions

J_B = total beam current

J_B^+ = beam current due to singly charged ions

J_B^{++} = beam current due to doubly charged ions

J_D = discharge current

J_{DCH} = discharge cathode heater current

J_p = primary electron current

J_{screen} = screen grid ion current

k = Boltzmann's constant

K = collision rate constant

K_{iz}^p = ionization collision rate constant due to primary electrons

K_{iz}^s = ionization collision rate constant due to secondary electrons

K_{ex}^s = excitation collision rate constant due to secondary electrons

K_{el}^s = elastic collision rate constant due to secondary electrons

K_{iz}^o = total ionization collision rate constant of neutral atoms

K_{ex}^o = excitation collision rate constant of neutral atoms

K_{iz}^+ = double ionization collision rate constant of single ions

K_{slow}^s = effective primary electron slowing rate constant due to secondary electrons

m = mass

m_e = electron mass

m_i = ion mass

$\dot{m}_d$ = discharge chamber propellant mass flow rate

$\dot{m}_{loss}$ = mass flow rate of propellant loss

$\underline{\underline{\mathbf{M}}}_e$ = electron mobility tensor

$\underline{\underline{\mathbf{M}}}_i$ = ion mobility tensor

$M_E^\perp$ = electric field perpendicular mobility

n_i = ion number density

n_+ = single ion number density

n_{++} = double ion number density

n_o = neutral atom number density

n_p = primary electron number density

n_s = secondary electron number density

$\dot{n}_i$ = total ion generation rate density

$\dot{n}_{++}$ = double ion generation rate density

$\dot{n}_i^p$ = ion generation rate density due to primary electrons

$\dot{n}_i^s$ = ion generation rate density due to secondary electrons

$\dot{n}_s$ = secondary generation rate density

$\dot{n}_{ex}^p$ = collision rate density for primary excitation of neutral ions

$\dot{n}_{slow}^p$ = collision rate density for primary slowing by secondary electrons

$\dot{n}_i^p$ = ion generation rate density due to primary electrons

$\mathbf{P}$ = pressure

P_E = total thruster input power

P_o = miscellaneous thruster input power

P_T = thrust (jet) power

P_{iz} = probability of ionization collision

P_{ex} = probability of excitation collision

P_{slow} = probability of slowing collision

(P_{ps}, P_{pw}, P_{piz}, P_{ps}, P_{sw}, P_{siz}, P_{sx}) = electron power loss mechanisms (Chapter 4)

q = electric charge

r = distance from thruster axis

r_{ce} = electron cyclotron radius

$\mathbf{R}_i$ = ion momentum transfer due to collisions

$\mathbf{R}_e$ = electron momentum transfer due to collisions

t = time

T_e = electron temperature

T_i = ion temperature

T_p = primary electron temperature

T_s = secondary electron temperature

T_s^{inel} = effective secondary electron temperature for inelastic collisions

T_o = neutral atom temperature

T_{ideal} = ideal thrust

T_{corr} = corrected thrust

u_{Bohm} = Bohm velocity

u_+^{Bohm} = Bohm velocity for single ions

$\mathbf{u}$ = drift velocity

$\mathbf{u}_e$ = electron drift velocity

$\mathbf{u}_i$ = ion drift velocity

V = view factor

V_{accel} = accelerator grid voltage

V_B = beam voltage

V_c = cathode operation voltage

V_{cell} = computational cell volume

V_D = discharge voltage

V_{DPP} = distributor pole piece voltage

V_{Fil} = filament voltage drop

V_p = primary electron voltage

w = particle velocity

y = neutral flux

Y = neutral flow rate

z = axial distance

Greek Symbols

α = double ion thrust correction

β = neutral ionization fraction (Neutral Atom Sub-Model)

γ_{nc} = non-classical collision parameter

Γ = particle flux

Γ_e = electron flux

δ_D = plasma magnetization

δ_v = electron collision ratio

ε_B = discharge loss

$\langle \varepsilon \rangle$ = average energy

ε_{iz} = ionization energy

κ = thermal diffusion coefficient

λ = mean free path

$\ln\Lambda$ = Coulomb logarithm

μ = mobility coefficients (defined in Appendix G)

μ^* = simplified mobility coefficients (Section 4.6)

ν = collision frequency

ν_{ie} = ion-electron collision frequency

ν_{ei} = electron-ion collision frequency

ν_{io} = ion-neutral collision frequency

ν_{eo} = electron-neutral collision frequency

ν_{CEX} = charge-exchange collision frequency

ν_{ei} = electron-ion collision frequency

$\nu_{e\text{-}o}$ = neutral-centered electron collision frequency

$\nu_{e\text{-}i}$ = ion-centered electron collision frequency

$\nu_{i\text{-}o}$ = neutral-centered ion collision frequency

$\nu_{e\text{-}gen}$ = effective collision frequency due to electron generation rate

$\nu_{i\text{-}gen}$ = effective collision frequency due to ion generation rate

σ = collision cross-section

ϕ = electric potential

ψ = effective potential

Ψ = configuration factor

ω_{ce} = electron cyclotron frequency

Ω_e = electron Hall parameter

η_E = electrical efficiency

η_T = total efficiency

η_{ud} = discharge propellant utilization efficiency

$\eta_{ud\,[Gas]}$ = discharge propellant utilization efficiency per Neutral Atom Sub-Model

$\eta_{ud\,[Beam]}$ = discharge propellant utilization efficiency per Ion Diffusion Sub-Model

$\eta_{ud\,[*]}$ = discharge propellant utilization efficiency (not corrected for double ions)

ζ_o = grid transparency to neutral atoms

ζ_i = grid transparency to ions

Units:

This thesis uses mks units of the International System (SI) with the exception that energies are frequently given in terms of electron volts (eV).

sccm $\equiv$ Standard Cubic Centimeters per Minute. For xenon: 1 sccm $\approx$ 0.09839 mg/s at STP.

eV/ion $\equiv$ (Watts of Discharge Power)/(Amp of Beam Current) for discharge loss, ε_B

Chapter 1

Introduction

Ion thrusters are highly efficient electrostatic ion accelerators used for in-space propulsion. Past experimental and analytical efforts have resulted in thruster designs that exhibit attractive performance; however, many of the processes involved with the discharge plasma are still not fully understood. A better understanding of these processes is necessary to advance the state of the art of ion thruster design and performance.

This chapter motivates this dissertation by identifying the needs of proposed ion thruster applications and the related benefits that come from a greater understanding of discharge processes. Section 1.1 presents the recent ion thruster applications that have proven the usefulness and efficiency of ion thrusters. Section 1.2 discusses the needs of proposed space missions, which require significant advancements in the performance, life, and scaling of ion thruster designs. Section 1.3 introduces the reasons why a better understanding of discharge processes is vital to designing efficient miniature ion thrusters and validating thruster life and performance for high-power, long-duration ion thruster missions. Section 1.4 provides a chapter-by-chapter overview of this dissertation and discusses how experimental and computational efforts are combined to reveal important discharge plasma processes and behavior.

In this dissertation "ring-cusp" ion thrusters are solely addressed. A description of ring-cusp ion thrusters and details of their operation are given in Chapter 2. Early ion thrusters used mercury and cesium propellant; however, ion thrusters are no longer being developed for these propellants due to concerns related to propellant handling, toxicity, and spacecraft contamination [1, 2]. Modern ion thrusters use noble gas propellants (typically xenon) which are significantly less contaminating to spacecraft surfaces and greatly simplify propellant handling [3]. This study focuses on ion thrusters using noble gas propellant. As discussed in Section 1.1, the first operational ion thrusters used xenon propellant.

In this dissertation ring-cusp ion thruster sizes will be categorized as follows:

1. **Conventional:** Discharge diameter ~10–30cm. Range of ion thruster sizes used for in-space operational applications as summarized in Section 1.1.
2. **Large:** Discharge diameter >30cm. Large ion thruster sizes that have not, to date, been used for in-space applications (refer to Section 1.2).
3. **Small:** Discharge diameter ~5–10cm. Range of small laboratory-model ion thruster sizes that have exhibited desirable performance (refer to Section 2.4).
4. **Miniature:** Discharge diameter <5cm. Laboratory-model and conceptual ion thruster sizes that had not demonstrated desirable performance at the inception of this study in 2001 (refer to Section 2.4).

1.1 Recent Ion Thruster Applications

Ion thrusters have been successfully used on Earth orbiting satellites, and have recently demonstrated desirable performance and lifetime for deep space, long duration missions [2]. In 1998, the first operational in-space ion thrusters were launched as part of a Hughes-built communication satellite. These 13cm diameter Xenon Ion Propulsion System (XIPS) thrusters, Figure 1.1-1, were successfully used for North-South station keeping (NSSK) [4]. The following year, 25cm XIPS thrusters were used for NSSK and final geosynchronous orbit insertion as part of the Boeing (formerly Hughes) 702 spacecraft bus. The 25cm XIPS thruster can operate at 4.2kWe maximum input power.

Figure 1.1-1. XIPS Ion Thruster
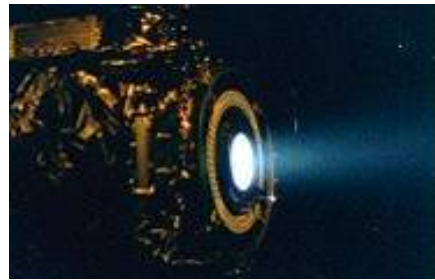
Figure 1.1-2. Flight NSTAR Thruster firing on Deep Space 1 Spacecraft During Solar Thermal Vacuum Test

The first ion thruster to be used as the main propulsion for a deep space exploration mission was launched in October 1998 as part of the New Millennium Deep Space 1 (DS1) spacecraft. This lightweight 30cm diameter ion thruster, shown in Figure 1.1-2, was developed under the NASA Solar Electric Propulsion Technology Application Readiness (NSTAR) project, and is commonly referred to as the NSTAR thruster. This thruster demonstrated 93mN of thrust and 3100 seconds specific impulse at maximum input power of 2.3kWe. The thruster successfully operated for 16,285 hours in flight, which is the longest time a thruster has been operated in space. A ground-based test of an identical thruster, which operated for over 30,000 hours, suggests that even greater thruster life was possible [5].

1.2 Proposed Ion Thruster Applications

Miniature Ion Thruster Applications

The minimum diameter of efficient ion thruster designs is typically over 5cm due to the challenges associated with reducing ion thruster size. Small ion thruster designs have historically exhibited poor discharge performance, and hence overall efficiency, which has precluded their consideration for many space missions [1]. A discussion of previous and recent efforts to miniaturize ion thrusters is given in Section 2.4.
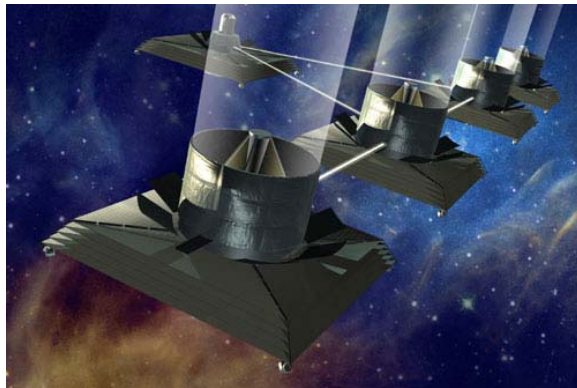
Figure 1.2-1. Proposed Terrestrial Planet Finder Interferometer (TPF-I)

Many missions will benefit greatly if the advantages of ion thrusters can be realized at smaller sizes. In particular, miniature ion thrusters (~3cm) may provide attractive performance for formation flying missions with medium sized spacecraft (~1,000kg). An example of such a mission is the proposed Terrestrial Planet Finder-Interferometer (TPF-I), Figure 1.2-1, which will use precise infrared interferometry to locate and analyze extra-solar planets. An analysis of the formation flying requirements for TPF-I, given in Appendix A, shows that this mission requires ~1.5mN of low-noise, continuous thrust. These conditions are met by a 3cm ion thruster that is discussed in Chapter 3. As a result of this study, the Miniature Xenon Ion (MiXI) thruster presented in Section 3.6 was recently chosen as the baseline for the TPF-I mission.

For large spacecraft (> 1,000kg), miniature ion thrusters (closer to ~5cm diameter) may be considered for attitude control. This could be attractive for missions that are already using noble gas propellant for the main propulsion. For small spacecraft (~100kg), a miniature ion thruster may be considered as primary propulsion. For example, small Earth orbiting satellites may use a miniature ion thruster for orbit raising and maintenance, as is done on a larger scale with many current commercial and military satellites. They could also be considered as primary propulsion for a scaled-down asteroid rendezvous mission similar to DS1. On another note, a small ion thruster may be considered for supplying continuous-thrust "artificial gravity" for an inspection and repair robot for a very large spacecraft.
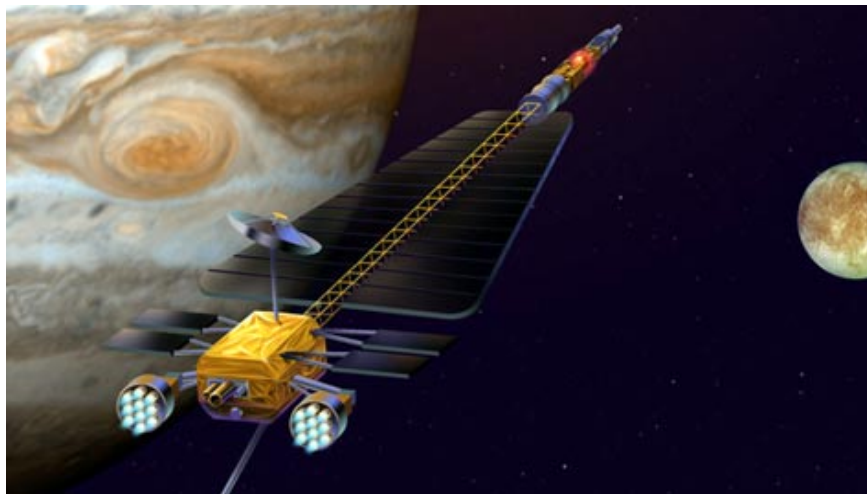
Figure 1.2-2. Proposed Jupiter Icy Moon Orbiter (JIMO)

Long Duration, High Power Missions

Past and recent missions, such as those using XIPS and NSTAR thrusters, require less than five years of effective thruster lifetime and have used "conventional" ion thruster sizes that range in characteristic diameter from 10-30cm. Large ion engines (~60cm diameter) are currently being considered for long duration (>10 years) deep space missions such as the proposed Jupiter Icy Moons Orbiter (JIMO)

and follow on efforts (Figure 1.2-2). These thrusters are currently required to operate for the life of the mission at over 20-30kWe of power and specific impulse over 6000 seconds [6]. From these requirements it is clear that future space missions may require far greater ion thruster lifetime, size, power, and specific impulse than thus far been demonstrated.

1.3 Purpose of Study

The following discussion shows that identifying the <u>discharge plasma processes of ring-cusp ion thrusters</u> is necessary to:

1. Understand the challenges of thruster miniaturization

2. Aid in the validation of thruster life and long-term performance

Previous efforts to reduce ion thruster size have failed to identify the fundamental mechanisms associated with the miniature discharges and have, consequently, not achieved desirable performance at thruster diameters less than 5cm [1]. This study uses a combination of experiments, theory, and computational modeling to identify the challenges of miniature discharges and demonstrate a design for an efficient miniature ion thruster.

The validation of high-power, long-life ion thrusters for the missions in Section 1.2 requires a better understanding of ion thruster performance, life, and scaling. Experimental life tests, such as the 8,200-hour and 30,000-hour NSTAR life test, are impractical and prohibitively expensive for validating ion thruster life and performance for future long-duration, high-power missions [7,5].   Thruster component wear changes the performance of the thruster over the life of the mission. As discussed in Section 2.4, existing ion thruster discharge theory and models are insufficient to provide necessary inputs to multi-dimensional computational models that are designed to predict the wear rates and long-life

performance behavior of thruster components (i.e., discharge cathode and grids) [8,9]. Therefore, a multi-dimensional discharge model that can be used with cathode and grid wear models is important to validating the long-term performance and life of future ion thrusters. Such a model can also be used to aid design efforts to increase propellant efficiency, which would yield significant propellant mass savings for large propellant throughput missions such as JIMO. This study presents a multi-dimensional computational model of an ion thruster discharge (Chapter 4) that self-consistently accounts for the behavior and interactions of the discharge plasma species for a large range of thruster geometries and magnetic fields. This Discharge Model is designed to help identify important discharge plasma processes, aid in the design of ion thrusters, and integrate thruster component and wear models.

1.4 Overview of Dissertation

In this section, a brief overview of the content and interrelationship of the chapters is given. Where appropriate, the chapters are introduced as part of a brief history of this four-year study to help the reader understand the order in which the material is presented.

Chapter 2 provides an overview of ring-cusp ion thruster operation and discharge chamber processes, including a review of previous work in this area and a discussion of important issues. Section 2.4 presents a history of ion thruster miniaturization and discharge chamber modeling. My interest in ion thrusters began when Dr. Jay Polk, my Space Propulsion instructor at Caltech, invited me to JPL to investigate a miniature ion thruster that had yet to produce stable discharge plasma. The thruster was the smallest of its kind (only 3cm in diameter), so I jumped at the chance to test the limits of this technology. A commonly-held perception at the time was that inordinately strong magnets were necessary for an efficient miniature ion thruster. Ignoring this perception, I was able to generate a

stable discharge using simple magnetic fields that I assembled using the existing thruster design and the available magnets. This initial effort, as reported in Appendix B, was considerable since I was able to maintain a stable plasma discharge and extract an ion beam (which had not been done before with this thruster). However, in this first effort, the efficiency was poor in comparison with conventional thruster sizes. As discussed in Section 3.1-3.2, I redesigned the thruster to accommodate a large range of discharge chamber configurations and compared their performance experimentally. The performance of many of these configurations was far superior to those investigated in Appendix B and previous miniature ion thrusters [1]. The highest magnetic field configurations that were tested exhibited very poor performance; this phenomenon was later attributed to discharge instabilities (Section 2.3). The best configuration from Section 3.2 was further investigated in hopes of realizing performance on par with larger thrusters. First, as discussed in Section 3.3 and Appendix D, I developed a non-intrusive technique to find the plasma density profile inside the thruster. Once found, the density values were used to investigate the performance of the ion extraction grids, per the analysis in Section 3.4. This analysis suggested that a simple modification of the ion optics resulted in thruster performance comparable to larger ion thrusters. These modifications were verified experimentally, thus demonstrating a significant improvement over the state of the art. Efforts to miniaturize and increase the efficiency of the thruster cathodes are presented in Section 3.5 and Appendix E, including a new propellant-less cathode concept that has shown impressive performance. In Section 5.6, experimental results from an improved, lightweight thruster design clearly show that an efficient miniature ion thruster can be designed using reasonable magnet sizes.

Since existing discharge chamber theory (as reviewed in sections 2.3 and 2.4) was insufficient to adequately explain the experimental behavior of the various configurations presented in Chapter 3, I decided to create a computational model to simulate the discharge chamber plasma. Such a computational model is also very

attractive for validating thruster life and long-term performance, as discussed in sections 1.3 and 2.4. The "Discharge Model" presented in Chapter 4 is designed to yield unprecedented levels of detail of discharge processes to aid in the understanding of ion thruster miniaturization and integrate with component wear models. This hybrid multi-component model self-consistently tracks the behavior of the dominate plasma species of arbitrary ring-cusp geometries (Section 4.1). To minimize run-time the neutral propellant atoms are treated using techniques similar to thermal transport view factors, as described in Section 4.2. High-energy primary electrons are tracked with a Boris-type predictor-corrector algorithm while secondary electrons are treated as a quasi-neutral component of the plasma (Section 4.3). An ion optics code that was independently developed at JPL is used to determine both ion and neutral transparency for the ion extraction grids (Section 4.4). The Ion Diffusion Sub-Model, presented in Section 4.5, assumes ambipolar plasma diffusion with a non-classical correction for perpendicular diffusion of secondary electrons. A correction is used to approximate double ion density and beam current. The non-uniform temperature of the secondary electrons is estimate using an electron thermal model (Section 4.6).

In Chapter 5 the Discharge Model is shown to compare well with beam profiles, performance data, and a discharge performance curve from NSTAR thruster tests conducted at JPL. In Section 5.2, the model is used to perform a discharge design analysis which suggests that the NSTAR thruster performance would be greatly improved by a simple modification to the magnetic field design. In Chapter 6 the Discharge Model is compared to the miniature thruster data from Chapter 3, and shows generally good agreement. The results for the miniature thruster show that the primary electron confinement is very poor in comparison to the NSTAR thruster. In Section 6.2, computational design sensitivity for the miniature ion thruster shows good agreement with experimental results, thus confirming that the Discharge Model can be used to aid thruster design efforts.

The results from this study are discussed in Chapter 7. Section 7.1 identifies the issues that bracket the performance of miniature ion thrusters: primary electron confinement efficiency and discharge stability. For conventional ion thrusters the results of the model suggest that primary electrons dominate the thruster performance, but not to the extent of the miniature discharge (Section 7.2). In Chapter 8 it is concluded that this study has advanced the understanding of ion thruster discharges considerably by investigating the performance of both miniature and conventional ion thrusters. Future efforts will yield improved performance of the miniature ion thruster develop herein and will also increase the usefulness of the computational model.

Chapter 2

Ion Thruster Discharges

Ion thrusters generate thrust by ionizing a propellant gas inside a discharge chamber and electrostatically accelerating the resulting ions through a set of ion extraction grids. This chapter provides an overview of these processes, performance parameters, and the importance of the discharge chamber to overall thruster performance. Section 2.1 discusses the basic processes of direct current (DC) ring-cusp ion thrusters. Section 2.2 presents the parameters by which thruster performance is assessed, showing that discharge performance is critical to achieving favorable efficiency for ion thrusters. The major aspects of ring-cusp ion thruster discharges are presented in Section 2.3. The areas of ion thruster discharge research that are critical to future missions are described in Section 2.4, including an overview of previous work in miniature ion thrusters and ion thruster modeling.

2.1 DC Ring-Cusp Ion Thrusters

Ion thrusters use three basic processes to generate thrust: propellant ionization in the discharge chamber, electrostatic acceleration of positive ions through grids, and beam neutralization. These processes are summarized in Figure 2.1-1 along with a

basic schematic of a DC ring-cusp ion thruster and a simplified electrical diagram of required power supplies. For a DC ring-cusp discharge, the energy necessary to ionize the propellant is provided by high-energy electrons that are emitted from a cathode and confined by a ring-cusp magnetic field. A detailed discussion of the discharge chamber is left for Section 2.3. A fraction of the ions in the discharge are accelerated through a pair of biased grids at the exit of the thruster to generate thrust. The positive ions that exit the thruster through the grids constitute a current that can cause the thruster and spacecraft to quickly obtain an overall negative charge. Consequently, a neutralizer cathode is placed near or in the beam to emit electrons into the positive ion beam. This process will keep the spacecraft from obtaining an overall negative charge while also preventing an increase in positive space-charge potential just outside of the thruster exit.
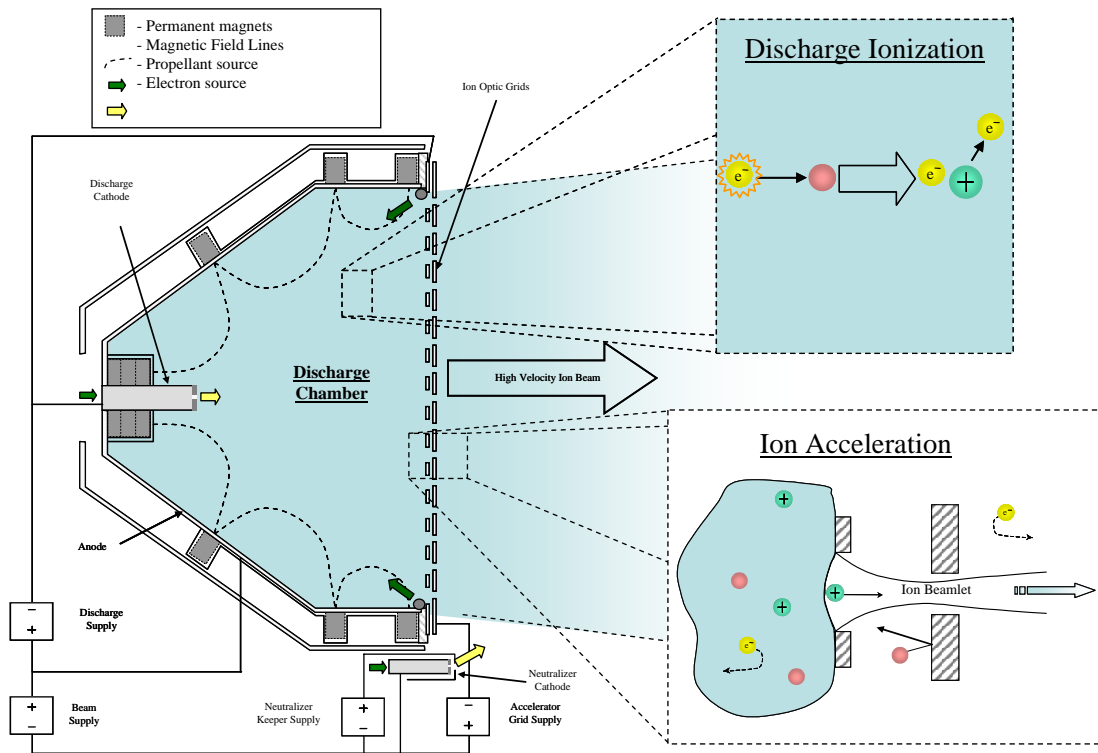

Figure 2.1-1. Example DC Ring-Cusp Ion Thruster Cross-Section with Basic Electrical Diagram (with Hollow Cathodes)

The ion extraction grids are placed at one end of the thruster and are designed to preferentially allow the ions to exit the thruster while containing un-ionized propellant. The grids must be adequately spaced to minimize the possibility of arcing between the grids (since the potential between the grids is typically over 1,000V). For many ion thrusters, the grids are typically dished to provide adequate rigidity and to control the direction of thermal deflections (i.e., to assure that both grids deflect in the same direction) [10].

The design of the ion extraction grids is critical to thruster lifetime and performance. Results in Chapter 3 show that careful consideration of the grid geometry was necessary for favorable performance of a miniaturized ion thruster. Figure 2.1-2 shows a single beamlet of a two-gird system where the screen grid is responsible for focusing the ions through the smaller accelerator or "accel" grid apertures. The screen grid is biased negative with respect to the chamber plasma to prevent discharge electron losses to this surface. For grid design, it is generally desirable to maximize ion transparency and minimize neutral atom transparency for a given range of upstream plasma conditions. In this way, the loss of un-ionized propellant is minimized and thruster efficiency is increased. The relatively smaller open area fraction of the accel grid reduces the loss of neutral propellant atoms from the discharge chamber. The accel grid aperture must be sufficiently large to allow extraction of the desired beamlet current without ions directly hitting the upstream side of the accel grid. For a given grid geometry, there is a range of discharge ion densities over which essentially all the ions exit the thruster without hitting the accel grid [11,12]. To prevent extreme accel grid erosion due to direct ion impingement, it is important to assure that the discharge plasma densities near the grids are within this range over the entire extent of the grids.

The accelerator grid is biased negative to space-ground potential to prevent the back-streaming of neutralizer electrons into the highly positive discharge chamber, since electron back-streaming reduces thruster efficiency. The magnitude of the

accel grid voltage necessary to avoid electron back-streaming is minimized by reducing the radii of the accel grid apertures or increasing the accel grid thickness.
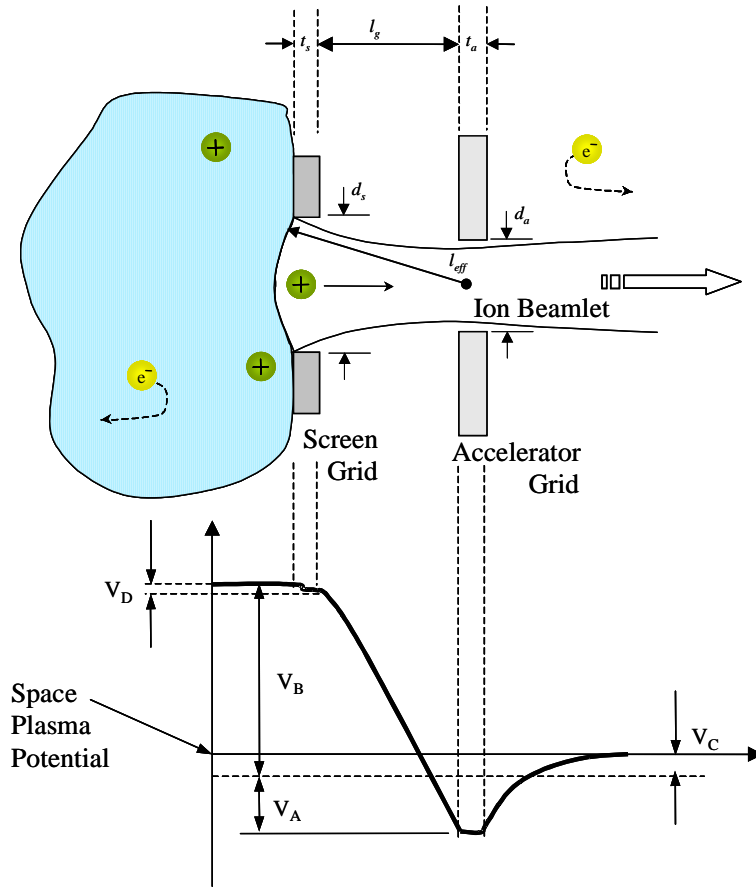
Figure 2.1-2. Detail of Ion Extraction Grid Beamlet

2.2 Thruster and Discharge Performance

This section presents a brief overview of thruster performance parameters and shows that discharge performance is indelibly tied to all major aspects of thruster performance. As shown below, discharge performance is judged by: the power needed to create beam ions, the fraction of propellant that leaves the thruster as ions, and the "flatness" of the beam profile.

The electrical efficiency, η_E, is the ratio of kinetic power in the beam and the total thruster input power, P_E, by

$$\eta_E \equiv \frac{J_B V_B}{P_E} \qquad \text{[2.2-1]}$$

where

$$P_E = J_B V_B + J_D V_D + P_o \qquad \text{[2.2-2]}$$

and J_B, V_B, J_D, V_D, P_o, are the beam current, beam voltage, discharge current, discharge voltage, and miscellaneous power (which includes cathode power). Combining these relationships results in an expression defined as the discharge loss, ε_B, which is inversely proportional to the engine efficiency:

$$\eta_E = \frac{J_B V_B}{J_B V_B + J_D V_D + P_O} = \frac{V_B}{V_B + \varepsilon_B + P_O / J_B} \qquad \text{[2.2-3]}$$

where

$$\varepsilon_B \equiv \frac{J_D V_D}{J_B} \qquad \text{[2.2-4]}$$

The discharge loss can be interpreted as the amount of discharge power used to create a single beam ion (assuming only singly charged ions in the beam) and has units of watts per beam ampere, or, as is typically used, eV/ion. The discharge loss is similar to the frozen flow losses in chemical propulsion.

Another important discharge performance parameter is the discharge propellant utilization, η_{ud} (the fraction of the discharge propellant flow that leaves the thruster as beam ions), which is calculated by

$$\eta_{ud} \equiv \frac{\left(J_B^+ + J_B^{++}/2\right) m_i}{e \dot{m}_d} \qquad \text{[2.2-5]}$$

where $\dot{m}_d$ and m_i are the mass flow rate of discharge propellant and the ion mass, e is electron charge, and J_B^+ and J_B^{++} are the beam currents due to single and double ions, respectively. Discharge performance for different thrusters and operating

15

conditions is commonly assessed using "performance curves," which are generated by plotting ε_B vs. η_{ud}, as shown in Figure 2.2-1. Performance curves typically show that discharge losses gradually increase with propellant efficiency until the "performance knee," beyond which the discharge losses increase rapidly. The knee is considered the optimal point of operation with regard to discharge performance [3]. These curves are used to compare discharge performance for multiple miniature ion thruster configurations in Chapter 3. For conventional and large ion thrusters, ε_B and η_{ud} are typically near 200eV/ion and >80%, respectively.
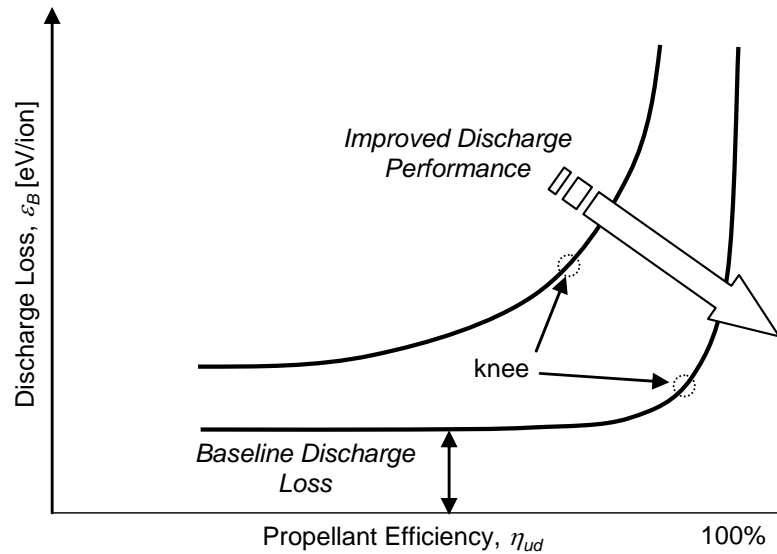
Figure 2.2-1. Discharge Performance Curves

In most experiments double ion current is not measured, so an ideal propellant efficiency is often used. By assuming the beam is entirely composed of single ions, the ideal discharge propellant efficiency is

$$\eta_{ud[*]} = \frac{\left(J_B\right)m_i}{e\dot{m}_d}$$

[2.2-6]

where

16

$$J_B \equiv J_B^+ + J_B^{++}$$

[2.2-7]

Using the ideal discharge propellant efficiency, the ideal thrust is given by

$$T_{ideal} = \dot{m}_d \eta_{ud[*]} u_B$$

[2.2-8]

where the velocity in the beam is $u_B = \sqrt{2eV_B/m_i}$. This allows the ideal thrust to be expressed as

$$T_{ideal} = J_B \sqrt{2m_i V_B/e}$$

[2.2-9]

Departure from ideal thrust for ion thrusters is primarily due to the effects of double ions and beam divergence. Thrust corrected for these conditions is expressed as

$$T_{corr} = \alpha F_T T_{ideal}$$

[2.2-10]

where α and F_T are the corrections for double ions and divergence respectively. The double ion thruster correction can be simply defined with the double- to single-ion ratio as

$$\alpha = \left(1 + \frac{J_B^{++}\sqrt{2}}{J_B^+ 2}\right) \bigg/ \left(1 + \frac{J_B^{++}}{J_B^+}\right)$$

[2.2-11]

The thrust correction due to beam divergence is defined as the ratio of the axially-aligned beam current to the total beam current. For a single ion species this is expressed as

$$F_T = \int_A j_B \cos(\phi) dA \bigg/ \int_A j_B dA$$

[2.2-12]

where j_B is the beam current density, ϕ is the local beam angle, and A is the area of the grids.

The total efficiency of the thruster is the ratio of the thrust power (jet power) divided by the input electrical power:

$$\eta_T \equiv P_T / P_E \qquad \text{[2.2-13]}$$

The total efficiency of a conventional ion thruster is typically >50%. Assuming no propellant is required for the neutralizer, the thrust power is defined as

$$P_T \equiv \frac{T_{corr}^2}{2\dot{m}_d} \qquad \text{[2.2-14]}$$

Combining the above equations, the total efficiency is shown to be directly proportional to the ideal discharge propellant utilization by

$$\eta_T \equiv (F_T \alpha)^2 \eta_{ud[*]} \eta_E \qquad \text{[2.2-15]}$$

Equations 2.2-11 and 2.2-15 show that it is desirable to maximize η_{ud} and minimize double ion content. Double ions also increase discharge loss, ε_B, due to the relatively high electron energy lost during a double ionization collision.

The specific impulse for ion thrusters is defined by the ratio of the thrust to the product of the propellant mass flow rate and the acceleration of gravity at Earth's surface using

$$I_{sp} \equiv \frac{T_{corr}}{\dot{m}_d g} \qquad \text{[2.2-16]}$$

where it is again assumed that no neutralizer propellant is required. Putting the specific impulse in terms of the discharge propellant utilization yields

$$I_{sp} = \frac{\alpha F_T \eta_{ud[*]}}{g} \sqrt{\frac{2eV_B}{m_i}} \qquad \text{[2.2-17]}$$

Grid Performance and Utilization

The fundamental purpose of the grids is to prevent the loss of propellant neutrals while allowing the ions to be extracted and accelerated. Therefore, utilization of

the grids can be determined by examining the beam and neutral loss profiles at the grid exit plane. To assess how evenly the ion extraction grids are being used, the beam flatness parameter, F_B, relates the average to the peak beam current density by

$$F_B = \frac{\int_0^R 2\pi r j_B(r) dr}{\pi R^2 j_{B\max}}$$

[2.2-18]

where r, R, j_B, and $j_{B\max}$ are the radial coordinate of the beam, the total grid radius, and local and maximum beam current density [13]. As discussed in many references [14,7], a low flatness parameter typically results in poor grid performance and localized grid wear. Ion optics grids exhibit optimum performance (typically measured by low beamlet divergence) for a relatively small range of upstream ion densities. Therefore, a low flatness parameter implies that a large fraction of the beamlets is performing below optimum levels. Since the beam flatness is directly related to the plasma distribution in the discharge chamber, a low flatness parameter, even though it manifests in low "grid" life and performance, is more appropriately attributed to poor discharge design.

2.3 Basic Discharge Characteristics

Ion thruster discharge chambers are used to create positive ions that are extracted to form the beam. DC ring-cusp ion thruster discharges use a ring-cusp magnetic field to contain the high-energy electrons that provide the energy to ionize the propellant.

DC Ring-Cusp Ion Thruster Discharges

For DC ion thrusters, the power needed to ionize the neutral propellant atoms comes from high-energy electrons that are emitted from the discharge cathode. These primary electrons (or "primaries") are accelerated to relatively high energies by the (~25V) voltage between the cathode and anode surfaces, which is applied by the discharge power supply. A magnetic field is used to prevent the loss of

electrons to the anode surface to increase ionization efficiency. For a ring-cusp discharge, as shown in Figure 2.1-1, alternating rings of high-strength magnets (typically SmCo) are used to provide magnetic confinement of the primaries at the magnetic cusps and throughout the discharge volume. For a typical ring-cusp thruster, the magnets are arranged so that the magnetic field lines primarily terminate on cathode potential surfaces or at cusps on the anode surfaces. In this way, primaries are confined by magnetic reflection at the cusps or by electrostatic forces at the cathode potential surfaces. The magnetic cusps are placed at anode surfaces to allow lower energy electrons ("secondaries") to be lost along the field lines to carry the discharge current and maintain discharge stability [15]. The low-energy secondaries are produced by primary electron collisions with plasma species and ionization by other secondaries. A discussion of primary and secondary electron collisions is given in Section 4.3.

Neutral propellant atoms are injected into the discharge chamber through a main propellant feed, the location of which varies from thruster to thruster. Most conventional DC thrusters use a hollow cathode, which requires propellant to run, so additional propellant is introduced through the hollow cathode orifice. At this time, the most widely used propellant is xenon due mainly to its high mass, low-risk handling, and relatively high second ionization threshold; however, other propellants may be used [3]. Discharge chambers should be designed to minimize double ionization to avoid the performance losses mentioned in Section 2.2. Measurements of the NSTAR thruster beam have shown a noticeable fraction of double ions [16]; thus showing that state-of-the-art thruster design may be improved by reducing this phenomenon.

Discharge Performance and Stability

DC ring-cusp ion thruster discharge performance is dominated by two competing parameters: plasma confinement efficiency and discharge stability. Plasma confinement efficiency requires sufficiently strong magnetic fields to confine the

plasma (including primaries) at the cusps and throughout the bulk of the plasma. Magnetic confinement of the bulk plasma is conventionally thought of as "closing" a certain B-field contour, typically on the order of 10s of Gauss as discussed in Beattie [17]. This concept is assumed to assure that the plasma is reasonably confined between the cusps. For larger diameter ring-cusp ion thrusters, such as NEXIS (~60cm) and NEXT (~40cm), additional magnetic rings were added to close a sufficiently high B-field contour for desirable plasma confinement [18].

Discharge stability for ring-cusp ion thrusters can be understood by examining the behavior of the plasma near the cusps. Many detailed experiments and models have been used to explain the behavior of the plasma in the cusp region [19,20,15,21,22]. Leung, et al [19] showed that primary electrons are typically very well confined at the cusp and that plasma losses to the cusps may be described using a hybrid ion-electron gyroradius. This parameter was used by Goebel [15] to explain the discharge instabilities that can result for cusp magnetic field strengths that are too high for certain plasma conditions. These discharge instabilities are due to overly high cusp B-field strengths that can cause an electron current continuity imbalance that leads to plasma discharge loss due to impedance shift instabilities. The continuity imbalance arises from the reduction in plasma loss area that results from increased cusp strengths, as observed by Leung and Hershkowitz [19,20]. If the cusp B-field is too strong then the plasma potential, which is normally positive, will tend negative to satisfy current continuity for a particular range of electron production rates in a cusp confined plasma. This lower plasma potential reduces the energy of the primary electrons emitted from the cathode, leading to a runaway of the plasma potential indicative of an unstable discharge. The discharge instabilities impose an upper-limit for the cusp B-field for a given plasma conditions. These instabilities are found for certain operating conditions in conventional ion thrusters and can be used to describe miniature ion thruster behavior as discussed in chapters 3 and 7.

21

2.4 Important Areas of Ion Thruster Discharge Research

A greater understanding of the plasma discharge processes is necessary to extend ion thruster technology to smaller discharge chambers and long-duration, high-power missions. In this dissertation, experimental testing and computational modeling are combined to achieve this understanding and is used to identify some basic discharge mechanisms. Previous investigations on these discharges have provided insight but do not allow detailed analysis of discharge processes and cannot provide the information needed for thruster wear predictions. As a result, current ion thruster discharges are designed almost exclusively with empirical methods and life validation requires extremely expensive long duration testing. Past designs of small ion thrusters have exhibited poor total efficiency that can be mainly attributed to low propellant efficiency and high discharge losses.

Miniature Ion Thruster Discharges

A comprehensive review of miniature ion thruster efforts before the year 2000, presented by Mueller [1], states,

> *"...at this point Micro-Ion engines have to be considered very advanced micropropulsion concepts that still have to overcome many feasibility concerns before they can be seriously considered for microspacecraft applications."*

The poor performance of smaller thrusters is largely attributed to high wall loss in the discharge due to inherently higher surface to volume ratio. The following review of past and recent ion thruster performance shows that small ion thrusters (5-10cm) have demonstrated efficiency near that of conventional thrusters, whereas miniature ion thrusters (<5cm) developed in other efforts have proven much less efficient.

As discussed in Chapter 1, ion thrusters using cesium and mercury are no longer developed and are not considered in this study; however, a significant range of ion

thruster sizes was investigated using these propellants in past efforts, and should be mentioned here. In the 1960s cesium contact ion thruster, typically ranging from 5 to 7cm in diameter, were developed and flown. Ground testing of a 1.3cm diameter (2.54cm in length) cesium contact ion thruster demonstrated poor total efficiency of 5-20% [1]. From the late 1960s through the early 1980s, mercury ion thrusters were developed ranging is size from 5cm to 150cm diameter, with a noticeable reduction in performance at smaller sizes [2].

Since the switch to noble gas propellants (i.e. xenon) in the early 1980s, ion thruster development has mainly focused on conventional ion thruster sizes (10-30cm), where discharge efficiency, measured by ε_B and η_{ud}, are typically near 200eV/ion and >80%, respectively. Some efforts to develop small ion thrusters (5-10cm) have yielded efficiencies on order, though noticeably less, than conventional ion thrusters. A 7cm diameter ring cusp ion thruster developed at Colorado State University exhibited discharge losses from 300-600eV/ion over a range of 25-70% propellant efficiency [23]. More recently, NASA Glenn tested an 8cm ring-cusp ion thruster over a range of $\varepsilon_B \sim$ 220-395eV/ion and $\eta_{ud} \sim$ 68-83% [24]. In 2000, Keldysh Research Center in Russia tested a Kaufman-type ion thruster (6cm discharge, 5.2cm anode) with performance of $\varepsilon_B \sim$ 220-525eV/ion and $\eta_{ud} \sim$ 77-81%. For conventionally-sized thrusters, Kaufman-type discharges have been essentially phased-out due to the superior performance of ring-cusp discharges [25] and concerns related to cathode pole piece wear [2].

In 1997, Yashko used a computational model to illustrate the perception that reducing ring-cusp ion thrusters to miniature sizes (<5cm) requires permanent magnet strengths beyond those currently available [26]. Due in large part to this perception, many recent miniature ion thruster efforts focused on magnet-less ion thruster concepts. The Hollow Cathode Micro-Thruster (HCMT) developed at NASA Glenn is a magnet-less ion thruster that is designed to accelerate the ions that are emitted from a discharge hollow cathode [27]. The original design of this

thruster produced very low discharge efficiency of $\varepsilon_B \sim$ 4200-4300eV/ion and $\eta_{ud} \sim$ 14%. Another magnet-less approach is to use a Radio-Frequency (RF) discharge, which uses an inductively coupled RF field to accelerate the ionizing discharge electrons. Reference [28] reports on a ~3cm diameter RF thruster that uses 5sccm of xenon flow to generate a plasma sufficient to create a predicted maximum thrust of 0.6mN at 1kV beam voltage. For these values, the propellant efficiency is ~8.4%. The "ion thruster-on-a-chip" concept [29], suggests using several parallel micro-machined linear channels, ~100μm × 300μm × 10cm, to create an RF generated plasma and accelerate the resulting ions. Yashko [26] predicted very high discharge losses on the order of 1100-5000eV/ion for this concept by using modified versions of Brophy's of Arakawa's models, which are discussed below.

The efforts summarized above show that an efficient miniature ion thruster has not been developed using a magnet-less approach. In Chapter 3 a relatively efficient miniature ion thruster is developed using magnetically confined discharge plasma. A comparison of this thruster's performance with other ion thrusters is given in Section 3.6. A similar electrostatic thruster technology (called a "microwave engine") using a magnetic miniature "open" discharge (i.e., without ion extraction grids) has been developed by the Advanced Technology Institute Ltd. in Japan [30]. This grid-less thruster uses a microwave discharge (1.6cm discharge with 1.9cm beam opening) and microwave neutralizer and has undergone nearly 7200 hours of operation [31]. The thruster nominally runs at 10.9% total efficiency, 0.5mN of thrust, and I_{sp} of 1371sec due to an accelerating voltage of only 250V. Since this thruster technology does not use ion extraction girds and operates at a lower regime of accelerating voltages, it will not be used for performance comparison is Chapter 3.

Long-Term Thruster Performance

Since ion thrusters provide relatively small levels of thrust they must run for extremely long times (>10,000 hours) to provide sufficient delta-v for most space

missions. Existing designs of conventional thruster sizes (>10cm) provide desirable performance; however, the challenge is to sustain this performance for the life of the missions. The 30,352 hour NSTAR Extended Life Test (ELT) identified two critical thruster wear mechanisms that degrade thruster performance over time and limit thruster life: accel grid erosion and discharge cathode erosion [5].

Figure 2.4-1 shows the end-of-life wear of the NSTAR accel grid, which resulted in increased hole sizes and "pits and groove" wear patterns between the grids. Over the life of the thruster, this erosion caused a monotonic, and substantial, decrease in the thruster performance and increased electron back-streaming, and would have eventually led to grid failure [7,5]. As discussed in Reference [12], accel grid erosion results primarily from charge-exchange (CEX) ions that are produced in the ion beamlet. Two- and three-dimensional computational models have been developed to predict accel grid erosion [12,9]. At this time, the upstream plasma and neutral atom conditions that are used in these models are inferred from experimental data; however, accurate determination of accel grid erosion and its effects on ion thruster performance will require detailed discharge plasma and neutral atom information over the life of the thruster. The Discharge Model, presented in Chapter 4, is designed to provide this information.
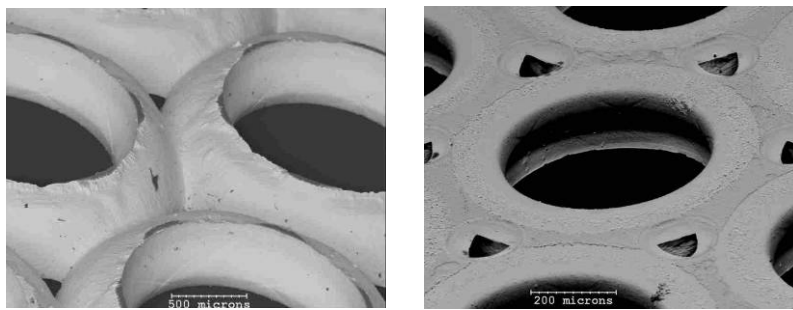

Figure 2.4-1. NSTAR Accel Grid Erosion (30,352 hours)

During the ELT, the discharge cathode experienced significant erosion of the keeper face and cathode orifice. As shown in Figure 2.4-2, the keeper face was completely eroded away during the test, which resulted in significant erosion of the

cathode heater that would have eventually resulted in complete loss of the discharge cathode. In addition, erosion of the cathode orifice resulted in changes in cathode and discharge performance. A two-dimensional model of the cathode insert region (located inside the cathode) and near-cathode region of the discharge chamber is currently under development that will integrate with the Discharge Model that is presented in Chapter 4 [8]. The combined cathode and discharge models will be used to increase the understanding of the mechanisms that cause keeper erosion, investigate methods to minimize the erosion, and determine long-term performance.

| 0 hours | 30,352 hours |
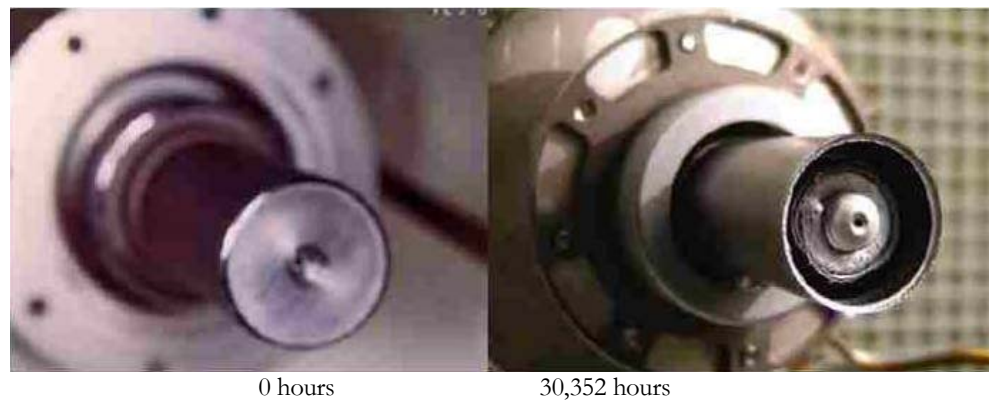
Figure 2.4-2. NSTAR Discharge Cathode Erosion

Ion Thruster Discharge Modeling

Existing analytical models of ion thruster discharges are useful for quantifying some of the discharge performance characteristics of existing thruster designs; however, they are rarely used for design. Many of these models are based on an analytical model that was originally presented by Brophy [32] in 1984. Brophy's model uses discharge current and power balance equations, along with volume-averaged relationships, to develop simple algebraic equations that very clearly describe the overall performance trends of ion thrusters. This model is useful for understanding the general performance of known thruster designs, but does not explain discharge characteristics that are imperative to advancing the state of the art of discharge design.

To date, multi-dimensional modeling of ion thrusters has been almost entirely limited to predicting two important parameters in Brophy's model: the primary utilization factor, C_o, which is proportional to the average distance a primary would travel in the absence of inelastic collisions, and, f_B, the fraction of discharge ions extracted to the beam. Arakawa and Ishihara [33], presented a model (combined with models in references [34] and [35]) that determines values for C_o and f_B, which are then used in Brophy's model to predict the thruster performance. Arakawa and Ishihara's 2-D model tracks primary electron motion and only considers elastic neutral collisions to determine a relative primary density and C_o. The relative primary density is then used to determine ion generation, which is applied to a simplified ion diffusion equation to determine f_B. By ignoring inelastic collisions in the primary electron algorithm, the model does not self-consistently account for the interaction of the plasma species. Arakawa and Ishihara's model is limited to simple cylindrical discharges and assumes no double ionization, uniform neutral density, and uniform ion, secondary electron, and neutral temperatures. Yashko [26] used Arakawa's model to investigate thruster scaling but found Arakawa's magnetic analysis to produce erroneous results. After integrating a commercial magnetic solver, MAGNETO, in place of Arakawa's magnetic solver, he found that the model produced largely different values for thruster performance. Sandonato et al., [36] expanded Brophy's analytical model to investigate plasma stability and double ion effects. This model used a particle-pushing numerical code to estimate C_o but did not explicitly determine f_B. Some recent efforts have focused on determining C_o to compare thruster designs [37,38], however, these efforts have not been expanded to account for other effects.

Brophy's and Arakawa's models have provided useful information to the performance of conventional ion thruster designs; however, these models have not been used to successfully guide the design of an efficient miniature ion thruster and are not designed to predict long-term performance. The models also do not provide sufficient information to provide input to cathode and grid wear models [9,8]. The

27

Discharge Model that is presented in Chapter 4 represents a significant improvement over previous discharge models. The model self-consistently treats the non-uniform behavior and distribution of the primaries, secondaries, ions, and neutrals. It also determines non-uniform temperatures of the species and estimates the effects of double ions. Results from the model are presented in chapters 5 and 6. As discussed in Chapter 7, the Discharge Model provides useful insight to small and conventional discharge performance and provides sufficient information for cathode and grid wear models.

Discharge Performance Questions and Issues

Existing discharge theory and modeling are insufficient to confidently identify some of the basic characteristics of ion thruster discharges. This dissertation provides insight to the following questions about DC ring-cusp ion thruster discharges:

1) What is the relative importance of the primary and secondary electron species?

2) Why do some thrusters have poor beam profiles (low beam flatness)? If the profile possesses a double ion peak, what mechanisms are causing the double ions?

3) What is the diffusive behavior of the discharge plasma? Does it behave as weakly or fully ionized plasma?

4) To what degree is the discharge plasma magnetized?

5) How does miniature ion thruster sizes?

6) What are factors that lead to low performance for miniature ion thrusters?

In the following chapters, experimental analysis of a 3cm ion thruster and computational modeling of conventional and miniature discharges will be used to answer these questions.

Chapter 3

Miniature Ion Thruster: Testing and Optimization

Miniature ion thrusters (<5cm) have historically exhibited poor performance due, in large part, to challenges related to discharge chamber efficiency. This chapter describes the development of a 3cm miniature ion thruster that is used to help elucidate the discharge plasma processes of small diameter DC ion thruster discharges and compare with Discharge Model results for small thruster sizes. The 3cm discharge diameter size of the thruster developed herein is sufficiently small to address miniaturization issues but is not intended to represent a limit to ion thruster miniaturization. A DC discharge was chosen in hopes of capturing some of the inherent performance and efficiency advantages of this technology when compared with wave-generated discharges. A discussion of the relative performance of DC and wave-generated discharge ion thrusters is given in Appendix E.

The performance of the thruster head is the fundamental challenge to miniature ion thruster operation; therefore, miniaturization issues associated with components not within the thruster "head," such as propellant flow control and the power-processing unit (PPU), are not addressed. Sections 3.1-3.5 describe the

chronological development and optimization of the discharge chamber, ion optics, and discharge cathode for a 3cm diameter ion thruster (a brief overview of these sections is found in Section 1.4). It was found that a 3-ring-cusp magnetic field and Small Hole Accelerator Grid (SHAG) optics could be used to obtain desirable discharge performance; however, additional work is necessary to determine the best discharge and neutralizer cathode options. The knowledge gained from these experimental and computational efforts was used to design an improved miniature ion thruster configuration that is presented in Section 3.6.

3.1 Experimental Setup

The testing facility used to conduct the experiment is composed of four parts: the thruster (or "thruster head"), thruster subsystems, diagnostics, and vacuum system. The thruster head and probe diagnostics reside inside the vacuum bell jar during testing to simulate a low-pressure space environment while the thruster subsystems and power diagnostics are kept outside the vacuum system.

The thruster head is composed of the discharge chamber, discharge and neutralizer cathodes, ion extraction grids, propellant distributor, and ground screen. The experiments discussed in the following sections of this chapter predominantly used the Micro-Ion thruster shown in Figure 3.1-1. This thruster was designed to test a wide variety of magnetic field options (including electromagnets) with the use of large diameter ferromagnetic flanges and interchangeable anode geometries, as shown in Section 3.2. Results presented in Section 3.3 demonstrate that the geometry of the ion optics has a significant effect on thruster performance. In anticipation of this phenomenon, multiple isolation grid mounts were constructed to allow grid geometries to be tested very quickly and without having to disassemble and realign the grids between every test. The Micro-Ion thruster was also used for initial testing of cathode materials as discussed in Section 3.5. An optimized

thruster design was developed using the knowledge gained for the Micro-Ion thruster testing as discussed in Section 3.6.
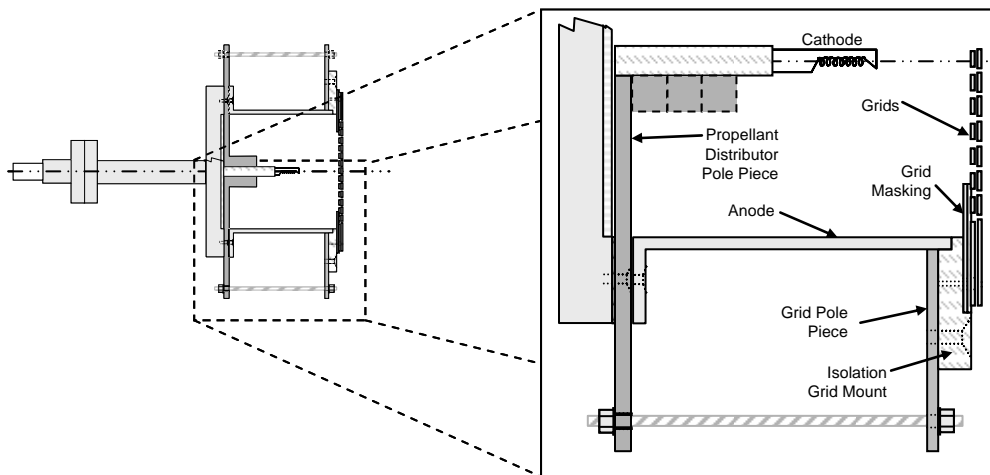
Figure 3.1-1. Micro-Ion Thruster (3cm diameter)

For the discharge and ion optics testing, described in sections 3.2–3.4, the thruster was outfitted with tungsten filaments as placeholders for the discharge and neutralizer cathodes. The filament cathodes allowed for relatively expeditious testing and evaluation of various configurations while field emission array (FEA) cathodes, small hollow cathodes, and other cathode technologies were being

developed. As shown in Figure 3.1-1, the discharge filament is oriented axially to maintain the axial symmetry of the thruster. This orientation avoids a radial imbalance of electron emission due to the 5 to 10V potential drop across the ~4mm filament during thruster operation. For the discharge analysis in Section 3.2, the most negative end of the discharge filament cathode was located downstream in hopes of increasing ionization close to the exit grids. In tests thereafter, the negative end of the cathode was upstream in an effort to simulate the electron distribution expected in a hollow cathode-type discharge.
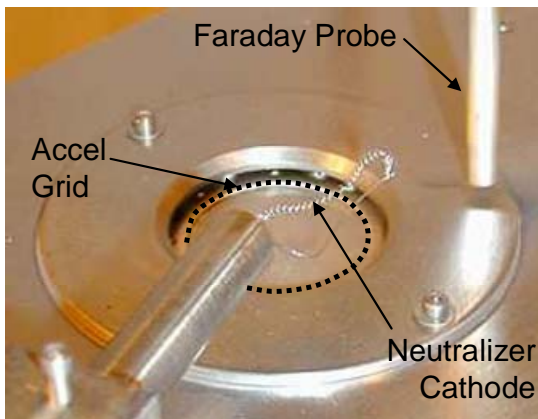
Figure 3.1-2. Micro-Ion Thruster Inside Ground Screen, with filament Neutralizer Cathode and Miniature Faraday Probe

Figure 3.1-2 shows the ground screen, in this case an aluminum box, which surrounds the entire thruster assembly except for a small opening to allow for beam extraction. A stand, located near the opening, holds the neutralizer cathode. The propellant feed line and electrical leads are on the opposite side of the box. The thruster faced vertically upward during testing. The neutralizer filament cathode was placed ~2cm downstream of the thruster exit, and a miniature Faraday probe, oriented parallel to the thruster axis, was used for diagnostics of the thruster plume. This location and orientation of the neutralizer cathode was sufficient to neutralize the beam while not noticeably heating the thruster or effecting plume measurements. The miniature Faraday probe, designed specifically for this

experiment, interrogated the thruster plume to obtain the results described in Section 3.3. The probe was oriented parallel to the thruster axis and swept radially across the plume to generate beam current density profiles.
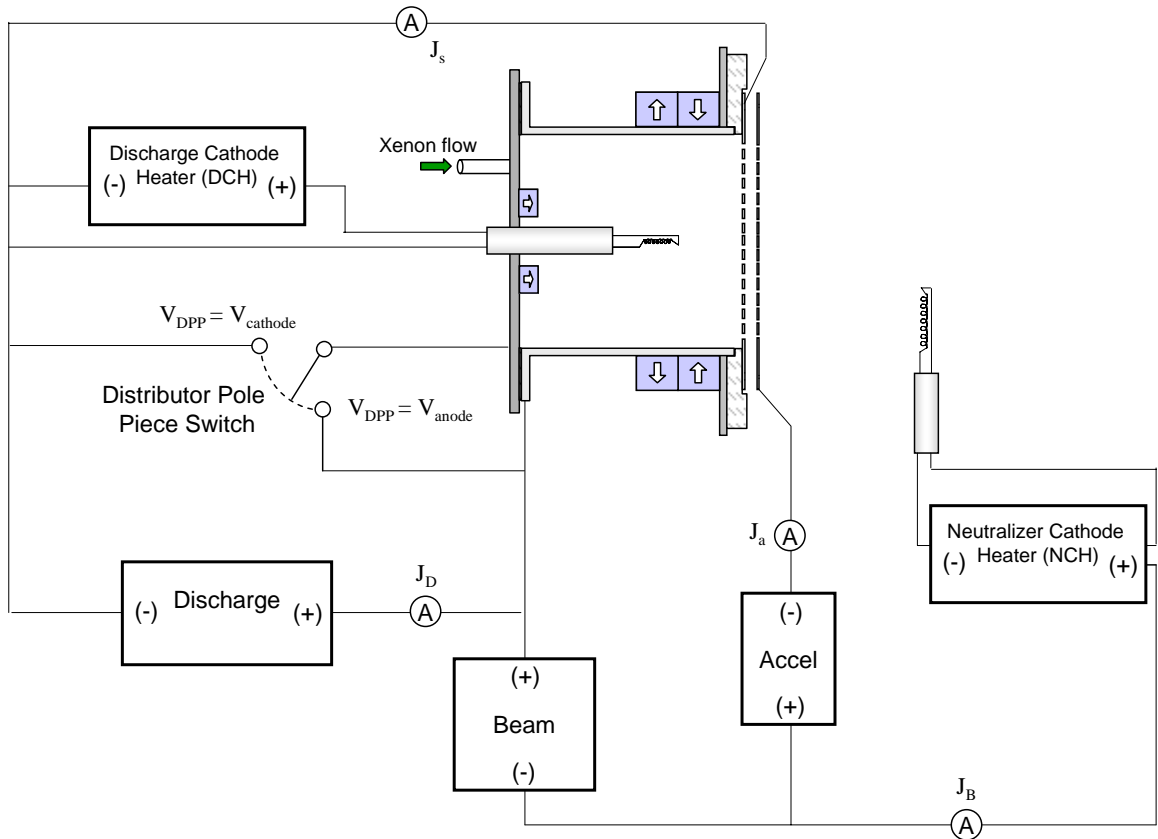
Figure 3.1-3. Simplified Electrical Diagram for Micro-Ion Thruster

Figure 3.1-3 shows a simplified schematic of the electrical system and the location of diagnostic instruments. The tests described in sections 3.2-3.5 were performed using the power, propellant control, and diagnostic systems that are described in Appendix B. Important aspects of the system are repeated here for convenience. Laboratory power supplies simulated the thruster PPU and were controlled locally. The multimeters were integrated in the thruster electrical system to display the voltages and currents used for estimating thruster performance. This configuration required manual observation and tabulation of the values from the multimeters, resulting in low data rates. The setup was eventually upgraded to remotely

controlled power supplies and automated diagnostics, as described in Section 3.6. The propellant feed system was composed of a pressurized xenon (Xe) supply tank, flow meter control, and flow controller/readout . The flow valve was located inside the vacuum chamber to avoid the ingestion of contaminants. A discussion of the error analysis for the diagnostic system and flow meter, including calibration results, is presented in Appendix B. Due to the extremely low propellant mass flow rates used in the experiment, the variability of mass flow rate far outweighed the error associated with the power system diagnostics.

The vacuum was maintained within a 1.2m tall / 0.6m diameter glass dome. The tests in sections 3.2-3.5 used a mechanical and oil diffusion pump tandem assembly, which is described in Appendix B. This system was eventually replaced by a cryogenic pumping system to reduce the relative partial pressure of cathode contaminants such as water and oxygen. Both systems maintained a ~3e-7 Torr base pressure; however, the diffusion tandem maintained near half the average pressure of the cryogenic pump during operation with xenon propellant. Operating pressure ranged from 10^{-6} to 10^{-4} Torr depending on xenon flow rate.

The thruster was "baked-out" in the vacuum environment before testing by slowly increasing the thruster's applied voltages and cathode power until the high operating voltages could be maintained without significant recycle rates (<4 per hour). The recycle rate is the frequency that continuous arc between the screen and accel grids occur. Flight ion thrusters are designed to maintain recycle rates below 1 per hour. The bake-out process took an average of one to two hours. Steady-state data were recorded if the thruster maintained consistent performance for several seconds. The maximum thruster operating conditions were limited by the maximum operating temperature of the magnets and the highest voltage that could be applied to the grids. Thermocouples were used to monitor the temperature of the magnets to ensure that it did not exceed the maximum operating temperature due to heating from the plasma discharge.

3.2 Experimental Analysis of Discharge Chamber Design

The 3cm diameter Micro-Ion thruster was designed such that multiple magnetic field, chamber, and electric field configurations could be tested. In this section, the performance of a large range of configurations is compared to help understand the behavior of miniature ion thruster discharges and determine an efficient configuration. A discussion of the possible plasma mechanisms that distinguish the performance of the different configurations is reserved for Chapter 7.

Figure 3.2-1. Micro-Ion Anode of L/D = 1.0, 0.75, and 0.5

Chamber Geometry

For larger ion thrusters, the length-to-diameter ratio (L/D) has been shown to have a noticeable effect on performance [13]. To test the sensitivity of chamber L/D for a 3cm diameter discharge, three cylindrical discharge anodes with L/D values of 1.0, 0.75, and 0.5 were fabricated (Figure 3.2-1). The discharge configurations created using these anodes are presented below. These nonmagnetic (stainless steel) chambers allowed the magnets to be placed outside the thruster while imposing an unimpeded magnetic field inside the chamber. This allows the magnet configurations to be changed quickly, without having to access the interior of the discharge chamber. The thin chamber walls, less than 1-mm thick, minimize the distance between the exterior magnets and the chamber interior, to yield the maximum field inside the chamber for the cusp configurations.

Magnetic Field

A wide range of magnetic field configurations were considered in hopes of finding a configuration that works efficiently at small discharge sizes. Historically, the most common magnetic configurations used for ion thruster studies have been the divergent axial, axial, ring-cusp, multipole, and line cusp [13,40,42]. Schematics of these configurations are shown in Appendix B. Previous investigations of axial ion thrusters aimed to ensure that the cyclotron radius of the primary is a constant fraction of the ion chamber diameter, implying that the magnetic field strength should vary inversely with the ion chamber diameter for ion thrusters with axial fields [39,40]. This leads to the assumption that a small ion thruster with an axial field should exhibit better discharge chamber performance if using strong magnetic fields; however, increasing the magnetic field has been shown to decrease performance beyond certain field strengths [39]. Cusped magnetic field configurations, as discussed in Chapter 2, depend on a locally strong magnetic field near the anode surface to prevent electrons from being lost to the anode before they have a chance to ionize a propellant neutral. Similarly, high magnetic field strength is assumed desirable for cusped configurations, but very high magnetic field strength may yield poor performance due to discharge instabilities [15].

Appendix B contains a preliminary experimental analysis of axial and line cusp configurations for a 3cm discharge. Knowledge gained from this analysis was used to design the Micro-Ion thruster head and to determine specific magnetic field configurations presented in this section. The divergent axial and ring-cusp magnet configurations used in the discharge design analysis below were chosen since it has been shown that these magnetic fields yield favorable beam flatness profiles and overall performance for conventionally sized ion thrusters [41,42,13].

Identically sized samarium cobalt (Sm_2Co_{17}) permanent magnet rectangular blocks were used for most of the magnetic field configurations. Since the operating temperature of an ion thruster is on the order of $200^{o}C$ it is important to consider

how the strength of a magnet varies with temperature. Appendix B shows the B-field, as a function of distance and temperature, along the centerline of the block samarium cobalt magnets used for this study. This plot suggests that the distance from the magnet (i.e., thickness of the anode wall) is a more important issue than temperature, as long as the maximum operating temperature is not reached. Above the maximum operating temperature a magnet will permanently lose a percentage of its magnetic strength, and will become permanently demagnetized at its Curie temperature [43]. The maximum operating and Curie temperatures for the samarium cobalt magnets used in this investigation are 350 and 800°C, respectively. Due to early budget constraints, the magnets used for this analysis were rejects from another experiment that had been run above their maximum operating condition and were partially demagnetized. If fully magnetized, the magnets would have exhibited ~3,500 Gauss at the magnet surface; however, a Tesla meter was used to show that the partially demagnetized magnets registered only ~2,500 Gauss at the magnet surface.

Larger ring-cusp ion thrusters typically use multiple rectangular block magnets for all of the magnetic rings (e.g., cathode ring, mid ring, grid ring); however, the overall diameter of this thruster is small enough that single ring-shaped magnets were used for the cathode ring (for the configurations employing a magnet at that location). These ring-shaped magnets are samarium cobalt (Sm_2Co_{17}) and were magnetized in the axial direction. Ring-shaped magnets were not considered for other parts of the magnetic field due to concerns of cost, possible breakage due to non-commensurate thermal expansion coefficients with surrounding materials, and loss of magnetic field configurability.

The rectangular permanent magnets for all configurations were placed on the exterior of the nonmagnetic chamber. Ferromagnetic "grid" and "distributor" pole pieces (Figure 3.1-1) were fabricated to provide a large range of possibilities for the magnetic field design. The ferromagnetic pole pieces provided a convenient and

quick means to fix the magnets in place. This control over the exact placement of the magnets was particularly important for the cusp configurations to ensure that the magnets were flush with the chamber walls so that sufficient field strengths existed inside the chamber for the magnetic mirror effect. The thruster was also designed to accommodate axial and cusp electromagnetic fields. The pole pieces were designed to accommodate up to eight electromagnets oriented in the axial or radial directions. By using electromagnets, it was assumed the field strength could be varied at high resolution and without having to open the vacuum chamber regularly as is required for permanent magnet field reconfiguration. Unfortunately, preliminary tests showed that electromagnets generated an extreme amount of heat while producing insufficient magnetic field strengths. When used in conjunction with permanent magnets the magnetic field output of the electromagnets was less than the thermal reduction of the permanent magnet strength. Therefore, electromagnets were not used for the discharge analysis.

The distributor pole piece was electrically isolated from the anode so that it could be biased from cathode to anode potential. Depending on the magnetic field configuration and cathode placement, the plasma losses to this surface may be minimized if the correct potential is used.

Discharge Configurations

The discharge configurations tested in this investigation are shown in Table 3.2-1. All magnetic field configurations were intended to be tested for anodes of L/D = 1.0, 0.75, and 0.5; however, the smallest chamber, L/D = 0.5, could not accommodate the 3-ring-cusp or Anode-Ring cusp designs due to space limitations. Preliminary tests were conducted to determine the number of magnets that yielded the best performance for each magnetic field design and chamber size. The behavior of some of these "alternate configurations" is discussed below.

Table 3.2-1. Tested Configurations

L/D	Magnetic Field Configuration			
	2-Ring-Cusp	3-Ring-Cusp	Anode-Ring-Cusp	Axial
1.0				
0.75				
0.5		Not Configurable	Not Configurable	
Axial View				

The potential drop across the 4mm, axially oriented discharge cathode filament ranged from 5 to 10V depending on the heater current required. The more negative end of the filament was positioned closest to the grids to encourage ionization near the grids. The default location for the downstream end of the filament for a given anode L/D is 5mm upstream of the screen grid since this location yielded favorable results in preliminary tests.   A schematic of the default cathode location for each configuration is shown in Figure F-1 (Appendix C). All configurations used grid set "A," from Table 3.4-1. A nominal grid spacing of 300 microns was used since it was the closest spacing that did not cause significant recycle rates.

Table 3.2-2. Test Parameter Ranges

Parameter	Typical Test Value(s)
$\dot{m}_T$	0.29, 0.44, 0.58 (sccm)
J_B	7.5, 10, 12.5, ... (mA)
J_D	Typical Range (60 – 600mA)
V_B	700 (V)
V_A	~150 – 280 (V)
V_D	25V(nominal), 28-33V(Axial)
V_{DPP}	Anode ($=V_B$) and Cathode ($=V_B$- V_D)
J_{DCH}	2.0 - 2.6 (A)

Performance Testing Matrix

The parameter ranges used to assess the performance of the various discharge configurations (from Table 3.2-1) are summarized in Table 3.2-2. Three propellant mass flow rates, $\dot{m}_T$, corresponding to low, medium, and high values were used. At each flow rate the cathode filament current was adjusted to produce the discharge current, J_D, necessary to attain beam current, J_B, values of 7.5mA or greater, at increments of 2.5mA. Originally the discharge voltage was to be maintained at a nominal value of 25V for all configurations, since this value yielded desirable performance in the preliminary tests. This discharge voltage produced a stable plasma discharge for all the Ring-Cusp configurations; however, as discussed below, V_D had to be increased to 28-33V for the Axial configuration. All other parameters were held constant to the extent possible. A minimum J_B of 7.5mA was chosen since lower values of J_B do not produce desirable efficiency values (<20%). The maximum J_B for a configuration was defined at the maximum discharge cathode heater current, J_{DCH}, and discharge voltage, V_D, 2.6A and 33V, respectively. The maximum J_{DCH} of 2.6A was found to be the limit beyond which

the 5mil tungsten filament would often break or the magnets' temperature would exceed their maximum operating temperature. A relatively low beam voltage, V_B, of 700V was chosen to avoid arcing problems that had occurred regularly at higher values.

Performance Results and Comparison

The relative performance of the thruster configurations from Table 3.2-1 are compared below with the aid of "discharge performance plots" of the beam ion energy cost, ε_B, versus discharge propellant utilization efficiency, η_{ud}. As discussed in Chapter 2, these plots are an effective way of relating the discharge performance of thruster configurations. In the following discussion, the performance of the thrusters from Table 3.2-2 is compared by first separately discussing the behavior and performance of each magnetic field type. Then the performance curves of the best configurations from each magnetic field type are compared and, using this information, the best overall configuration is identified. In the following discussion, the configurations are identified using the nomenclature:

"Magnetic Field Configuration" ("L/D ratio" , "V_{DPP}")

For example, for the 3-Ring magnetic field configuration, with L/D=0.75 chamber, and V_{DPP} equal to Cathode potential is identified as 3-Ring(.75,C). To reduce the number of configurations in the discharge performance plots, if a configuration consistently obtained lower performance for a particular V_{DPP} choice or if the configuration was unable to attain a beam current of at least 7.5mA, then the results of that configuration are excluded.

2-Ring-Cusp Thruster

The discharge performance plots from Figure C-2 (Appendix C) show that the L/D=0.75 chamber exhibited generally better performance than the L/D=1 chamber. A benefit of V_{DPP} at anode potential is noticed at the lower propellant

flow rates for L/D=1, whereas the performance of the L/D=0.75 chamber appears generally unchanged with choice of V_{DPP}. The L/D=0.5 configuration was unable to achieve beam currents of 7.5mA and is therefore not included in the comparison.

3-Ring-Cusp Thruster

The results in Figure C-3 show that the performance of the different chambers somewhat depends on the mass flow rate. Only data for the L/D=1 configuration with V_{DPP} at cathode potential is given since it was consistently more efficient at that potential. This however was not the case for the L/D=0.75 geometry since 3-Ring(.75,C) was more efficient at the low flow rate, while 3-Ring(.75,A) was more efficient at the high flow rate. Some difference in maximum achievable η_{ud} (or beam current) is noticed for the two chamber sizes at different flow rates; however, all three configurations appear to operate near their performance knees at η_{ud} values of 60-75%.

Anode-Ring-Cusp Thruster

The plots for the Anode-Ring-Cusp configuration, in Figure C-4, show that the L/D=0.75 chamber performance is generally superior to that of Anode-Ring(1,C). Many of the ε_B values for Anode-Ring(0.75,A) are almost identical to Anode-Ring(0.75,C), however, Anode-Ring(0.75,C) was able to achieve higher beam current (and hence, higher η_{ud}) for all flow rates, making it the most desirable of the Anode-Ring configurations tested.

Axial Thruster

The L/D=1, Axial configuration proved to be the only configuration tested that did not show its best performance at (or near) the default cathode location. Figure C-5 shows the results of a cathode position sensitivity study which "Axial(1,C)uc," "Axial(1,C)mc," and "Axial(1,C)" indicate the data for the cathode in upstream (20mm from grids), midstream (12mm from grids), and downstream (default, 5mm

from grids) locations. The Axial(1,C) data reveal very high ε_B for the downstream cathode location, while the Axial(1,C)mc and Axial(1,C)uc data show that the midstream location yields the best performance for the L/D=1 Axial configuration.

In general, the L/D=0.75 configuration exhibited lower ε_B, while the L/D=1 configurations were able to achieve higher beam currents, and hence, propellant efficiency. The short chamber (L/D=0.5) is not included in the comparison because it could not attain beam currents over 1.4mA. Results where V_{DPP} was held at anode potential could not achieve beam currents of 7.5mA, and were also excluded. A unique aspect of the Axial configuration was the need to raise the discharge voltage to over 70V to initiate the plasma discharge. Once the discharge was initiated, the discharge was somewhat stable at $V_D \cong 28\text{-}33\text{V}$; at lower values it would extinguish. Many of the high propellant efficiency data points for the Axial configuration were obtained at V_D from 30-33V, since these high discharge voltages were necessary to maintain a stable discharge. The "hard-starting" and unstable discharge behavior of the Axial configuration made it difficult to obtain data at consistent values and resulted in an increased rate of cathode filament breakage.

Comparison of All Configurations

The performance curves for the best configurations for each magnetic field type are compared in Figure 3.2-2. The 3-Ring configurations consistently produced comparatively better performance for the flow rates investigated. 3-Ring(1,C) yielded the best performance ($\eta_{ud} = 60\text{-}81\%$, $\varepsilon_B = 378\text{-}752\text{eV/ion}$) at the lower flow rates; however, 3-Ring(.75,A) attained the highest $J_B = 32.5\text{mA}$ of all configurations, with propellant efficiency $\eta_{ud} \sim 80\%$ at $\dot{m}_p = 0.58$ sccm. For $J_B = 32.5\text{mA}$ and $V_B = 700\text{V}$, the ideal thrust is 1.429mN.

Axial(.75,C) yields low ε_B at the lowest flow rate but is noticeably worse at higher flow rates. 2-Ring(.75,A) exhibited generally low ε_B but was unable to attain $\eta_{ud} >$

60% for all flow rates. The Anode-Ring configuration was consistently worse in both η_{ud} and ε_B for all flow rates. From these results it is clear that, for the chosen operating conditions, the 3-Ring magnetic field is the best overall configuration from Table 3.2-1 and the optimal length of the anode depends on the desired operating range of the thruster.
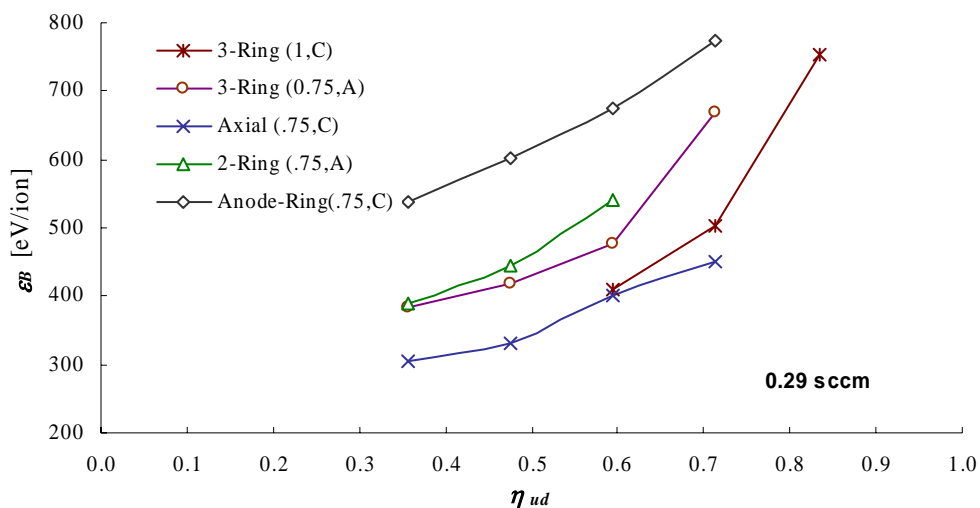
Figure 3.2-2a. Comparison of Micro-Ion Configurations at 0.29sccm Xenon Flow Rate
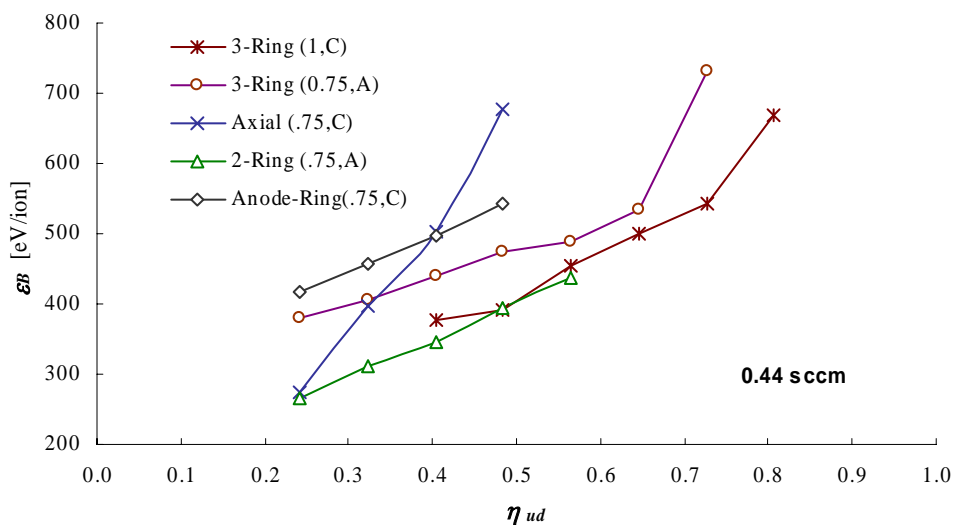

Figure 3.2-2b. Comparison of Micro-Ion Configurations at 0.44 sccm Xenon Flow Rate
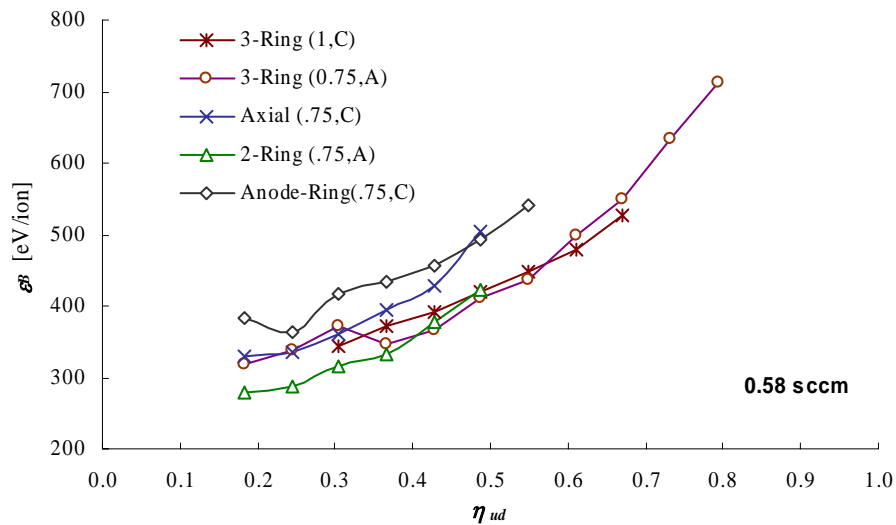

Figure 3.2-2c. Comparison of Micro-Ion Configurations at 0.58 sccm Xenon Flow Rate

45

Magnetic Field Sensitivity Results

A sensitivity analysis of the axial location of the mid magnet ring of the 3-ring (L/D=1) configuration was conducted by spacing the anode magnet rings as shown in Figure 3.2-3.   The results of these tests suggests that the discharge losses, ε_B, decrease noticeably if the mid magnet ring is spaced less than 2mm from the grid magnet ring at beam current levels of 10mA and 12.5mA.
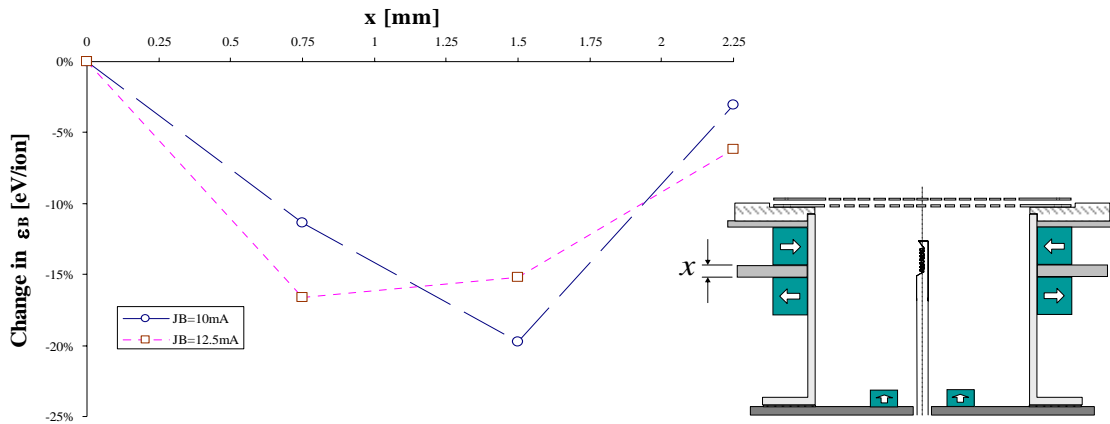

Figure 3.2-3. Change in Discharge Loss vs. Magnet Spacing in 3-Ring (L/D=1) Configuration

Preliminary tests were used to determine magnetic field strengths that yielded favorable performance for the configurations from Table 3.2-1. Diagrams of some of these early configurations, all at L/D=1, are given in Appendix C, along with some comments on their performance. In general, it was found that *higher* magnetic fields resulted in *worse* performance for the 3-Ring, Anode-Ring, and Axial thrusters.
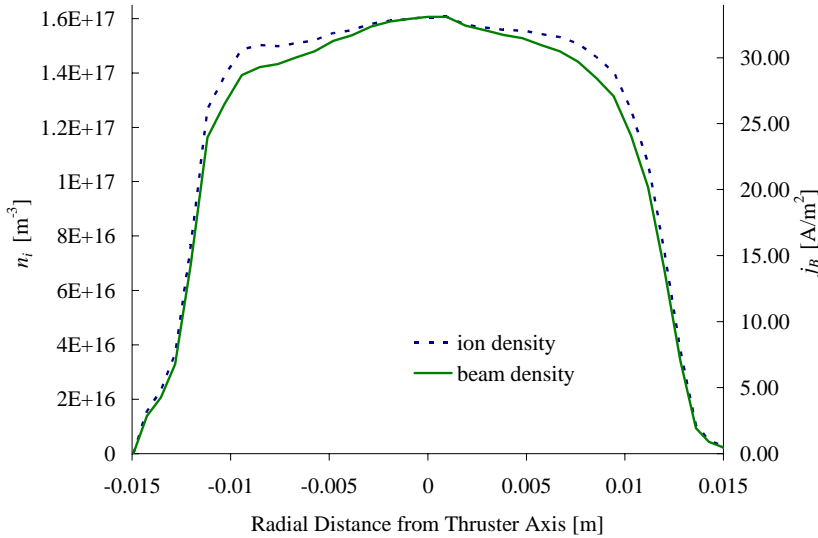
Observations from Discharge Testing

In general, the performance values presented herein, particularly for the 3-ring thruster, show that a conventional magnet size can be used to achieve good discharge performance for a 3cm diameter ion thruster. The results from the discharge tests show that the Micro-Ion thruster is highly sensitive to the magnetic

field configuration and strength, the length of the chamber, the discharge cathode location, and the choice of discharge chamber surface potentials. Therefore, subtle changes in design parameters should be considered carefully when designing small ion thrusters. Comparisons of the performance show that the 3-ring configurations at L/D=1 and 0.75 give the best performance for the range of test parameters used. Refinement of the design, including optimization of magnet placement, will likely yield noticeable increases in performance. For the other magnetic field configurations, the L/D=0.75 anode generally yielded the best performance. The strong dependence of performance on chamber length suggests that alternate anode shapes, such as the conical surface of NSTAR, may be considered for further performance enhancement. Increasing the magnetic field, as recommended by several studies, actually resulted in decreased performance for three out of four configurations. The cause of the decreased performance for the high magnetic field 3-ring and anode configurations may be due to the discharge stability issues that are discussed in Chapter 2. An important advantage of the cusp configurations is that they do not require the high starting voltages necessary for the divergent axial configuration. The sensitivity of the designs to V_{DPP} suggests that the optimal voltage for the distributor pole piece surface may be between anode and cathode potential.

3.3 Discharge Diagnostics Using Beam Profile Analysis

Knowledge of the discharge plasma density is important to understanding and improving the Micro-Ion thruster discharge and is useful for comparing with Discharge Model results. Direct plasma measurements inside the discharge chamber were difficult to obtain due to the magnet locations and small size of the Micro-Ion thruster. Appendix D presents the method for approximating the discharge chamber ion density of the Micro-Ion thruster just inside the grids by determining the beam profile at the exit plane. Some additional results from this

investigation are given in this section to provide experimental comparison for the results of Discharge Model simulations of the Micro-Ion Thruster in Chapter 6. The profiles shown in Figure 3.3-1 were obtained using the technique described in Appendix D for the operating conditions in the accompanying table. In this plot, the location of the ion density profile is just inside the ion extraction grids and the beam current density is at the exit plane of the grids. The flatness parameters for the exit beam and ion profiles in Figure 3.3-1 are 0.64 and 0.68, respectively. Similar density and beam flatness values were obtained for other operating conditions. The analysis from Appendix C found that the maximum beam divergence angle was 14.5^o and the averaged divergence angle of the entire beam, using Equation 2.2-12, was found to be 5.88^o.

Operating Conditions	
V_B	911 V
V_D	25 V
J_B	14.05 mA
J_D	293.5 mA
$\dot{m}_d$	0.29 sccm
P_{cb}	9.70E-6 Torr
$Temp$	248 ^{o}C
T_{ideal}	0.705 mN
I_{sp}	2477 s
ε_B	522 eV/ion
η_{ud}	0.669
Values ignore doubly charged ions and beam divergence	

Figure 3.3-1. Ion and Beam Density Profiles for Micro-Ion Thruster

3.4 Ion Optics for a Small Diameter Beam

The analyses in sections 3.2 and 3.3 used flat micro-machined molybdenum grids with matched circular hole patterns. The aperture diameters, and corresponding open area fractions, for the grids are given in Table 3.4-1. All the grids had a useful beam diameter of 2.85cm and all the grids were made from 100μm-thick molybdenum; however, grid sets B and SHAG were constructed with a reinforced flange in an effort to increase their resistance to the deformations due to thermal cycling that were observed during the testing of grid set A. Figure 3.4-1 is a magnified picture of Grid Set B, upstream of the grid plane (as would be seen from the discharge chamber). The analysis in Appendix D demonstrated the advantages of using the Small Hole Accelerator Grid (SHAG) optics for the Micro-Ion thruster. The implications of this result for the design of small diameter ion thruster grids are presented below.

Table 3.4-1. 3cm Ion Optics Grids

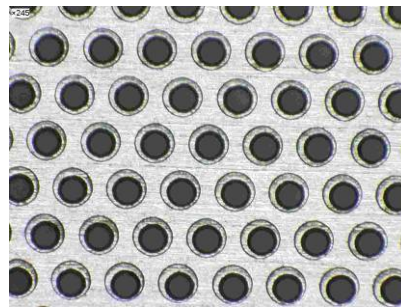| Grid Set	Screen Grid		Accelerator Grid	
	Aperture Diameter (μm)	Open Area Fraction	Aperture Diameter (μm)	Open Area Fraction
A	340	48.7%	220	20.4%
B	324	37.8%	191	15.3%
SHAG	324	37.8%	110	5.1%

Figure 3.4-1. Upstream View of Aligned Grid Set B

Small Diameter Grid Design

Small ion thrusters have some clear advantages over larger ion thrusters with respect to grid design. The smaller diameter of the grids implies greater resistance to vibrations and lower grid deformation in the presence of thermal loads. The smaller surface area of the grids results in a lower probability of arcing between the grids during beam extraction. These factors combine to allow the grids of a miniature ion thruster to be spaced more closely together than larger ion thruster grid sets. The advantage of closer grid spacing was demonstrated with the Micro-Ion thruster using a combination of computational and experimental analysis, as discussed in Appendix C. In this study, it was shown that SHAG optics could be used to yield better neutral confinement without decreasing ion current for given upstream plasma conditions. Small accelerator grid apertures are possible since the steep potential gradients arising from close grid spacing results in tight focusing of the ion beamlet. Experimental measurements confirmed that the switch to SHAG optics for the Micro-Ion thruster resulted in noticeable improvements in discharge loss ($\Delta\varepsilon_B \approx$ -100eV/ion) and propellant efficiency ($\Delta\eta_{ud} \approx 10\%$). The results from the above discussion show that close grid spacing yields inherently high perveance for a given open area fraction [11], thus allowing smaller ion thrusters to achieve high thrust densities.

To increase the viability of small ion thrusters, it is desirable to develop thick, robust, grids to maximize accelerator grid life and minimize the large thermal deformation of the screen grid that was experienced with the 100μm-thick grids from Table 3.4-1. To aid the design effort, the Ion Optics Sub-Model (described in Section 4.4) was used to analyze the performance of many possible configurations. The anticipated ion trajectories for three SHAG-type geometries at high density discharge conditions ($n_i \sim$ 6e17 m^{-3}), are shown in Figure 3.4-2; all plots reflect a total thrust of ~3.25mN. These plots show that the ~3.25mN thrust level is allowed over a large range of accel grid thicknesses. This combination of SHAG and thick accelerator grids (TAG) requires another acronym, possibly "SHTAG." The

chemical etching process used to make the grids limits the aperture diameter-to-thickness ratio to ~1, thus ruling out Design 2 and 3 until more advanced techniques can be afforded. As a result, Design 1 from Figure 3.4-2 was constructed and is used in the results discussed in Section 3.6. The grids were manufactured from molybdenum since it is much cheaper than the longer-life carbon-based grid materials that will be considered for future designs.
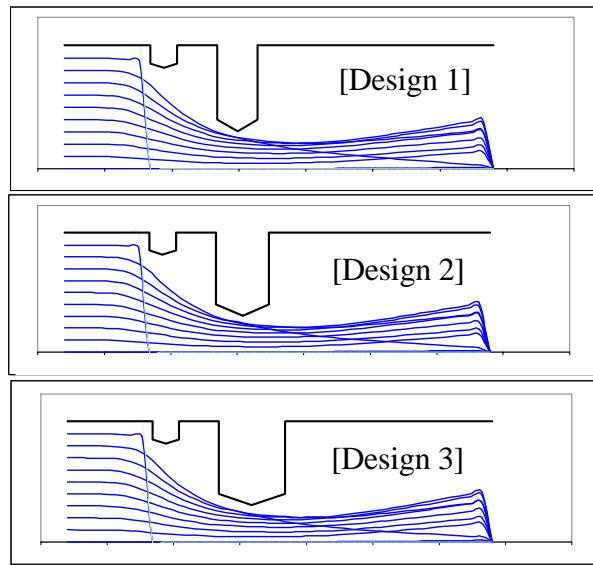

Figure 3.4-2. Ion Trajectories for SHAG Grids of Increasingly Thicker Accel Grids

An aspect of the grid geometry that becomes increasingly important with reduced diameter and SHAG optics is the propellant loss in the radial direction between the grids. Though this effect is somewhat mitigated by the close spacing, the radial loss area at the edge of the grid hole area is on the order of the axial loss area for SHAG optics at the Micro-Ion scale. Several methods have been devised to address this problem in future studies, but since its resolution will simply result in a reduction of required propellant, it is assumed to not affect the performance optimization methodology discussed herein.

3.5 Cathodes

The results presented in the previous sections show that attractive performance is possible for the Micro-Ion thruster if low-power electron sources can be incorporated. The experimental effort discussed in Appendix E focuses on cathode technology options that can yield desirable lifetime and performance, and shows that the use of conventionally-sized hollow cathodes presents a considerable efficiency challenge for miniature ion thrusters.

Discharge Cathode

To generate the primary electrons in the discharge, conventional ion thrusters use hollow cathodes. Hollow cathodes are a mature technology and typically require less power per amp of emitted electrons than other discharge cathode options. The main disadvantage to hollow cathodes for a miniature discharge is the requirement for a designated propellant feed that can exceed the propellant needs for the entire discharge chamber. Therefore, using hollow cathodes for a miniature discharge may result in very low efficiencies and poor throttleability, as discussed in Appendix E. However, the impressive performance of hollow cathodes may be realized for miniature ion thrusters if low-flow and low-power miniature hollow cathodes can be successfully designed, built, and implemented. As a result, two miniature hollow cathodes were designed and built specifically for the MiXI thruster. These cathodes, shown in Figure 3.5-1, will be tested with the MiXI thruster once the Internal Conduction (IC) cathode (described below) testing is complete. If successful, these miniature hollow cathodes can simply scale to thruster sizes greater than 3cm.
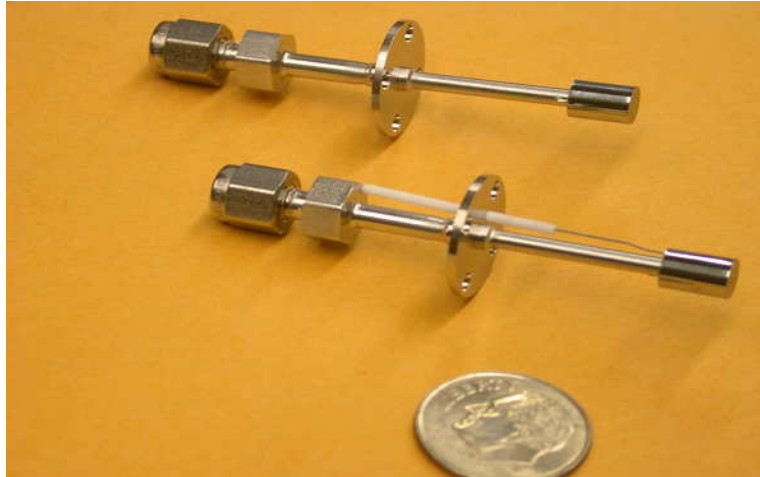
Figure 3.5-1. Miniature Hollow Cathodes

For precision formation flying missions such as TPF-I, it is possible that discharge cathode cycling times, shorter than those for hollow cathodes, could prove attractive. Direct emission cathodes, using robust cathode materials such as LaB_6 and CeB_6, do not require propellant, possess cycling times typically lower than hollow cathodes, and may increase thruster throttleability. As discussed in Appendix E, conventional configurations of such cathodes either require prohibitively large heater currents or are self-poisoning in an ion thruster discharge environment. To address these issues, a new cathode called the Internal Conduction (IC) cathode was developed as part of this dissertation and built by Applied Physics Technology, Inc. specifically for the MiXI thruster presented in Section 3.6. A prototype of the IC cathode is shown in Figure 3.5-2. Initial discharge tests (without beam extraction) have shown that the cathode requires as little as 9W of heater power (at only 3.5A heater current) to provide the discharge current necessary for the maximum projected operating conditions of the MiXI thruster.

Cycling time of the IC cathode is on the order of several seconds; however, additional testing is necessary to assure that fast cycling does not lead to eventual cathode failure. Tests using the IC cathode with an improved thruster design are presented in Section 3.6. As discussed in Appendix E, direct emission hexaboride

53

cathodes, such as the IC cathode, can operate at lower propellant purity levels than conventional barium-tungsten insert hollow cathodes. This translates to sizeable propellant cost savings.

Figure 3.5-2. Internal Conduction (IC) Cathode

Neutralizer Cathode

As discussed in Appendix E, a neutralizer cathode requiring minimal designated propellant flow is necessary to achieve miniature ion thruster efficiencies near those of larger thrusters. The tests discussed herein used a simple filament cathode as a placeholder for the neutralizer cathode. Current carbon nanotube and Spindt-type cathodes are not capable of surviving the beam plasma environment or neutralizing the higher beam currents produced by a 3cm ion thruster. A possible solution is to use a Spindt-type cathode that incorporates Cathode Lens and Ion Repeller (CLAIR) technology [44,45], in which a series of electrodes are used to protect the emitter tips. If successful, this technology could easily scale to smaller (< 3cm), and possibly larger, ion thruster sizes. The miniature hollow cathodes discussed earlier represent a more conservative option for beam neutralization, which provides a familiar, though maybe not optimal, solution to beam neutralization.

3.6 Improved Miniature Thruster Design

With the lessons learned from the Micro-Ion thruster studies summarized in the previous sections, a compact and lightweight 3cm Miniature Xenon Ion (MiXI) thruster was built and is shown in Figure 3.6-1. The MiXI thruster is designed to investigate the ring-cusp design used for the Micro-Ion thruster at a reduced size and weight of the thruster head. The total weight of the thruster head with magnets is only 200 grams. The default configuration of the MiXI thruster is the 3-ring magnetic field similar to the L/D=1 design that yielded attractive performance for the Micro-Ion thruster, but it is designed to allow further optimization of the magnetic field strength and geometry. The MiXI thruster is also designed to accommodate an array of discharge cathode options, test various grid geometries, test neutralizer cathode options, and perform a preliminary life test (~1,000 hrs).

Figure 3.6-1. MiXI Thruster

Figure 3.6-2 shows the performance of the MiXI thruster, using the IC discharge cathode and MiXI grid Design 1 from Figure 3.4-2. These data are plotted against Micro-Ion thruster data that used a filament discharge cathode and the SHAG grid set from Table 3.4-1. It is reasonable to attribute the superior performance of MiXI thruster to the higher ion transparency of the MiXI grids ($\zeta_i \sim 70\%$) compared to the

SHAG grids ($\zeta_i \sim 60\%$). Further analysis is needed to determine the performance related to the MiXI magnetic field. The difference in performance in Figure 3.6-2 is not likely influenced by the differences in cathode technologies since neither metric used in the figure includes cathode power directly. The lower operating temperature of the IC cathode may manifest only a slight improvement in MiXI performance by lowering neutral loss rate.
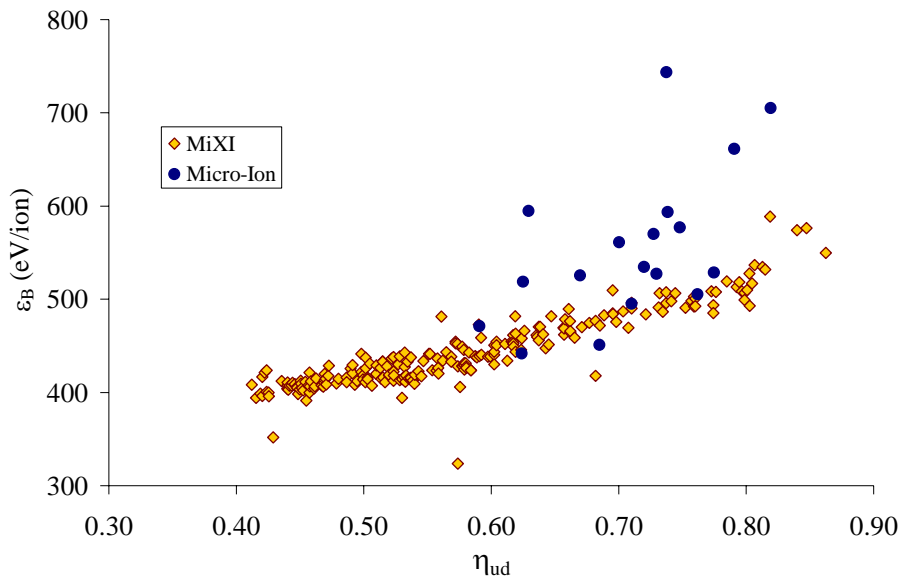

Figure 3.6-2. Comparison of MiXI and Micro-Ion Performance at Nominal Operating Conditions

The MiXI data presented in Figure 3.6-2 were obtained at a xenon flow rate of 0.2 sccm, using an automated data acquisition system that was constructed just before MiXI testing was undertaken. The Micro-Ion data was obtained using the original technique described in Section 3.1 for a xenon flow range of 0.2-0.44 sccm. The automated data acquisition system was specifically designed for this experiment, thus exhibiting relatively small errors for current and voltage measurements; however, the feed system from Section 3.1 was used for the propellant system, which introduced the comparatively large errors discussed in Appendix B. Additional testing of the MiXI thruster at higher flow rates resulted in discharge losses as low as 250eV/ion.

Ion Thruster Discharge Performance Comparison

Table 3.6-1 compares the discharge performance of the MiXI thruster with the performance of the small, miniature, and conventional ion thrusters that are discussed in Chapter 2. This comparison shows that the MiXI thruster performance is comparable to small ion thrusters and is noticeably better than other miniature ion thrusters. Since the MiXI thruster uses conventional SmCo magnets and has a total thruster head weight of only 200g, this study has clearly demonstrated that desirable miniature thruster performance is possible with low thruster and magnet weight.

Table 3.6-1. Comparison of Discharge Performance for Miniature and Small Ion Thrusters

Thruster Name or Experimental Group	Diameter / Type	$\eta_{ud[*]}$ [max]	ε_B [eV/ion]	Reference
MiXI	3cm ring-cusp	87%	250-550	
Miniature RF-Ion Thruster (MRIT)	3cm RF	8.4%	Data not available	[28]
Hollow Cathode Micro-Thruster (HCMT)	4.8cm hollow cathode	14%	>1000	[27]
Keldysh Research Center, Moscow	6cm Kaufman	81%	220-525	[46]
Colorado State University	7cm ring-cusp	70%	300-600	[23]
Glenn Research Center, NASA	8cm ring-cusp	83%	220-395	[24]
NSTAR	30cm ring-cusp	91%	180-200	[5]

The 3cm diameter MiXI thruster represents the lower limit of ring-cusp ion thruster discharges currently under development; while the 60cm Nuclear Electric Xenon

Ion System (NEXIS) that currently being developed for the JIMO mission (Section 1.2) represents the upper limit. Figure 3.6-3 shows the author with four ring-cusp ion thrusters ranging from MiXI to NEXIS diameters.

Figure 3.6-3. The Author with (from left to right) the Micro-Ion thruster (3cm), a thruster similar to the 13cm XIPS, NSTAR (30cm), and NEXIS (60cm)
(Note: The ion extraction grids are removed from the thrusters to show the discharge chambers)

Chapter Summary

The results presented in this chapter illustrate that desirable performance of a DC miniature ion thruster is possible with low magnet and thruster weight. An efficient discharge configuration was found by comparing the performance of a large range of chamber geometries and magnetic field designs. A large increase in performance was achieved by combining experimental and computational analysis to optimize the grid design. Ion densities inside the thruster were estimated by extrapolating downstream beam profiles to the exit plane. These data are used in Chapter 6 to compare with Discharge Model simulations of the Micro-Ion thruster.

Chapter 4

Discharge Model: Theory and Formulation

In chapters 1 and 2 it is shown that a better understanding of ion thruster plasma discharges is necessary to meet the needs of future space missions. The hybrid computational model ("Discharge Model") presented in this chapter is intended to help better understand the discharge plasma behavior and aid in the design of ion thrusters. The model is designed to integrate with thruster component wear models so that the long-term performance and life of the thruster can be determined. Within a DC ion thruster discharge chamber there are four species that dominate the plasma behavior: neutral propellant atoms, secondary electrons, primary electrons, and ions (both singly and doubly charged ions). Also, five main physical characteristics drive discharge chamber design: chamber geometry, magnetic field, discharge cathode, propellant feed, and ion extraction grids. The model accounts for all five chamber design parameters and self-consistently tracking the effects of the four plasma species. This chapter provides an overview of the Discharge Model (Section 4.1) and details the individual sub-models in sections 4.2-4.6.

4.1 Overview of Discharge Model

The two-dimensional axisymmetric Discharge Model is a self-consistent combination of 2-D and 2.5-D sub-models. The plasma behavior is resolved in a two-dimensional radial plane of the axisymmetric domain. Figure 4.1-1 shows the general flow of the Discharge Model, the relations of the individual sub-models, and examples of important parameters that are generated and passed by the sub-models.   The model input requires only thruster voltages, discharge current, geometry, magnet properties and locations, and discharge chamber surface transparencies and temperatures.   The discharge surface temperatures can be assumed uniform if adequate information is not available. A relaxation method is used to converge on a steady-state solution as described below.   The cathode plume sub-model and wear sub-models are indicated for completeness in Fig. 4.1-1, but are not discussed here.
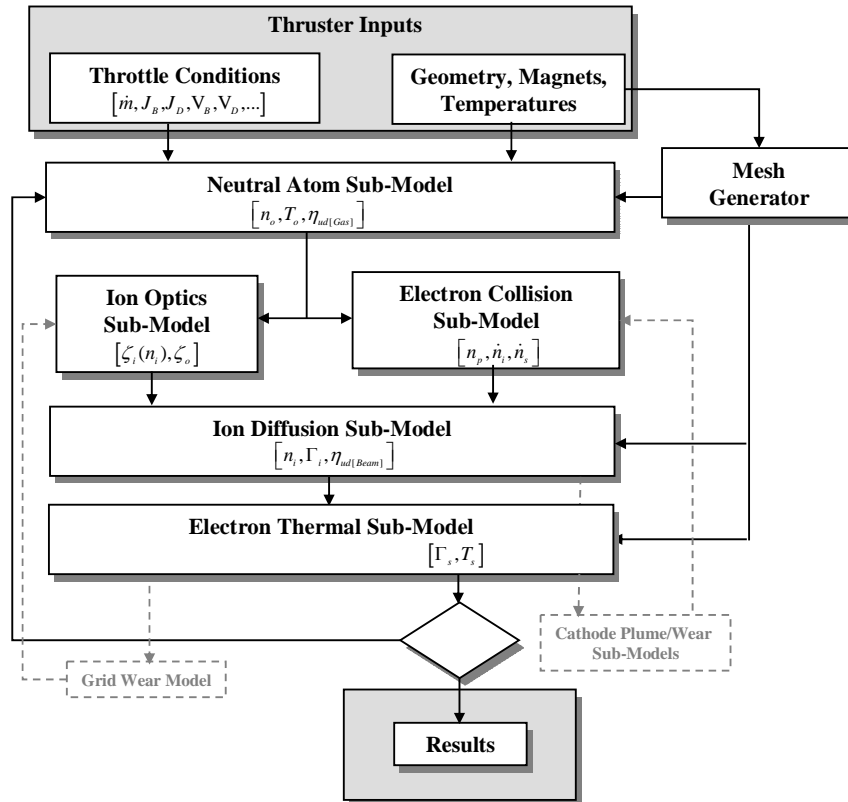

Figure 4.1-1. Discharge Model Overview

In this chapter, all sub-models of the Discharge Model in Figure 4.1-1 are discussed in detail except for the cathode and optics sub-models. Both the cathode plume and wear sub-models are under development and are important to future versions of this model but are not used for the model presented herein. A general description of the optics sub-models is given in Section 4.4; however details of these models can be found in references [12,8].

Discharge Model Inputs and Computational Domains

To simulate a certain operating condition, the model uses basic thruster inputs, i.e.:

1) J_D - discharge current

2) V_B, V_D, V_{accel} – beam, discharge, and accel grid voltage

3) $\dot{m}_d$ - discharge propellant flow rates

4) Thruster geometry

5) Magnet properties and location

6) Ion optics geometry (to determine ζ_i (n_i), ζ_o)

7) Surface temperatures

The Discharge Model simulates thruster surfaces made up of axisymmetric geometric shapes such as cylinders, cones, planes, and spheres. This allows the model to simulate almost any axisymmetric discharge shape of interest. In the model, these surfaces are simply defined in the model input as a contour of the discharge surface as shown in Figure 4.1-2. Each element of the Boundary Mesh is assigned a voltage (cathode or anode), temperature, and transparency. The ion extraction grid transparency to ions and neutrals is a function of the local densities as described in Section 4.4. On-axis propellant feeds, such as hollow cathodes, are considered point sources while off-axis feeds are assumed to be uniformly distributed plenums. The magnet configuration must also be axisymmetric but is generated by inputs of discrete magnets as discussed in Appendix F.
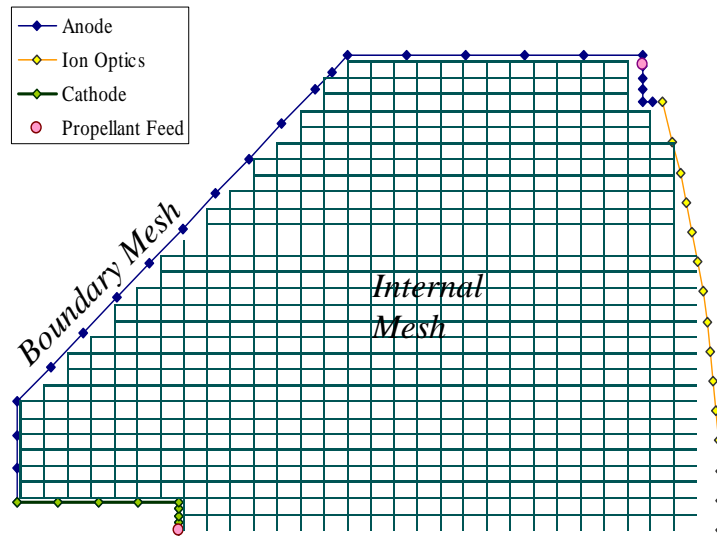
Figure 4.1-2. Internal Mesh and surrounding Boundary Mesh with surface type definitions and propellant feed locations

The Boundary Mesh is used in all sub-models as a precise representation of the internal surfaces of the thruster. The volume of the thruster is defined by a 2-D Internal Mesh that is used to track the properties determined in each sub-model. Figure 4.1-2 shows an example of an Internal Mesh and Boundary Mesh for the NSTAR geometry. For this example the meshes are not entirely commensurate due mainly to the curved grids and the conical surface; however, simple blending methods are used to communicate between the meshes and conserve appropriate quantities. It was found that the model results did not change noticeably with increased mesh resolution beyond that shown in Figure 4.1-2.

For early versions of the model, the Internal Mesh was a 2-D Magnetic Field Computational Mesh (B-Mesh) that was aligned with the magnetic field lines and the magnetic potential contours. The details of the B-Mesh and results from early versions of the model using this mesh are discussed in references [47] and [48]. Other models of magnetized plasma have used B-field oriented computational meshes for domains much simpler than that of a ring-cusp ion thruster [49]. It was eventually found that, due to the complexity of the ring-cusp magnetic field, the automated B-Mesh generation technique was prohibitively sensitive to small

changes in the magnetic field strength or geometry. Since one of the primary intentions of the model is to investigate a large range of ion thruster geometries, magnetic fields, and sizes, the B-Mesh was eventually replaced with a simpler orthogonal Internal Mesh, such as the one shown in Figure 4.1-2. Comparisons of runs using the B-Mesh and Internal Mesh for the NSTAR thruster showed similar behavior for the ion diffusion sub-model results. It was later found that calculations of the highly anisotropic (magnetized) motion of the secondary electrons were extremely difficult without a magnetically oriented mesh, though this calculation was not within the original scope of the model. Chapter 8 discusses the possible advantages of using a B-Mesh for future versions of this model. Though not ideal, the orthogonal mesh has some attractive characteristics for the three-ring thruster configurations. Specifically, the mesh is nearly aligned with the B-field in the highest magnetic field regions near the cusp, where magnetic effects are particularly important. The Internal mesh is composed only of elements fully contained within the discharge chamber. It is not completely necessary for this mesh to fully resolve the chamber boundary since the precise shape of the boundary is fully resolved by the Boundary Mesh.

The method for creating the magnetostatic solution for the computational domain is described in Appendix F. A simple corrected dipole solution technique is employed so that the primary electron tracking algorithm (described later) can calculate the magnetic field exactly at each point in its trajectory to avoid inaccuracies that can arise from magnetic field interpolation methods. This magnetostatic solution technique results in faster run times and design modification times in comparison to using external magnetostatic solution packages. The near-magnet correction of the corrected dipole solution described in Appendix F is important for smaller ion thruster discharges (i.e., 3cm diameter) where the inaccuracy of a simple magnetic dipole approximation would introduce magnetic field errors of well over 40% for more than half the chamber volume. It is also important at the magnetic cusps, where the artificially high near-magnet field

strength predicted by a simple dipole approximation greatly over predicts primary electron confinement.

Convergence and Mixing Techniques

The model reaches a steady-state solution by first assuming very low density thermal plasma (at least an order of magnitude less than the anticipated final condition) and incrementally increasing the primary electron current until full primary current is reached. Mixing parameters are used to avoid overly large gradients for the self-consistent solution of an iteration. Key parameters, such as ionization rates, ion density, and primary density are mixed at the beginning of an iteration of the model using relaxation parameters. Model convergence is tracked by determining relative values of "gas" and "beam" discharge propellant efficiencies, given by

$$\eta_{ud[Gas]} = \frac{\dot{m}_d - \dot{m}_{loss}}{\dot{m}_d} \qquad\qquad [4.1\text{-}1]$$

$$\eta_{ud[Beam]} = \frac{\left(J_B^+ + J_B^{++}/2\right)m_i}{e\dot{m}_d} \qquad\qquad [4.1\text{-}2]$$

where J_B^+ and J_B^{++} are the beam currents due to single and double ions, respectively; $\dot{m}_d$ is the total propellant flow rate into the discharge chamber. Equation 4.1-1 is the propellant efficiency that is calculated by the Neutral Atom Sub-Model by tracking the loss of unused propellant, $\dot{m}_{loss}$. Equation 4.1-2 is the propellant efficiency from the Ion Diffusion Sub-Model that calculates the rate at which ions (of all charges) are extracted into the beam. The equality of propellant efficiency per equations 4.1-1 and 4.1-2 implies conservation of propellant such that $\dot{m}_d = \dot{m}_{loss} + \left(J_B^+ + J_B^{++}/2\right)m_i/e$. When conservation of propellant ($\eta_{ud\ [Gas]} \sim \eta_{ud\ [Beam]}$) persists for several iterations, it is found that all other parameters determined by the Discharge Model (e.g., densities, temperatures) are very near their steady-

state solution. This correlation can be clearly seen in the solution convergence plots shown in chapters 5 and 6 (Figures 5.2-1, 5.2-2, 6.2-1, and 6.2-2). It was found that the Discharge Model can be considered converged when the values of propellant efficiency predicted by both models are within ~0.5% agreement for over 10 iterations. The time for convergence depends on the input conditions; however, for the results presented herein the model needed ~1-1.5 hours on a modern laptop computer.

As discussed in Chapter 2, many experimental results calculate propellant efficiency by assuming that the beam is entirely composed of single ions, resulting in the expression

$$\eta_{ud[*]} = \frac{\left(J_B^+ + J_B^{++}\right)m_i}{e\dot{m}_{prop}}$$

[4.1-3]

Using Equation 4.1-3, the model calculates propellant efficiency values to compare with experimental data.

Discharge Plasma Parameter Ranges

One of the main difficulties associated with modeling an ion thruster discharge is the wide range of plasma parameters throughout the full extent of the domain. Table 4.1-1 gives approximate plasma conditions on-axis (r=0), in the bulk of the plasma (r=R/2), and near the anode (r=R), for the NSTAR (R=30cm) and MiXI (R=3cm) thrusters. These *approximate* conditions were determined from experimental measurements and early computational evaluations. The mean free paths, cyclotron radii, and Hall parameters for these conditions are given in Table 4.1-2 (see Reference [50] and Appendix G for formulations). The results from this table are used in the following sections to guide to formulation of the various sub-models.

Table 4.1-1. Approximate NSTAR and MiXI Plasma Conditions

	n	n_o	T_s	E_p	T_o	$|B|$
	[m^{-3}]	[m^{-3}]	[eV]	[eV]	[eV]	[G]
NSTAR (TH15)						
r=0	1E+17	5E+18	3.5	20	0.04	5
r=R/2	2.5E+17	2.5E+18	4	20	0.06	30
r=R	5E+17	8E+17	4.5	20	0.11	100
MiXI (mTH1)						
r=0	1E+17	2E+19	2	21	0.04	100
r=R/2	2E+17	1.5E+19	2	21	0.04	200
r=R	3E+17	1E+19	2	21	0.04	500

Table 4.1-2. Approximate NSTAR and MiXI Plasma Parameters

	λ_n	λ_p	$\lambda_{p\text{-}n}$	λ_{slow}	λ_i	r_{ci}	r_{ce}	Ω_i	Ω_e
	[cm]	[cm]	[cm]	[cm]	[cm]	[cm]	[cm]		
NSTAR (TH15)									
r=0	37.15	59.2	62.0	1327.7	2.166	44.2	0.285	0.05	601
r=R/2	65.32	101.3	124.0	552.2	1.459	39.4	0.254	0.04	512
r=R	114.18	164.1	387.5	284.7	1.016	12.5	0.081	0.08	1377
MiXI (mTH1)									
r=0	9.53	15.9	16.1	1904.5	0.688	8.4	0.054	0.08	8950
r=R/2	12.52	20.8	21.4	792.1	0.460	4.2	0.027	0.11	17164
r=R	18.22	29.8	32.1	408.3	0.349	1.7	0.011	0.21	40890

4.2 Neutral Atom Sub-Model

The 2.5-D neutral atom sub-model is based on techniques that have been successfully used to calculate thermal transport view factors [51]. This technique provides an order of magnitude savings in run-time compared to a simple 2.5-D steady-state Monte Carlo simulation that was used in preliminary versions of the code. The following section shows how the "view factor" formulation uses the

Boundary Mesh to determine the neutral atom distribution and temperature regardless of the Internal Mesh type or resolution.

The Neutral Atom Sub-Model accommodates axisymmetric propellant feed configurations, including hollow cathode and plenum configurations used in conventional thrusters. Local temperatures are assigned to each feed location and atoms emitted from these locations are assumed at the thermal velocity determined by that temperature. Atoms that collide with the thruster walls are spectrally reemitted at the temperature of the incident wall. This functionality is desirable for conventional ion thrusters where the neutral propellant temperatures at the cathode and plenum feeds can differ by almost an order of magnitude and large variations in wall temperature exist [52]. The Ion Diffusion Sub-Model determines the flux of ions to the chamber surfaces, where incident ions are assumed to undergo three-body recombination and are then spectrally reemitted as neutrals with the temperature of the incident wall. In this way, all the wall elements are treated as "sources" of neutrals as described below. As discussed in Section 4.5, the recombination rate of ions in the bulk discharge is negligible compared to the recombination rate at the walls. The local wall temperatures are determined from thermal models [52] or experimental data.

For the first iteration of the Discharge Model, a uniform volume-averaged ionization rate is assumed in the Neutral Atom Sub-Model to expedite solution convergence. During subsequent iterations, the Neutral Atom Sub-Model uses the species density distributions determined in the Primary and Plasma sub-models. For the results herein, the Neutral Model uses the Internal Mesh for tracking species temperatures and densities; however, one of the fundamental advantages of the Neutral Model is its compatibility with arbitrary meshes such as the B-Mesh.

Neutral Atom Continuity Using View Factors

For a typical electron bombardment ion thruster, the mean free path of a neutral atom for interatomic and charge-exchange collisions is sufficiently long to warrant a collisionless approximation. For the NSTAR and Micro-Ion thrusters investigated herein, the average Knudsen number for neutral collisions (including neutral-neutral and charge-exchange) is greater than 1.0 [53,54]. Thus, atoms can be assumed to collide only with the chamber walls and with electrons, where they are "lost" by ionization. For a collisionless gas the steady neutral flux balance for all chamber surfaces may be determined using thermal transport view factors [51]. The following method accounts for ionization and wall recombination rates and allows for the determination of gas properties (density and temperature) at any point inside the chamber, regardless of cell size and with relatively short computational times.

The first step of the Neutral Atom Sub-Model is determining the steady-state flux of neutral atoms emitted from the walls and propellant sources using neutral atom continuity and view factors as described below. With this solution, view factors are again used to compute the neutral densities on the Boundary and Internal meshes.
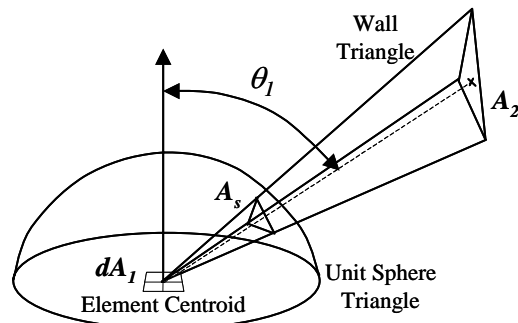

Figure 4.2-1. Configuration Factor between Areas A_2 and dA_1

The flux balance for the chamber walls is determined with the use of configuration factors and view factors. Referring to Figure 4.2-1, assuming a cosine emission distribution from a differential surface, dA_1, to a finite triangular surface, A_2, the configuration factor $\Psi_{d1\text{-}2}$ is [51]

$$\Psi_{d1-2} = \frac{1}{\pi} \int_{A_s} \cos(\theta_1) dA_s \qquad \text{[4.2-1]}$$

This equation represents the fraction of neutral atom flow from element dA_1 intercepted by A_2 due to the relative orientation of the two surfaces. Assuming cosine emission from all surfaces this expression is also the reciprocal configuration fraction of neutral flow *incident to* area dA_1 from area A_2. Assuming θ_1 is constant for a relatively small area, A_2, this becomes

$$\Psi_{d1-2} = \frac{A_s}{\pi} \cos(\theta_1) \qquad \text{[4.2-2]}$$

where the area of a spherical triangle on a unit sphere can be related to its three interior angles (γ_1, γ_2, γ_3) by the relation

$$A_s = (\gamma_1 + \gamma_2 + \gamma_3 - \pi) \qquad \text{[4.2-3]}$$

For an internal node (not on the Boundary Mesh) the configuration factor from a triangular surface, Ψ_{2-m}, will be independent of θ_1 and is simply the ratio of the spherical triangle area to the area of the entire unit sphere

$$\Psi_{2-m} = \frac{A_s}{4\pi} \qquad \text{[4.2-4]}$$

The additional effect of the depletion of neutral flow passing through the plasma of ionizing electrons is captured using a view factor, which is defined as the product of the configuration factor and the neutral ionization fraction, β:

$$V \equiv \beta \Psi \qquad \text{[4.2-5]}$$

The neutral ionization fraction, β, is the ratio of the final and initial neutral flow as a result of the neutrals traversing a path through a field of ionizing particles from the plasma. Assuming a constant neutral velocity along this trajectory, β can be defined as the ratio the final and initial neutral densities:

$$\beta \equiv \frac{n_o^f}{n_o^i} \qquad\qquad\qquad [4.2\text{-}6]$$

This ratio is found by integrating the ionization rates along the neutral flow path. For an ion thruster the neutrals can be treated as particles passing through a field of electrons, where the local ionization rate is the sum of the primary and secondary electron ionization rates

$$\dot{n}_i = \dot{n}_i^p + \dot{n}_i^s = n_0 \left(n_s K_{iz}^s + n_p K_{iz}^p \right) \qquad\qquad [4.2\text{-}7]$$

where the rate constants, K, are defined in Section 4.3 and Appendix G. The neutral loss rate is the negative of the ion generation rate

$$\dot{n}_o = -\dot{n}_i = -n_o \left(n_s K_{iz}^s + n_p K_{iz}^p \right) \qquad\qquad [4.2\text{-}8]$$

Solving Equation 4.2-8 yields the relationship of the initial and final neutral densities

$$n_o^f = n_o^i \exp\left[-\int \left(n_s K_{iz}^s + n_p K_{iz}^p \right) dt \right] \qquad\qquad [4.2\text{-}9]$$

Consequently the neutral loss rate, β, is found by integrating along the straight-line path between the centroids of dA_1 and A_2 by the expression

$$\beta = \exp\left[-\int \left(n_s K_{iz}^s + n_p K_{iz}^p \right) dt \right] \qquad\qquad [4.2\text{-}10]$$

Neutral Atom Sub-Model Formulation

With the use of configuration and view factors, as described above, the Neutral Atom sub-model can determine the density of atoms for any node inside the chamber. This is done by first defining the chamber walls as 1-D elements of the Boundary Mesh. The actual surface represented by each 1-D element is then defined as a collection of triangular elements. By defining these triangles, the

proper configuration factors and neutral loss integration paths between the Boundary Mesh elements may be determined. The ionization properties (i.e., $n_s, K_{iz}^s, n_p, K_{iz}^p$) along the integration paths are determined from the plasma properties in the 2-D solution space of the Internal Mesh. For a simple cylindrical chamber, as shown in Figure 4.2-2, the wall elements at the ends of the cylinder would be defined by triangles as shown in Figure 4.2-3. Since the domain is assumed axisymmetric, only 180° of the chamber surface need to be defined. In an actual discharge some surfaces protrude into the chamber. These surfaces, such as the cathode cylinder and the grid flange, shadow some of the chamber surfaces. The 3-D effects of this shadowing are treated by defining the protruding shape as a simple geometric shape (e.g., cylinder) that is infinitesimally smaller than the shape as defined on the Boundary Mesh. If the trajectory between two points intersects this shape then these surfaces are assumed to be shadowed from each other.
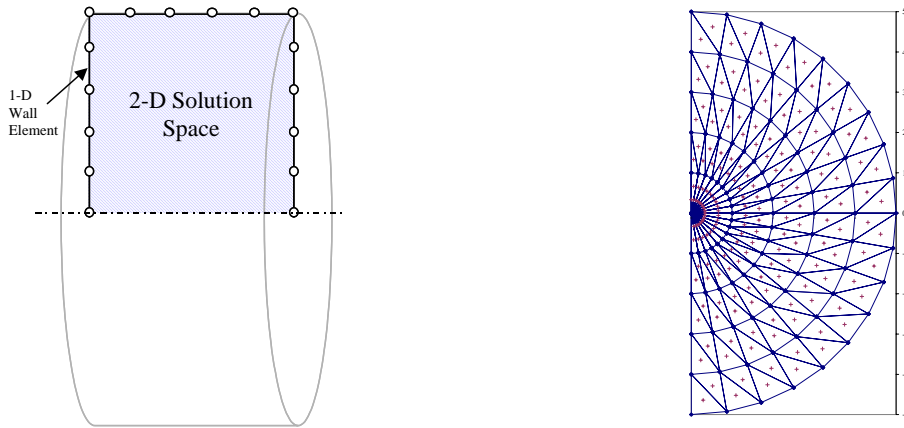

Figure 4.2-2. Example Cylindrical Discharge Chamber   Figure 4.2-3. Triangular Elements for Cylinder Ends

To determine the neutral flow balance for the 1-D wall elements, a matrix is developed that represents the interrelationship of the wall elements. The first step is normalizing the configuration factors to assure that the entire flow of atoms from each element is seen by the rest of the chamber. By continuity, the summation of the configuration factors of an element should equal 1. If this condition is not identically met then the configuration factors for a given wall element, h, are

71

normalized using an identical factor to satisfy continuity of neutral atom flux, such that

$$\sum_m \Psi_{hm} = \sum_m \sum_{t_m} \Psi_{ht_m} \equiv 1$$

[4.2-11]

where t_m indicates the wall triangle associated with wall element m. To determine the neutral flow balance matrix the total influence of a wall element m on an element h is expressed using the reciprocal view factor, V_{mh}. To include the influence from all triangles representing element m, the view factor is

$$V_{mh} = \sum_{t_m} \beta_{t_m h} \Psi_{t_m h}$$

[4.2-12]

where $\Psi_{t_m h}$ is the reciprocal configuration factor.

With the view factors between wall elements defined, an expression for the neutral atom flow continuity between the wall elements can be determined. For steady-state continuity the atom flow, Y, from a given wall element, h, must equal the flow it receives from all other wall elements (m), gas sources (s), and local wall recombination (r). Using the appropriate view factors and any wall transparencies, ζ_o, (i.e., grids)

$$Y_h = \sum_m V_{mh} Y_m (1 - \zeta_{o,m}) + \sum_s V_{sh} Y_s + Y_{rh}$$

[4.2-13]

where Y_h, Y_m, and Y_s represent the neutral flow (#/s) from elements h and m, and source s, respectively. The effective atom flow from wall element, h, from wall recombination, Y_{rh}, is described at the end of this section. Combining Equation 4.2-13 for all wall elements yields a matrix that is nonsingular in the condition that $\zeta \neq 0$ for at least one wall element (i.e., gas can exit the chamber). By defining the discharge chamber and plasma characteristics, the following global continuity matrix is solved for the neutral atom flow balance:

$$
\begin{bmatrix}
1 & \left(-V_{21}(1-\zeta_{o,2})\right) & . & . \\
\left(-V_{12}(1-\zeta_{o,1})\right) & 1 & \left(-V_{13}(1-\zeta_{o,3})\right) & . \\
. & . & . & . \\
. & . & . & .
\end{bmatrix}
\begin{bmatrix}
Y_1 \\
Y_2 \\
. \\
.
\end{bmatrix}
=
\begin{bmatrix}
\sum_s V_{s1}Y_s + Y_{r1} \\
. \\
. \\
.
\end{bmatrix}
\qquad \text{[4.2-14]}
$$

With the solution to the global continuity matrix, the density, average temperature, and velocity of the atoms at any point in the chamber, or on the chamber boundary, can be obtained using the conservation of momentum for a given location. To do this the neutral flux, y (#/s/m^2), from the wall elements is expressed as the ratio of the total flow and total area of that wall element or triangle (i.e., $y_m = Y_m/A_m$). By assuming the propellant sources emit with a cosine distribution, the neutral flux from a source, s, at a location k is given by

$$
y_{sk} = Y_s \beta_{sk} \Theta_{sk} \qquad \text{[4.2-15]}
$$

where

$$
\Theta_{sk} = \frac{\cos(\theta_{sk})}{\pi \Delta_{sk}^2} \qquad \text{[4.2-16]}
$$

and Δ_{sk} is the distance between the source and the location of interest. For internal node, k, the density expressed as the sum of flux contributions from wall elements and sources by the relationship

$$
n_k = 4 \sum_m V_{mk}(1-\zeta_{o,m})\left(\frac{y_m}{\overline{C}_m}\right) + 4 \sum_s \frac{y_{sk}}{\overline{C}_s} \qquad \text{[4.2-17]}
$$

where y represents flux and $\overline{C}$ is the mean speed from the Maxwellian distribution for thermal velocity for temperature of the emitting discharge surface or propellant source.

$$
\overline{C} = \sqrt{\frac{8kT}{\pi m}} \qquad \text{[4.2-18]}
$$

Using the flux solution from the global continuity matrix, Eq. 4.2-14, the total flux to node k is found from the expression

$$y_k = \sum_m V_{mk}(1 - \zeta_{o,m})y_m + \sum_s y_{sk}$$

[4.2-19]

An approximation of the local thermal velocity is obtained by dividing the total flux to node k by the local neutral density. This velocity is then used to find the local temperature from Equation 4.2-18.

To determine the density at a wall element, h, the properties of both the incident and outgoing flux for the unit hemisphere surrounding the element are used. Since the chamber temperature is not uniform, the resulting expression for the neutral density of a wall element, h, depends on the thermal velocity and one-sided flux by

$$n_h = 2\frac{y_h}{\bar{C}_h} + 2\sum_m V_{mh}(1 - \zeta_{o,m})\frac{y_m}{\bar{C}_m} + 2\sum_s \frac{y_{sh}^w}{\bar{C}_s}$$

[4.2-20]

where, for this calculation, the effect of a source on the wall element is given by the collective effects per the triangles, t_h, that make up the element

$$y_{sh}^w = Y_s \beta_{sh} \Theta_{sh} = Y_s \left(\frac{\displaystyle\sum_{t_h} \beta_{st_h} \Theta_{st_h} A_{t_h}}{\displaystyle\sum_{t_h} A_{t_h}} \right)$$

[4.2-21]

Neutral Atom Boundary Conditions

Propellant is either extracted through the grids as ions or lost through the grids as "unused" neutral atoms. The total loss rate of neutral atoms through a grid element, m, of the Boundary Mesh is found by multiplying the neutral flow incident to a Boundary Mesh element from Equation 4.2-13 by the grid transparency to neutrals

$$\dot{m}_{loss}^h = Y_h \zeta_{o,h}$$

[4.2-22]

74

The grid transparency to neutral atoms, ζ_o , is determined from the product of the geometric open area fraction and is adjusted by the Clausing factor to account for the thickness of the grids [55]. The sum of neutral losses is then used to calculate the propellant efficiency per the Neutral Atom Sub-Model by

$$\eta_{ud[Gas]} = 1 - \frac{\sum_h \dot{m}_{loss}^h}{\sum_s J_s} = \frac{\dot{m}_d - \dot{m}_{loss}}{\dot{m}_d}$$

[4.2-23]

this is identical to Equation 4.1-1.

The main sources of neutrals in this sub-model are the propellant feeds; however, neutrals are also "re-created" when ions recombine with electrons. Ion recombination predominantly occurs on chamber surfaces and results in an effective neutral flux from the interior chamber surfaces. The flux of ions to the chamber walls is calculated by the Ion Diffusion Sub-Model, Section 4.5, and is treated as a source of neutrals on the RHS of the global continuity matrix, Equation 4.2-14. Ions that recombine on discharge chamber surfaces are assumed to be reemitted at mean Maxwellian velocity per the local temperature of the wall. The following section explains how the local ion generation rates are determined.

4.3 Electron Collision Sub-Model

DC ring-cusp ion thruster plasmas are populated by high-energy "primary" electrons that are emitted from the cathode and lower-energy "secondary" electrons. The following section describes the methods used to account for the collisions of these electrons with other species of the plasma, including each other. In general, the primaries are treated using a particle tracking algorithm, while the secondaries are considered to be a thermalized component of the quasi-neutral plasma. In the Electron Collision Sub-Model, the ionization rates due to both electron species are found and summed to yield the total ionization rate

$$\dot{n}_i = \dot{n}_i^p + \dot{n}_i^s$$

<div align="right">[4.3-1]</div>

Other results from this sub-model, such as secondary electron production rates and the rate of loss of primary electron energy to the secondary population, are used in the Electron Thermal Sub-Model. Charge-exchange (CEX) ionization does not affect the total number of ions inside the chamber so it is not considered in this sub-model; however, the CEX effects on ion motion are considered in Section 4.5.

Primary Electron Tracking

Primary electrons ("primaries") represent the main source of energy input to the discharge chamber. The degree of utilization of this energy for creating a uniform density of beam ions is directly related to the overall efficiency of the thruster. Thus, it is important to be able to identify the general behavior, distribution, and interactions of primaries in the discharge chamber. The mean free path for a primary in an ion thruster discharge chamber is several times the diameter of the thruster. In this regime, a particle-tracking method, with collisions to describe interactions with other species, is sufficient to describe their behavior. Between collisions, the primary motion may be treated as the motion of a charged particle in the presence of an electromagnetic field, which is described by the Lorentz equation

$$m_e \frac{d\mathbf{w}}{dt} = q\left(\mathbf{E} + \mathbf{w} \times \mathbf{B}\right)$$

<div align="right">[4.3-2]</div>

where $\mathbf{w}$ is the average speed of the primary population defined in Appendix G. The Electron Collision Sub-Model tracks the motion of the primary electrons in the discharge chamber to find the spatially distributed ionization rate and secondary electron production rates. In this sub-model, the primaries are emitted from the cathode as macro quasi-particles (or simply "particles"), where each particle represents a fraction of the cathode current. The particles are assumed to exit the cathode with a cosine distribution with respect to the cathode normal. The current

represented by a particle is gradually reduced by collisions with other species of the plasma as described below. A particle is assumed to maintain its energy until particle current is essentially depleted by collisions (<0.1%), or it physically intersects a surface. The energy at which the primaries are emitted is discussed later as a boundary condition. This sub-model is effectively 2.5-D since the primary particle trajectories are followed in a 3-D magnetic field and chamber geometry while the properties such as primary density and ionization rate are kept on the 2-D Internal Mesh that is passed to other sub-models.

The motion of the particles between elastic collisions can be described with an implicit particle-pushing algorithm. For this sub-model, the Lorentz forces on the particle are decomposed into electric and magnetic forces based on the Boris particle-pushing technique [56]. Electrostatic forces are assumed to act half at the beginning, and half at the end of a given time step. This allows the circular motion of the particle due to the magnetic field to be treated in the absence of the electric field. The general equations of motion are then

$$m_e \frac{d\mathbf{w}}{dt} = \frac{1}{2}q\mathbf{E}, \ \left(t = 0 \rightarrow \frac{\Delta t}{2}\right) \ \Rightarrow \ \mathbf{w}_1 = \mathbf{w}_o + \frac{q\Delta t}{2m_e}\mathbf{E} \qquad \text{[4.3-3]}$$

$$m_e \frac{d\mathbf{w}}{dt} = q(\mathbf{w} \times \mathbf{B}), \ \left(t = 0 \rightarrow \Delta t\right) \ \Rightarrow \ \text{See Equation 3.3-11} \qquad \text{[4.3-4]}$$

$$m_e \frac{d\mathbf{w}}{dt} = \frac{1}{2}q\mathbf{E}, \ \left(t = \frac{\Delta t}{2} \rightarrow \Delta t\right) \ \Rightarrow \ \mathbf{w}_f = \mathbf{w}_2 + \frac{q\Delta t}{2m_e}\mathbf{E} \qquad \text{[4.3-5]}$$

The circular gyromotion of the particle simply rotates the velocity vector about the axis of rotation. A sufficiently small time step, $\Delta t << 2\pi r_{ce}/|\mathbf{w}|$, is calculated before each calculation to ensure accuracy of the trajectory. A maximum time step is imposed in low B-field regions to assure that the particle travels a very small distance (<<1mm) during any given time step. A predictor/corrector particle-tracking algorithm determines the particle trajectory for each time step by first

predicting the midpoint of the trajectory assuming the magnetic field at the starting position. The magnetic field at the "predicted" midpoint is calculated and then used to determine a "corrected" final position and velocity orientation. A schematic of this process is shown in Figure 4.3-1, where, in this particular example, the B-field at the midpoint is greater than that of the starting point. Both the predictor and the corrector approximate the circular gyromotion of the charged particle by equations 4.3-6 – 4.3-11, which simply rotate the perpendicular velocity vector. The velocity along the magnetic field axis remains unchanged and acts only to move the particle along the axis. This method has several advantages, when compared with other techniques, in both accuracy and speed. In particular, the use of simple low-order calculations takes advantage of the fact that modern computers are well suited for simple, fast calculations, so that small time steps can be used to attain high accuracy [56].
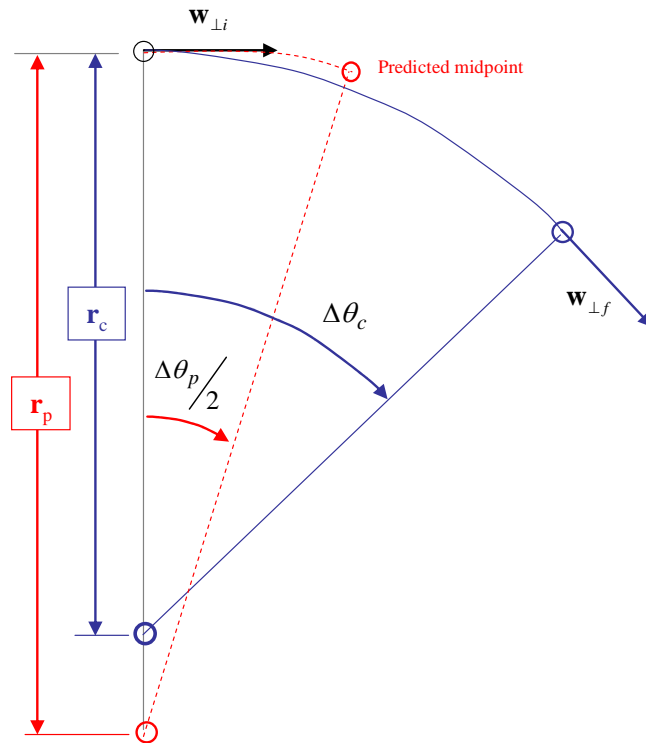
Figure 4.3-1. Primary Electron Gyromotion Using Predictor/Corrector

At each time step the directions parallel to the B-field, along the gyroradius, and along the perpendicular velocity of the diamagnetic rotation of the electron about the B-field are defined respectively by

$$\hat{h}_{\parallel} = \frac{\mathbf{B}}{|\mathbf{B}|}, \quad \hat{h}_r = \hat{h}_{\parallel} \times \frac{\mathbf{w}}{|\mathbf{w}|}, \quad \hat{h}_{\perp} = \hat{h}_{\parallel} \times \hat{h}_r \qquad \text{[4.3-6]}$$

The center of rotation is then defined by

$$\mathbf{x}_c = \mathbf{x}_i + r_{ce}\hat{h}_r \qquad \text{[4.3-7]}$$

$$\text{where, } r_{ce} = \frac{|\mathbf{w}_{\perp}|}{\omega_{ce}} \text{ and } \omega_{ce} = \frac{q|\mathbf{B}|}{m_e} \qquad \text{[4.3-8]}$$

The time step is defined by desired number of steps per revolution, ρ, and the gyrofrequency, whereas the minimum time step is defined by a minimum distance:

$$\Delta t = \frac{2\pi}{\omega_{ce}\rho} < \Delta t_{min} = \Delta x_{min} / |\mathbf{w}| \qquad \text{[4.3-9]}$$

The rotational step is then taken as

$$\Delta\theta = \omega_{ce}\Delta t \qquad \text{[4.3-10]}$$

Using the results from the above equations, the change in position and rotation of the velocity vector can be defined by

$$\Delta x_{\parallel} = (\mathbf{w} \cdot \hat{h}_{\parallel})\hat{h}_{\parallel}\Delta t$$

$$\Delta x_{\perp} = r_{ce}\sin(\theta)\hat{h}_{\perp}$$

$$\text{[4.3-11]}$$

$$\Delta x_r = -r_{ce}\left[1 - \cos(\theta)\right]\hat{h}_r$$

$$\mathbf{w}_f = \mathbf{w}_{\parallel} + |\mathbf{w}_{\perp}|\left[\cos(\theta)\hat{h}_{\perp} + \sin(\theta)\hat{h}_r\right]$$

79

Primary Electron Collisions

The interaction of the primaries with other discharge species may be treated as a collection of inelastic and elastic collisions with neutrals, ions, and secondary "thermalized" electrons. The method for determining the rate constants for electron collisions is described in Appendix G. For the typical lifetime of a primary in the discharge, the average fraction of initial kinetic energy lost by electrons incident on field particles due to elastic collisions is less than 0.1%. Therefore, a primary's energy is assumed to remain unchanged during elastic collisions. The scattering angles due to elastic collisions are estimated by three-dimensional probabilistic hard-sphere scattering [57]. Elastic collisions contribute to the diffusion of primary electrons by altering the particle trajectory. In the primary sub-model, elastic collisions are treated collectively for each time step, Δt. If the probability for an elastic collision, Equation 4.3-12, is greater than a randomly generated number between 0 and 1, then the macro-particle's trajectory is altered using a probabilistic hard-sphere scattering angle [57].

$$P_{el} = 1 - \exp(-\Delta t K_{el}^{p} n_o)$$
[4.3-12]

where the rate constant is described in Appendix G.

During an inelastic collision with an atom, the incident primary will lose energy essentially equivalent to the energy absorbed by the atom. For ground energy level neutral xenon, the first excitation energy is 8.32eV (12.1 and 21.2eV for single and double ionization), which indicates that an incident electron will lose at least 8.32eV of energy during an inelastic collision [58]. The energy of a primary electron in an ion thruster discharge is on the order of 20eV. Consequently, by using the Spitzer particle-field slowing rate for electron populations, Appendix G, the equilibration rate of a primary electron to the background secondary electron population is several times faster after an inelastic collision with a ground state neutral [59]. Therefore primaries are considered to join the secondary population after a single inelastic collision. In this approximation, inelastic primary electron

collisions are assumed to simply deplete the current represented by the primary electron particle, J_p. The rate at which this depletion occurs is derived by considering the change in flux for particles during time-step Δt through a collection of species densities, n, with respective rate constants, K [50]:

$$\Gamma(t + \Delta t) = \Gamma(t)\exp\left(-\Delta t \sum(Kn)\right)$$

[4.3-13]

The sum of the effects of inelastic collisions with neutrals, ions, and secondaries is

$$\sum(Kn) = n_o\left(K_{iz}^o + \sum K_{ex}^o\right) + n_i\left(K_{iz}^+\right) + n_s\left(K_{slow}^s\right)$$

[4.3-14]

where K_{iz}^o, K_{ex}^o, and K_{iz}^+ are the rate constants for single ionization and excitation of neutrals, and for double ionization of single ions. The rate constant, K_{slow}^s, is determined using the Spitzer particle-field slowing time [59]. The techniques for determining these collision rate constants are described in Appendix G. Primary electron recombination with ions and excitation of ions are neglected since these collisions are over an order of magnitude slower than the Spitzer particle-field slowing rate [57, 59].

Using Equation 4.3-13 and assuming the primary electron macro-particle starts with current J_p, the total current lost, ΔJ_p, during time-step Δt, is then

$$\Delta J_p = J_p P_{tot}$$

[4.3-15]

where P_{tot}, the percentage of current lost due to all collisions, is

$$P_{tot} = \left[1 - \exp\left(-\Delta t \sum(Kn)\right)\right]$$

[4.3-16]

Using the result for ΔJ_p, the amount of current lost to each type of collision is determined by weighting the percentage loss of each collision type. For example, the percentage lost due to ionization collisions, P_{iz}, is

$$P_{iz} = \left[1 - \exp\left(-\Delta t \left(K_{iz}^o n_o + K_{iz}^+ n_i \right) \right) \right]$$

[4.3-17]

and is similarly defined for excitation and slowing effects. The primary current lost to ionization is then

$$\Delta J_p^{iz} = \frac{P_{iz}}{\sum P} \Delta J_p$$

[4.3-18]

where

$$\sum P = P_{iz} + P_{ex} + P_{slow}$$

Since ΔJ_p^{iz} is equal to the ion generation rate, the total ionization rate for each cell is then determined by summing all the primary ionization found in that cell

$$\dot{n}_i^p = \left(\sum \Delta J_p^{iz} \right) / V_{cell}$$

[4.3-19]

where V_{cell} is the volume of the cell in which the particle resides during the time step.

An inelastic collision results in a neutral or ion being raised to a higher energy quantum state, which predominantly manifests in a valence electron being raised to an excited energy level. For an ionization collision, the valence electron is assumed to be lost to the secondary electron population and the neutral atom becomes a singly charged ion or the ion becomes doubly charged, and so on. From the above discussion, it is then reasonable to assume that an ionization collision due to a primary electron simply results in an ion and two energetic secondary electrons. Higher order interactions with ions and metastable states are neglected. During an excitation collision, a valence electron of the incident atom assumes a higher energy state for a very short period of time and then releases a photon as it relaxes to a lower energy state. While at the excited energy level, an atom is more susceptible to ionization; however, at typical ion thruster discharge conditions the de-excitation

rate of the atom is predominantly much faster than any external collision frequency. This implies that the relaxation process is essentially instantaneous. An exception to this scenario is the case of metastable atomic states where the de-excitation rate is relatively slow; however, in this analysis metastable states are not included. The escape probability of the photon emitted during de-excitation of the atom is high enough to consider the plasma to be optically thin. Therefore, the energy transferred during excitation collisions is considered lost from the plasma. The aforementioned assumptions, however, do not imply that energy is explicitly conserved in the model.

Additional energy loss or effect collisional mechanisms for primary and secondary electrons may arise from anomalous effects such as Buneman, ion acoustic, and lower-hybrid drift instabilities. Recent numerical simulations of the plasma inside a hollow cathode suggest that anomalous mechanisms may persist in the near-orifice region. Hollow cathode theoretical and experimental work is currently being extended to include the cathode orifice and the near-cathode regions, and will help clarify if such effects are important in the discharge plasma [8]. Since anomalous collisions have to be characterized for the discharge chamber, they are not directly treated in this model.

Secondary Electron Energy Distribution and Ionization

In general, the secondaries are assumed to have a Maxwellian velocity distribution; however, results from similar plasma discharges suggest that high-energy electrons in the tail of the Maxwellian distribution can become depleted, resulting in a "depleted tail" distribution [60]. Since the degree to which this occurs in ion thrusters is unknown at this time, the Electron Collision Sub-Model approximates the depleted tail distribution by using a corrected temperature for inelastic collisions. To simulate this tail depletion a secondary inelastic collision fraction, f_{inel}, is chosen. The product of this fraction and the secondary electron temperature,

T_s (note: T_s is determined by the Electron Thermal Sub-Model), yields the secondary electron temperature for inelastic collisions, T_s^{inel}, such that

$$T_s^{inel} = f_{inel} T_s$$ [4.3-20]

Inelastic collisions for secondaries, such as those that contribute to electron cross-field diffusion, are still assumed to behave at the 5eV electron temperature. The secondary inelastic collision fraction may also be used to approximate an augmented tail distribution. With this approximation, the ionization due to secondary electrons is added to the total volumetric ionization rate for each cell using

$$\dot{n}_i^s = K_{iz}^s n_o\, n_s + K_{iz}^{+s} n_i\, n_s$$ [4.3-21]

where the temperature, T_s^{inel}, is used to find the rate constant (Appendix G). A value of $f_{inel} \sim 0.8$ gave good agreement with experimental data as discussed in Chapter 5. Since primaries are assumed to join the secondary population immediately following inelastic collisions, the production rate of secondary electrons due to both primary collisions and secondary electron ionization is

$$\dot{n}_s = 2\dot{n}_i^p + \dot{n}_{ex}^p + \dot{n}_{slow}^p + \dot{n}_i^s$$ [4.3-22]

Primary Electron Boundary Conditions

Ion thrusters are designed so that the average energy of the primaries is less than the sheath potential at the cathode surfaces. Consequently, the primaries are assumed to be reflected by these surfaces at all angles of incidence. In the case of a hollow cathode discharge, some of the high-energy electrons in the tail of an accelerated half-Maxwellian distribution (see Appendix G) are at energies greater than the sheath potential. At this time these effects are assumed negligible, however this energy loss mechanism warrants consideration in future versions of the model. The

energy with which the primary electrons are emitted from the cathode is discussed in Appendix G. Results from the Ion Optics Sub-Model show that the negative potential contours just inside the grids are curved into the discharge chamber, creating an essentially "bumpy" potential surface. To capture the effect of this somewhat random potential structure, the particles are reflected with a cosine distribution normal to the grid surface. If the path of the particle intersects any anode surface, it is assumed to be lost since the particle's energy is much greater than the anode sheath potential. A discussion of secondary electron boundary conditions is reserved for Section 4.6.

An example of the path of a *single* primary electron particle in the NSTAR discharge chamber is shown in Figure 4.3-2. As expected, the particle originates at the hollow cathode orifice and is magnetically confined at the cusps, reflected from cathode potential surfaces, scattered by elastic collisions, and lost to an anode surface.
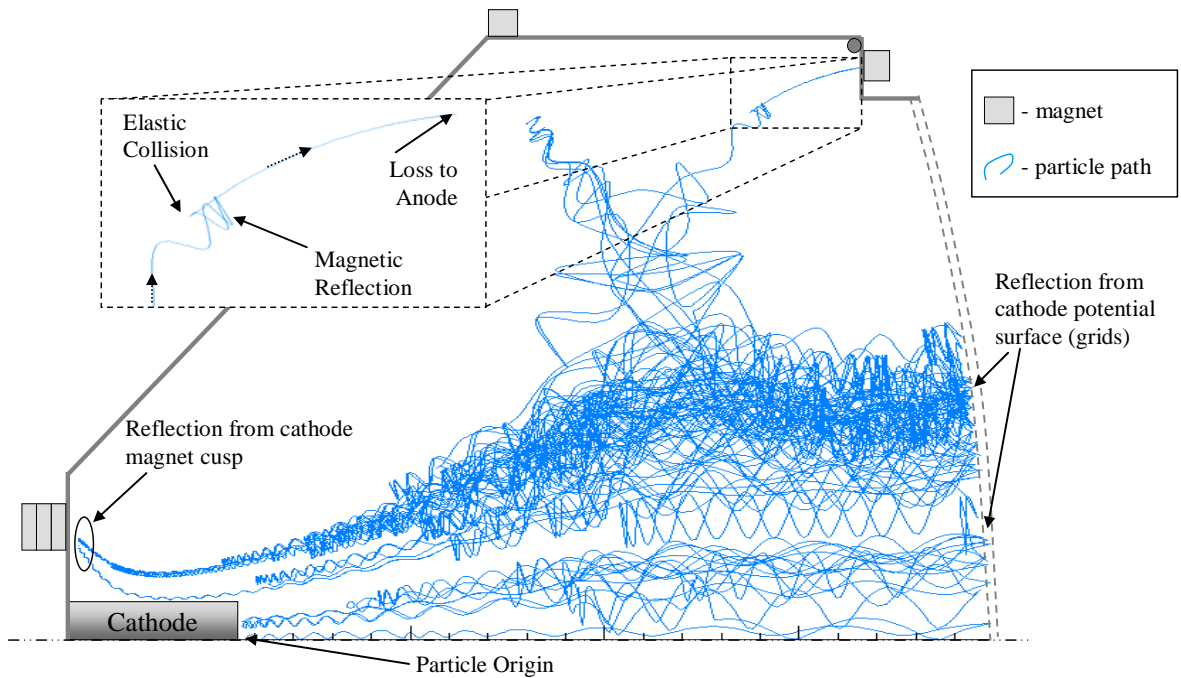
Figure 4.3-2. Simulated Path of a Single Primary Electron Inside the NSTAR Discharge Chamber

4.4 Ion Optics Sub-Models

A 2-D ion optics model that was developed at JPL [12] is used to determine the extraction grids' transparency to ions, ζ_i, which is mainly a function of ion density, electron temperature, and beam voltage. This result defines the boundary conditions for the ions at the grid elements of the Boundary Mesh as discussed in Section 4.5. Results from the 2-D ion optics model are shown in Chapter 3 and Appendix D, where the model was used to improve the grid design of a miniature ion thruster.

A 3-D ion optics code, also developed at JPL [9], is designed to use the results of the Discharge Model to generate detailed projections of grid wear and life. Since grid wear significantly changes the grid geometry, the combined Discharge Model and ion optics models can determine the effects of grid erosion on the long-term performance of a thruster. This functionality will allow the grid design to be optimized for the life of the thruster.

4.5 Ion Diffusion Sub-Model

The Ion Diffusion Sub-Model uses the ion generation rates found in the Electron Collision Sub-Model to determine the ion density distribution on the Internal Mesh. In this section, a classical ambipolar ion diffusion equation is derived from the combined single ion and electron motion equations. This equation is then recast to include a correction for non-classical perpendicular diffusion as a function of the relative importance of electron-ion collisions. These equations are formulated to determine the *total* ion densities and fluxes in the thruster. With this solution, the double ion densities are approximated using double-to-single ion generation rates and a simple time-stepping algorithm. The single and double ion densities are then used to determine the beam current and the loss rate of ions to the chamber walls.

Ion Diffusion Theory

The motion of the ions in an ion thruster-type discharge can be described by separately considering their behavior parallel and perpendicular to the magnetic field. The parallel motion is described using a classical ambipolar treatment; however, for computational models of similar plasma regimes, the perpendicular motion is described using either classical or non-classical descriptions, or some combination [49,33]. For example, Arakawa [33] separately used classical and Bohm (non-classical) perpendicular ion motion descriptions. Arakawa's model generally showed better agreement with experimental results using a classical description. In this formulation, the classical ambipolar diffusion equation is derived for partially ionized plasma of single ions, unequal ion and electron generation rates, and non-uniform temperatures. Following this derivation, a method for estimating the effects of non-classical diffusion effects is presented.

Conservation Equations

The ambipolar equations are derived by combining the continuity and momentum equations for ions and electrons. From the zeroth moment of the collisional Vlasov (Boltzmann) equation for partially ionized plasma, the continuity equation of quasi-neutral plasma with singly charged ions is

$$\frac{\partial n}{\partial t} + \nabla \cdot (n\mathbf{u}) = \dot{n} \qquad \text{[4.5-1]}$$

The momentum equation, from the first moment of the Boltzmann equation for partially ionized plasma, is given by

$$m\left[\frac{\partial(n\mathbf{u})}{\partial t} + \nabla \cdot (n\mathbf{u}\mathbf{u})\right] = nq(\mathbf{E} + \mathbf{u} \times \mathbf{B}) - \nabla \cdot \mathbf{P} - \mathbf{R} \qquad \text{[4.5-2]}$$

$$\mathbf{R} \equiv nm\sum_a \langle \nu_a \rangle (\mathbf{u} - \mathbf{u}_a) \qquad \text{[4.5-3]}$$

87

where **R** represents the transfer of momentum to a given species by collisions with all plasma species. Expanding the LHS of Equation [4.5-2] and combining it with equations [4.5-1] and [4.5-3] yields

$$m\left[n\frac{\partial \mathbf{u}}{\partial t}+n\mathbf{u}\cdot\nabla(\mathbf{u})+\mathbf{u}\left(\frac{\partial n}{\partial t}+\nabla\cdot(n\mathbf{u})\right)\right]=nq(\mathbf{E}+\mathbf{u}\times\mathbf{B})-\nabla\cdot\mathbf{P}-\mathbf{R}$$
[4.5-4]

$$mn\left[\frac{\partial \mathbf{u}}{\partial t}+\mathbf{u}\cdot\nabla(\mathbf{u})\right]=nq(\mathbf{E}+\mathbf{u}\times\mathbf{B})-\nabla\cdot\mathbf{P}-\mathbf{R}-m\mathbf{u}\dot{n}$$
[4.5-5]

For a steady or quasi-steady state solution $\partial \mathbf{u}/\partial t = 0$ and assuming stationary diffusive plasma conditions, the continuity and momentum equations reduce to the following forms [61]:

$$\nabla\cdot(n\mathbf{u})=\dot{n}$$
[4.5-6]

$$nq(\mathbf{E}+\mathbf{u}\times\mathbf{B})=\nabla\cdot\mathbf{P}+\mathbf{R}+m\mathbf{u}\dot{n}$$
[4.5-7]

For this diffusion formulation, the anisotropy due to the magnetic field is expressed by the 2-D axisymmetric pressure dyad in perpendicular and parallel components:

$$\mathbf{P}=\begin{bmatrix} p_{\perp} & 0 \\ 0 & p_{\parallel} \end{bmatrix}$$
[4.5-8]

Assuming a scalar pressure for a given direction, the divergence of the pressure dyad, for a given direction, becomes

$$\nabla\cdot\mathbf{P}\rightarrow\nabla p$$
[4.5-9]

88

Assuming that the plasma generally behaves as an ideal fluid for a given direction, the gradient of the scalar pressure becomes $\nabla p = k\nabla(nT)$, resulting in the momentum equation

$$nq(\mathbf{E}+\mathbf{u}\times\mathbf{B}) = k\nabla(nT) + \mathbf{R} + m\mathbf{u}\dot{n} \qquad [4.5\text{-}10]$$

In the following analysis, Equation 4.5-10 is used with the continuity equation [Eq. 3.5-6] to describe the coupled ion and secondary electron motion.

Anisotropic Mobility from Coupled Ion and Electron Motion

The motion of electrons and ions are coupled by their mutual Coulomb interactions and are often treated using ambipolar diffusion as discussed in references [50,66,61]. For magnetized plasma, these treatments discuss a regime of equal generation rates of electrons and ions where divergences of the species fluxes may be equated. For a DC discharge this is not necessarily the case since the generation of secondary electrons from collisions of high-energy primary electrons causes an imbalance of the generation rates of secondary electrons and ions. To approximate this phenomenon, Koch [22] assumed a constant ratio between ion and secondary generation rates. This approximation is not used in this analysis since the density of primary electrons, and hence local production rates, can be highly non-uniform for DC ion thrusters [62], which results in large differences in generation rates. Another characteristic of DC discharges that is commonly ignored is the effect of electron temperature gradients that may be non-negligible in some regions of the chamber. An ambipolar plasma equation is developed below to describe the coupled electron and ion motion for a DC discharge with non-uniform ion and secondary production rates and temperatures.

The ambipolar mobility equations are determined by combining the ion and secondary electron momentum equations. Assuming quasi-neutral plasma of singly charged ions the momentum equations are

$$\mathbf{R}_i + \mathbf{u}_i m_i \dot{n}_i = ne\mathbf{E} + ne\mathbf{u}_i \times \mathbf{B} - k\nabla(nT_i)$$ [4.5-11]

$$\mathbf{R}_e + \mathbf{u}_e m_e \dot{n}_e = -ne\mathbf{E} - ne\mathbf{u}_e \times \mathbf{B} - k\nabla(nT_e)$$ [4.5-12]

where $q = e$ for ions and $q = -e$ for electrons. To combine equations 4.5-11 and 4.5-12, the generation and momentum transfer terms on the LHS are recast. The generation terms are expressed using effective collision frequencies as follows:

$$\nu_{i-gen} = \dot{n}_i / n$$ [4.5-13]

$$\nu_{e-gen} = \dot{n}_e / n$$ [4.5-14]

The momentum transfer terms are then rewritten in terms of collision frequencies as well. In typical ion thruster discharges, the electron-ion and ion-electron Coulomb collision frequencies, ν_{ei} and ν_{ie}, cannot be ignored in comparison to the electron-neutral, ν_{eo}, and ion-neutral, ν_{io}, collision frequencies. In addition to these collisions, the ion-neutral charge-exchange frequency, ν_{CEX}, is included. The neutral drift velocities are typically assumed negligible compared to the electron and ion drift velocities for ion thrusters, thus $\mathbf{R}_i$ and $\mathbf{R}_e$ may be written as

$$\mathbf{R}_i \equiv nm_i \sum_a \langle \nu_{ia} \rangle (\mathbf{u}_i - \mathbf{u}_a) = nm_i \nu_{ie} (\mathbf{u}_i - \mathbf{u}_e) + nm_i \nu_{io} \mathbf{u}_i + nm_i \nu_{CEX} \mathbf{u}_i$$ [4.5-15]

$$\mathbf{R}_e \equiv nm_e \sum_a \langle \nu_{ea} \rangle (\mathbf{u}_e - \mathbf{u}_a) = nm_e \nu_{ei} (\mathbf{u}_e - \mathbf{u}_i) + nm_e \nu_{eo} \mathbf{u}_e$$ [4.5-16]

Momentum conservation requires that

$$nm_i v_{ie} \left(\mathbf{u}_i - \mathbf{u}_e \right) = -nm_e v_{ei} \left(\mathbf{u}_e - \mathbf{u}_i \right)$$
[4.5-17]

Combining these expressions, the momentum equations become

$$nm_i v_{i-o} \mathbf{u}_i - nm_e v_{ei} \left(\mathbf{u}_e - \mathbf{u}_i \right) = ne\mathbf{E} + ne\mathbf{u}_i \times \mathbf{B} - k\nabla \left(nT_i \right)$$
[4.5-18]

$$nm_e v_{e-o} \mathbf{u}_e + nm_e v_{ei} \left(\mathbf{u}_e - \mathbf{u}_i \right) = -ne\mathbf{E} - ne\mathbf{u}_e \times \mathbf{B} - k\nabla \left(nT_e \right)$$
[4.5-19]

where the neutral-centered ion and electron frequencies are

$$v_{i-o} \equiv v_{io} + v_{CEX} + v_{i-gen}$$
[4.5-20]

$$v_{e-o} \equiv v_{eo} + v_{e-gen}$$
[4.5-21]

Collision frequencies v_{ei}, v_{io}, v_{CEX}, and v_{eo} are defined in Appendix G. The electron temperatures used for Equation 4.5-19 are determined by the Electron Thermal Sub-Model. Since ion energy is not conserved in this model, a method for estimating the ion temperature is derived from experimental results that show the ion temperature is generally between the neutral temperature and the electron temperature for ion thruster-type plasma conditions [63]. These experimental results suggest that the ion temperature is about one-half to one order of magnitude less than the electron temperature depending on ion mass. For the results presented in chapters 5 and 6, the local ion temperature of the relatively massive xenon (used for the thruster simulations herein) is assumed to be one-tenth the local electron temperature, $T_i = 0.1T_e$.

As discussed earlier, this analysis considers plasma motion in a two-dimensional radial plane of the axisymmetric domain. In this plane the directions parallel and perpendicular to the B-field are identified by the symbols ∥ and ⊥, respectively.

Plasma motion and gradients in the azimuthal direction are not addressed in this problem.

equations 4.5-18 and 4.5-19 are coupled by the electron-ion collisions. In an analysis similar to that shown in Koch [22], the coupled ion and electron motion may be resolved in the parallel and perpendicular directions, resulting in the expressions

$$nu_i = -\mu_{ii}\nabla^{\parallel}\left(nT_i\right) - \mu_{ie}\nabla^{\parallel}\left(nT_e\right) + n\mu_i E^{\parallel} \qquad \text{[4.5-22]}$$

$$nu_e = -\mu_{ei}\nabla^{\parallel}\left(nT_i\right) - \mu_{ee}\nabla^{\parallel}\left(nT_e\right) - n\mu_e E^{\parallel} \qquad \text{[4.5-23]}$$

$$nu_i^{\perp} = -\mu_{ii}^{\perp}\nabla^{\perp}\left(nT_i\right) - \mu_{ie}^{\perp}\nabla^{\perp}\left(nT_e\right) + n\mu_i^{\perp} E^{\perp} \qquad \text{[4.5-24]}$$

$$nu_e^{\perp} = -\mu_{ei}^{\perp}\nabla^{\perp}\left(nT_i\right) - \mu_{ee}^{\perp}\nabla^{\perp}\left(nT_e\right) + n\mu_e^{\perp} E^{\perp} \qquad \text{[4.5-25]}$$

The effective ion and electron mobilities (μ_{ii}, $\mu_{ie}^{\perp}$, etc.) are defined in Appendix G. To determine the ambipolar coefficients for the plasma, these parallel and perpendicular momentum equations are combined with the continuity equations, yielding

$$\dot{n}_i = \nabla \cdot \left(n\mathbf{u}_i\right) = \nabla \cdot \left(nu_i + nu_i^{\perp}\right) =$$
$$-\nabla \cdot \left(-\mu_{ii}\nabla^{\parallel}\left(nT_i\right) - \mu_{ie}\nabla^{\parallel}\left(nT_e\right) + n\mu_i E^{\parallel} - \mu_{ii}^{\perp}\nabla^{\perp}\left(nT_i\right) - \mu_{ie}^{\perp}\nabla^{\perp}\left(nT_e\right) + n\mu_i^{\perp} E^{\perp}\right) \qquad \text{[4.5-26]}$$

$$\dot{n}_e = \nabla \cdot \left(n\mathbf{u}_e\right) = \nabla \cdot \left(nu_e + nu_e^{\perp}\right) =$$
$$-\nabla \cdot \left(-\mu_{ei}\nabla^{\parallel}\left(nT_i\right) - \mu_{ee}\nabla^{\parallel}\left(nT_e\right) - n\mu_e E^{\parallel} - \mu_{ei}^{\perp}\nabla^{\perp}\left(nT_i\right) - \mu_{ee}^{\perp}\nabla^{\perp}\left(nT_e\right) + n\mu_e^{\perp} E^{\perp}\right) \qquad \text{[4.5-27]}$$

To couple the ion and electron motion, equations 4.5-26 and 4.5-27 are multiplied by the mobilities μ_e and μ_i, respectively, and then the resulting equations are added:

$$\mu_e \dot{n}_i + \mu_i \dot{n}_e =$$

$$-\mu_e \nabla \cdot \left(-\mu_{ii} \nabla^{\parallel} \left(nT_i \right) - \mu_{ie} \nabla^{\parallel} \left(nT_e \right) + n\mu_i E^{\parallel} - \mu_{ii}^{\perp} \nabla^{\perp} \left(nT_i \right) - \mu_{ie}^{\perp} \nabla^{\perp} \left(nT_e \right) + n\mu_i^{\perp} E^{\perp} \right)$$

$$-\mu_i \nabla \cdot \left(-\mu_{ei} \nabla^{\parallel} \left(nT_i \right) - \mu_{ee} \nabla^{\parallel} \left(nT_e \right) - n\mu_e E^{\parallel} - \mu_{ei}^{\perp} \nabla^{\perp} \left(nT_i \right) - \mu_{ee}^{\perp} \nabla^{\perp} \left(nT_e \right) - n\mu_e^{\perp} E^{\perp} \right)$$

[4.5-28]

It is apparent by comparing μ_e and μ_i that electrons move much more freely than ions along field lines since these mobilities are inversely proportional to mass. Consequently, the electron mobility, μ_e, is several orders of magnitude greater than the ion mobility, μ_i. In addition, the electron generation rate for a DC discharge, though typically larger, is on the same order of the ion generation rate. These observations allow the electron generation to be removed from the LHS of Equation 4.5-28 by

$$\mu_e \dot{n}_i + \mu_i \dot{n}_e = \left(\mu_e + \mu_i \right) \dot{n}_i + \mu_i \left(\dot{n}_e - \dot{n}_i \right) \approx \left(\mu_e + \mu_i \right) \dot{n}_i$$

[4.5-29]

Equation 4.5-29 shows that mass and momentum diffusion of the plasma is dominated by the ions. The RHS of Equation 4.5-28 may be simplified if the mobilities can be brought inside the divergences. Using experimental measurements of ion thruster discharge parameters to approximate the values of the terms in the equation shows that moving the mobilities inside the divergences introduces a relatively minor error for a computational formulation [64,65]. Therefore, Equation 4.5-28 may be rewritten as

$$\dot{n}_i \left(\mu_e + \mu_i \right) = -\nabla \cdot \left(\begin{array}{l} \left[\mu_e \mu_{ii} + \mu_i \mu_{ei} \right] \nabla^{\parallel} \left(nT_i \right) + \left[\mu_e \mu_{ii}^{\perp} + \mu_i \mu_{ei}^{\perp} \right] \nabla^{\perp} \left(nT_i \right) + \\ \left[\mu_e \mu_{ie} + \mu_i \mu_{ee} \right] \nabla^{\parallel} \left(nT_e \right) + \left[\mu_e \mu_{ie}^{\perp} + \mu_i \mu_{ee}^{\perp} \right] \nabla^{\perp} \left(nT_e \right) + \\ \left(\mu_i \mu_e^{\perp} - \mu_e \mu_i^{\perp} \right) nE^{\perp} \end{array} \right)$$

[4.5-30]

thus removing the parallel electric fields from the equation. Therefore, Equation 4.5-30 accounts for the parallel component of the ambipolar electric field. Since the electrons are much more mobile along the magnetic field lines, the parallel

ambipolar electric field serves to mutually decelerate the electrons and accelerate the ions. The behavior and treatment of the perpendicular electric field is discussed below. Dividing by the sum of the mobilities on the LHS and inside of the gradient on the RHS allows Equation 4.5-30 to be simplified using anisotropic mobility coefficients. Again using experimental data, it can be shown that dividing the sum of the mobilities *inside* the divergence almost entirely removes the error associated with commuting the mobilities inside the divergence as done in Equation 4.5-28. Moving the mobilities inside the divergence allows the coupled ion-electron motion to be expressed more simply in terms of anisotropic mobilities tensors, resulting in the following expression

$$\dot{n}_i = -\nabla \cdot \left(\underline{\underline{\mathbf{M}}}_i \nabla \left(nT_i \right) + \underline{\underline{\mathbf{M}}}_e \nabla \left(nT_e \right) + M_E^{\perp} nE^{\perp} \right) \qquad [4.5\text{-}31]$$

where

$$\underline{\underline{\mathbf{M}}}_i \equiv \begin{bmatrix} M_i & 0 \\ 0 & M_i^{\perp} \end{bmatrix} \quad , \quad \underline{\underline{\mathbf{M}}}_e \equiv \begin{bmatrix} M_e & 0 \\ 0 & M_e^{\perp} \end{bmatrix} \quad , \quad M_E^{\perp} = \frac{\mu_i \mu_e^{\perp} - \mu_e \mu_i^{\perp}}{\mu_e + \mu_i}$$

$$[4.5\text{-}32]$$

$$M_i = \frac{\mu_e \mu_{ii} + \mu_i \mu_{ei}}{\mu_e + \mu_i} \quad , \quad M_e = \frac{\mu_e \mu_{ie} + \mu_i \mu_{ee}}{\mu_e + \mu_i} \quad , \quad M_i^{\perp} = \frac{\mu_e \mu_{ii}^{\perp} + \mu_i \mu_{ei}^{\perp}}{\mu_e + \mu_i} \quad , \quad M_e^{\perp} = \frac{\mu_e \mu_{ie}^{\perp} + \mu_i \mu_{ee}^{\perp}}{\mu_e + \mu_i}$$

With approximations of the species temperatures, perpendicular electric field, ion production rates, and species collision frequencies, the ion motion equation, Equation 4.5-31, may be used to approximate the plasma density distribution and ion fluxes of weakly ionized plasma. As discussed in references [66,61], the perpendicular electric field can be nearly "short-circuited" in discharges where large imbalances of fluxes along the magnetic field lines are possible. This is commonly the case for ring-cusp ion thruster discharges [67]. This "short-circuit effect" was identified by Simon [68] for finite length plasma columns in conducting containers, and is also described in Reference [69]. Therefore, to first order, the effects of the perpendicular electric fields in the bulk of the plasma are assumed negligible such that $E^{\perp} \approx 0$, simplifying the ion motion equation to

$$\dot{n}_i = -\nabla \cdot \left(\underline{\underline{\mathbf{M}}}_i \nabla \left(nT_i \right) + \underline{\underline{\mathbf{M}}}_e \nabla \left(nT_e \right) \right)$$

[4.5-33]

The potential at the cusp regions is resolved as discussed in Section 5.6. A parallel effort to resolve the potential structure in the near-cathode region is currently underway as described in [8].

Non-Classical Mobility

To this point the perpendicular motion has been assumed to obey classical diffusion for partially ionized plasma, where the electron-neutral collisions are assumed important [50]. To aid the discussion below, two new collision terms are defined. The frequency $\nu_{e\text{-}n}$ represents all the collisions in the neutral reference frame. For this problem the effective electron-neutral-centered collision frequency, $\nu_{e\text{-}o}$, is defined by

$$\nu_{e-o} \equiv \nu_{eo} + \nu_{e-gen}$$

[4.5-34]

where the effective collision frequency for electron generation, $\nu_{e\text{-}gen}$, is considered to be neutral centered since the drift velocity of the electrons produced from collisions is assumed equal to the neutral drift velocity. The second frequency defined here is $\nu_{e\text{-}i}$, which represents all electron collisions in the ion reference frame. For this problem the effective electron-ion-centered collision frequency, $\nu_{e\text{-}i}$, is identically equal to the electron-ion collision frequency since no other ion-centered collisions are assumed:

$$\nu_{e-i} \equiv \nu_{ei}$$

[4.5-35]

These parameters, $\nu_{e\text{-}i}$ and $\nu_{e\text{-}n}$, are used below for a mixture technique to determine the appropriate coefficient for perpendicular electron diffusion. In this technique it is assumed that higher $\nu_{e\text{-}i}$, in comparison to $\nu_{e\text{-}o}$, is indicative of more fully ionized plasma. Early results from the Discharge Model showed that in the on-axis regions of the discharge plasma the effective electron-ion collision frequency, $\nu_{e\text{-}i}$, is on

order of the effective electron-neutral collisions, ν_{e-n}. In these "intermediately ionized" regions, it is reasonable to consider that the perpendicular electron diffusion is somewhere between that of weakly and fully ionized plasma. Schweitzer and Mitchner [70] proposed mixture rules between weakly ionized (Lorentzian) and fully ionized plasma approximations to estimate the tensor conductivity for the entire range of plasma ionization levels; however this method is prohibitively complex. The following discussion presents a simple mixture technique to describe electron perpendicular transport for plasma regions that are between weakly and fully ionized plasma.

The classical description for perpendicular transport of electrons that is given above is sufficient for weakly ionized regions [50]; however, in fully ionized regions, i.e. as $\nu_{e-i}/\nu_{e-o} \to \infty$, a different method is typically used. A classical derivation of motion in fully ionized plasma shows a B^{-2} dependence for the perpendicular diffusion that is not observed in most experiments [50,49]. Bohm [71] introduced a relationship that describes the perpendicular diffusion of fully ionized plasma as inversely proportional to the magnetic field by

$$D_{\perp} = D_B \equiv \frac{kT_e}{16eB}$$

[4.5-36]

where $\Gamma_{\perp} = D_{\perp} \nabla_{\perp} n$. The Bohm diffusion coefficient, D_B, has shown agreement with several experiments of fully ionized plasmas [50]. For stable discharges, Bohm diffusion has shown to provide sufficient damping to prevent the exponential growth of azimuthal drift instabilities [71,49,69].

Computational models of Hall thruster plasma, which are in a similar regime as ion thrusters, have demonstrated good agreement with experiments by uniformly adding a fraction of Bohm diffusion to the weakly ionized approximation for perpendicular electron mobility [49]. Arakawa's model (described in Section 2.4) suggests that Bohm diffusion may also be important for ion thrusters [33]. To

assess the non-uniform importance of Bohm-type non-classical diffusion for the Ion Diffusion Sub-Model, Equation 4.5-37 was developed to weigh the classical and non-classical perpendicular mobility of the electrons per the relative dominance of the electron-neutral-centered or electron-ion-centered collisions

$$\left(M_e^{\perp}\right)_{eff} = \frac{\nu_{e-o}}{\nu_{e-o} + \gamma_{nc}\nu_{e-i}} M_e^{\perp} + \frac{\gamma_{nc}\nu_{e-i}}{\nu_{e-o} + \gamma_{nc}\nu_{e-i}} M_B^{\perp} \qquad \text{[4.5-37]}$$

where "Bohm mobility" is defined by

$$M_B^{\perp} \equiv \frac{k}{16eB} \qquad \text{[4.5-38]}$$

The non-classical diffusion parameter, γ_{nc}, serves to mitigate the influence of the Bohm mobility in partially-ionized regions. As discussed in Chapter 4, this parameter was found to best match experimental results using $\gamma_{nc} \approx \frac{1}{4}$. For non-zero values of γ_{nc}, the effective perpendicular electron mobility, $\left(M_e^{\perp}\right)_{eff}$, yields fully classical mobility for very weakly ionized regions, and Bohm mobility for fully ionized plasmas. Using Equation 4.5-37 the effective anisotropic mobility for electrons is

$$\left(\underline{\underline{\mathbf{M}}}_e\right)_{eff} \equiv \begin{bmatrix} M_e & 0 \\ 0 & \left(M_e^{\perp}\right)_{eff} \end{bmatrix} \qquad \text{[4.5-39]}$$

The final ion motion equation is then

$$\dot{n}_i = -\nabla \cdot \left(\underline{\underline{\mathbf{M}}}_i \nabla\left(nT_i\right) + \left(\underline{\underline{\mathbf{M}}}_e\right)_{eff} \nabla\left(nT_e\right) \right) \qquad \text{[4.5-40]}$$

Formulation of Equation 4.5-40 in a control volume analysis is discussed in Appendix G.

Ion Flux Boundary Conditions

For the computational boundaries the local temperatures are assumed constant. Also, perpendicular electric fields are not resolved at the boundaries. These assumptions allow the cell-centered ion motion to be described by

$$\dot{n}_i = -\nabla \cdot \left(\underline{\underline{\mathbf{D}}} \nabla (n) \right) \qquad \text{[4.5-41]}$$

where

$$\underline{\underline{\mathbf{D}}} = \begin{bmatrix} D_\parallel & 0 \\ 0 & D_\perp \end{bmatrix} = T_i \underline{\underline{\mathbf{M}}}_i + T_e \left(\underline{\underline{\mathbf{M}}}_e \right)_{eff} \qquad \text{[4.5-42]}$$

Referring to Figure 4.5-1, the flux at the boundaries is found by equating the cell-centered flux, $\Gamma = D_{eff} \nabla n$, to the ion flux at the edge of the sheath, $\Gamma = n_w u_w$, where n_w is the density at the edge of the sheath and u_i is the characteristic loss velocity of the ions at the sheath.
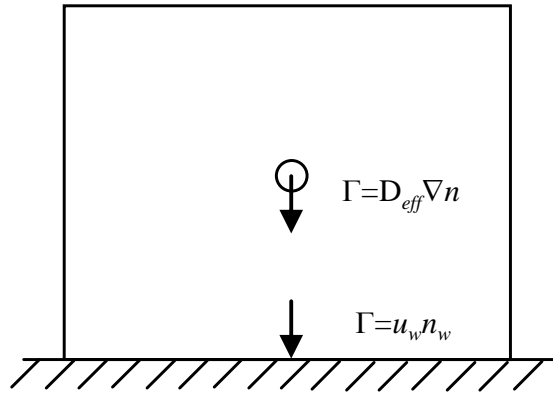
Figure 4.5-1. Ion Flux at Internal Mesh Boundary

An effective diffusion coefficient, D_{eff}, along the direction of ∇n is determined using the control volume formulation in Appendix G. With D_{eff} the fluxes can be equated to yield the flux simply in terms of the element centered density, n_E, by

$$\Gamma = D_{eff} \nabla n = n_w u_w$$

$$D_{eff} \frac{n_E - n_w}{\Delta x} = n_w u_w$$

$$n_w = \frac{n_E}{1 + \frac{u_w \Delta x}{D_{eff}}} \qquad [4.5\text{-}43]$$

$$\Gamma = \left(\frac{1}{\frac{1}{u_w} + \frac{\Delta x}{D}} \right) n_E$$

The characteristic loss velocity of ions, u_w, is assumed to satisfy the Bohm criterion for a positive sheath [66]:

$$u_w = u_{Bohm} = \sqrt{\frac{kT_e}{m_i}} \qquad [4.5\text{-}44]$$

The ion flux is determined for all the boundary surfaces of the Internal Mesh. The flux value at these boundary surfaces is then used to calculate the flux to the nearest element of the Boundary Mesh. To assure continuity, the total calculated current of ions to Boundary Mesh is normalized to be exactly equal to the ion current lost from the Internal Mesh. Ion flux to the chamber walls is assumed to undergo three-body recombination and is reintroduced as a flux of neutrals from the walls in the Neutral Model. Ion flux incident to grid surfaces is multiplied by the ion transparency from the Ion Optics Sub-Model to calculate the ion beam current as is shown later for the double ion correction.

Ion Flux to Cusp Regions

This model does not resolve the cusp regions of the discharge chamber. Several previous efforts have shown that the effective loss area at the cusps can be approximated using the hybrid loss radius [19,20] using

$$r_{loss} = 2.1\sqrt{r_{ce} r_{ci}} \qquad [4.5\text{-}45]$$

where r_{ce} and r_{ci} are the local electron and ion cyclotron radii. The effective loss area for a magnetic cusp of length L_{cusp} is then

$$A_{cusp} = 2\sum L_{cusp} r_{loss} \qquad\text{[4.5-46]}$$

This area is assumed to be the area at the cusp to which the plasma ions and electrons are freely lost along the magnetic field lines. The boundaries of the Internal Mesh that are closest to the magnets are identified as "cusp boundaries." At these boundaries the ions are assumed lost in two ways: First, the ion current to cusp is assumed to be

$$J_i^{cusp} = \Gamma_{\parallel} A_{cusp} \qquad\text{[4.5-47]}$$

where $\Gamma_{\parallel}$ is the flux to the surface from Equation 4.5-43 using only parallel diffusion. The rest of the cusp boundary is assumed to receive ions via perpendicular diffusion, such that

$$J_i^{\perp} = \Gamma_{\perp} \left(A_{cb} - A_{cusp} \right) \qquad\text{[4.5-48]}$$

where A_{cb} is the total area of the cusp boundary. The flux to the cusp boundary is then

$$\Gamma_{cb} = \frac{J_i^{cusp} J_i^{\perp}}{A_{cb}} \qquad\text{[4.5-49]}$$

Double Ion Correction

NSTAR beam measurements have shown double-to-single ion current ratios on the order of 0.15 [16]. A method to correct the single ion solution for the effects of double ions is given below. The double ion density near the grids is calculated and used to determine a corrected beam current to compare with experimental results.

The local generation rates of double ions are determined by comparing the relative rates of total and double ion production using the rate constants discussed in Section 4.3 and Appendix G. The Ion Optics Sub-Model assumes that double ions follow the same path lines as the single ions solution [12]. In this way, the double ion density, n_{++}, is determined from the local double ion production rates by the continuity equation for double ions:

$$\frac{\partial n_{++}}{\partial t} + \nabla \cdot \left(n_{++} u_+ \sqrt{2} \right) = \dot{n}_{++} \qquad \text{[4.5-50]}$$

where the double ion drift velocities, due to their charge, are assumed to be greater than the single ion drift velocities, u_+, by a factor of $\sqrt{2}$. This equation is applied at the end of an iteration using the upwind time-step control volume formulation described in Appendix G. The effect of the double ions on the beam current density is determined using the ratio of double ions to total ions

$$R_{++} = n_{++} / n_i \qquad \text{[4.5-51]}$$

where only single and double ions are assumed. Assuming ions enter the ion optics sheath with Bohm velocity, for an element on the Boundary Mesh with transparency to ions, ζ_i, the single ion beam current density becomes

$$j_B^+ = \zeta_i e u_+^{Bohm} n_+ = \zeta_i e u_+^{Bohm} n_i \left(1 - R_{++} \right) \qquad \text{[4.5-52]}$$

where n_+ and u_+^{Bohm} are the density and Bohm velocity for single ions. The double ion beam current density for the same element will then be

$$j_B^{++} = \zeta_i 2e \left(\sqrt{2} u_+^{Bohm} \right) n_{++} = \sqrt{8} \zeta_i e u_+^{Bohm} n_i R_{++} \qquad \text{[4.5-53]}$$

As discussed in Section 2, the discharge propellant efficiency is the ratio of propellant that leaves the thruster as an ion (of any charge) to the flow rate of propellant into the chamber. By this definition, the actual propellant efficiency is

calculated by summing over the ion flux contributions from all Boundary elements, m, such that

$$\eta_{ud} = \frac{\sum \left[j_B^+ + j_B^{++}/2 \right]_m A_m}{e\dot{m}_d} = \frac{\left(J_B^+ + J_B^{++}/2 \right) m_i}{e\dot{m}_d} \qquad [4.5\text{-}54]$$

To compare with experimental data, the Ion Diffusion Sub-Model also calculates discharge propellant efficiency that would be observed in experiments where the efficiency is not corrected for double ion content

$$\eta_{ud[*]} = \frac{\sum \left[j_B^+ + j_B^{++} \right]_m A_m}{e\dot{m}_d} = \frac{\left(J_B^+ + J_B^{++} \right) m_i}{e\dot{m}_d} \qquad [4.5\text{-}55]$$

Since the double ion correction results in a slight increase in the rate of total ions to the beam, the ion flux to the internal surfaces is normalized to maintain ion continuity.

The screen grid current densities are determined by recasting the beam current density equations [Eqns. 4.5-52 and 4.5-53] for the grid elements as

$$j_{screen}^+ = \left(1 - \zeta_i \right) e u_+^{Bohm} n_i^{tot} \left(1 - R_{++} \right) \qquad [4.5\text{-}56]$$

and

$$j_{screen}^{++} = \sqrt{8} \left(1 - \zeta_i \right) e u_+^{Bohm} n_i^{tot} R_{++} \qquad [4.5\text{-}57]$$

The screen current is then found by

$$J_{screen} = \sum \left[j_{screen}^+ + j_{screen}^{++} \right]_m \qquad [4.5\text{-}58]$$

The screen current is used to determine the primary current from the cathode as discussed in Chapter 5.

Ion Diffusion Post-Run Analysis

For post-run analysis, the ratio of the electron-neutral-centered and electron-ion-centered collision frequencies from equations 4.5-34 and 4.5-35 is used to assess the effective level of ionization of the plasma. This "electron collision ratio" is defined as

$$\delta_v \equiv \nu_{e-o}/\nu_{e-i} \qquad \text{[4.5-59]}$$

In a similar manner, the ratio of the diffusion coefficients from Equation 4.5-42 are used to quantify the "magnetization," δ_D, of the plasma motion in different regions of the thruster by

$$\delta_D = D_\parallel/D_\perp \qquad \text{[4.5-60]}$$

These ratios are calculated in chapters 5 and 6 for the NSTAR and Micro-Ion thruster discharges.

4.6 Electron Thermal Sub-Model

Early versions of the Discharge Model simply used a uniform value for secondary electron temperature, T_s , as an input into the model. Results of the model proved to be strongly dependent on the choice of T_s [48]. Also, experimental measurements have shown that the secondary electron temperature is non-uniform along the thruster axis for the NSTAR thruster [65]. Comparing the relative importance of the slowing frequency of primaries by secondaries, in Appendix G, to other collision frequency shows that the secondary electron energy is strongly related to the primary electrons energy. The following section describes a method for approximating the secondary electron temperature. This is done by first using effective potentials to obtain the electron flux and then imposing electron energy conservation to find T_s.

Electron Flux using Effective Potential

The density solution from the ion motion equation [Eq. 4.5-40] may be used in the electron continuity equation to approximate the electron flux, which can then be used later in the electron energy equation. Combining the electron motion equations, equations 4.5-23 and 4.5-25, with electron continuity gives

$$\dot{n}_e = \nabla \cdot \left(\underbrace{-\underline{\underline{\mu}}_e n\mathbf{E} - \underline{\underline{\mu}}_{ee} \nabla\left(nT_e\right) - \underline{\underline{\mu}}_{ei} \nabla\left(nT_i\right)}_{\Gamma_e} \right) \qquad \text{[4.6-1]}$$

where

$$\underline{\underline{\mu}}_e \equiv \begin{bmatrix} \mu_e & 0 \\ 0 & \mu_e^\perp \end{bmatrix} \;, \quad \underline{\underline{\mu}}_{ee} \equiv \begin{bmatrix} \mu_{ee} & 0 \\ 0 & \mu_{ee}^\perp \end{bmatrix} \;, \quad \underline{\underline{\mu}}_{ei} \equiv \begin{bmatrix} \mu_{ei} & 0 \\ 0 & \mu_{ei}^\perp \end{bmatrix} \qquad \text{[4.6-2]}$$

Ignoring non-classical effects in Equation 4.5-37, the subject of the divergence is the electron flux. Integrating over the volume of individual computational cells, a control volume formulation was used to find the potential distribution that is commensurate with the ambipolar solution for the plasma density. However, it was found that the computational formulation of this method produced artificial vorticity for the electrons in the presence of strong pressure gradients, which made convergent solutions nearly impossible to find. It was concluded that the electron behavior was due to small computational averaging errors that generated macroscopic inconsistencies. To eliminate these errors, the effective potential was defined by using a simplified electron equation, where the combined electron continuity and momentum equation give [50]

$$\dot{n}_e = \nabla \cdot \left(\underbrace{-\underline{\underline{\mu}}_e^* n\mathbf{E} - \underline{\underline{\mu}}_e^* \nabla\left(nT_e\right)}_{\Gamma_e} \right) \qquad \text{[4.6-3]}$$

where

$$\underline{\underline{\mu}}_e^* \equiv \frac{e}{m_e\left(\nu_{e-i} + \nu_{e-o}\right)} \begin{bmatrix} 1 & 0 \\ 0 & \frac{1}{1+\Omega_e^2} \end{bmatrix} \qquad \text{[4.6-4]}$$

and Ω_e is the electron Hall term. Using this formulation and assuming the electron temperatures are approximately constant across a given surface of a computational volume, the gradients in the electron flux from Equation 4.6-3 can be expressed as follows:

$$\Gamma_e = \underline{\underline{\mu_e^*}} n \left(-\mathbf{E} - \frac{\nabla(nT_e)}{n} \right) = \underline{\underline{\mu_e^*}} n \left(\nabla\phi - T_e \frac{\nabla n}{n} \right) \qquad \text{[4.6-5]}$$

assuming $T_e \nabla(n)/n = \nabla T_e \int (\nabla(n)/n) = \nabla(T_e \ln(n/n_c))$

$$\Gamma_e = \underline{\underline{\mu_e^*}} n \left(\nabla\phi - \nabla\left(T_e \ln\frac{n}{n_c} \right) \right) = \underline{\underline{\mu_e^*}} n \left(\nabla\left(\phi - T_e \ln\frac{n}{n_c} \right) \right) \qquad \text{[4.6-6]}$$

where the relation $\mathbf{E} = -\nabla\phi$ was used and n_c is the reference density for the constant of integration. Defining an *effective* potential, ψ, Equation 4.6-6 becomes

$$\Gamma_e = -\underline{\underline{\mu_e^*}} n \nabla\psi \qquad \text{[4.6-7]}$$

where

$$\psi \equiv T_e \ln\frac{n}{n_c} - \phi \qquad \text{[4.6-8]}$$

and Equation 4.6-3 can now be rewritten simply as

$$\dot{n}_e = -\nabla \cdot \underline{\underline{\mu_e^*}} n \nabla\psi \qquad \text{[4.6-9]}$$

By coupling this equation with the following boundary conditions, the control volume formulation from Appendix G may be used to find the effective potential, ψ, on the Internal Mesh.

Secondary Electron Boundary Conditions

Discharge secondary electrons are assumed repelled from cathode potential surfaces, such as the cathode keeper and ion extraction grids. Experimental studies show that the electrons are almost entirely lost at the magnetic cusp and that

105

electron flux between the cusps approximately equals the ion flux [67]. The resulting secondary electron boundary conditions are

$$\Gamma_e^{cath} = 0 \quad \text{(cathode potential surfaces)}$$

$$\Gamma_e^{anode} = \Gamma_i^{BC} \quad \text{(between magnetic cusps)}$$

$$\Gamma_e^{cusp} = \frac{n\overline{w}_e}{4} e^{\left(-\phi/T_e\right)} \quad \text{(at magnetic cusps)}$$

where $\overline{w}_e = \sqrt{8kT_e/\pi m_e}$. The loss area at the cusps is determined by the hybrid loss width from Equation 4.5-46. The exponential term of Equation 4.6-12 can be expanded in a Taylor series about an appropriate ratio of $R_\phi = \phi_{guess}/T_e$ as

$$e^{\left(-\phi/T_e\right)} \approx e^{-R_\phi}\left[(1+R_\phi)-\frac{\phi}{T_e}\right]$$

thus allowing the boundary condition to be approximated simply as a function of ϕ of the local cell. The disadvantage to this method is that the slope of the linear approximation approaches zero for larger values of R_ϕ, which may present inaccuracy at intermediate solutions of the model. To assure a finite slope at all values of R_ϕ, a linear approximation from $R=0$ to $R= R_\phi$ is used such that

$$e^{\left(-\phi/T_e\right)} \approx m_{sl}\frac{\phi}{T_e}+b_{int}$$

where

$$m_{sl} = \frac{e^{-R_\phi}-1}{R_\phi} \quad \text{and} \quad b_{int} = e^0 = 1$$

Combining equations 4.6-8, 4.6-12, and 4.6-14 gives the electron flux to the cusps as a function of the effective potential, ψ, as

$$\Gamma_e^{cusp} = \frac{n\overline{w}_e}{4}\left(m_{sl}\ln\frac{n}{n_c}+1-\frac{m_{sl}\psi}{T_e}\right) \qquad \text{[4.6-16]}$$

With these boundary conditions and Equation 4.6-9, the control volume formulation from Appendix G is used to find the solution of the effective potential, ψ. This solution is then used to find the electron flux with Equation 4.6-7 and the flux to the cusps, Γ_e^{cusp}, with Equation 4.6-16. With Γ_e^{cusp}, the potential at the cusps relative to anode, ϕ_{cusp}, may be found from Equation 4.6-12 by

$$\phi_{cusp} = -T_e\ln\left(\frac{4\Gamma_e^{cusp}}{n\overline{v}_e}\right) \qquad \text{[4.6-17]}$$

Using the cusp potential solution from Equation 4.6-17, the flux of energy to the cusp, P_{wall}, is found by multiplying the energy dissipation due to secondary electrons penetrating the anode sheath, ε_{wall}, by the flux of electrons to the wall

$$P_{wall} = \varepsilon_{wall}\Gamma_e^{cusp} \qquad \text{[4.6-18]}$$

The energy dissipation per electron of a Maxwellian population at temperature, T_e, is approximated by the average convective electron energy loss through a plasma sheath at potential, ϕ_{cusp}, by

$$\varepsilon_{wall} = 2kT_e + e\phi_{cusp} \qquad \text{[4.6-19]}$$

The purpose of finding the secondary electron fluxes and potentials is to provide values to the electron energy equation, presented below, which is used to find the solution for non-uniform electron temperatures on the Internal Mesh.

Electron Energy Conservation

The electron energy conservation is determined by multiplying the Boltzmann equation by $\frac{1}{2}mv^2$ and integrating over velocity to yield [72]

$$\frac{\partial}{\partial t}\left(\frac{nm}{2}u^2 + \frac{3}{2}nkT\right) + \nabla \cdot \left\{\left(\frac{nm}{2}u^2 + \frac{5}{2}nkT\right)\mathbf{u} + \mathbf{q}\right\} = en\mathbf{E}\cdot\mathbf{u} + \mathbf{R}\cdot\mathbf{u} + Q_{el} + Q_c \qquad \text{[4.6-20]}$$

where viscous effects are ignored and **R** is the mean change of momentum of electrons due to collisions with other species. For simplicity the subscript for electrons is not used; however, a subscript of β will be used in the following equation to indicate properties of heavy species, i.e., ions and neutrals. Neglecting thermoelectric effects for collisions, the heat generated by elastic collisions with other species, Q_{el}, can be decomposed into frictional, Q_f, and thermal, Q_{th}, terms as

$$Q_{el} \equiv Q_f + Q_{th} = -\sum_{\beta} \mathbf{R}_\beta \cdot \left(\mathbf{u} - \mathbf{u}_\beta\right) - 3\sum_{\beta} \frac{m}{m_\beta} \nu_\beta n\left(T - T_\beta\right) \qquad \text{[4.6-21]}$$

The change in energy density, Q_c, due to inelastic collisions of primary and secondary electrons may be approximated by

$$Q_c = -\left(\dot{n}_i^s \varepsilon_c\right)\Big|_s + \sum_w \left(\dot{n}_w \varepsilon_w\right)\Big|_p \qquad \text{[4.6-22]}$$

where $\dot{n}_i^s$ is the ionization rate due to secondaries, ε_c is the effective energy lost per secondary ionization event due to inelastic collisions, $\dot{n}_w$ is the secondary production rate due to primary collisional process w, and ε_w is the average energy of the secondary electrons created by process w. The change in energy density due to primary collisions is approximated using values determined in the Electron Collision Sub-Model by

$$\sum_w \left(\dot{n}_w \varepsilon_w\right)\Big|_p = \left[\dot{n}_i^p\left(\langle\varepsilon_p\rangle - \varepsilon_{iz}\right) + \dot{n}_{ex}^p\left(\langle\varepsilon_p\rangle - \langle\varepsilon_{ex}\rangle\right) + \left(\dot{n}_{slow}^p\right)\langle\varepsilon_p\rangle\right] \qquad \text{[4.6-23]}$$

The average secondary energy lost due to inelastic collisions per ionization collision, $\langle\varepsilon_c\rangle$, is determined from the relation [66].

$$\left(K_{iz}^s \left\langle \varepsilon_c \right\rangle \right)\bigg|_s = \left[K_{iz}^s \varepsilon_{iz} + K_{ex}^s \left\langle \varepsilon_{ex} \right\rangle + K_{el}^s \frac{3m_e}{m_i} T_e \right] \qquad \text{[4.6-24]}$$

where the rate constants are determined using the methods in Appendix G. The kinetic energy terms from Equation 4.6-20 can be removed by combining them with the electron continuity and momentum equations to rewrite the energy equation as

$$\frac{\partial}{\partial t}\left(\frac{3}{2}nkT \right) + \nabla \cdot \left(\frac{5}{2}nkT\mathbf{u} + \mathbf{q} \right) - \mathbf{u}\cdot\nabla\left(nkT \right) = Q_{el} + Q_c - \frac{\dot{n}mu^2}{2} \qquad \text{[4.6-25]}$$

From the analysis in Braginskii [72] and assuming that the bulk plasma electric field effects are negligible compared to the cusp electric fields, this electron energy equation may be combined with Ohm's law to yield

$$\frac{\partial}{\partial t}\left(\frac{3}{2}nkT \right) + \nabla \cdot \left(\frac{5}{2}kT\Gamma + \mathbf{q} \right) \approx Q_{th} + Q_c \qquad \text{[4.6-26]}$$

where we assumed $Q_c \gg \dot{n}mu^2/2$. For steady-state ion thruster conditions, where the losses due to inelastic collisions far exceed those due to elastic collisions, i.e., $Q_{th} \ll Q_c$, this reduces to the energy equation

$$\nabla \cdot \left(\frac{5}{2}kT\Gamma + \mathbf{q} \right) = Q_c \qquad \text{[4.6-27]}$$

The electron flux, Γ, in Equation 4.6-27 is determined by the electron continuity and momentum equations that were defined earlier. Ignoring thermoelectric effects [72], the electron heat flux vector, $\mathbf{q}$, is defined using anisotropic thermal conductivity (such that $\mathbf{q} = -\underline{\underline{\kappa}}\nabla T$). The thermal conductivity in a magnetic field, determined by Braginskii, is approximated by

$$\underline{\underline{\kappa}} = \begin{bmatrix} \kappa_\parallel & 0 \\ 0 & \kappa_\perp \end{bmatrix}$$

$$\kappa_\parallel = 3.16\kappa_e \quad , \quad \kappa_\perp = \kappa_e \frac{\Omega_e \left(2.5\Omega_e^2 + 21.67 \right)}{\Omega_e^4 + 14.79\Omega_e^2 + 3.77} \qquad \text{[4.6-28]}$$

$$\text{where } \kappa_e = \frac{k}{m_e} p_e \tau_e$$

Combining equations 4.6-22 and 4.6-27 the conservation of electron energy becomes

$$\nabla \cdot \left(\frac{5}{2} kT\Gamma - \underline{\underline{\kappa}}\nabla T \right) = -\left(\dot{n}_i^s \langle \varepsilon_c \rangle \right)\Big|_s + \sum_w \left(\dot{n}_w \varepsilon_w \right)\Big|_p \qquad \text{[4.6-29]}$$

This equation, with the above boundary conditions, is used to approximate the secondary electron temperature distribution in the thruster by applying the control formulation from Appendix G.

Chapter Summary

The Discharge Model is a multi-component model that separately treats the four plasma species (neutrals, primaries, ions, and secondaries) to obtain a self-consistent solution for a ring-cusp ion thruster. In addition to basic ion thruster performance parameters, the model determines the non-uniform distribution of all plasma species. Chapters 5 and 6 show that the model yields good agreement with experimental results for different discharge chamber sizes and shapes.

Chapter 5

Discharge Model: Validation and Results

In this chapter, results from the Discharge Model are compared with experimental data from the NSTAR thruster. For the chosen operating conditions, the model gives good agreement with NSTAR beam profiles and performance curves. The model analyses show that the peak observed in the NSTAR beam profile is due to double ions that are created by over-confinement of primary electrons on the thruster axis. This over-confinement of primaries on-axis also results in neutral density just inside the grids that is over an order of magnitude less on-axis than that at the radial extent of the grids. The Discharge Model was used to perform a first-level design analysis of the NSTAR thruster that showed that the performance and beam flatness may be increased significantly by simply increasing the middle magnet ring strength.

5.1 Inputs and Assumptions

A 2-D diagram of the NSTAR thruster geometry used for the model is shown in Figure 5.1-1. Most of the propellant comes from the plenum located next to the grid magnet ring, while the rest (~10-20%) of the propellant enters through the hollow cathode. The magnetic field is created by rings of rectangular samarium cobalt (SmCo) magnets. The cathode magnets are significantly larger than the middle and grid magnets and are stacked three-deep to create a strong magnetic field in the cathode region. The grid and middle rings are very similar in size. The exact sizes and locations of the magnets were used in the Magnetostatic Sub-Model. Comparisons of the measured magnetic field and that predicted by the model are given in Appendix F and show very good agreement in the experimentally measured regions. A contour plot of the magnetic field for the default NSTAR configuration and a modified configuration are shown in Figure 5.3-3.
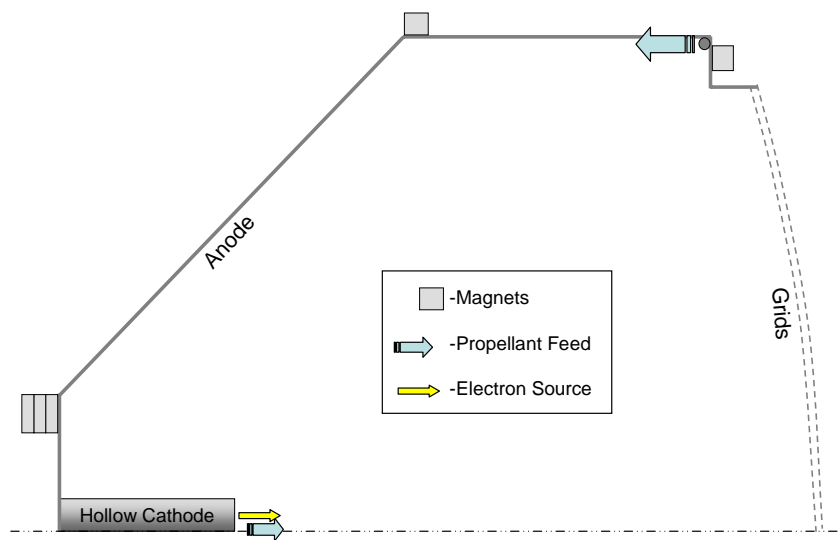
Figure 5.1-1. NSTAR Thruster Geometry

The TH15 and TH12 beginning-of-life throttle points for NSTAR are shown in Table 5.1-1. The grid voltages, along with the grid geometry, were used to find the ion and neutral transparency in the Ion Optics Sub-Model. The current of primaries from the hollow cathode is determined from charge conservation by $J_p = J_D - J_{screen}$, where J_{screen} is the ion current to the screen grid determined by the Ion Diffusion Sub-Model.

Table 5.1-1. NSTAR Throttle Points [Beginning of Life]

Throttle Points	Main Flow [sccm]	Cathode Flow [sccm]	J_B [A]	J_D [A]	V_D [V]	V_B [V]	V_{accel} [V]	Model Specific Inputs	
								Vp [V]	Tp [eV]
TH12	19.85	2.92	1.59	10.87	25.4	1100	-249	21	3
TH15	23.42	3.73	1.76	13.13	25.1	1100	-249	20	2.5

In the absence of a near-cathode model, the two thruster inputs to the Discharge Model that are not determined directly from thruster operating conditions are the accelerated half-Maxwellian characteristics of the primary electrons (V_p and T_p). As described in Appendix G, for hollow cathode discharges such as NSTAR, initial estimates of these parameters are inferred from the discharge voltage, and measurements of cathode operating voltage, plasma potential, and cathode insert electron temperature. Experimental measurements [73] show the electron temperature of a NSTAR-type hollow cathode plasma is on the order of 2-3eV; therefore, $T_p \sim$ 2-3eV was used. The primary electron accelerating voltage, V_p, is related to the discharge voltage but cannot be determined exactly without knowing the accelerating potential structure in the near-cathode region. As presented in Appendix G, this voltage can be estimated using measurements of the NSTAR cathode operating voltage ($V_c \sim$6V) and plasma potential ($\phi \sim$2-3V) [73] as $V_p \sim V_D + \phi - V_c$. These estimates of V_p and T_p were used as starting point values, and were

then adjusted to attain the desired beam current for a given throttle point. For the results herein, the values of V_p and T_p that were used to compare with NSTAR data are shown in Table 5.1-1.

The Electron Collision Sub-Model assumes that the secondary inelastic collision factor, f_{inel}, is uniform throughout the discharge. Preliminary results from the model were used to determine a value that provided reasonable agreement with the secondary electron measurements from [65]. Depending on the assumed primary electron energy, values ranging from 0.7 to 0.9 showed good agreement with the experimental measurements. To minimize the number of free parameters, the average value of $f_{inel} = 0.8$ was assumed for all the Discharge Model results discussed herein.

The non-classical diffusion parameter, γ_{nc}, was investigated against experimental data for both conventional and small ion thruster sizes. At a value of 1, the ion losses to the wall were very large, resulting in unreasonably poor performance. For $\gamma_{nc} = 0$ (weakly ionized assumption) the ion and double ion densities were very high on-axis, yielding unreasonably low beam flatness values. Good agreement with TH15 experimental data was generally found for $\gamma_{nc} \sim \frac{1}{4}$, therefore this value was used for all simulations.

5.2 Model Results and Experimental Comparison

The results in this section are for the Discharge Model at the TH15 operating point from Table 5.1-1, unless otherwise noted. Model results at TH12 are given in Appendix H. To avoid large gradients in the early iterations, the Discharge Model assumes a low primary electron current (~5-10%) for the first iteration and then incrementally increases the primary current to its full value, after which the model converges to a steady state solution.

Solution Convergence

Figure 5.2-1 shows the results for propellant efficiency vs. iteration where the primary current reached full strength after 10 iterations. In this figure nud[Gas], nud[Beam], and nud[*] are the propellant efficiencies per equations 4.1-1, 4.1-2, and 4.1-3, respectively.
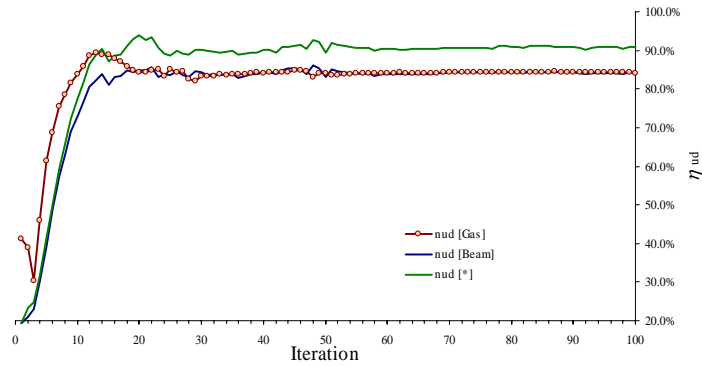
Figure 5.2-1. Propellant Efficiency vs. Iteration for TH15

At the end of an iteration, the volume-averaged densities are determined. The convergence of these averaged density values, shown in Figure 5.2-2, is indicative of the convergence of the non-uniform values on the Internal Mesh. Contour plots of parameters on the Internal Mesh are given below.
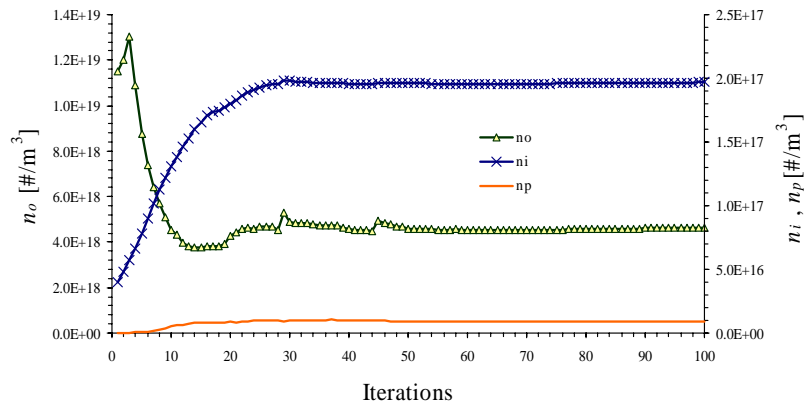
Figure 5.2-2. Volume-Averaged Densities vs. Iteration for TH15

115

Comparison with Experimental Results

The beam current density profiles along the dished exit plane of the thruster, as calculated by the Discharge Model, are shown in Figure 5.2-3. In this figure, jB[+] assumes that all beam ions are singly charged (i.e., jB[+] = $\left[j_B^+ + j_B^{++}/2 \right]$), while jB[++] includes doubly charged ion effects (i.e., jB[++] = $j_B^+ + j_B^{++}$). The variables j_B^+ and j_B^{++} are described in equations 4.5-52 and 4.5-53. Comparing these profiles shows the radially dependent effect of double ions on measured beam current. For this case, the model agrees with experimental data that show that the peak on the axis of the beam profile is largely due to double ion current. The "Data" profile is extrapolated from the NSTAR TH15 data found in Reference [7]. The jB[++] profile shows generally good agreement with the Data profile, though some discrepancy is found near r ~ 3cm and r ~ 13cm. Figure 5.2-3 also includes the neutral atom density predicted by the model just inside the grids, showing over an order of magnitude drop in neutral density from the edge of the grids to the center.
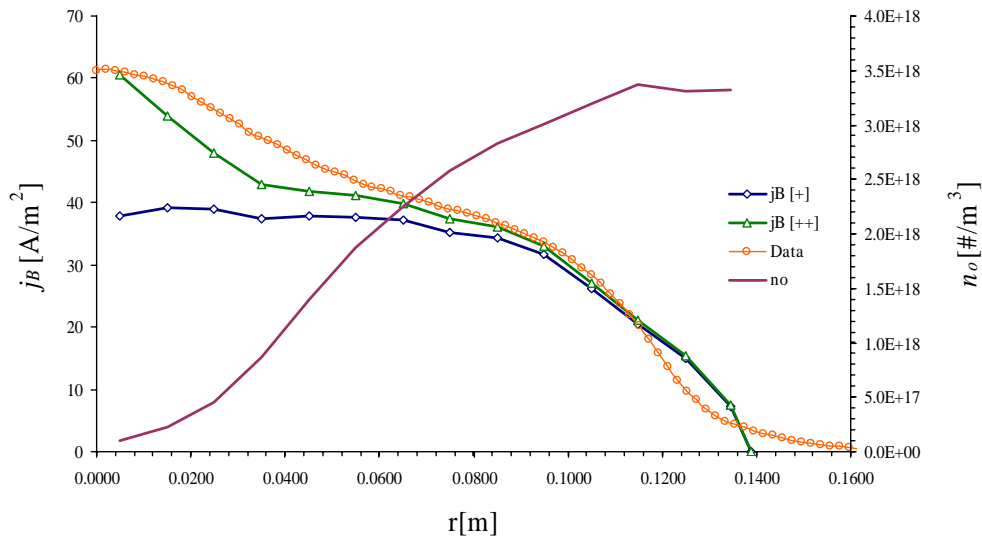
Figure 5.2-3. Beam and Neutral Density Profiles at Grids for TH15

The 8,200 hour test [7] also included a performance sensitivity analysis that was conducted after the thruster had operated for several thousand hours. During this

analysis, the main flow rate was changed over a range of ± 9%, while the beam current was kept constant, resulting in the discharge performance trend shown in Figure 5.2-4. For each value of main flow rate used in the analysis, the beam current, 1.76A, was kept constant by adjusting the discharge voltage and current. To compare the performance sensitivity of the model with this data, the Discharge Model was first used to match the performance at the nominal (TH15) operating condition at the middle of the curve. Then, holding all other parameters constant, the flow rate and discharge current in the model were changed to the maximum and minimum values used in the tests. The resulting discharge performance curve in Figure 5.2-4 suggests that the Discharge Model yields good agreement over the range of performance shown. In this analysis, the primary electron energy was held constant. This approximation was made since cathode flow rate was held constant in the experimental analysis and the cathode operating conditions have been shown to be strongly dependent on this parameter [73]. For the assumptions of this comparison, the model over-predicts the propellant efficiency by 1.5-2%. This discrepancy may be related to lack of knowledge of the near-cathode conditions for the different operating conditions.
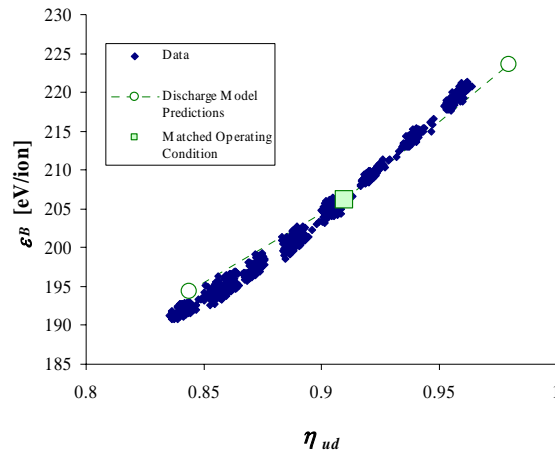
Figure 5.2-4. Comparison of Discharge Model and
NSTAR Performance Curve Data at TH15

Discharge Performance Parameters

Table 5.2-1 shows several of the discharge parameters (defined below) that were determined by the Discharge Model at TH15. These parameters are important to understanding the fundamental behavior of the discharge, as described in Reference [32]. Where possible, these values are compared with the NSTAR data from Reference [7]. The values for $\eta_{ud\ [*]}$ and ε_B are very similar since they are determined by the conditions that define the throttle points from Table 5.1-1. The parameters in Table 5.2-1 are defined as follows:

$\eta_{ud\ [*]}$ – discharge propellant efficiency defined in Equation 4.1-3

η_{ud} – discharge propellant efficiency defined in Equation 4.1-2

ε_B – discharge loss [eV/ion]

$J_{B++}\ /J_{B+}$ - ratio of beam current due to doubly- and singly charged ions

J_i – current of ions created in discharge [A]

J_{ip} – current of ions created in discharge by primaries [A]

n_i – average density of ions [m^{-3}]

n_p – average density of primary electrons [m^{-3}]

n_o – average density of neutrals [m^{-3}]

f_A – fraction of ion current to anode surfaces

f_B – fraction of ion current to the beam

f_C – fraction of ion current to cathode surfaces

F_B – beam flatness as defined by jB [++] profile

F_{B*} – beam flatness as defined by jB [+] profile

The results in Table 5.2-1 show that the Discharge Model predicts double ion content within the range observed by experimental measurements [16]. Previous measurements have shown that efficient ion thruster discharges should extract ~50% of the ions to the beams [32]; however, the Discharge Model predicts f_B =

29% for NSTAR TH15. This result is improved slightly in the modified NSTAR design in Section 5.3.

Table 5.2-1. Discharge Performance Parameters
(NSTAR - TH15 Simulation vs. Data)

Discharge Parameters	$\eta_{ud\,[*]}$	η_{ud}	ε_B	J_{B++}/J_{B+}	J_i	J_{ip}	n_i	n_p	n_o	f_A	f_B	f_C	F_B	F_{B*}
Units	%	%	eV/ion	-	A	A	m-3	m-3	m-3	-	-	-	-	-
Model Results	90.9	85.6	187	0.129	6.08	3.73	1.97 $*10^{17}$	9.25 $*10^{15}$	4.64 $*10^{18}$	0.66	0.29	0.05	0.47	0.674
Data	90.8	83.8-85.7	187	0.126-0.184									0.47	

Electron Power Loss

The Electron Collision and Electron Thermal sub-models track the power lost by the primary and secondary electron populations. Table 5.2-2 shows the percentage of the total input power lost by all the electron power loss mechanisms considered by the model. The *total* input energy is defined by the total primary current and the average primary energy as defined in Appendix G. The secondary electron energy losses are referenced to the *total* input power to assess their contribution to the overall power balance of the discharge. Therefore, by the following definitions, $P_{ps} = P_{sw} + P_{siz} + P_{sx}$.

P_{ps} – primary power transferred to secondary population

P_{pw} – primary loss to wall

P_{piz} – primary ionization of propellant

P_{px} – primary excitation of propellant

P_{sw} – secondary loss to walls

P_{siz} – secondary ionization of propellant

P_{sx} – secondary excitation of propellant

The results in Table 5.2-2 show that most of the primary energy is transferred to the secondary electrons, and most of the secondary energy is subsequently lost to the chamber walls. These results also show that the primaries contribute to most of the ionization for NSTAR TH15; however, secondaries account for nearly 40% of the ionization. In Chapter 6, the results from Table 5.2-2 are compared with results from Micro-Ion thruster simulations to contrast the behavior of conventional and miniature discharges.

Table 5.2-2. Electron Power Loss Mechanisms
(NSTAR TH15)

Mechanism	Primary Electron Losses				Secondary Electron Losses		
	P_{ps}	P_{pw}	P_{piz}	P_{px}	P_{sw}	P_{siz}	P_{sx}
% of Total Input Power Lost	69%	0.7%	13.7%	16.6%	49.1%	7.5%	12.5%

Two-Dimensional Plots of Discharge Characteristics

The Discharge Model generates 2-D data of the non-uniform characteristics of the discharge plasma on the Internal Mesh. In this section, Discharge Model results at the NSTAR TH15 operating condition are presented. Some observations of the plots accompany the figures in this section; however, a discussion of the collective implications of these results to the important discharge plasma processes of conventional ring-cusp ion thrusters is reserved for Chapter 7.

The total ion density distribution and some approximate ion streamlines are plotted on the Internal Mesh in Figure 5.2-5. This plot shows that the ions are preferentially lost at the cusps and the grids; however, some loss between the cusps occurs.
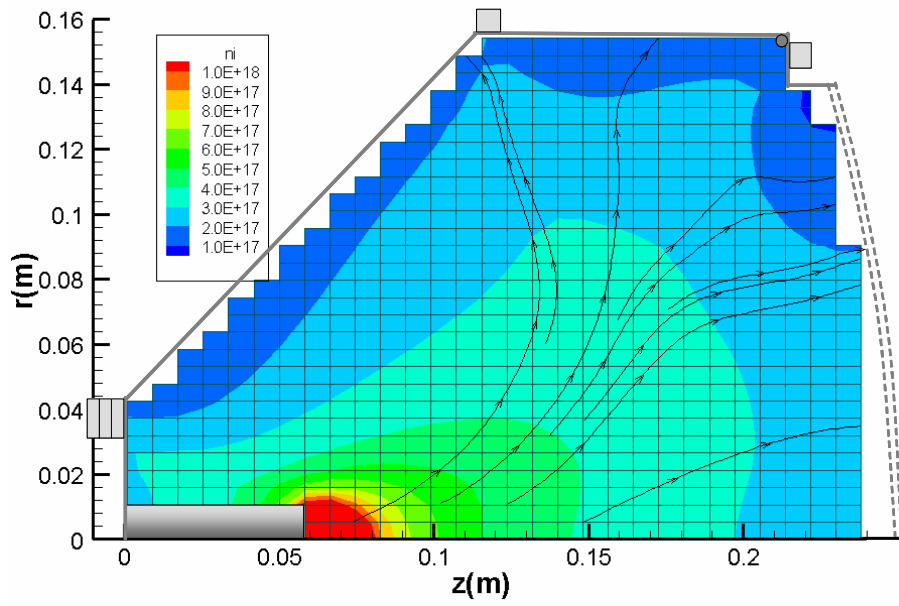
Figure 5.2-5. Total Ion Density [m^{-3}] and Streamlines - TH15
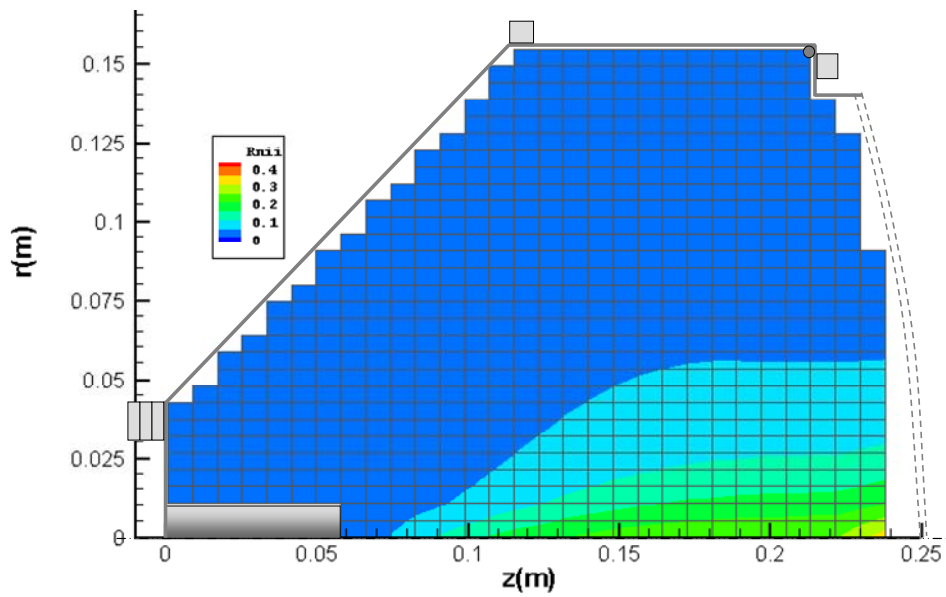
Figure 5.2-6. Double Ion Ratio ($R_{++} = n_{++}/n_i$) - TH15

121

The contours of double- to single-ion density ratio, Figure 5.2-6, show that the double ions reside primarily on-axis. This phenomenon can be explained by the high density of high-energy primary electrons on-axis as shown in Figure 5.2-7 and the slightly higher secondary electron temperature in that region, Figure 5.2-8. These combined effects also result in a high ionization rate on axis, Figure 5.2-9. The values from figures 5.2-6–5.2-8, and the rate constants derived from Appendix G, show that the double ionization on-axis is almost entirely (>99%) due to primary electron collisions.

The neutral density predicted by the model, Figure 5.2-10, is highly non-uniform. From the neutral and ion density plots it is apparent that the plasma is nearly 50% ionized in the on-axis region near the grids. In the presence of high-energy electrons, this region experiences a relatively high ratio of double- to single-ion generation rates.

As discussed in Chapter 4, the Discharge Model predicts the non-classical behavior of the plasma by considering the relative frequency of electron-neutral-centered and electron-ion-centered collisions. Figure 5.2-11 presents a plot of the distribution of the ratio of these frequencies, $\delta_v = v_{e\text{-}n}/v_{e\text{-}i}$, which shows that intermediate levels of ionization exists throughout the chamber and increasingly on-axis. This shows that the non-classical correction to the diffusion is important to the perpendicular diffusion results. The resulting level of anisotropy of the plasma motion, predicted by the model, is measured by the ratio of parallel and perpendicular diffusion coefficients, $\delta_D = D_\parallel / D_\perp$. The distribution of δ_D predicted by the Discharge Model is plotted in Figure 5.2-12. This plot suggests that the plasma is nearly unmagnetized in the highly ionized regions on-axis, and of course, in the low magnetic field region in the middle of the thruster.
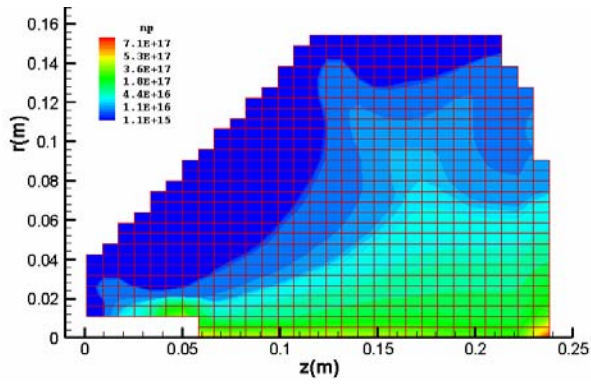
Figure 5.2-7. Primary Electron Density [m^{-3}] - TH15
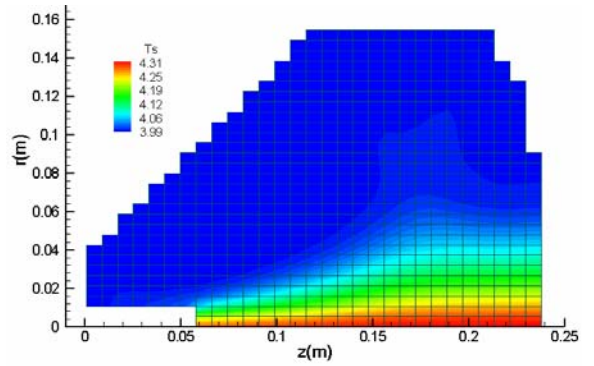
Figure 5.2-8. Secondary Electron Temperature [eV] - TH15
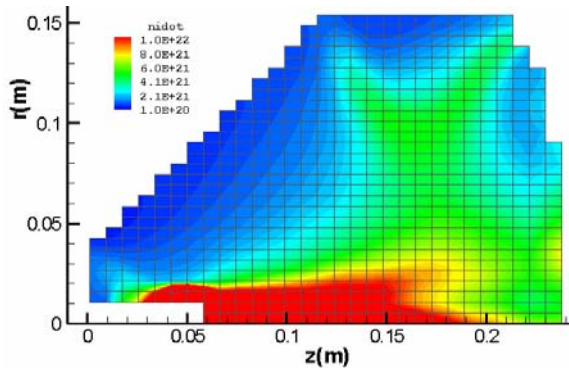
Figure 5.2-9. Ion Generation Rate Density [s^{-1} m^{-3}] - TH15
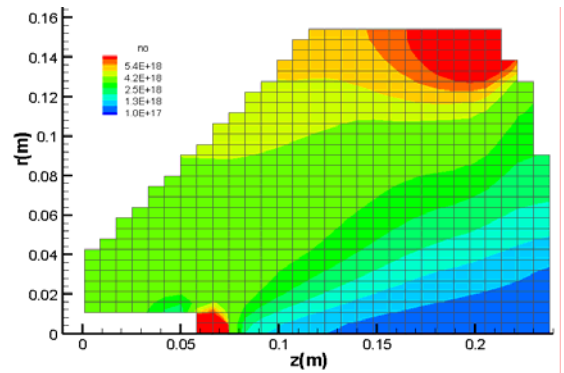
Figure 5.2-10. Neutral Atom Density [m^{-3}] - TH15
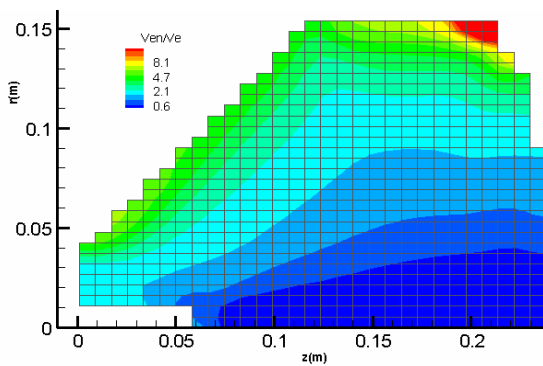
Figure 5.2-11. Electron Collision Frequency Ratio $(\delta_v = \nu_{e\text{-}n} / \nu_{e\text{-}i})$ - TH15

123
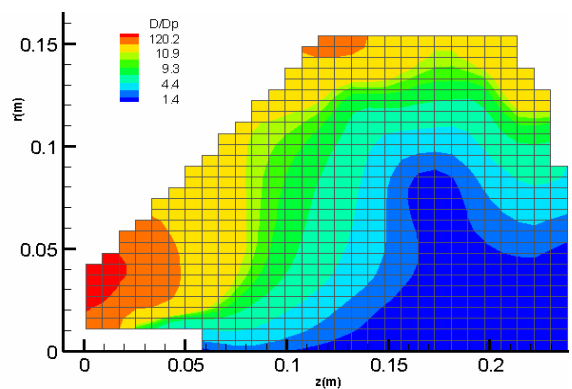
Figure 5.2-12. Ion Diffusion Coefficient Ratio $(\delta_D = D_{||}/D_{\perp})$ - TH15

5.3 Conventional Ion Thruster Design Analysis

The Discharge Model was used to perform a design analysis for the NSTAR thruster by doubling the strength of the magnets on the middle magnetic ring. The middle magnet ring was strengthened by increasing the length (along the axis of magnetization) for the permanent magnet dimension that is used by the magnetostatic solution (refer to Figure 5.3-3). The modified thruster design was simulated at TH15 operating conditions. The impact of this modification on the discharge parameters is shown in Table 5.3-1 by comparing discharge performance with the original NSTAR configuration.

Table 5.3-1. Discharge Performance Parameters
(NSTAR TH15 - Original vs. Modified Design)

Discharge Parameters	η_{ud} [*]	η_{ud}	ε_B	J_{B++}/J_{B+}	J_i	J_{ip}	n_i	n_p	n_o	f_A	f_B	f_C	F_B	F_{B*}
Units	%	%	eV/ion	-	A	A	m-3	m-3	m-3	-	-	-	-	-
Original	90.9	84.5	187	0.16	6.08	3.73	$1.97 *10^{17}$	$9.25 *10^{15}$	$4.64 *10^{18}$	0.66	0.29	0.05	0.47	0.674
Modified	94.2	90.2	179	0.093	5.94	3.83	$1.85 *10^{17}$	$7.99 *10^{15}$	$3.96 *10^{18}$	0.64	0.31	0.05	0.68	0.71

Figure 5.3-1 shows the beam and neutral density profiles that were predicted by the Discharge Model for the modified NSTAR design. The experimental TH15 beam profile "Data" for the original NSTAR design is included in this figure for reference. According to these results, a simple modification to the existing NSTAR design can yield increased performance and will likely result in longer life due to increased beam flatness, greater neutral atom uniformity across the grids, and lower double ion content. These results should be verified by experimental testing but this type of simple analysis shows that the Discharge Model can serve as a useful tool for aiding in the optimization of thruster life and performance.

Figure 5.3-2 shows the primary electron distribution for the modified NSTAR thruster. Comparing this result to those for the original thruster, Figure 5.2-7, suggests that the more uniform profile of the modified thruster is due in large part to the more even distribution of primary electrons. The tendency for the primary electrons to not be mainly confined to the thruster axis, as in the original design, can be understood by comparing the magnetic field lines in Figure 5.3-3. For the modified thruster, a large percentage of the near-axis magnetic field lines will guide the primaries away from the axis, instead of confining them to the axis as the original design appears to do. In this way, the modified design improves primary electron utilization.

Table 5.3-2. Electron Power Loss Mechanisms
(NSTAR TH15- Original vs. Modified Design)

Mechanism / Thruster	Primary Electron Losses				Secondary Electron Losses		
	P_{ps}	P_{pw}	P_{piz}	P_{px}	P_{sw}	P_{siz}	P_{sx}
Original	69.0%	0.7%	13.7%	16.6%	49.1%	7.5%	12.5%
Modified	65.7%	4.2%	13.7%	16.4%	48.3%	6.6%	10.9%

Comparing the electron power loss mechanisms, Table 5.3-2, would actually lead a designer to believe that the modified design would result in lower performance due to the higher loss to the walls, and lower power due to ionization. The discrepancy arises from the power wasted by the original design in double ionization near the axis and the greater propensity of the modified design to extract single ions to the beam.
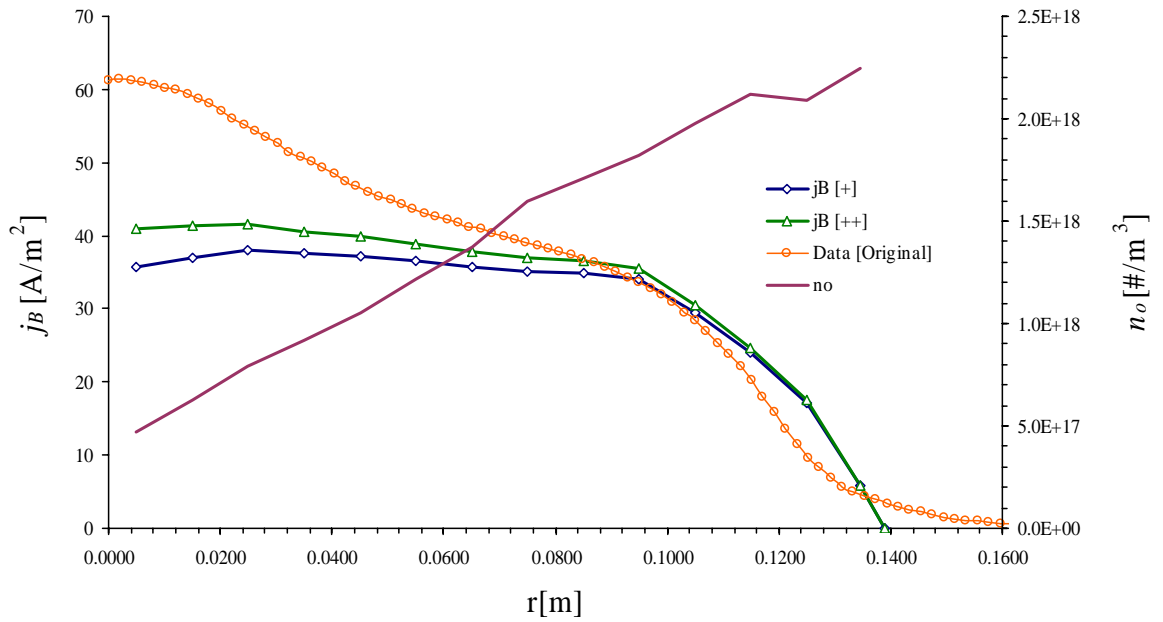
Figure 5.3-1. Beam and Neutral Density Profiles for Dimply Modified NSTAR Thruster - TH15
(note: "Data" values are from original thruster configuration)
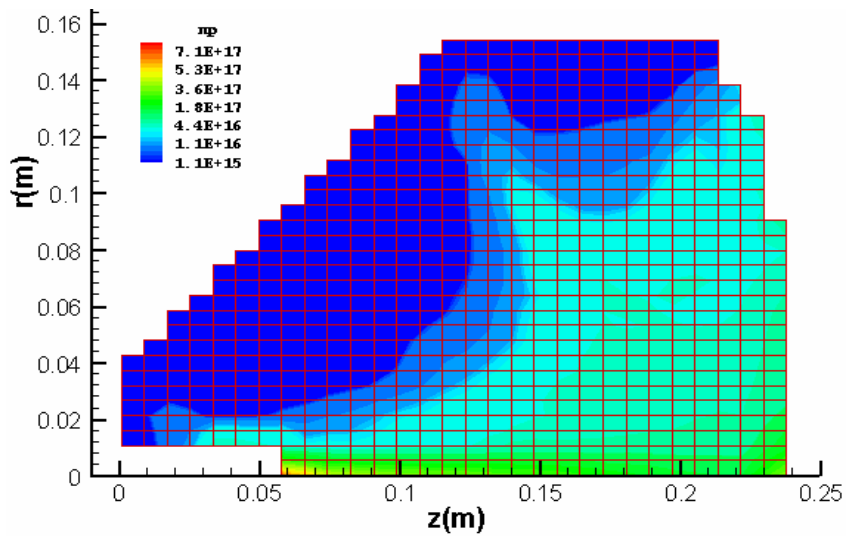
Figure 5.3-2. Modified NSTAR - Primary Electron Density [m⁻³] - TH15

The original and modified NSTAR magnetic fields are shown in Figure 5.3-3. Comparing the contours of these two plots shows that the original NSTAR field closes the 27 Gauss contour between the mid and cathode magnet rings, while the modified design closes the 37 Gauss contour at this location. Between the mid and grid rings the original NSTAR closes the 30 Gauss contour and the modified design closes the 46 Gauss contour. This correlation of improved performance with closing the higher B-field contour (near ~40 Gauss) agrees with previous studies [17,18] that experimentally observed this phenomenon for ring-cusp ion thrusters.
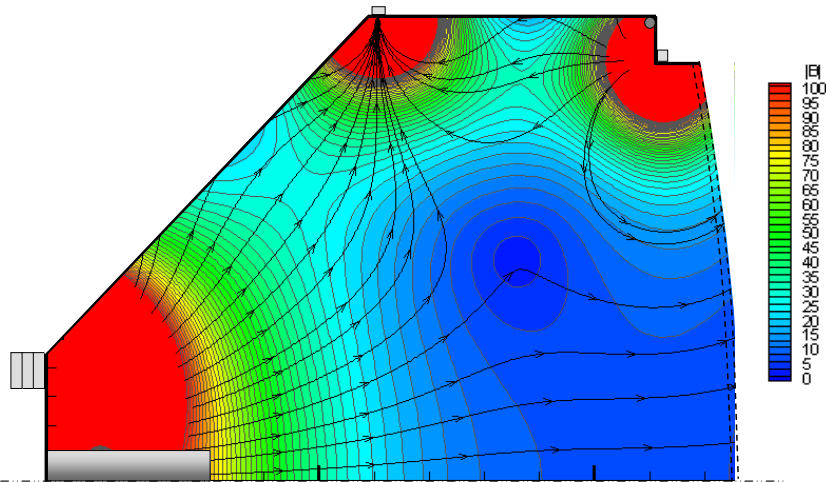
Figure 5.3-3a. Original NSTAR Magnetic Field [Gauss] with Example Magnetic Field Lines
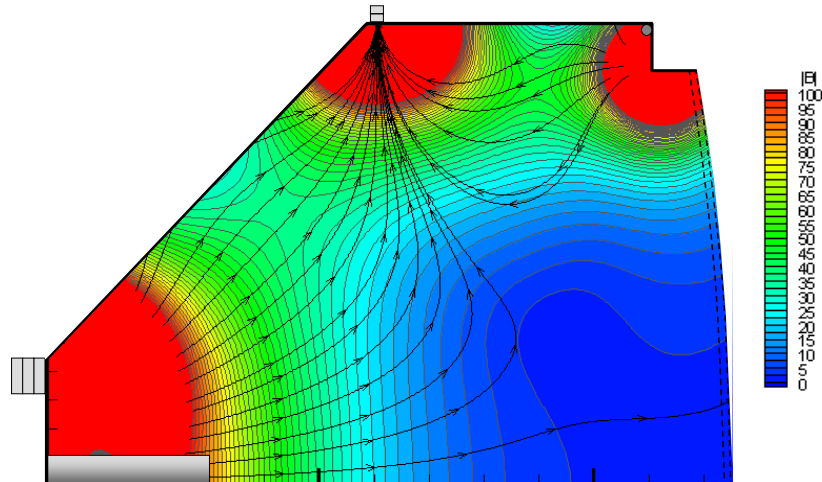
Figure 5.3-3b. Modified NSTAR Magnetic Field [Gauss] with Example Magnetic Field Lines
(note: double mid magnetic ring)

Chapter 6

Miniature Ion Thruster: Discharge Model Results

The results from Chapter 5 suggest that the Discharge Model provides reasonably good agreement with conventional thruster data. In this chapter, model results are compared with the miniature ion thruster data from Chapter 3 to assess the accuracy of the model at smaller scales. Comparisons of the model results with the 3-Ring Micro-Ion thruster data show that the model appears to anticipate the general behavior of the small thruster, but not to the degree found in Chapter 5. The lower accuracy of the magnetic field model at the smaller scale may contribute to this disparity. The Discharge Model results suggest that the ionization in the Micro-Ion thruster is almost entirely due to the primary electrons. A design sensitivity analysis of the Micro-Ion thruster middle magnet location agrees with the trend found with the experimental results in Chapter 3.

6.1 Inputs and Assumptions

The Micro-Ion thruster geometry used for the model is shown in Figure 6.1-1. All the propellant for the Micro-Ion thruster comes from a diffusion plate at the forward most surface of the chamber. Comparisons of the measured magnetic field and that predicted by the model are given in Appendix F and show some discrepancy in the magnetic field, but the general shape and strength of the field is consistent.
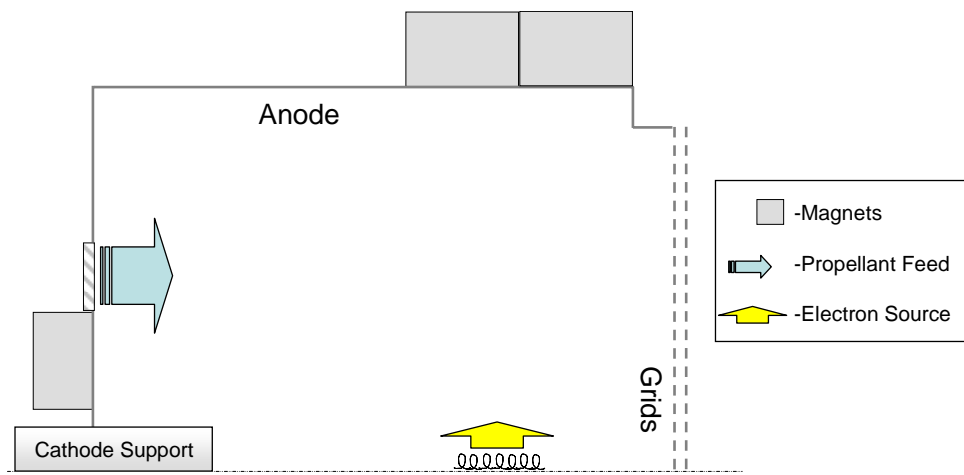
Figure 6.1-1. Micro-Ion Thruster 3-Ring Geometry for the Discharge Model

The Discharge Model simulated the Micro-Ion thruster operating conditions from Figure 3.3-1, which are repeated in Table 6.1-1 for convenience. This Micro-Ion throttle point is identified here as "mTH1." The primary current and wall transparency were determined as in Chapter 5. As discussed in Appendix G, the filament cathode electrons are assumed to behave as single-energy primary electrons, implying $T_p \approx 0\text{eV}$. Using the voltages in Table 6.1-1 and assuming the plasma potential to be 2-3V, the initial guess for primary energy was $V_p \sim 22\text{V}$. Ultimately, a voltage of $V_p = 21\text{V}$ gave good agreement with the beam current for mTH1, so this value was used for the results herein. As discussed in Chapter 4, the

secondary inelastic collision factor, f_{inel} , is assumed equal to 0.8, and the non-classical diffusion parameter, γ_{nc} is ¼.

Table 6.1-1. Micro-Ion Throttle Point mTH1

Total Flow [sccm]	J_B [mA]	J_D [mA]	V_D [V]	V_{Fil} [V]	V_B [V]	V_{accel} [V]	Model Specific Inputs	
							Vp [V]	Tp [eV]
0.29	14.05	293.5	25.0	10.7	911	-211	21	0

6.2 Model Results and Experimental Comparison

The results in this section are for the Discharge Model at mTH1, unless otherwise noted. The Micro-Ion simulations required relatively slow growth rates of the primary electron current, in comparison to NSTAR simulations, to avoid large gradients for the early iterations.

Solution Convergence

Figure 6.2-1 shows the results for propellant efficiency vs. iteration where the primary current reached full strength after 30 iterations. In this figure, nud[Gas], nud[Beam], and nud[*] are the propellant efficiencies per equations 4.1-1, 4.1-2, and 4.1-3, respectively. Since the single-energy primary electron value of 21V is below the double ionization threshold, double ion effects will not be seen in these results and nud[Beam] = nud[*]. That is not to say that double ions do not exist, but, rather, that their effects are neglected by the simple single-energy approximation. The presence of double ions is likely very small for the Micro-Ion thruster because $n_o \gg n_i$, as shown below.
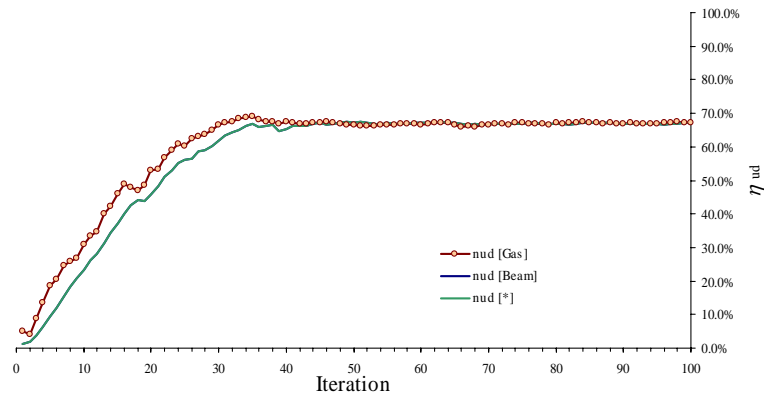
Figure 6.2-1. Propellant Efficiency vs. Iteration for mTH1

The convergence of the volume-averaged densities is shown in Figure 6.2-2. In comparison to TH15 for NSTAR, the ion and primary densities are of the same order; however the neutral density is an order of magnitude higher. Plots of these values on the Internal Mesh are given below.
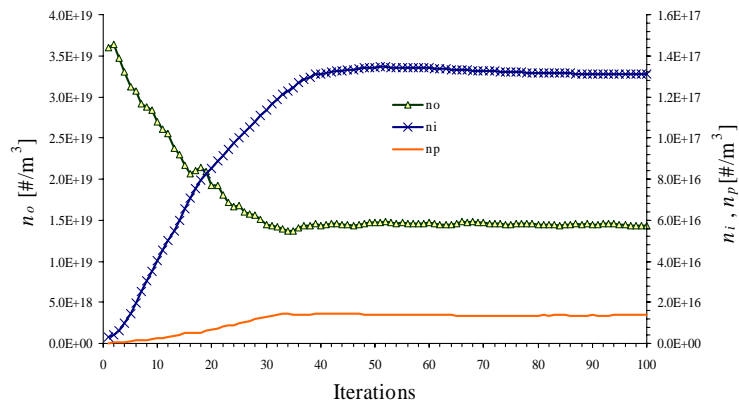
Figure 6.2-2. Volume-Averaged Densities vs. Iteration for mTH1

Comparison with Experimental Results

The beam current density profiles along the flat exit plane of the thruster, as calculated by the Discharge Model, are shown in Figure 6.2-3. The "Data" profile is the experimentally derived profile from Section 4.3. In the absence of double ions, the jB [++] profile used in Chapter 4 is not necessary. The profile from the Discharge Model shows generally good agreement with the Data profile, except for

the higher densities predicted near the center and the edge of the grids. The neutral atom profile is very flat, especially in comparison to the results for the NSTAR thruster.
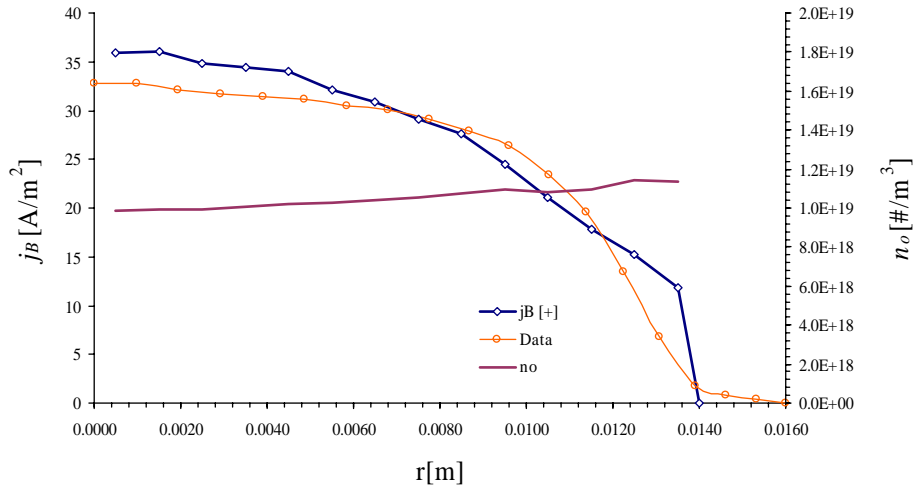
Figure 6.2-3. Beam and Neutral Density Profiles at Grids for mTH1

Discharge Performance Parameters

As in Chapter 4, the results of the model are expressed by averaged discharge performance parameters at the Micro-Ion mTH1 operating condition and are compared to the thruster data in Table 6.2-1. The agreement of $\eta_{ud[*]}$ and ε_B is a consequence of the choice of throttle point, as discussed in Chapter 5. Comparing J_i and J_{ip} shows that the primary electrons are responsible for ion generation in the Micro-Ion thruster. The results in Table 6.2-1 are used for comparison with a thruster modification in Section 6.3.

Table 6.2-1. Discharge Performance Parameters for mTH1
(Micro-Ion Simulation vs. Data)

Discharge Parameters	η_{ud} [*]	η_{ud} [act]	ε_B	J_{B++}/J_{B+}	J_i	J_{ip}	n_i	n_p	n_o	f_A	f_B	f_C	F_B	F_{B*}
Units	%	%	eV/ion		mA	mA	m^{-3}	m^{-3}	m^{-3}	-	-	-	-	-
Model Results	67.1	67.1	520	0	56.8	56.5	$1.31 *10^{17}$	$1.39 *10^{16}$	$1.44 *10^{19}$	0.54	0.25	0.21	0.64	0.64
Data	66.9	-	522	-			$\sim 2.0 *10^{17}$						0.67	-

Electron Power Loss

The power loss parameters defined in Chapter 4 are used here to compare the electron behavior in Micro-Ion and NSTAR discharge chambers. The results in Table 6.2-2 show that the primary electrons are more likely lost to the wall before losing energy to other plasma species, which results in the >500eV/ion discharge loss.

Table 6.2-2. Electron Power Loss Mechanisms

(Micro-Ion vs. NSTAR)

Mechanism	Primary Electron Losses				Secondary Electron Losses		
	P_{ps}	P_{pw}	P_{piz}	P_{px}	P_{sw}	P_{siz}	P_{sx}
Micro-Ion (mTH1)	20.9%	58.2%	12.1%	8.8%	20.6%	0.1%	0.2%
NSTAR (TH15)	69.0%	0.7%	13.7%	16.6%	49.1%	7.5%	12.5%

Two-Dimensional Plots of Discharge Characteristics

In the following figures, Discharge Model results for mTH1 are presented. Some observations of the plots accompany the figures in this section; however, a discussion of the collective implications of these results to the important discharge plasma processes of the small ring-cusp ion thrusters is reserved for Chapter 7.

The non-uniform behavior of the Micro-Ion thruster at mTH1 can be summarized by plotting the distributions of the ion and neutral density, and the ion generation rate. The total ion density distribution is plotted on the Internal Mesh in Figure 6.2-4. As discussed above, the double ion content is zero for the primary energy chosen. The neutral densities shown in Figure 6.2-5 show that n_o is nearly two orders of magnitude greater than n_i throughout the chamber. Figure 6.2-6 shows the distributed ion generation rate, which is almost entirely due to primary electron ionization since $J_{ip}/J_i \sim 1$. For the nearly uniform neutral density, this ionization profile essentially mimics the primary electron density profile. A plot of five example primary electron paths, Figure 6.2-7, shows that the 3-Ring configuration confines the primary electrons near the grids, resulting in a relatively high ionization rate in that region. The secondary electron temperature, not shown, was essentially uniform at $T_s \sim 2$ for all the Micro-Ion thruster simulations herein.
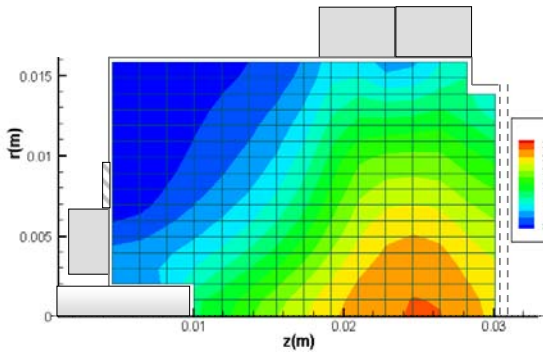
Figure 6.2-4. Total (Single) Ion Density [m^{-3}] - mTH1   Figure 6.2-5. Neutral Atom Density [m^{-3}] – mTH1
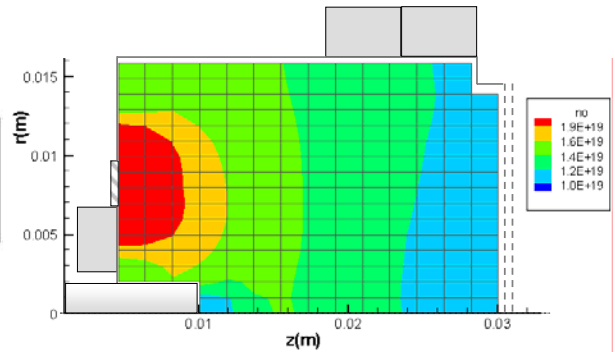
A plot of the distribution of the electron-neutral-centered vs. electron-ion-centered collision ratio, $\delta_\nu = \nu_{e-n}/\nu_{e-i}$, in Figure 6.2-8 shows that even in the presence of a relatively high neutral density, intermediate levels of ionization exist throughout the chamber and increasingly on-axis. Referring to Figure 6.2-9, the resulting level of anisotropy of the plasma motion, or magnetization δ_D, is similar to that determined for the NSTAR thruster.
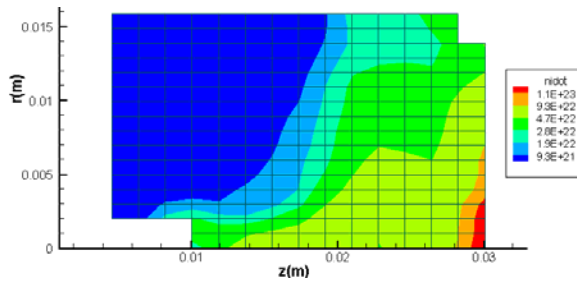
Figure 6.2-6. Ion Generation Rate Density [$s^{-1}m^{-3}$] - mTH1
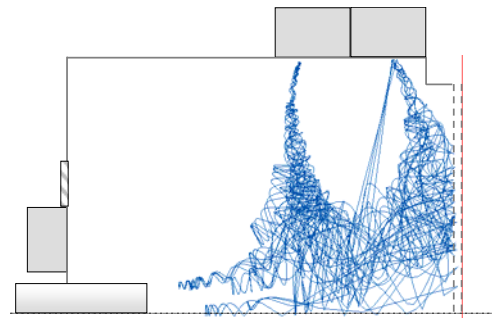
Figure 6.2-7. Example Primary Electron Paths – mTH1
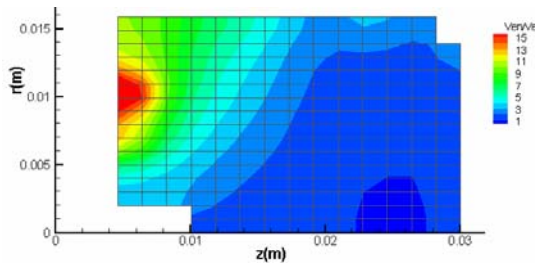
Figure 6.2-8. Electron Collision Ratio $(\delta_\nu = \nu_{e\text{-}n}/\nu_{e\text{-}i})$ - mTH1
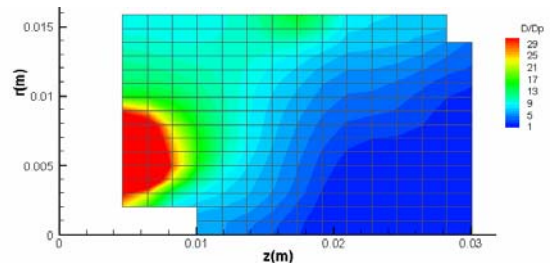
Figure 6.2-9. Magnetization, Plasma Diffusion Coefficient Ratio $(\delta_D = D_{||}/D_\perp)$ - mTH1

6.3 Miniature Thruster Design Analysis

The Discharge Model was used to mimic the design analysis for the Micro-Ion thruster that is given in Section 3.2 by increasing the spacing between the anode ring magnets by 1.5mm for the 3-Ring configuration.   The impact of this modification on the discharge parameters is shown in Table 6.3-1 by comparing the discharge performance parameters with the original thruster.

Table 6.3-1. Discharge Performance Parameters at mTH1
(Micro-Ion Original vs. Modified Design)

Discharge Parameters	η_{ud} [*]	η_{ud} [act]	ε_B	J_{B++}/J_{B+}	J_i	J_{ip}	n_i	n_p	n_o	f_A	f_B	f_C	F_B	F_{B*}
Units	%	%	eV/ion	-	mA	mA	m^{-3}	m^{-3}	m^{-3}	-	-	-	-	-
Original	67.1	67.1	520	0	57.4	57.1	1.31×10^{17}	1.39×10^{16}	1.44×10^{19}	0.66	0.29	0.05	0.64	0.64
Modified (1.5mm magnet spacing)	67.7	67.7	490	0	61.9	61.6	1.5×10^{17}	1.62×10^{16}	1.44×10^{19}	0.56	0.23	0.21	0.57	0.57

Referring to Figure 6.3-1, the model predicts better performance for the 1.5mm magnet spacing; however, the reduction in discharge loss is not as drastic as found in the experimental results in Figure 3.2-6. The profiles for the modified design, Figure 6.3-2, show the more peaked profile in comparison to the experimental "Data." Therefore, though many of the discharge parameters in Table 6.2-1 are favorable for the modified design, the profile data (and resulting F_B) suggest that this design may not be preferable due to the non-uniformity of the beam, depending on the life and performance requirements.
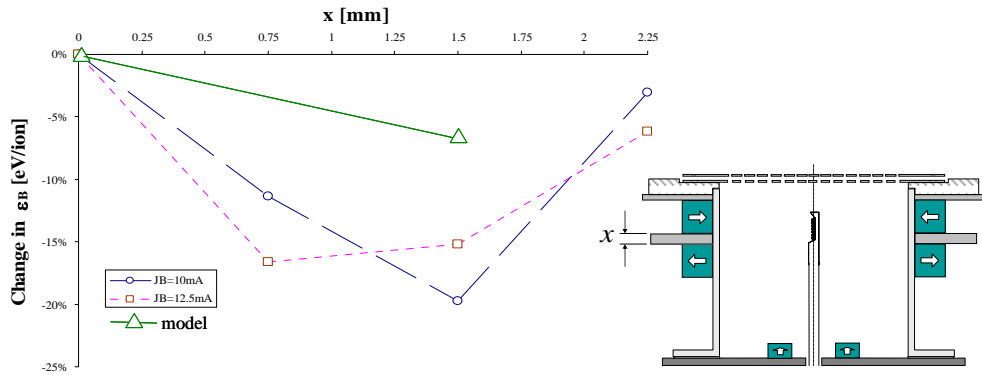
Figure 6.3-1. Change in Discharge Loss vs. Magnet Spacing in 3-Ring (L/D=1) Configuration of Micro-Ion Thruster, Compared with Discharge Model Result
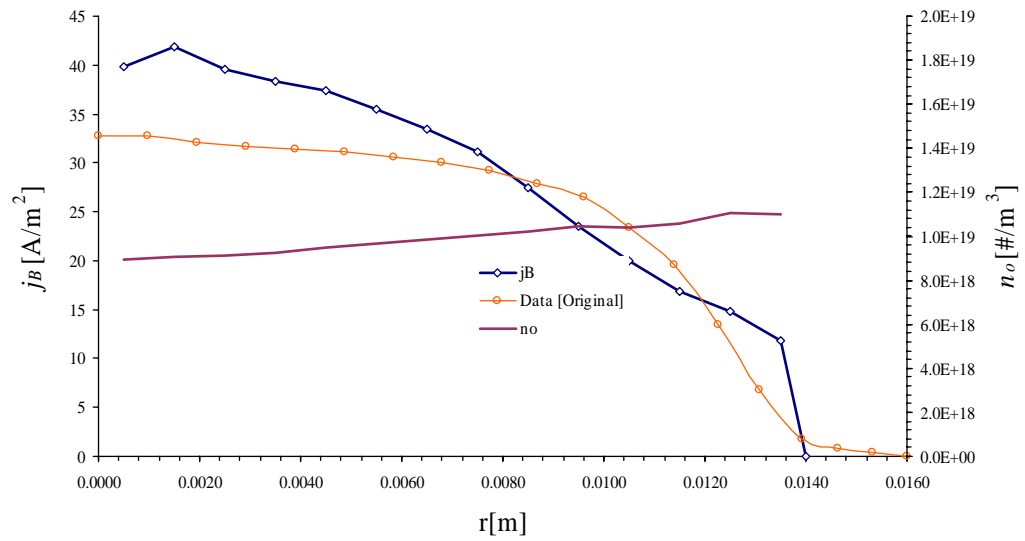
Figure 6.3-2. Beam and Neutral Density Profiles for the Modified Micro-Ion Thruster - mTH1
(note: "Data" values are from original thruster configuration)

Chapter 7

Discussion of Findings

In this chapter the experimental and modeling results from chapters 3, 5, and 6 are discussed and used to answer the questions that are posed in Section 2.4. Section 7.1 discusses the importance of the miniature ion thruster development effort and the subsequent miniature discharge modeling efforts. The results from the Micro-Ion thruster simulations and experiments are used in Section 7.1 to show that miniature discharge processes are dominated by the primary electrons and that very high cusp field strengths likely lead to an unstable discharge; however, even with this limit to stable thruster design, desirable miniature thruster efficiencies are possible with conventional magnet sizes. Section 7.2 discusses the NSTAR results, showing that primary electrons produce most of the ions, cause the double ion peak in the profile, and dominate the performance behavior of the thruster, but not to the extent of the miniature thruster. The results also show that good agreement with experimental results is attained by incorporating non-classical mobility as described in Chapter 4. The importance of the miniature discharge analysis to future missions and thruster development is discussed in Section 7.3, along with a discussion on the applicability of the Discharge Model to aiding design, optimization, and life validation efforts.

7.1 Miniature Thrusters

The Micro-Ion and MiXI thruster results from Chapter 3 show that desirable performance of a DC miniature ion thruster is possible with reasonable magnet and thruster weight. This observation dispels a commonly held belief that extreme magnet strengths are needed for desirable performance of miniature ion thrusters. As discussed in Section 3.4, the small grid diameter of miniature ion thrusters allows close spacing of the grids, permitting SHAG optics, which results in increased thruster efficiency. Favorable performance of the miniature discharge and grids was demonstrated; however, integration of flight cathodes is necessary to fully mature the MiXI thruster technology.

Discharge Model results for the Micro-Ion thruster show that the discharge ionization is almost entirely due to primary electrons. For the conditions tested in Chapter 6, over half of the primaries are lost to the walls before having an inelastic collision. The high wall losses for the miniature chamber yield meager secondary temperatures of only about 2eV, resulting in negligible secondary ionization. The low ionization efficiency of the miniature discharge requires proportionally high propellant flow rates, and hence densities, to attain ion densities similar to those found in the NSTAR thruster. This results in neutral densities nearly two orders of magnitude greater than the ion density. Nonetheless, the electron collision ratio, δ_ν, results suggest that the miniature discharge plasma diffusion is in a similar regime to that of the NSTAR discharge. This result can be explained by the sharp drop-off of the total electron-neutral collision cross-section for $T_s \sim 2\text{eV}$. Low values of the electron collision ratio result in low levels of plasma magnetization, δ_D, for the Micro-Ion discharge.

Recognizing the poor primary confinement of the Micro-Ion discharge leads to the consideration of higher magnetic fields to better confine the primaries. As discussed in Chapter 3, higher magnetic fields resulted in poor performance for the 3-ring configuration. This poor performance can be explained by the onset of

discharge instabilities due to overly high cusp magnetic field strengths (see Chapter 2). In this way, miniature ion thruster discharges demand careful consideration of the competing effects of efficiency and stability. The larger surface-to-volume ratio requires high cusp B-field strength for favorable primary utilization; while the cusp B-field strength for a given magnetic field geometry must be sufficiently low to assure discharge stability through the desired range of operating conditions. These observations suggest that miniature ion thruster performance is bracketed by primary electron utilization and discharge stability.

The experimental efforts outlined in Chapter 3 were able to identify a relatively efficient miniature discharge configuration; however, additional optimization of the precise magnetic field strength and placement should lead to noticeable improvements in discharge performance. In its present form, the model can be used to determine thruster designs that yield improved primary electron confinement, while experimental testing can be used to assess the stability of these designs. The performance degradation due to high magnetic field strengths (i.e., discharge stability) will need to be characterized and incorporated into future versions of the model.

7.2 Conventional Thrusters

For the original NSTAR design, the primaries are well-confined by the cusp magnetic field and are mainly confined to the thruster axis. This on-axis confinement leads to the double ion peak at the center of the beam profile and large radial neutral density gradients. Results for a modified design of the NSTAR thruster suggest that the double ion content may be significantly reduced by designing the magnetic field to avoid on-axis confinement of primaries. Comparison of these results with the original NSTAR design shows the importance of assuring that the primaries are allowed to move to regions of the thruster where they can produce the largest fraction of singly charged beam ions. For NSTAR,

this means letting the primaries travel to the edge of the grids where there is a large volume of high density neutral propellant that is not utilized by the original configuration. The electron power results in Table 5.3-2 show that simply preventing the primaries from being collected at the walls does not imply superior performance. The results from Chapter 5 show that secondary electrons account for nearly 40% of the ionization in the NSTAR discharge; however, the management of the primary electrons is the dominate consideration for discharge chamber design.

Good agreement with the experimental data was found by incorporating the effects of non-classical mobility in a non-uniform manner as proposed in Chapter 4, using $\gamma_{nc} = \frac{1}{4}$. The electron collision ratio, δ_ν, was on the order of unity throughout most of the discharge, thus implying that the plasma is neither fully nor weakly ionized, but in an intermediately ionized regime. Substituting $\gamma_{nc} = \frac{1}{4}$ and $\delta_\nu \sim 1$ into Equation 4.5-37 shows that the coefficient for Bohm mobility (Eq. 4.5-38) may be closer to $\sim 1/80$, instead of 1/16 for ion thruster conditions. This value is close to the $\sim 1/100$ coefficient reported for Hall thruster electron diffusion in Reference [74]. The low values of δ_ν on-axis suggest the importance of non-classical effects in this region. Consequently, the magnetization of the plasma motion, δ_D, was found to be small on-axis, even near the cathode where the B-field is on the order of 50 Gauss. In contrast, the plasma is significantly more magnetized, and hence confined, in near-wall regions between the cusps where the B-field is also on the order of 50 Gauss.

The non-classical diffusion correction used herein does not imply that the specific mechanisms of the plasma diffusion have been identified. Further analyses, both experimental and theoretical, are needed to characterize the specific mechanisms that contribute to the plasma diffusion.

7.3 Applications

The miniature ion thruster performance obtained in this dissertation demonstrates that the advantages of ion thrusters can be realized at a miniature scale that was previously unavailable to space mission designers. The many possible applications for the miniature ion thruster are discussed in Section 1.2. Such a plasma discharge source can be applied to terrestrial applications where miniature sources are desirable (e.g. material processing). The IC cathode, Section 3.5, may prove useful for miniature ion thruster discharges and can be also be used as an electron source for scanning electron microscopes (SEMs), transmission electron microscopes (TEMs), electron lithography systems, electron accelerators, x-ray sources, free electron lasers, accelerators, melting furnaces, or similar applications.

The Discharge Model is a useful tool for determining the performance of a large range of ion thruster sizes. The model output reveals important plasma processes that govern the performance of the thruster, which can be used to guide the design and optimization process. The NSTAR thruster simulations from Section 5.3 show that the model can be used to identify undesirable characteristics of an existing design and show the advantages (or disadvantages) of design modifications. The Discharge Model is a valuable design tool since the simplicity of the model inputs allows quick assessment of the five physical characteristics that drive discharge chamber design:

1) Chamber geometry

2) Magnetic field geometry and strength

3) Discharge cathode location and properties

4) Propellant feed

5) Ion optics design

To fully assess the performance of an ion thruster requires consideration of the change in performance with time [7]. By working with component wear models the Discharge Model will be able to assess the long-term performance of the thruster [12,9,8]. In this way, the model will be able to optimize the discharge design for the full thruster life. For example, the modified NSTAR design exhibits relatively high beam flatness, and with the aid of wear models, the Discharge Model can be used to predict the anticipated increase in grid life without requiring lengthy and costly life tests [5].

Chapter 8

Summary and Conclusions

In this dissertation experimental and computational methods were used to investigate the behavior of DC ring-cusp ion thruster discharges. A 3cm ion thruster was developed to help understand the issues related to miniature discharges. From the array of miniature discharge configurations tested, a 3-ring design was found to produce the best performance. Since the small diameter grids of the miniature thruster can be very closely spaced, small-hole accelerator grids were used to improve performance. The performance of the MiXI thruster shows that an efficient miniature ion thruster is possible with reasonable thruster and magnet weight. Results from the Discharge Model show that primary confinement of the Micro-Ion thruster is very poor since low cusp magnetic field strengths are necessary to ensure a stable discharge. In this way, the design of miniature discharge is bounded by concerns of primary electron confinement efficiency and discharge stability.

The multi-dimensional "Discharge Model" was developed to identify the important plasma processes of ion thruster discharges for a large range of chamber sizes and to supply input to thruster component wear models. This model self-consistently accounts for the behavior of the four dominant plasma species: primary electrons,

secondary electrons, ions, and neutral atoms to determine the non-uniform and interrelated behavior of these species in the discharge. The Discharge Model represents a significant advancement in the state of the art of ion thruster discharge modeling because it does not rely on the results of simple analytical models to assess performance. Results from the Discharge Model agree well with several ion thruster operating conditions at conventional and miniature ion thruster sizes. The information provided by the model on the non-uniform discharge parameters, (i.e., densities, production rates, etc.) allows for detailed analysis of the discharge performance for a given configuration. The results show that the primary electrons cause at least 60% of the ionization and that their behavior is very important to thruster performance for all thruster sizes.

Results from the NSTAR thruster show that the double ion peak measured in experimental beam profiles is due to the magnetic field, which confines the primary electrons to the near-axis region. This confinement results in high ion density and low neutral density on-axis, which, when coupled with a high concentration of energetic primaries, results in high levels of double ionization. This illustrates the importance of considering non-uniform neutral and primary densities. Comparing these results with a modified NSTAR design shows that a higher ion extraction fraction, f_B, is achieved by guiding the primary electrons to regions where they are most likely to make single ions that will be extracted to the beam. On the other hand, simply increasing primary confinement does not guarantee better performance.

Proper treatment of secondary electron motion is necessary to accurately predict the plasma diffusion. The Discharge Model results for both thruster sizes show that the perpendicular diffusion of secondary electrons is described by combining classical treatment with Bohm diffusion. The effect of non-classical perpendicular electron mobility showed good agreement with experimental data for values of γ_{nc} near ¼. The specific mechanisms related to this value for γ_{nc} have not been identified;

145

however, in the context of the treatment herein, a value of γ_{nc} between 0 and 1 suggests that ion thruster plasma may be considered intermediately ionized, as described in Section 4.5. Good agreement with experimental measurements of T_s were found by assuming some tail depletion of the secondary population, namely $f_{inel} \sim 0.8$.

In addition to aiding thruster design, the detailed information from the Discharge Model provides useful input for wear models of the discharge cathode and ion extraction grids. By working with wear models, the Discharge Model can be used to assess long-term thruster performance and validate thruster life. These results may in turn be used to improve the thruster design to maximize the thruster lifetime performance.

8.1 Future Work

In future analyses, the Discharge Model can be used to iterate through a large design space to allow optimization of the performance of the miniature thruster. The large surface-to-volume ratio yields inherently large discharge losses; however, significant improvements to the discharge efficiency are possible through optimization of the primary confinement within the limits of discharge stability. Future experimental efforts for the miniature discharge should focus on fully characterizing the discharge instabilities that occur at high field strengths and identifying these stability limits. Optimization of magnet strength, magnet configuration, and cathode placement should be performed once the final cathode technology is chosen. Improvements to miniature cathode technologies for the small thruster are imperative to the viability of the thruster and should be investigated further.

In future versions of the Discharge Model detailed modeling of the near-cathode region will provide accurate information of the primary electron energy distribution [8]. Knowledge of the near-cathode electron energies will provide self-consistent

values for the two Discharge Model input parameters that are not simply identified by operational thruster inputs: V_p and T_p, the primary half-Maxwellian characteristics. Combining the Discharge Model with cathode and grid wear models will allow for long-term performance assessments and thruster life predictions [9,12].

The Discharge Model currently uses Bohm diffusion to approximate non-classical effects. Experimental measurements within the discharge chamber should be used to determine the existence and importance of anomalous effects such as azimuthal drift waves and ion acoustic waves, which may arise from the high-velocity stream of electrons emitted from the cathode. Knowledge of the importance of these types of non-classical mechanisms will improve the accuracy of the Discharge Model.

The Discharge Model can also be improved with a better treatment of the secondary electron population. For example, a more detailed electron energy balance treatment for primaries and secondaries will improve the predictions of secondary electron temperature and the secondary inelastic collision parameter. Another way to improve the secondary electron treatment is to use a magnetically aligned mesh ("B-Mesh"), which was used in original versions of the model [47,48]. This complex meshing technique was abandoned in this study for reasons discussed in Section 4.1; however, it is much better suited to treating the highly anisotropic nature of the electron motion, and should be considered for future versions of the model. The simpler formulation of the electron motion equation that is possible with the B-Mesh may allow the electric fields to be solved self-consistently. In this way, the effects, or lack thereof, of perpendicular electric fields can be assessed. With a reliable electric field solution, the Discharge Model may also be expanded to include the effects of discharge instabilities [15]. Future experimental efforts should characterize discharge instabilities for high magnetic field cusp configurations to assure that these effects are accurately reproduced by the Discharge Model.

BIBLIOGRAPHY

[1] - Mueller J., et al., "An Overview of MEMS-Based Micropropulsion Developments at JPL," IAA Paper B3-1004, 3rd International Symposium on Small Satellites for Earth Observation, International Academy of Astronautics (IAA), Berlin, Germany, April 2001

[2] - Sovey J. S., Rawlin V. K., and Patterson M. J., "Ion Propulsion Development Projects in U. S.: Space Electric Rocket Test 1 to Deep Space 1." Journal of Propulsion and Power, Vol. 17, No. 3, May-June 2001, pp. 517-526

[3] – Wilbur P. J., Rawlin V. K., Beattie J. R., "Ion Thrust Development Trends and Status in the United States," Journal of Propulsion and Power, Vol. 14, No. 2, September 1998

[4] - http://www.boeing.com/defense-space/space/bss/factsheets/xips/xips.html

[5] - Sengupta A., Brophy J., Goodfellow K., "Status of the Extended Life Test of the DS1 Flight Spare Ion Engine after 30,352 Hours of Operation, AIAA-2003-4558, 40th AIAA Joint Propulsion Conference, Fort Lauderdale, FL, July 11-14, 2004

[6] – Oleson S., "Electric Propulsion Technology Development for the Jupiter Icy Moons Orbiter Project," AIAA-2004-3449

[7] – Polk J., et al., "An Overview of the Results from an 8200 Hour Wear Test of the NSTAR Ion Thruster," AIAA 99-2446

[8] – Mikellides I., Katz I., Goebel D., Polk J., "Theoretical Model of Hollow Cathode Insert Plasma," AIAA-2004-3817, 40th Joint Propulsion Conference, Ft. Lauderdale, FL, July 11-14, 2004

[9] – Andersen J., Katz I., "Numerical Simulation of Two- Grid Ion Optics Using a 3D Code," AIAA-2004-3782, 40th Joint Propulsion Conference, Ft. Lauderdale, FL, July 11-14, 2004

[10] - Snyder J. S., Brophy J. R., "Performance Characterization and Vibration Testing of 30cm Carbon-Carbon Ion Optics," AIAA-2004-3959, 40th JPC, Ft. Lauderdale, FL, July 2004

[11] - Aston, G., Kaufman, H., Wilbur, P., "Ion Beam Divergence Characteristics of Two-Grid Accelerator Systems," AIAA Vol. 16, No. 5, 1978

[12] - Brophy J.R., Katz I., Polk J., Anderson J., "Numerical Simulations of Ion Thruster Accelerator Grid Erosion," AIAA-2002-4261, 38th AIAA/ASME/SAE/ASEE Joint Propulsion Conference & Exhibit, Indianapolis, IN, July 2002

[13] - Beattie J.R., "Cusped Magnetic Field Mercury Ion Thruster," NASA-CR – 135047, July 1976

[14] – Beattie J.R., Poeschel R.L., "Ring-Cusp Ion Thrusters", IEPC Paper 84-71, May 1984

[15] - Goebel, D., "Ion source discharge performance and stability," Physics of Fluids, Volume 25, Issue 6, June 1982, pp.1093-1102

[16] – Brophy J., "Ion Thruster 'Engine-T' Throttle Table," JPL Interoffice Memorandum 353-04-067, November 2004

[17] Beattie J., Matossian J., "Inert-Gas Ion Thruster Technology," NASA CR191093, March 1993

[18] – Goebel, D., "NEXIS Discharge Chamber Model and Performance," AIAA-2004-3813, 40th JPC, Ft. Lauderdale, FL, July 2004

[19] – Leung K., Hershkowitz N., MacKenzie K., "Plasma Confinement By Localized Cusps," Phys. Fluids 19(7), July 1976

[20] - Hershkowitz N., Cho M., Pruski J., "Mechanical variation of plasma potential, electron temperature, and plasma density," Plasma Sources Sci. Technol. 1 1992 pp 87-93

[21] – Hirakawa M., Arakawa Y., "Plasma Particle Simulation in Cusped Ion Thrusters," IEPC-93-242

[22] – Koch C., Matthieussent G., "Collisional diffusion of a plasma in multipolar and picket fence devices," Phys. Fluids 26 (2), February 1983

[23] – Vaughn J., Wilbur P., "Ring Cusp / Hollow Cathode Discharge Chamber Performance Studies," IEPC-88-064, 1988

[24] - Patterson M., "Low-Power Ion Thruster Development Status," AIAA-98-3347, 1998

[25] – Matossian J., Beattie J., "Characteristics of Ring-Cusp Discharge Chambers," Journal of Propulsion and Power, Vol. 7, No. 6, Nov-Dec 1991, pp. 968-974

[26] – Yashkov G., "Ion Micro-Propulsion and Cost Modeling for Satellite Clusters," MIT Masters Thesis, 1998

[27] – Patterson M., Foster J., "Hollow Cathode Micro Thruster Performance," IEPC-01-226, 2001

[28] – Mistoco V., et al., "Development and Chamber Testing of a Miniature Radio-Frequency Ion Thruster for Microspacecraft," AIAA-2004-4124

[29] – Mueller J., Brophy J., Polk J., Blandino J., " The JPL Ion Thruster-on-a-Chip Concept," 7th NASA-OSAT Advanced Space Propulsion Workshop, Pasadena, CA, 1996

[30] – Kim S-W, et al., "Endurance Test of a 27W Microwave Engine," AIAA-2003-5014

[31] – Kim S-W, et al., "Endurance Test of Microwave Engine," AIAA-2004-4126

[32] - Brophy, J. R., "Ion Thruster Performance Model," NASA-CR-174810, December, 1984

[33] – Arakawa Y., Ishihara K., "A Numerical Code for Cusped Ion Thrusters," IEPC-91-118, 1991

[34] – Arakawa Y., Yamada T., "Monte Carlo Simulations of Primary Electron Motions in Cusped Discharge Chambers," IEPC paper AIAA-90-2654

[35] – Arakawa Y., Wilbur P., "Discharge Plasma Calculations in Cusped Ion Thrusters Using the Finite Element Method," IEPC-88-079, 1988

[36] – Sandonato M., et al., "Magnetic Confinement Studies for Performance Enhancement of a 5-cm Ion Thruster," IEEE Transaction on Plasma Science, Vol. 24, No. 6, Dec. 1996

[37] – Deshpande S., Mahalingam S., Menart J., "Computational Study of Primary Electrons in the Cusp Region of an Ion Engine's Discharge Chamber," AIAA 2004-4109

[38] – Mahalingam S., Menart J., "Primary Electron Modeling in the Discharge Chamber of an Ion Engine," AIAA 2002-4262

[39] - Reader, P.D., "Scale Effects on Ion Rocket Performance," ARS-IAS Joint Meeting, May 1962

[40] - Kaufman, H. R., "Technology of Electron-Bombardment Ion Thrusters," Advances in Electronics and Electron Physics, Vol. 36, Academic Press, Inc. New York, 1974 pp. 265-373

[41] - Knauer, W., Poeschel, R., "Discharge Chamber Studies for Mercury Bombardment Ion Thrusters," NASA-CR-72350

[42] - Poeschel, R. L., Vabrenkamp, R., "The Radial Magnetic Field Geometry as an Approach to Total Ion Utilization in Kaufman Thrusters," International Telecommunications Satellite Consortium (INTELSAT), 1973

[43] - Magnet Sales and Manufacturing Inc., "High Performance Magnets 7," 1995

[44] - Marrese C., et al., "Performance of Field Emission Cathodes in Xenon Electric Propulsion System Environments," Micropropulsion for Small Spacecraft, Progress in Astronautics and Aeronautics Vol. 187, AIAA, 2000

[45] - Marrese-Reading C., Polk J., Mackie B., Dandeneau D., Koel B., Quinlan M., "Field Emission Array Cathode Material Selection For Compatibility With Electric Propulsion Applications," 100th Electrochemical Society Conference, 2002

[46] – Gorshkov, O., Grigor'yan V., Muravlev V., "Development of the Low-Power Xenon Ion Thruster for Lightweight Satellites," Journal of Propulsion and Power, Vol. 16, No. 6, Nov-Dec 2000

[47] - Wirz R., Katz I., 'A Preliminary 2-D Computational Model of an Ion Thruster Discharge Chamber', AIAA-2003-5163, 39th AIAA/ASME/SAE/ASEE Joint Propulsion Conference, Huntsville, AL, July 20-23, 2003

[48] - Wirz R., Katz I., "2-D Discharge Chamber Model for Ion Thrusters," AIAA-2004-4107, 40th JPC, Ft. Lauderdale, FL, July 2004

[49] – Fife M., "Hybrid-PIC Modeling and Electrostatic Probe Survey of Hall Thrusters," MIT Thesis, September 1998

[50] - Chen F., "Plasma Physics and Controlled Fusion Vol. 1," 2nd Edition, 1984

[51] - Siegel, R., Howell, J., "Thermal Radiation and Heat Transfer," 1972

[52] – Bond T., Christensen J., "NSTAR Ion Thruster and Power Processors," NASA/CR-1999-209162

[53] – Miller J., et al., "Xenon Charge Exchange Cross Sections for Electrostatic Thruster Models," Journal of Applied Physics, Vol. 91, No. 3, Feb 2002

[54] – Vincenti W., Kruger C., "Introduction to Physical Gas Dynamics," 1965

[55] - Clausing P., "The Flow of Highly Rarefied Gases Through Tubes of Arbitrary Length," Journal of Vacuum Science and Technology, Vol. 8, No. 5

[56] – Boris J.P., "Relativistic plasma simulations—Optimization of a hybrid code," Proc. 4th Conf on Num Sim of Plasmas, NRL Washington, Washington DC, 1970

[57] – Mitchner M., Kruger C., Partially Ionized Gases, John Wiley & Sons, New York, pp. 88-93, 1973

[58] - Bell, Djuric, Dunn, "Electron-impact ionization of In+ and Xe+," Phys Rev A, Vol. 48, No. 6, p4286, 1993

[59] – Spitzer L. Jr., "Physics of Fully Ionized Gases," Interscience, New York, p. 127-135, 1962

[60] – Schwabedissen A., Benck E., Roberts J., "Langmuir probe measurements in an inductively coupled plasma source," Phys. Rev. E., Vol. 55, No. 3, March 1997

[61] - Goldston, R., Rutherford, P., "Introduction to Plasma Physics," 1995

[62] – Hayakawa Y., "Measurements of Electron Energy Distributions in a 14 cm Diameter Ring-Cusp Ion Thruster," AIAA-89-2715

[63] - McKillop J. S., Forster J. C., Holber W. M., "Doppler profile measurement of Ar and Ar+ translational energies in a divergent magnetic field electron cyclotron resonance source" Appl. Phys. Lett., Vol. 55, No. 1, 1989

[64] – Herman D., Gallimore A., "Near Discharge Cathode Assembly Plasma Potential Measurements in a 30cm NSTAR-type Ion Engine Amidst Beam Extraction," AIAA-2004-3958

[65] - Herman D., Gallimore A., "Discharge Chamber Plasma Structure of a 30cm NSTAR-type Ion Engine," AIAA-2004-3794

[66] - Lieberman, M., Lichtenberg, A., "Principles of Plasma Discharges and Materials Processing," ©1994

[67] – Foster J., Patterson M., "Enhanced Discharge Performance in Ring-Cusp Plasma Source," NASA/TM-2000-209765

[68] – Simon A., Phys. Rev. 98, 317, 1955

[69] – Boeschoten F., "Plasma diffusion and rotation in a conducting container of finite length in the presence of a longitudinal magnetic field," Plasma Physics, Vol. 9, pp. 745-747, 1967

[70] – Schweitzer S., Mitchner M., "Electrical Conductivity of a Partially Ionized Gas in a Magnetic Field," Physics of Fluids, Vol. 10, No. 4, April 1967

[71] – Bohm D., "The Characteristics of Electric Discharges in Magnetic Fields," (Guthrie A., Wakerling R.) pp. 1-76, 1949

[72] – Braginskii S.I., "Transport Processes in Plasmas," Reviews of Plasma Physics, Vol. 1, pp. 205-311, 1965

[73] – Goebel D., Jameson K., Watkins R., Katz I., "Cathode and Keeper Plasma Measurements Using an Ultra-Fast Miniature Scanning Probe," AIAA-2004-3430, 40th Joint Propulsion Conference, Ft. Lauderdale, FL, July 11-14, 2004

[74] – Batishchev O., Martinez-Sanchez M., "Charge Particle Transport in the Hall Effect Thruster," IEPC 03-188

[75] - Jackson J., "Classical Electrodynamics," 2nd Edition, 1962

[76] - Medicus, G. "Theory of Electron Collection of Spherical Probes" J. App. Phys. Vol.32 Num.12 1961

[77] – Rapp D., Englander-Golden P., "Total Cross-Sections for Ionization and Attachment in Gases by Electron Impact, I. Positive Ionization," J. Chem. Phys., 43, pp. 1464-1479 1965

[78] - Specht L.T., et. al., "Electron Ionization and Excitation Coefficients for Argon, Krypton and Xenon in the Low E/N Region," JAP, V. 51, pp. 166-170, Jan. 1980.

[79] – Huba J., "NRL Plasma Formulary," NRL

- Appendix A -

Terrestrial Planet Finder (TPF) Thrust Requirements

Terrestrial Planet Finder (TPF)
Formation Rotation Thrust Requirements

Richie Wirz, Caltech/JPL
May 2004 (Updated Feb 2005)

The following investigation addresses the thrust requirements for TPF-I formation rotation maneuvers in L2 Halo orbit. Required thrust for individual thrusters is estimated by assuming four possible thruster configurations. Delta-v requirements for a given rotation maneuver are estimated. Recommendations for reducing mission delta-v are given; however, a complete mission delta-v is not calculated.

The current methodology for TPF-I formation rotations consists of many-sided polygon approximations of a circular rotation, where the transit time at each side of the polygon, Δt, is 60 seconds[1]. Currently, the assumed duty cycle is 10% at each 60-second leg of the rotation, which implies that for each "side" of the polygon there are 6 seconds of burn time, 54 seconds of quiescent time.

The choice of duty cycle has a profound effect on the thrust requirements for TPF. We demonstrate this by first defining the delta-v required for a polygon rotation trajectory (derived in Addendum) as

$$\Delta v = \frac{4Rn}{P}\sin\left(\frac{\pi}{n}\right)\left[1 + n\sin\left(\frac{\pi}{n}\right)\right] \tag{1}$$

where, P is the total time of the rotation, R is the rotation radius, and n is the number of sides of the polygon defined by $n = P/\Delta t$. The thrust required for a given delta-v and burn time is determined by

$$T = \frac{m_{sc}\Delta v}{\Delta t_{burn}} \tag{2}$$

Following References [A1] and [A2], we can use these expressions to calculate the maximum required delta-v and thrust using the fastest rotation time and radial location of the outer collector. Therefore we can calculate the maximum effective thrust per TPF-I collector as a function of duty cycle, using the parameters

Collector mass: m_{sc} = 1622.47 kg
Outer Collector radial location: R = 80 m
Total rotation time: P = 480 min

where duty cycle is defined as $\Delta t_{burn}/P$. The results of this calculation are shown in Figure A-1. According to the plot, approximately 33 mN of *effective* thrust per spacecraft is required for a 10% duty cycle while ~3mN of thrust is required for a 100% duty cycle, i.e., continuous thrust. Since these results show the maximum *effective*

A-2

thrust per *spacecraft*, we must look at the possible thruster configurations to determine the maximum thrust required *per thruster*.
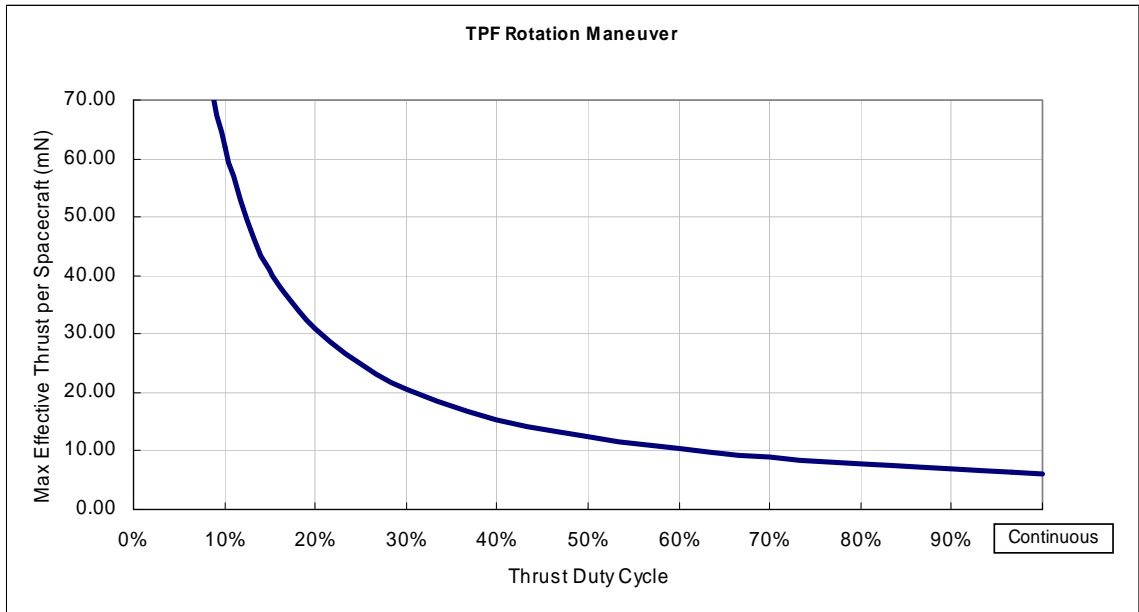
Figure A-1.

Thruster Configuration

Each spacecraft will be outfitted with four groups of four thrusters (16 thrusters total) and must be able to perform all mission functions with the loss of any single thruster group [A2]. This suggests that each spacecraft must be able to fully operate with three of the four thruster groups at any given time. Reference [A1] assumes that each thruster should be canted 45° away from the spacecraft to prevent spacecraft self-contamination and contamination of neighboring spacecraft.

For a fixed four-thruster group it can be assumed that at any given time the desired thrust direction is in-line with a single thruster (the component in the plane of rotation) or shared by two thrusters. The former orientation yields a conservative estimate of required thrust while the latter constitutes a conservative approximation of delta-v. Therefore, in the following analysis the maximum thrust requirement is approximated by assuming the use of three thrusters oriented along the desired thrust direction. The maximum delta-v for the fixed thruster configuration is estimated assuming six thrusters oriented at 45° with respect to the desired thrust direction.

In the case of a gimbaled thruster arrangement, both the thrust and delta-v requirements are approximated by three thrusters oriented in-line with the desired

A-3

thrust direction. As a result, the maximum thrust requirements will be identical for the fixed and gimbaled configurations.

Thrust and Delta-v per Rotation Maneuver

Figure A-2 shows conservative thrust requirements per single thruster versus thrust duty cycle. These results show that the max thruster requirement increases to over 10 mN if burn times on the order of six seconds are required. The conservative delta-v required for the different configurations is shown in Figure A-3 (the delta-v that may possibly be required to correct for out-of-plane canted angle thrust is ignored).
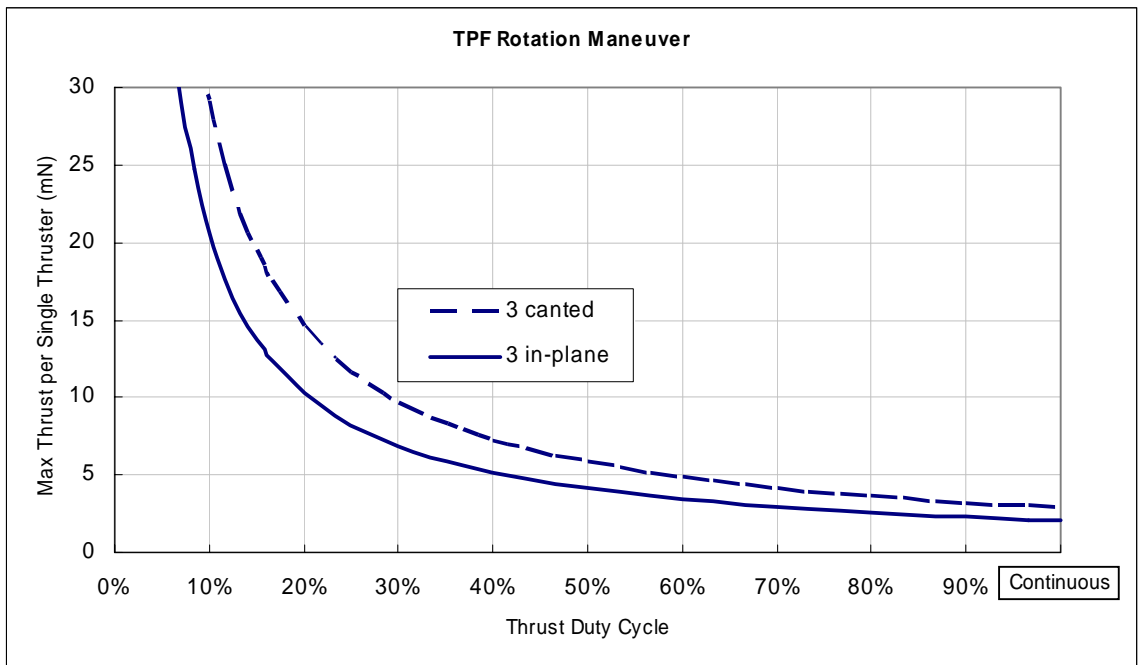
Figure A-2.

Figure A-3.

A-4
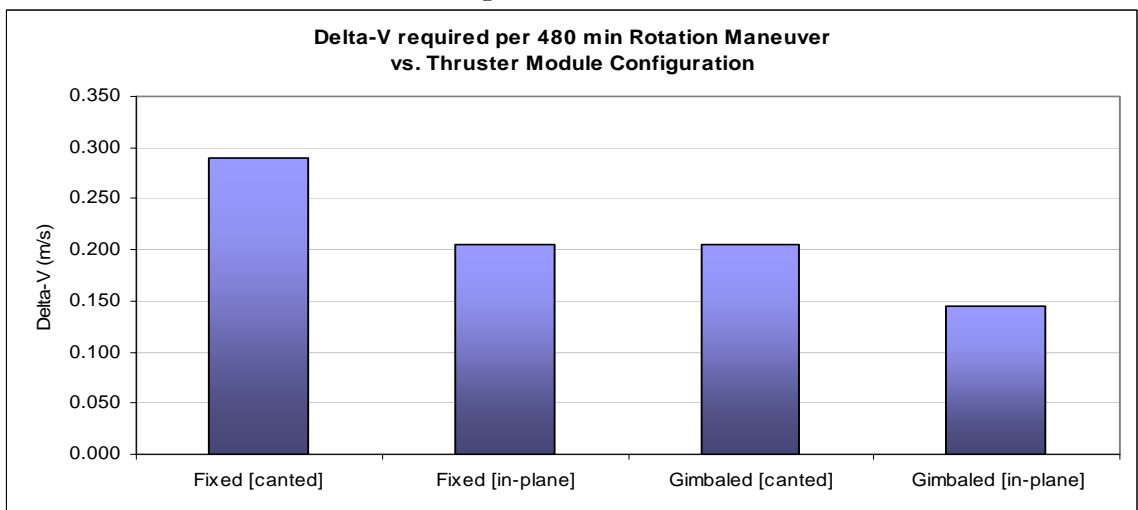
Discussion

Thruster Canting
Thruster canting will decrease the effective thrust for a given thruster by ~30%. This requirement also introduces an out-of-plane force that will likely require corrective thrust maneuvers to maintain the L2 Halo orbit. Corrective thrust maneuvers, if in the direction of the sensitive optics, may actually result in increased contamination risks. Therefore, it is desirable to use thruster types that do not require canting, such as those using non-contaminating propellant.

Gimbaled Thruster Configuration
Gimbaled thrusters will reduce mission delta-v and mitigate contamination by reducing the amount of superfluous thrust.

Low-Thrust Trajectory
Figure A-2 shows that the max thrust requirement per single thruster is only ~2mN if continuous thrust is used (i.e., duty cycle = 100%). If a continuous low-thrust trajectory, i.e., circular, is used then it is important to that the propulsion option provide low-noise thrust so that measurements can be made during operation.

References:

[A1] Mitchell, S., "TPF Delta-V Requirements," JPL Internal Document from Ball Aerospace, Feb 2, 2004
[A2] Hamlin, L., "TPF Current Status - Overview and Propulsion Needs," JPL Presentation, March 4, 2004
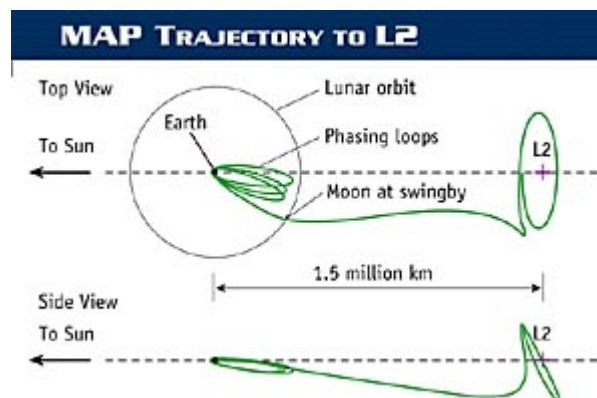
<u>Addendum. Polygon Trajectory Analysis</u>

The following is a derivation of the delta-v for a single polygon-shaped rotation. For the polygon trajectory it is assumed that the spacecraft follows the perimeter of the polygon perfectly. A more detailed trajectory analysis will yield only minor changes to the results.

n = number of sides of polygon

P = time for rotation maneuver [s]

R = radius of rotation

Derivation

$$\Delta\theta = \frac{2\pi}{n}$$

$$\Delta x = 2R\sin\left(\frac{\Delta\theta}{2}\right)$$

$$\Delta t = \frac{P}{n}$$

$$\Delta v_i = \frac{\Delta x}{\Delta t} = \frac{2Rn}{P}\sin\left(\frac{\pi}{n}\right)$$

$$\Delta v_m = 2\Delta v_i \sin\left(\frac{\Delta\theta}{2}\right) = 2\Delta v_i \sin\left(\frac{\pi}{n}\right)$$

$$\Delta v = 2\Delta v_i + \Delta v_m n = 2\Delta v_i\left[1 + n\sin\left(\frac{\pi}{n}\right)\right]$$

$$\therefore \Delta v = \frac{4Rn}{P}\sin\left(\frac{\pi}{n}\right)\left[1 + n\sin\left(\frac{\pi}{n}\right)\right]$$

$$\lim_{n\to\infty}[\Delta v] = \frac{4R\pi}{P}[1 + \pi]$$

Note: As expected, Δv for ($n \to \infty$) is identical to the Δv for a circular trajectory

$$\dot\theta = \frac{2\pi}{P}$$

$$\Delta v_i = \dot\theta R = \frac{2\pi}{P}R$$

$$F = m\Delta v_i\dot\theta = mR\left(\frac{2\pi}{P}\right)^2$$

$$\Delta v_m = \frac{FP}{m} = \frac{4\pi^2 R}{P}$$

$$\Delta v_{circular} = 2\Delta v_i + \Delta v_m = \frac{4R\pi}{P}(1 + \pi) = \lim_{n\to\infty}[\Delta v]$$

A-6
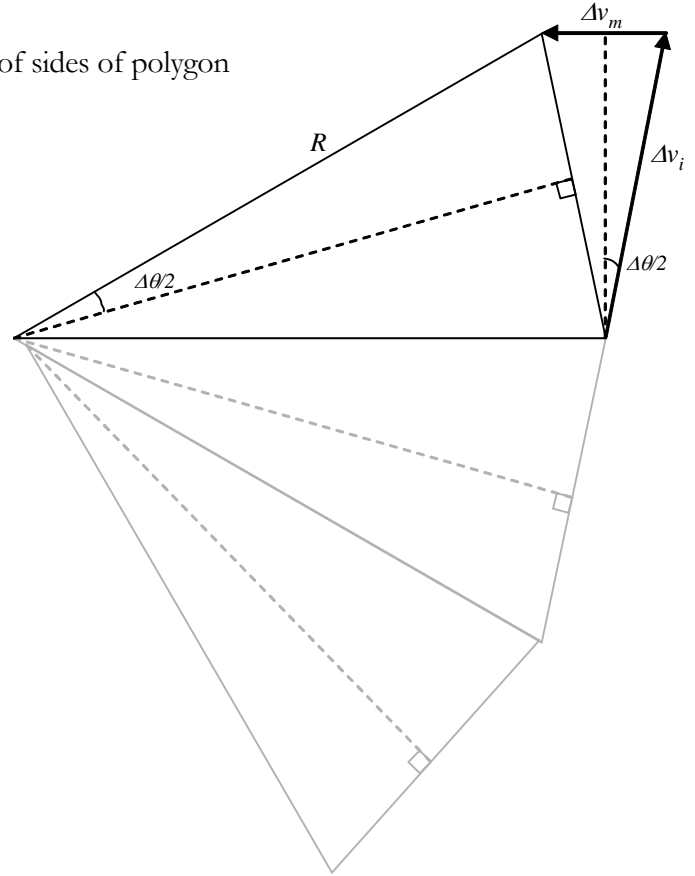
- Appendix B -

Preliminary Miniature Ion Thruster Tests

Overview of Appendix B

The current development of many microspacecraft concepts increases the need for effective micropropulsion systems. Micro-Ion propulsion offers advantages over other low-thrust propulsion concepts, such as Field Emission Electric Propulsion (FEEP) and Pulsed Plasma Thrusters (PPTs), and merits further development. A micro-ion engine assembly was developed at Caltech/JPL for testing and optimization of various system parameters. This project applies the many design optimization techniques historically used for larger ion engines to the micro-ion engine scale. Theoretical, empirical, and semi-empirical knowledge from previous ion thruster studies was used to develop and analyze the configurations used herein. At the micro-ion scale the discharge chamber performance is an important issue due the large surface-to-volume ratio of the chamber. A discharge chamber of 3cm diameter was deemed sufficiently small to experimentally assess the behavior of miniature ion thrusters. Several magnetic field configurations, including line cusp and strongly divergent, were tested to determine their behavior at this smaller operating scale. The accelerator system is composed of two micro-machined molybdenum grids. Concurrent efforts in field emission array (FEA) cathodes should supply a large increase in the overall integrity of the design. Operational parameters were optimized for each configuration independently to allow performance comparisons based primarily on propellant utilization, ion production cost, and total efficiency. Several system parameters were adjusted in an effort to find the best performance possible for each configuration tested. These parameters included cathode and anode voltage, accelerator grid voltage, and xenon propellant feed rate. To simulate space-operating conditions, tests were performed using a vacuum chamber. The results suggest that the performance of the two-grid accelerator system is not limiting the small thruster performance for the relatively low operating conditions used. Some aspects of the magnetic field and anode designs demonstrated relative increases in performance; however, further improvements to these, and other designs, are necessary to achieve desirable performance levels. Several magnetic field designs, in addition to those tested herein, merit further investigation.

Table of Contents

Introduction

Background and Motivation

With the advent of many new microspacecraft concepts and mission initiatives, the need for effective micropropulsion systems is significant. A micro-ion thruster offers a unique combination of high specific impulse (I_{sp}), high efficiency, low thrust, and benign propellants, with the capability for a continuous mode of operation[1]. This combination lends itself well to many possible missions such as interferometry and large inflatable craft. An interferometry mission requires precise control of a constellation of craft without the possibility of significant self or craft-to-craft propellant contamination. A large inflatable craft may require a quasi-continuous, low-level thrust to offset solar pressure induced disturbance torques. Proposed miniaturized spacecraft components and sensors are sensitive to propellant contamination levels considered acceptable for components of larger spacecraft, thus increasing the need for small propulsion systems using benign propellants.

Micro-Ion propulsion offers the advantage of benign propellants and the potential for greater power efficiency in comparison with other low-thrust propulsion concepts such as Field Emission Electric Propulsion (FEEP) and Pulsed Plasma Thrusters (PPTs). However, there are many difficulties associated with a miniaturized xenon ion engine design. The typical anode diameter of current ion thrusters ranges from over 30cm to no less than 10cm. Ion engines require gaseous discharge containment and inherently suffer from increased ion wall losses at greater surface-to-volume ratios indicative of smaller discharge chambers. Consequently, maintaining desirable plasma discharge efficiency presents a formidable challenge. Hollow cathodes, typically used in larger ion thrusters, have not been scaled to the sizes and power consumption values necessary for an efficient micro-ion thruster. The development of a small low-power cathode is integral to miniaturized ion thrusters[2]. Previous studies sufficiently addressed the issue of fabricating miniaturized accelerator grids[1]. Theoretically, the performance of the accelerator grids scales favorably with decreasing size; however, the performance of smaller grid sizes at the required high voltages is still unknown. A micro-ion thruster also requires the development of appropriately sized power conditioning units and propellant feed system.

Objective

This report investigates the performance of the discharge chamber and ion accelerator grids of a 3cm diameter micro-ion thruster and addresses the unique operational and performance issues of an ion engine at this scale. The Jet Propulsion Laboratory (JPL) originally developed the micro-ion engine assembly used herein. This assembly utilizes micro-machined exit grids and cathodes and is capable of testing a range of discharge chamber configurations. Previous efforts were unable to assess the micro-ion engine's capabilities since they could not get the thruster to run properly[3]. Consequently, the earliest part of this investigation was devoted to reconciling fundamental performance pathologies.

Data Analysis

The performance of the thruster was assessed using the ion engine performance relations shown in the Theory and Analysis section of this report. For each discharge chamber configuration tested, the various electrical operating parameters for the thruster were adjusted (for a given propellant flow rate) until optimal performance values are found. The locus of operating points near the best performance for each configuration is used to compare their relative efficiency of the configurations.

Equipment and Procedure

The experiment was performed at JPL, in Building 148 of the Advanced Propulsion Technology Laboratories. The testing facility used to conduct the experiment, shown in Figure 1, was composed of four primary systems:

1) Thruster assembly
2) Vacuum chamber (and cooling supply)
3) Power conditioning and diagnostics
4) Propellant (Xe) feed system
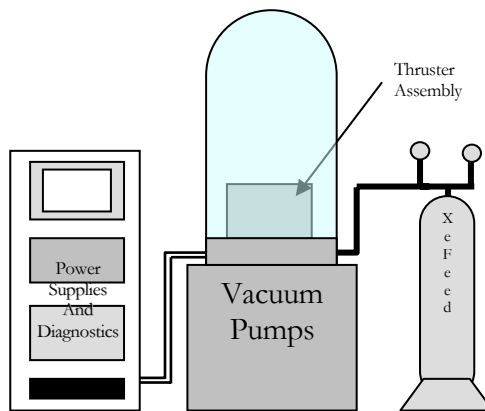
Figure 1. Primary Experimental System

The components of the systems are listed in Table 1.   The Experiment Equipment section (Figures B-1 – B-7)contains pictures of the main components and the experimental setup.

The micro-ion thruster assembly included the thruster, an isolation box, and a neutralizer cathode. The "thruster" was essentially a 3cm diameter discharge chamber, two molybdenum accelerator grids, propellant feed lines and diffusion plate, and discharge and neutralizer cathode filaments. Please refer to the Theory and Analysis section of this report for a complete description of the functional significance of these components. An isolation box prevented ambient electrons from impinging on the thruster's exterior components. The box had a small opening for thrust extraction and

a stand to hold the neutralizer cathode, as shown in Figure 2. The propellant feed line and electrical leads to the thruster were located on the opposite side of the box. The box could be opened to allow access to the thruster.
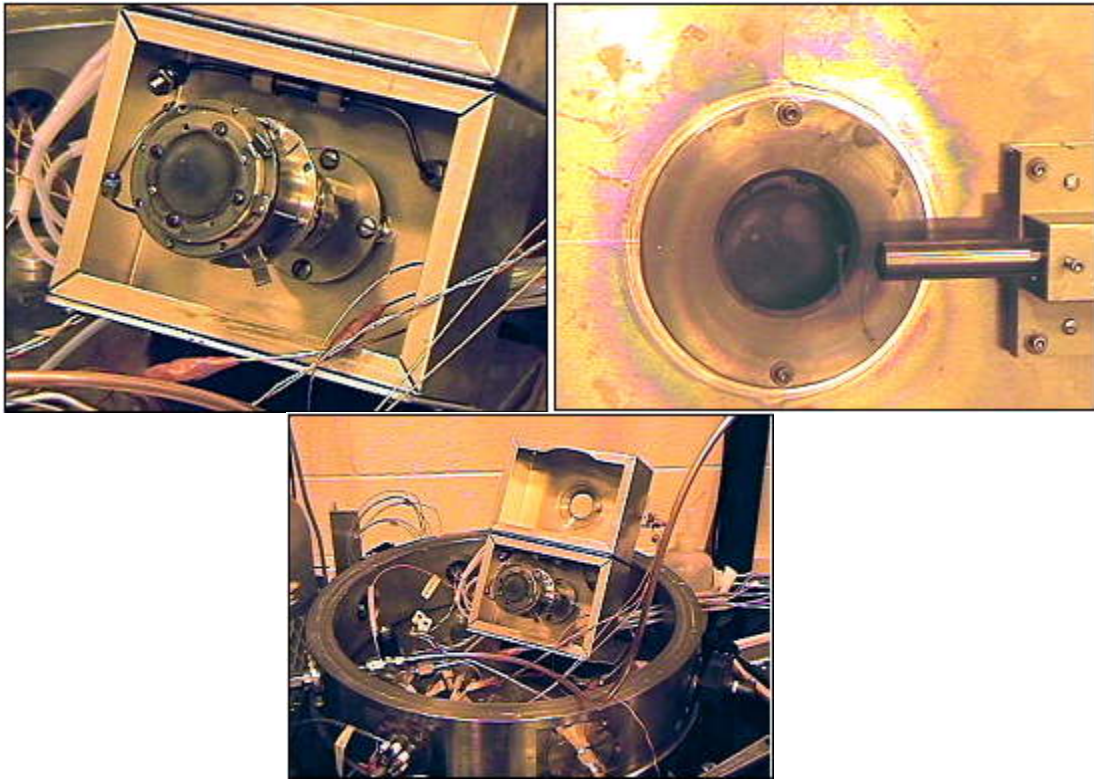
Figure 2. Thruster Assembly

A mechanical diffusion pump tandem assembly created the vacuum environment, while an in-house water-cooling supply loop cooled the diffusion. The vacuum was maintained within a ~1.2 m tall / 0.6m diameter glass dome. Interfaces for the vacuum pumps, electrical power supply, and diagnostics were located at the base of the chamber (see the Experiment Equipment section).

A general schematic of the electrical system and associated diagnostics is shown in Figure 3. The specific components used are described in Table 1. A discussion of the functional significance of these components and their interrelationship is contained in the Theory and Analysis section of this report.

The propellant feed system was composed of a pressurized xenon (Xe) supply tank, digital monitor, flow valve, rate monitor, and the associated control devices. There was an inherent lag between the time the flow rate was adjusted and the time the desired flow rate was achieved. The components of the feed system are listed in Table 1 and shown in Addendum B.
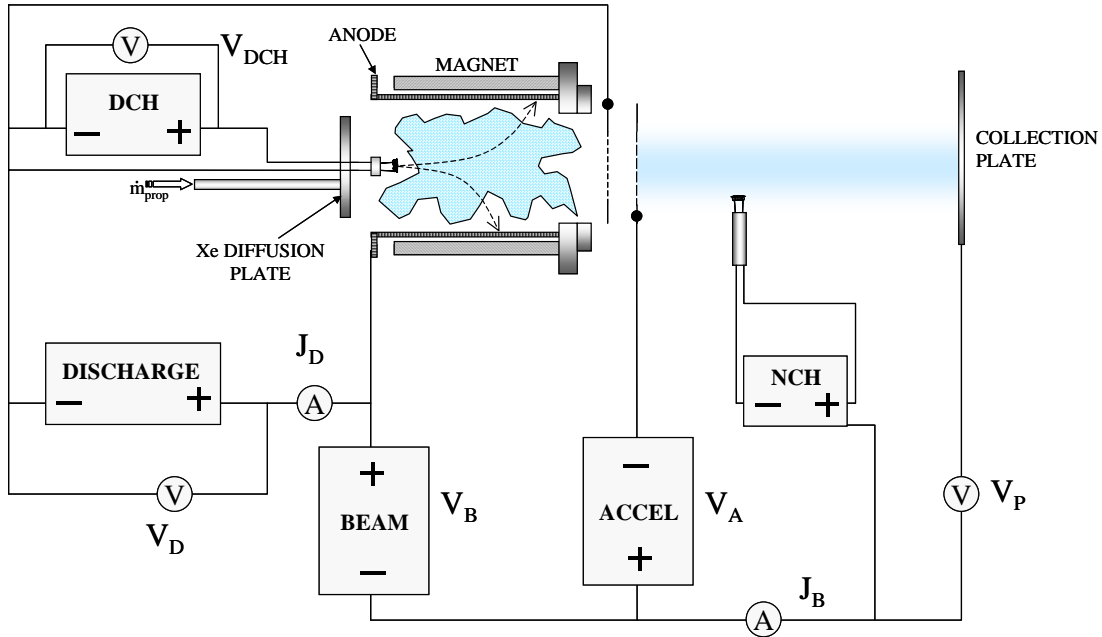
Figure 3. Electrical Diagram of the Thruster, Power Supplies, and Digital Diagnostic Equipment

Table 1. Experimental System Components

Equipment	Description
Vacuum Chamber:	
Vacuum Maintenance	Veeco RG-3A Diffusion Pump Assembly
High Pressure Gauge	Veeco Instruments Inc. TG-70, TC Gauge Control
Vacuum Pressure Gauge	Granville-Phillips 358 Micro-Ion Controller with Micro-Ion Gauge
Power Supply and Conditioning:	
Beam Power Supply [BEAM]	Hipotronics HV/DC Model 801-1A/DS13-827 Max: 1kV/ 1A [Max DC]
Acceleration Grid Power Supply [ACCEL]	JPL Assembled DC Power Supply - 1kV / 100mA [Max]
Neutralizer Cathode Heater [NCH]	Hewlett-Packard 6284A DC Power Supply - 115V/2A [Max]
Discharge Cathode Heater [DCH]	Hewlett-Packard 6290A DC Power Supply - 120V/2A [Max]
Discharge Power Supply [DISCHARGE]	JPL Assembled DC Power Supply - 125V / 5A [Max]
Multimeters	Fluke 787 Process Meter - 1000V, 440 mA digital multimeter
Propellant Flow Control:	
Flow Meter	UNIT Instruments URS-20 O-SCCM
Flow Valve Control	MKS Instruments Type 250 Solenoid Valve
Flow Monitor	UNIT Instruments Digital Metal Z-Seal Model 1661 500 max PSI / 3,500 kPa

Experimental Procedure

Testing of the micro-ion thruster was typically done in the following manner: The thruster configuration to be tested was first assembled and then tested for proper electrical conductivity and isolation. The thruster was then mounted within the isolation box, inside the vacuum chamber, and connected to the power supply leads through the vacuum chamber interfaces. The system was once again tested for proper electrical conductivity and isolation before the pump down procedure is initiated. Once the chamber was pumped down to approximately 10^{-4} Torr, the voltages of the thruster components were gradually increased to reasonable operating voltages. The thruster was often run at low voltages for at least an hour prior to data collection to "burn-off" any potential sources of failure at high voltages.

Since the performance characteristics of the different thruster configurations can vary significantly, the first test iterations were used to determine the general behavior of the thruster. Subsequently, performance curve data were obtained through a systematic approach of changing only one parameter at a time. From the tests performed in this investigation it was found that the propellant flow rate is best kept constant while other parameters are changed since the flow meter and control valve system possesses inherent lag times that can increase data collection times significantly. The phenomenon of electron back-streaming, as described in the Theory and Analysis section of this report, can generate erroneous data points. As a result, the accelerator grid voltage was varied to determine the onset of electron back-streaming and validate datum sets.

Calibration

The calibration for the propellant flow control and meter tandem was performed using a JPL-built four-channel propellant feed calibration system, with LabView for calibration data collection. The flow and flow valve voltage response was determined three separate times at every 0.300 sccm (cm^3/min) from 0.300 to 1.500 sccm. The propellant line response time was 60 minutes to accommodate the low flow rates. The flow meter display was then calibrated by comparing the voltage response of the flow control valve with a range of flow meter display values. The voltages from both calibration efforts were then used to determine the actual flow rate in sccm corresponding to given display values. The results of this calibration are shown in Figure 4. The digital multimeters used for the power system diagnostics had a 0.1% DC voltage accuracy and a 0.05% DC current accuracy and were regularly calibrated on-site.
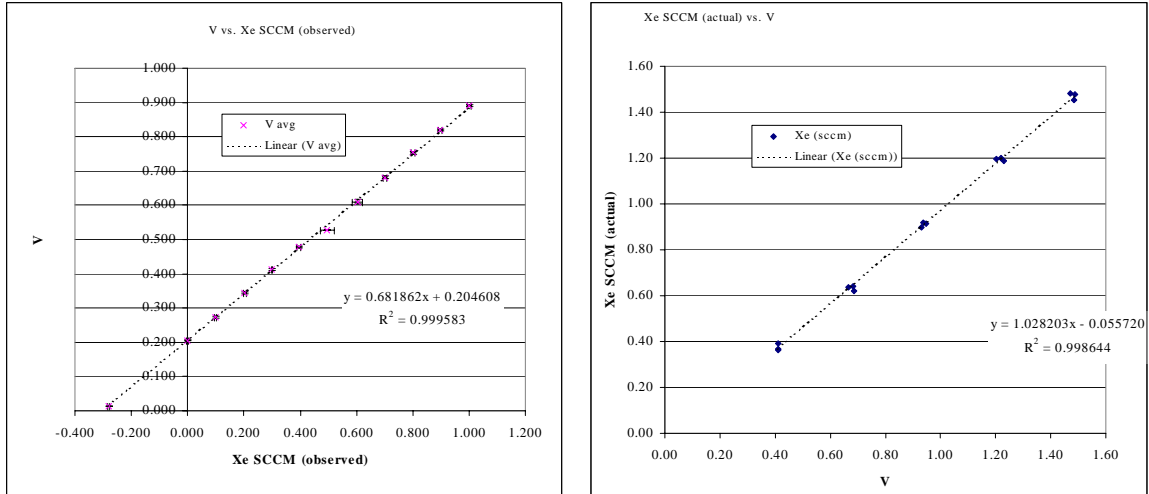
Figure 4. Propellant Mass Flow Calibration

Theory and Analysis

The operation of an ion thruster is best regarded as the culmination of three main processes. A schematic with regard to these processes is shown in Figure 5. The first process involves the generation of highly positive voltage plasma within the discharge chamber. This is achieved by the introduction of energetic electrons to a gaseous xenon propellant that is subsequently ionized through a number of particle interactions. Since these positive xenon ions are at a voltage on the order of +1000V with respect to space potential, considerably high velocities and high thruster specific impulse (Isp) values can be obtained. To properly contain the plasma and the energetic electrons, and to help focus the ion beam, a pair of electrostatic ion "acceleration" grids is placed at the exit of the thruster[4]. The positive ions that exit the thruster through the grids constitute the high velocity beam that is used to generate the thrust. However, this current of positive charge will cause the thruster and craft to quickly obtain an overall negative charge. As a result, a neutralizer cathode is placed near or in the beam to emit electrons into the positive ion beam. This process will keep the spacecraft from obtaining an overall negative charge while also preventing an increase in positive space-charge potential just outside of the thruster exit. It is also important to note that this neutralization process creates a relatively benign, quasi-neutral exhaust, especially in the case of noble-gas propellants such as xenon[5].
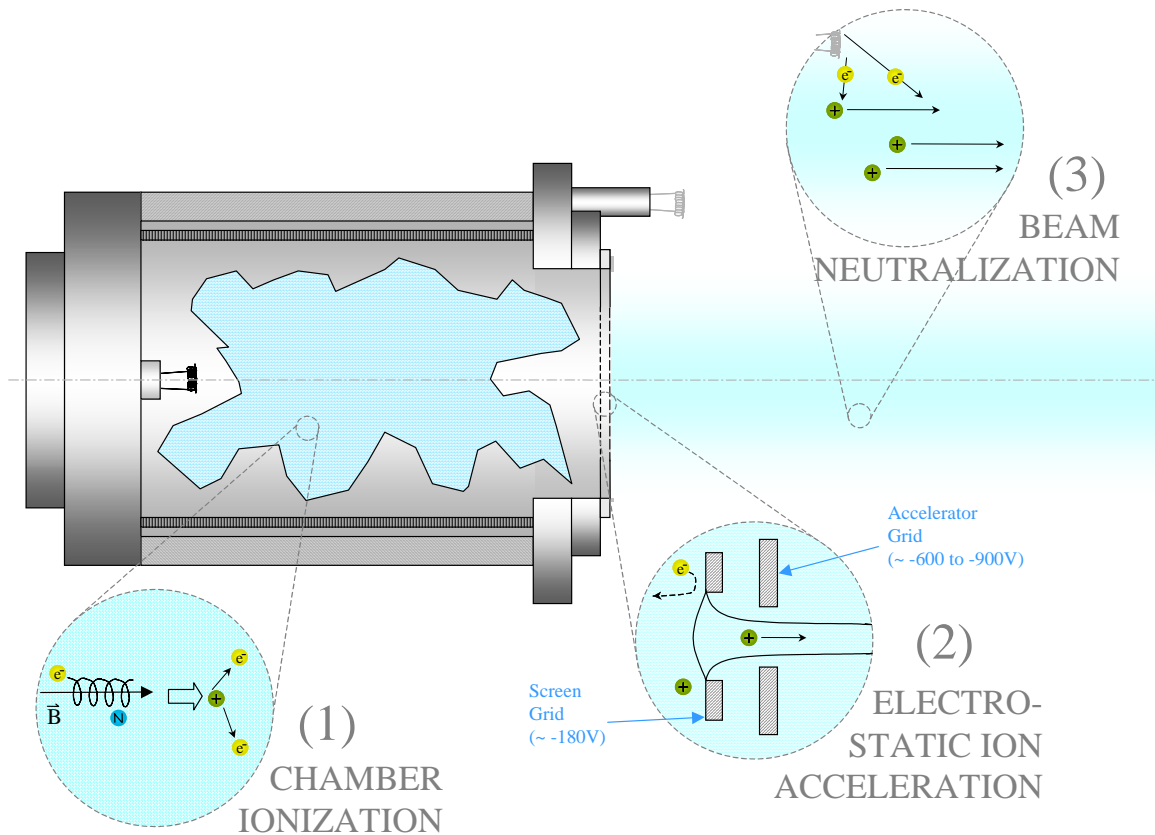
Figure 5. Ion Thruster Function

Although the exit grids are called the "accelerator" system, it is actually the beam voltage supply that raises the potential of the engine to an order of +1000V above ambient space potential that provides the acceleration potential[5]. Nonetheless, the screen and accelerator grids are an important part of the thruster operation. As shown in Figure 6, the screen grid is responsible for focusing the ions through the smaller accelerator grid apertures. The relatively negative voltage of the screen grid with respect to the chamber plasma attracts ions to the exit while preventing electrons from leaving the chamber. Essentially, the screen grid is relatively transparent to ions and not to electrons. The accelerator grid prevents back-streaming of neutralizer electrons into the highly positive discharge chamber. Electron back-streaming appears as an increase in the measured beam current, which results in false thrust and performance predictions in the experimental setup used in this investigation. Therefore it is important to assure electron back-streaming is not occurring for the voltages used. The accelerator grid apertures are typically smaller than the screen grid apertures to mitigate the loss of neutrals from the discharge chamber.
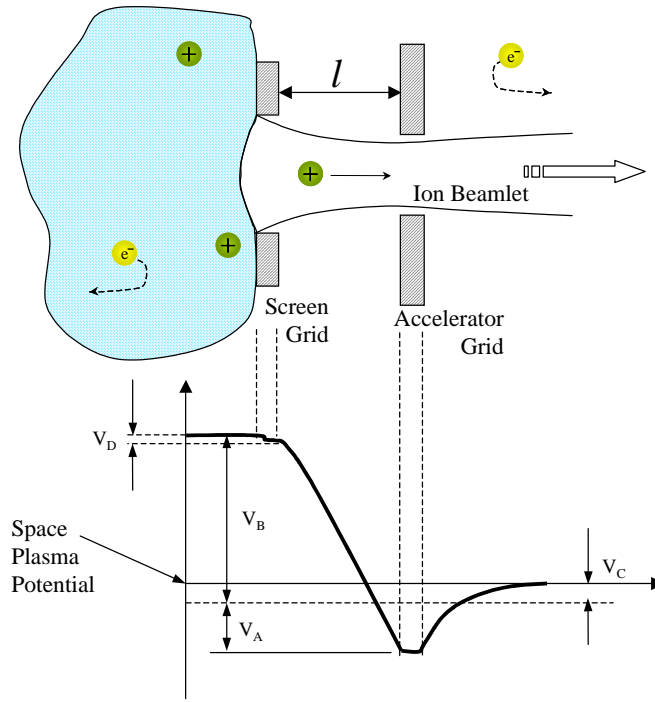
Figure 6. Ion Accelerator System

The ion engine is inherently a space-charge limited system[4]. With regard to the Child-Langmuir Law:

$$j = \frac{4\varepsilon_o}{9} \sqrt{\frac{2e}{m_i}} \left(\frac{(V_B + V_A)^{3/2}}{l} \right)$$

it can be seen that there is maximum current that may be drawn through a distance l for a given potential difference. There are also physical limitations on maximum beamlet current, termed the "perveance" limit.[4]

To relate and understand the discharge chamber performance, it is common to compare the amount of energy needed to make a single beam ion versus the propellant utilization efficiency[5]. If we define the engine electrical efficiency, η_E, and total engine power, P_E, as

$$\eta_E \equiv \frac{J_B V_B}{P_E} \qquad\qquad P_E = J_B V_B + J_D V_D + P_O$$

where:
J_B – beam current

B-8

V_B – beam voltage
J_D – discharge current
V_D – discharge voltage
P_o – minor miscellaneous power

Combining these relationships we can determine an expression that expresses the energy per beam ion, which is inversely proportional to the engine efficiency:

$$\eta_E = \frac{J_B V_B}{J_B V_B + J_D V_D + P_O} = \frac{V_B}{V_B + \varepsilon_B + \dfrac{P_O}{J_B}}$$

$$\varepsilon_B \equiv \frac{J_D V_D}{J_B} \qquad \underline{\text{Beam Ion Energy Cost (eV/ion)}}$$

We can see from the following equation that the propellant utilization, η_u, is directly proportional to the thrust, T, such that

$$T = \dot{m}_T \eta_u u \qquad\qquad u = \sqrt{\frac{2eV_B}{m_i}}$$

$$\eta_u \equiv \left(\frac{J_B}{\dot{m}_T}\right)\left(\frac{\dot{m}_i}{e}\right) \qquad \underline{\text{Propellant Utilization Efficiency}}$$

An effective way of relating chamber performance is to plot the beam ion energy cost, ε_B, versus the propellant utilization efficiency, η_u, as shown in Figure 7.
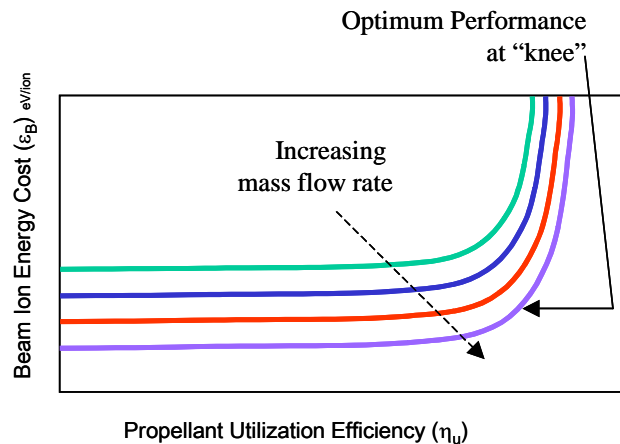
Figure 7. Typical plot of ε_B vs. η_u

Since the thrust is proportional to η_u, we see from the total efficiency equation that high η_u is desirable for good overall performance of the thruster:

$$\eta_T \equiv \frac{T^2}{2\dot{m}_T P_E}$$

where:

T - thrust

$\dot{m}_T$ - total propellant mass flow

P_E - engine power
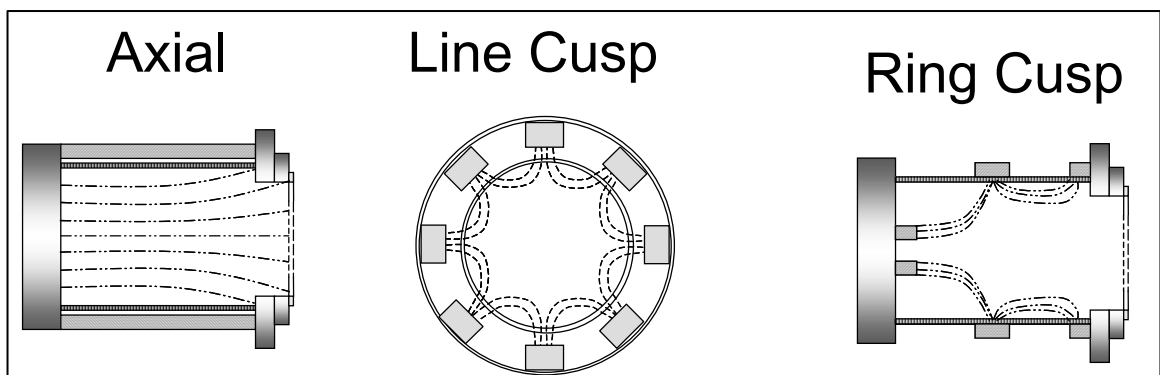
Figure 8. Magnetic Field Configurations

Due to the relatively high surface-to-volume ratio of the micro-ion chamber the electron residence time should be maximized to increase the probability that the electron will ionize the propellant before being collected by the anode. Assuming a stable discharge, the interaction of an externally applied magnetic field and the electron will typically increase the electron residence time and discharge efficiency. Three main categories of externally applied magnetic field configurations are shown in Figure 8. Due to the size and orientation of the available magnets, the ring-cusp configuration could not be incorporated into this investigation.

The strength of a magnetic field drops very quickly with distance from the poles by the relation[6]:

$$B = \frac{B_r}{\pi}\left[\tan^{-1}\left(\frac{d+l}{tw}\sqrt{t^2+w^2+(d+l)^2}\right) - \tan^{-1}\left(\frac{d}{tw}\sqrt{t^2+w^2+d^2}\right)\right]$$
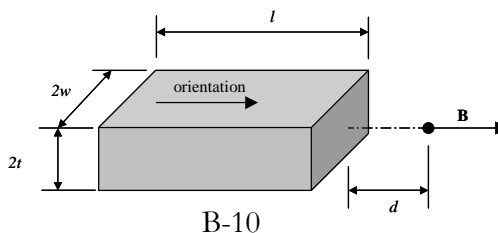
B-10

In addition, the strength of a magnet decreases with increasing temperature up to the maximum operating temperature, where it becomes completely demagnetized[7]. The distance and temperature behavior of the B-field of a rectangular samarium cobalt (SmCo) magnet of identical dimensions to those used in the thruster is shown in Figure 9. From this plot we see that distance from the magnet is a more important issue than temperature as long as the maximum operating temperature is not reached.
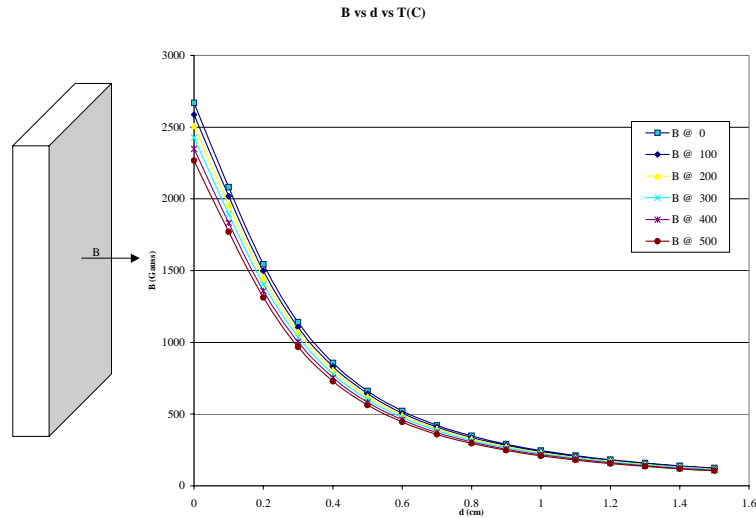
Figure 9. Variation of Magnetic Field with Distance and Temperature

Error Calculation

The greatest source of error in the micro-ion thruster tests was the propellant mass flow rate readings. The inaccuracies of the flow meter were especially pronounced at the relatively low flow rates used for the tests. The multimeters used for monitoring many of the voltage and current outputs contribute a fractional uncertainty of 0.1% for DC voltage and 0.05% DC current readings. The readings from the power supplies contribute error within one-half the resolution of their gauges[8]. The variability in mass flow rate far outweighed the error associated with the power system diagnostics. Table 2 shows the fractional uncertainties associated with the flow rates used in the tests. The fractional uncertainties of the thruster performance parameters, considering the flow meter and multimeters used, are shown in Table 2.

Table 2. Fractional Uncertainty for Performance Parameters

Xe mg/s	Fractional Uncertainty					
Actual	Xe mg/s	eta prop	Eb	Pwr	T	eta total
0.015	3.88%	3.88%	1.00%	0.26%	1.94%	5.49%
0.022	2.67%	2.67%	1.00%	0.26%	1.34%	3.79%
0.029	2.71%	2.71%	1.00%	0.26%	1.36%	3.85%
0.036	2.74%	2.74%	1.00%	0.26%	1.37%	3.89%
0.043	1.38%	1.38%	1.00%	0.26%	0.69%	1.97%
0.050	2.18%	2.18%	1.00%	0.26%	1.09%	3.09%
0.057	8.69%	8.69%	1.00%	0.26%	4.35%	12.29%
0.063	5.27%	5.27%	1.00%	0.26%	2.63%	7.46%
0.070	1.68%	1.68%	1.00%	0.26%	0.84%	2.39%
0.077	1.40%	1.40%	1.00%	0.26%	0.70%	2.00%
0.084	1.52%	1.52%	1.00%	0.26%	0.76%	2.17%
0.091	1.30%	1.30%	1.00%	0.26%	0.65%	1.86%

Results and Discussion

The magnetic field configurations tested are shown in Figure 10. In the following discussion, the performance of each configuration is assessed using plots of ε_B vs. η_{ud}. The legends in the plots indicate the mass flow rate, M, in units of mg/s. The configurations are also compared jointly on a final plot.
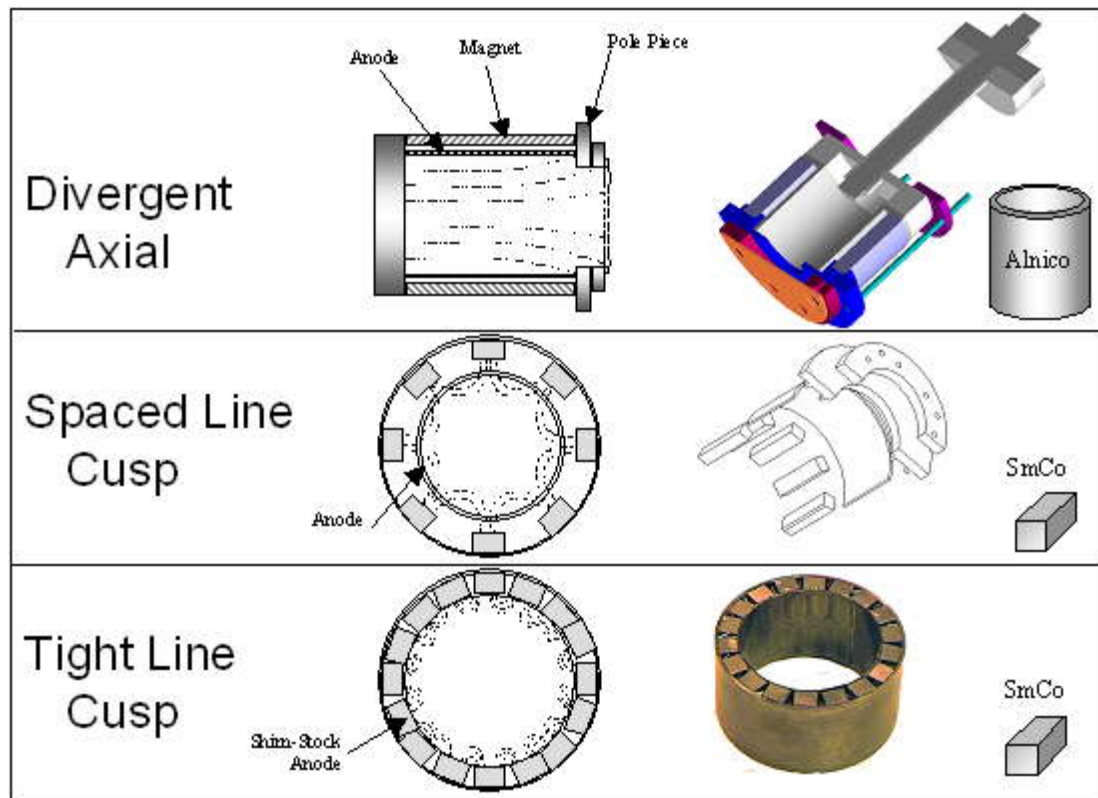
Figure 10. Magnetic Field Configurations Used During Tests

The first tests were performed using a divergent axial configuration using an Alnico-5 magnetic ring and a pole piece, pictured in Figure 10. This configuration was used to determine the general behavior of the experimental setup and to resolve issues associated with the cathode design. The earliest tests were usually cut short by the failure of the discharge or neutralizer cathode. Figure 11 shows the data collected during the tests using the initial cathode design (cathode design is discussed below) at beam voltages typically around 700V. Though some of the performance values are relatively good when compared with later tests, it is clear from the plot that the behavior of the thruster is quite unpredictable and does not follow typical ion engine performance trends. During the data collection for these test it was difficult to determine definitive operating points since the performance values being recorded

would drift considerably and the values attained at many of the operating points were not repeatable.
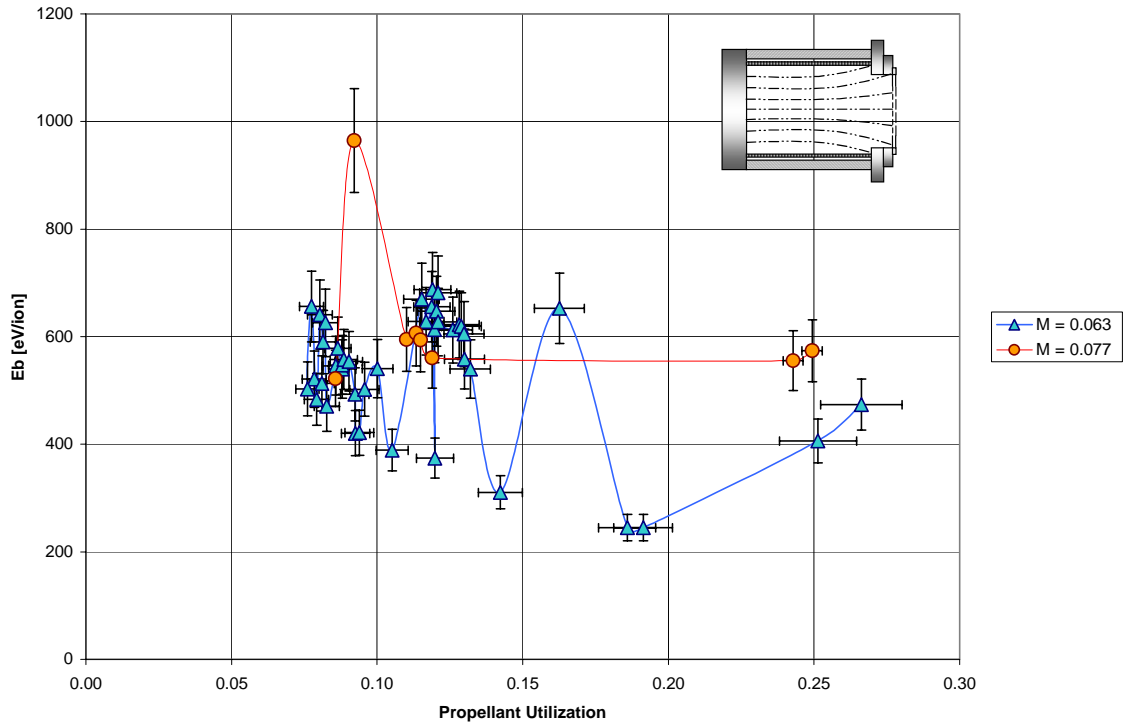
Figure 11. Axial Magnetic Field with Initial Filament Design [Test A]

It is clear from these initial results that a systematic assessment of the thruster's performance is almost impossible without a more robust cathode design. Consequently, a new cathode design was developed. The initial cathode design used a continuous 0.005 mm diameter tungsten wire that comprised both the leads and the filament coils. This design consistently failed at the leads since the rigidity of relatively thin filament was not sufficient for carrying the necessary current and supporting the filament coil for reasonable test times. A more robust filament was developed by using two 0.010mm tungsten wires for the leads that were capable of carrying the necessary current while supporting the 0.005mm diameter tungsten filament coil. As with conventional light bulbs, the smaller wire was used for the coil since the power required to cause 0.010mm tungsten to emit the necessary electrons is well beyond the capacity of the available power supplies and would likely overheat the discharge chamber. In addition, the discharge cathode interface was altered to accommodate two cathodes for redundancy. The dual cathode configuration also allowed for quick performance analyses with respect to axial cathode placement. The 0.005mm diameter filament generally failed above discharge heater currents above 2.41A, so the extent of the data herein reflects this limit.

The new cathode design was used with the axial magnetic field configuration and the performance of the thruster with the new filament was quite predictable as can be seen

by comparing figures 11 and 12. The expected trends in Figure 7 do not follow those in Figure 12. This discrepancy may be due to the fact that ion engines are rarely run at such low η_u values. The relatively poor performance values in Figure 12 are in part due to the lower beam voltages (450-550V) used for these data. The beam voltage was kept low to avoid grid shorting that occurred at higher voltages. This voltage standoff problem was resolved during the tight line cusp testing. Another likely reason for the poor performance was that the cathode was set off the chamber's axis of symmetry and far forward in the chamber. The off-axis placement causes a decrease in the ion efficiency, especially in such a small chamber. As will be shown in the following discussion, placing the discharge cathode on-axis and further aft in the chamber, closer to the screen grid, resulted in better performance for the cusp designs. Such a change in cathode location would likely benefit the divergent axial configuration as well.
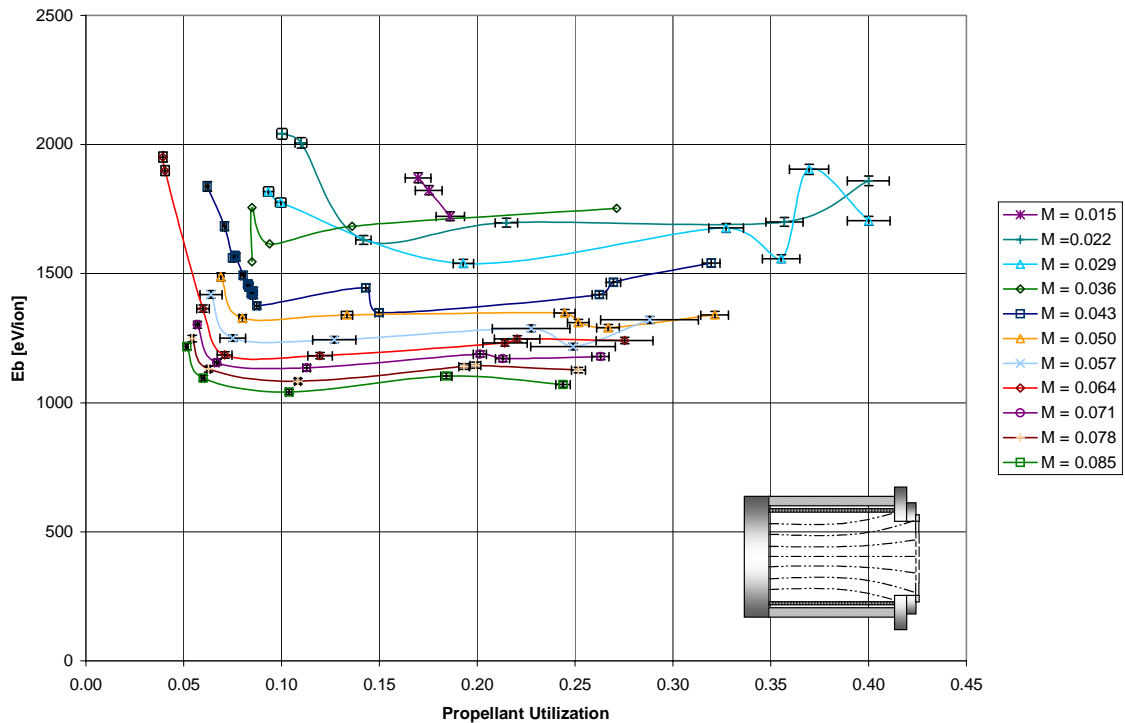
Figure 12. Axial Magnetic Field with Robust Cathode [Test B]

A spaced line cusp design was developed using samarium cobalt (SmCo) magnets as shown in Figure 10. The original motivation for spacing the magnets was to create a B-field that reached far into the chamber to affect electron behavior throughout the chamber volume. However, the spaced line cusp configuration performed relatively poorly, as can be seen in figures 13 and 14. The results in Figure 13, with respect to Figure 14, reflect the increased performance of the thruster due to placing the discharge cathode further aft. Placing the cathode further aft in the chamber encourages ionization closer to the screen instead of forward in the chamber where the ion is less likely to exit the chamber before being lost to the anode or recombining to

form a neutral. The poor performance of this configuration is most likely due to the distance of the anode from the magnets. This will result in a relatively weak magnetic field at the anode, which will not encourage ionization or the magnetic mirror effect[9]. In Figure 15, the regions where the majority of electron current was collected are clearly shown as black lines on the interior of the anode. Since the magnetic field strength at these points is small, it is unlikely that favorable magnetic confinement of electrons at the anode existed.
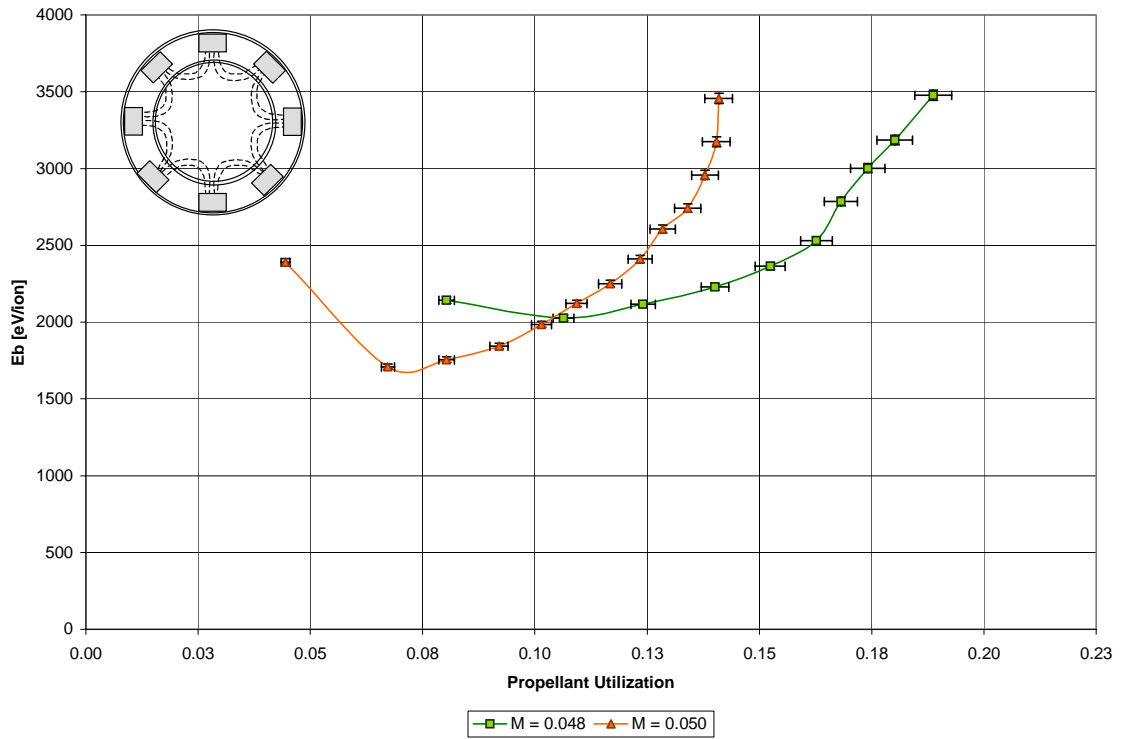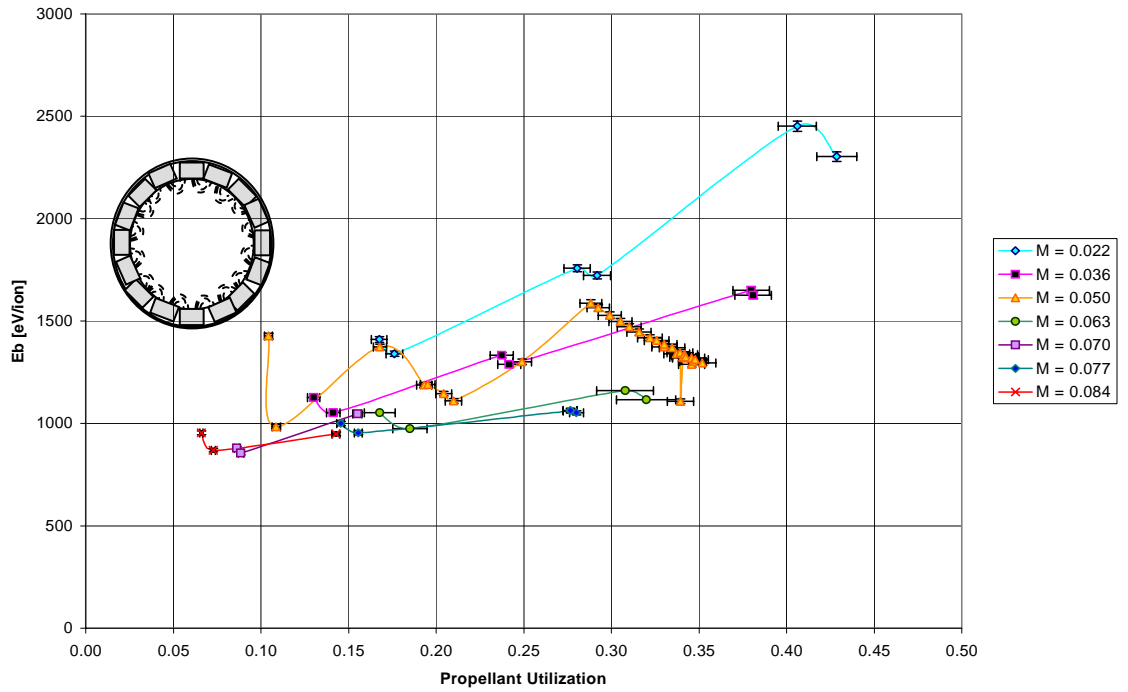

Figure 13. Spaced Line Cusp Magnetic Field with Aft Cathode Placement [Test C]
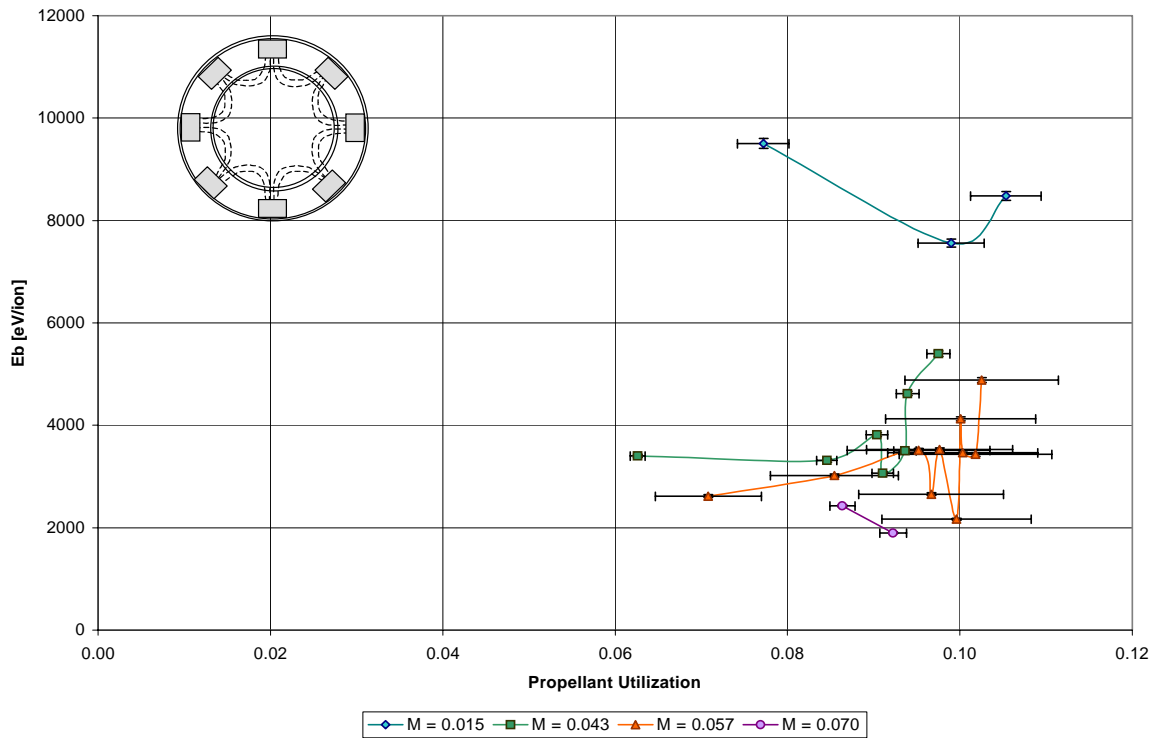
Figure 14. Spaced Line Cusp Magnetic Field, Forward Cathode Placement [Test D]

Figure 15. Electron Collection Pattern for Spaced Line Cusp Anode

To make sure the electrons see the greatest possible magnetic field near the anode the anode was reconfigured to be flush with the magnets (separated by a thin electrical insulator) and by using shim-stock steel as the anode, the distance between the magnets and the area within the discharge chamber was minimized. A tight line cusp configuration was used with this anode as shown in Figure 10. This configuration was developed to increase the electron confinement at the anode wall. The results of the

tests run with this configuration, with aft and forward cathode placement, respectively, are shown in figures 16 and 17. The results in Figure 17 were obtained by incrementally raising V_B by 100V from 300 to 1,000V for a given discharge operating condition. These results clearly show the benefit of using a higher beam voltage. The electron collection pattern on the interior of the thin, shim-stock anode is shown in Figure 18. This pattern shows that the magnetic field at the anode wall strongly affected the behavior of the electrons near the anode; however, this particular design may provide superfluous collection area.

After the tests were performed, inspections of the thruster showed that the shim-stock anode was possibly susceptible to leakage of the discharge plasma to the ambient environment. Slight modifications to the current anode design should easily rectify this concern. It should also be noted that the pole piece was electrically isolated from the anode in this configuration, which may have affected the performance. This was done in an effort to decrease unnecessary anode potential surface. Optimally, the line cusp configurations do not need the pole piece for magnetic field divergence, as in the case of the axial field. Operation of the line cusp configuration without the pole piece may increase performance since the pole piece in the present configuration creates a significant distance of separation between the ionization at the anode walls and the exit grids. Comparison of the results from the cusp designs shows that the tight cusp design is superior to the spaced cusp design at all operating conditions. This is likely due to the superior electron confinement at the anode surface for the tight cusp design. This comparison suggests that the discharge performance may improve if a spaced line cusp or ring-cusp configuration is used with the magnets flush with the anode as is done in the tight line cusp design (as well as in larger ion thruster designs).

Figure 16. Tight Line Cusp Magnetic Field with Aft Cathode Placement [Test E]
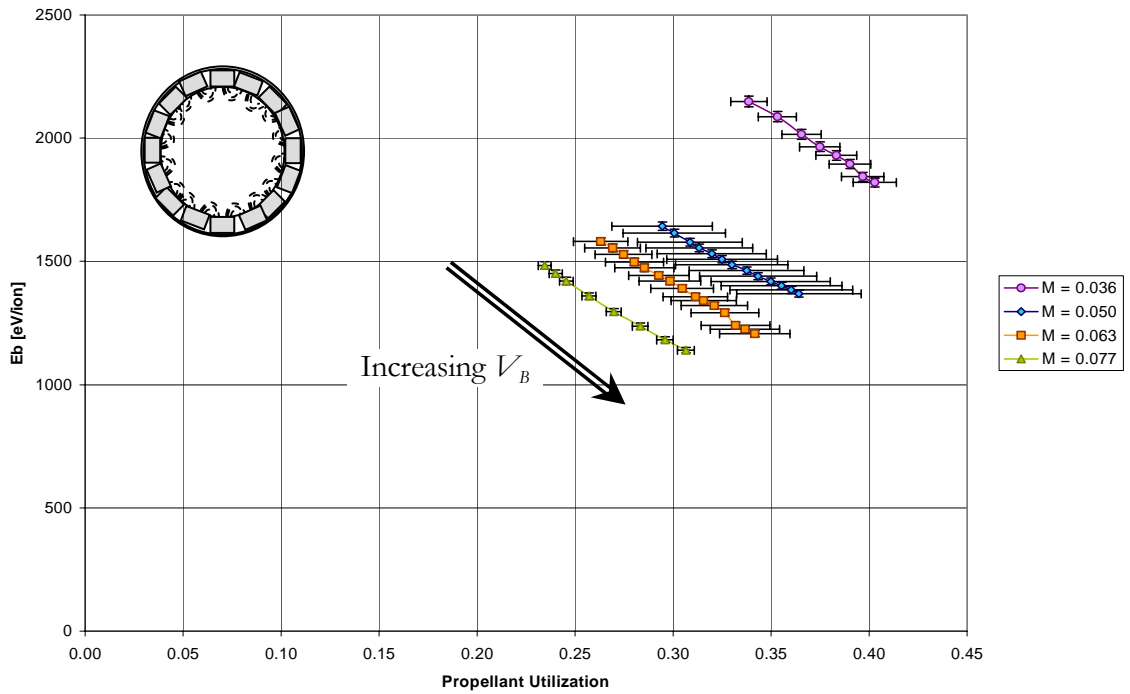
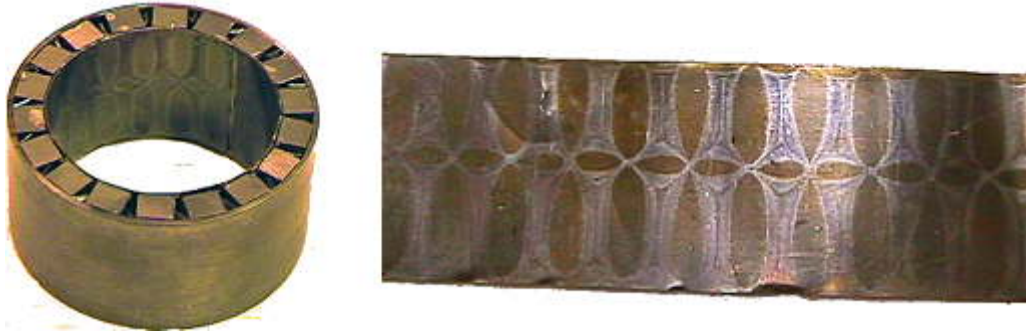Figure 17. Tight Line Cusp Magnetic Field with Forward Cathode Placement [Test F]

Figure 18. Ionization Pattern for Tight Line Cusp Anode

To determine the relative performance of the configurations the performance of all the thrusters has been plotted in Figure 19. Mass flow rates near 0.050 mg/s were chosen for this plot and data with $\varepsilon_B > 3000$ eV/ion are excluded. The fact that the thruster was run at different beam voltages (typically ranging from 500-700V) does not invalidate this comparison since the difference in the performance regimes is still clearly apparent. The spaced line cusp (tests C & D) is clearly inferior to the other configurations and many times required discharge voltages >30V, whereas the other configurations ran most efficiently at $V_D \cong 25$-30V. The tight line cusp (tests E & F) was able to achieve the highest propellant utilization efficiency but at the cost of relatively high ε_B. On the other hand, the divergent axial (tests A & B) had a lower beam ion energy cost but was unable to achieve high η_u for most of the flow rates tested. In general, the results herein suggest that discharge chamber design is important for small ion thruster since the discharge chamber efficiency was considerably lower than typical ion engines.
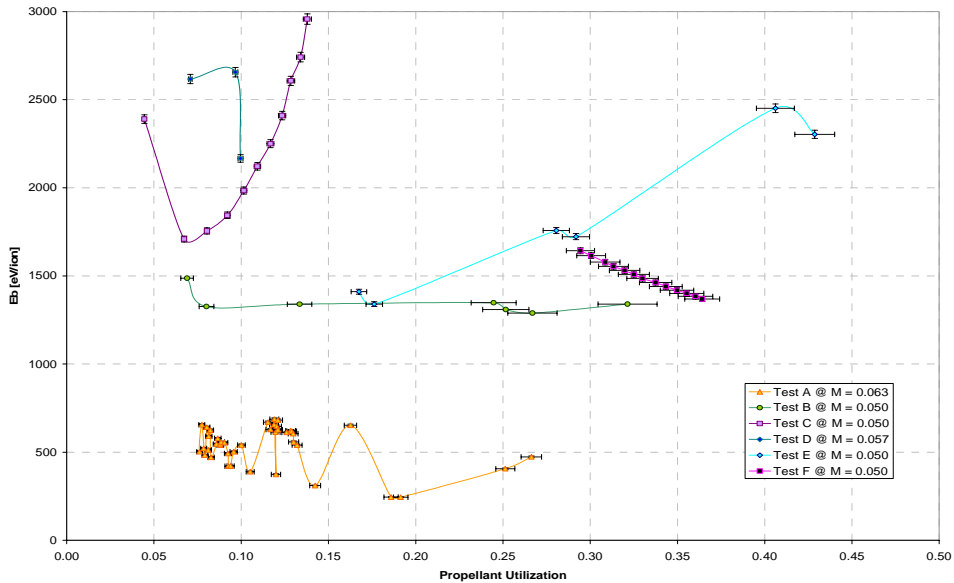
Figure 19. Comparison of All Thruster Configurations

Conclusions and Recommendations

This investigation demonstrates the difficulties related with miniaturizing an ion thruster. The discharge chamber performance is a significant design issue due to the high surface-to-volume ratio at this scale. Though some improvements in performance were noticed, significant efforts must be taken to obtain an efficient discharge chamber design. When designing the magnetic containment field it is important to consider the optimum anode design for that magnetic field. It is also important to consider issues such as chamber leakage, component voltages, and the localization of ionization events near the exit grid. The results of this investigation show that the location of the cathode along the axis of symmetry has a large effect on discharge chamber performance. Due to the consistent operational behavior of the accelerator grids, it is likely that considerable improvements in the chamber performance must be achieved before the limitations of the current grid system may be noticed.

There are many magnetic field options that merit further investigation. With the proper assortment of magnets, a simulation of the NSTAR thruster's ring-cusp configuration may likely yield favorable performance. However, it is possible that this configuration will not scale well. As suggested earlier in this report, a spaced line cusp with the shim-stock anode design may provide a good balance of desirable electron collection area and B-field lines that reach well into the chamber. Since an Alnico-5 magnet created the axial magnetic field in this investigation, it is likely that assembling a ring–like geometry of stronger SmCo magnets may attain increased performance for the divergent axial configuration.

This investigation is part of an ongoing effort to develop an efficient micro-ion thruster, a subject for which very little empirical data is available. The knowledge presented herein should be used to better determine the discharge chamber behavior through further theoretical analysis or computer simulations. The incorporation of more diagnostic equipment, such as thermocouples, will likely generate data useful to thruster modeling efforts. It will be useful to consider the optimal voltages of the discharge surfaces that will encourage better chamber performance. One example is to run all components, besides the anode, at cathode potential for better ionization concentration. It may also prove beneficial to mask or exclude the forward half of the anode to concentrate any ionization events near the exit grids. Shortening the chamber length may have the same effect. Though the grid performance was likely adequate for this investigation, a trade-off of possible grid geometries may yield considerable increases in performance.

References for Appendix B

[1] - Mueller, J., Tang, W., Li, W., Wallace A., "Micro-Fabricated Accelerator Grid System Feasibility Assessment for Micro-Ion Engines," IEPC Paper 97-071, 25th International Electric Propulsion Conference, Cleveland, OH, Aug 1997

[2] - Mueller, J., Marrese, C., Wang, J., Polk, J., "Design and Fabrication of a Micro-Ion Engine," AIAA Paper 2000-3264, 36th AIAA/ASME/SAE/ASEE Joint Propulsion Conference and Exhibit, Huntsville, AL, July 2000

[3] – Baccheschi, N., Amy, M., "Optimization of the Magnetic Field in a Micro-Ion Thruster," Worchester Polytechnic Institute, Project No. ME-NAG-0001, December 2000

[4] – Jahn, R., "Physics of Electric Propulsion," 1968

[5] – Brophy, J., "Ion Propulsion Technology," Presentation May 2001

[6] – Dexter Magnet Technologies, "Reference and Design Manual," 2001

[7] – Magnet Sales and Manufacturing Inc., "High Performance Magnets 7," 1995

[8] – Taylor, J., "Error Analysis – The Study of Uncertainties in Physical Measurements," Second Edition, 1982

[9] – Brophy, J., Technical Discussion, May 2nd, 200

Experimental Equipment

Figure B-1. Thruster Components: Base, Discharge Chamber, and Pole-Piece and Exit Grids
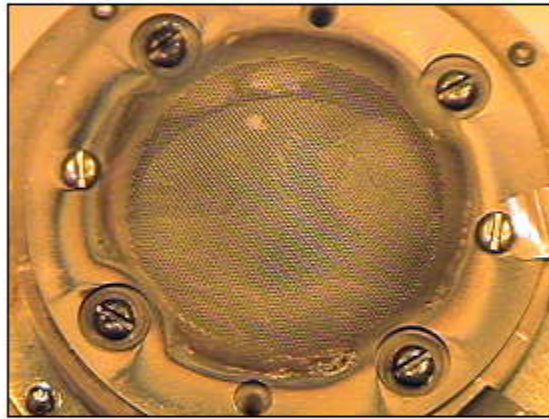
Figure B-2. Screen Grid
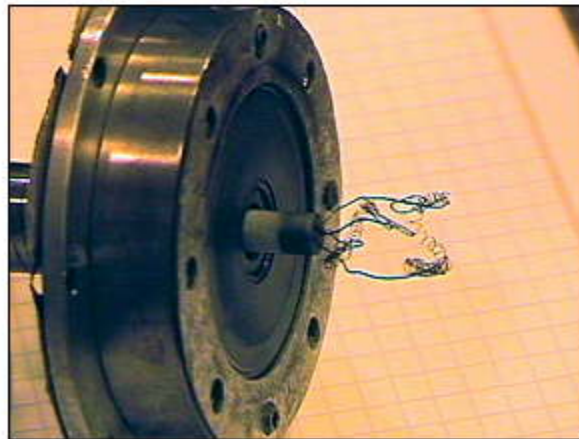
Figure B-3. Discharge Cathode and Propellant Diffusion Plate
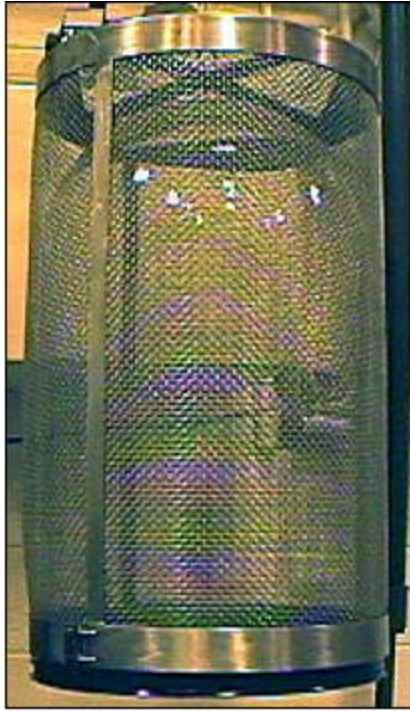
Figure B-4. Vacuum Chamber Dome
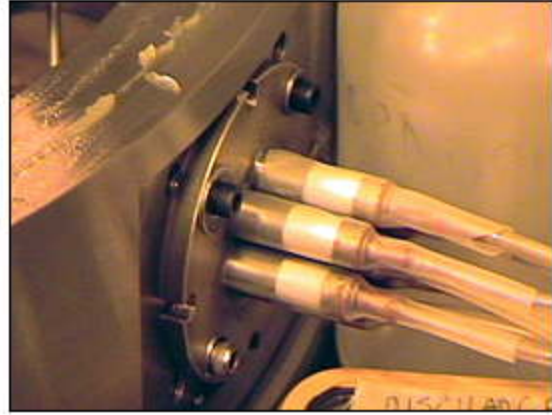
Figure B-5. Vacuum Chamber Electrical Interface

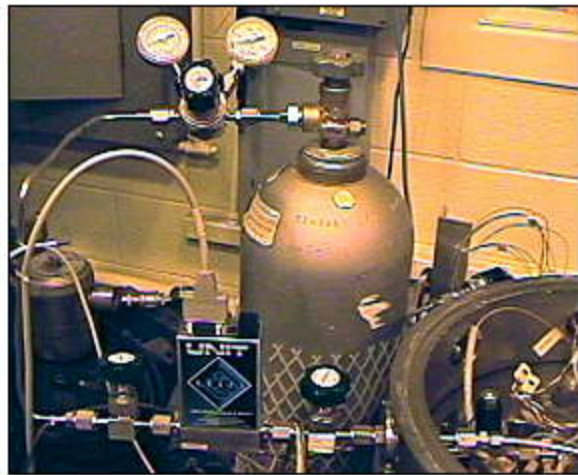**Figure B-6. Propellant Flow Calibration System**

Figure B-7. Xenon Propellant Feed System

- Appendix C -

Micro-Ion Thruster Performance Data

Default Cathode Locations

The default locations for the test conducted in Chapter 5 are shown in Figure C-1. As discussed in Chapter 5, the Axial configuration for L/D=1 was the only configuration to perform better at cathode locations other than the default configuration.
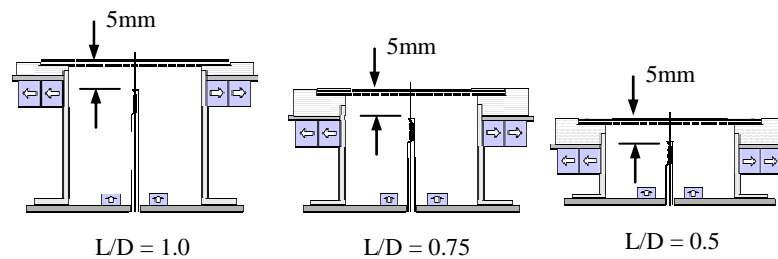
Figure C-1. Default Cathode Locations

Thruster Performance Results

The performance of the configurations from Table 5.2-1 is shown in the following plots. A discussion of these plots is given in Chapter 5.
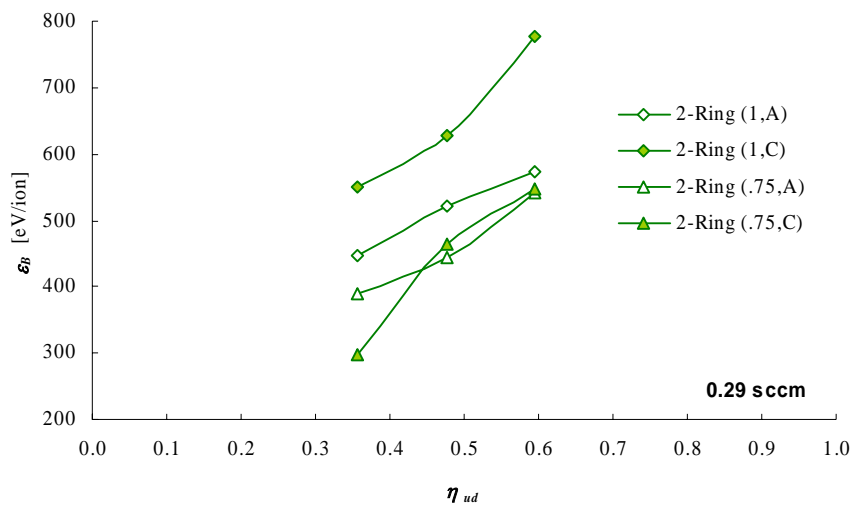
Figure C-2a. 2-Ring Performance at 0.29sccm Xenon Flow Rate
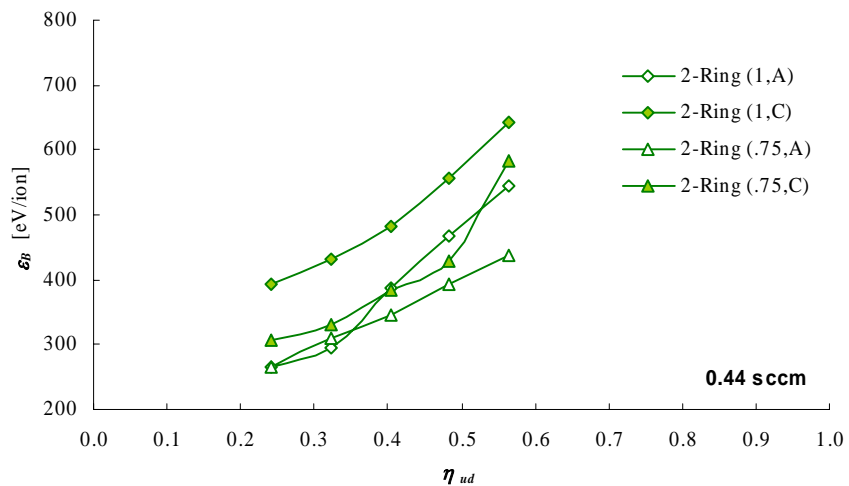
Figure C-2b. 2-Ring Performance at 0.44 sccm Xenon Flow Rate
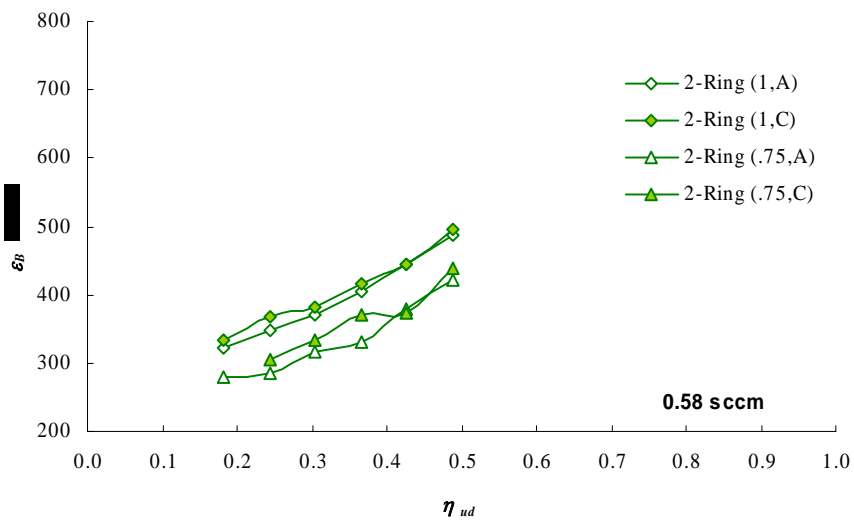
Figure C-2c. 2-Ring Performance at 0.58 sccm Xenon Flow Rate
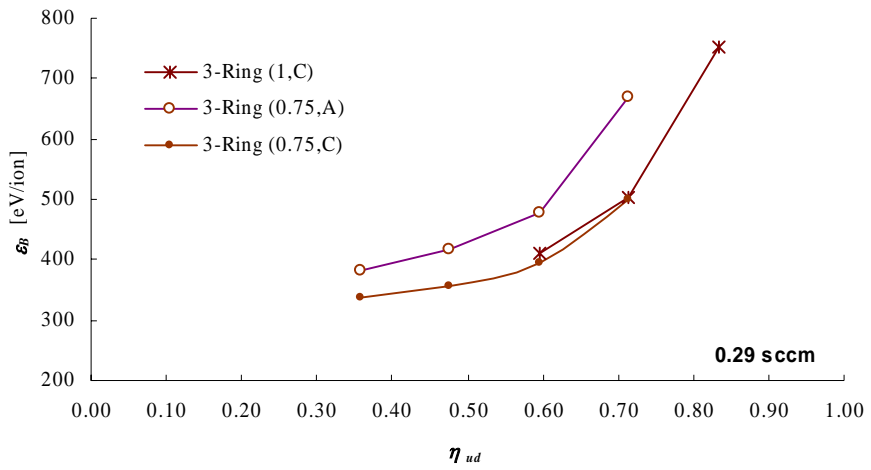
C-2

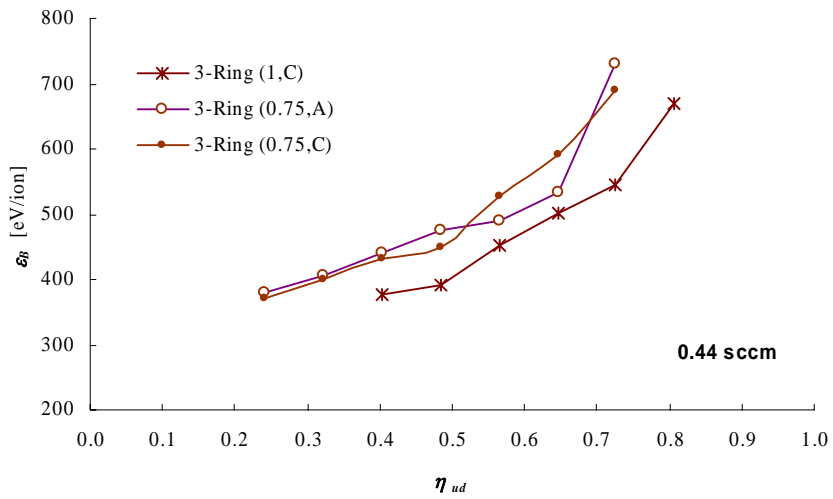Figure C-3a. 3-Ring Performance at 0.29sccm Xenon Flow Rate

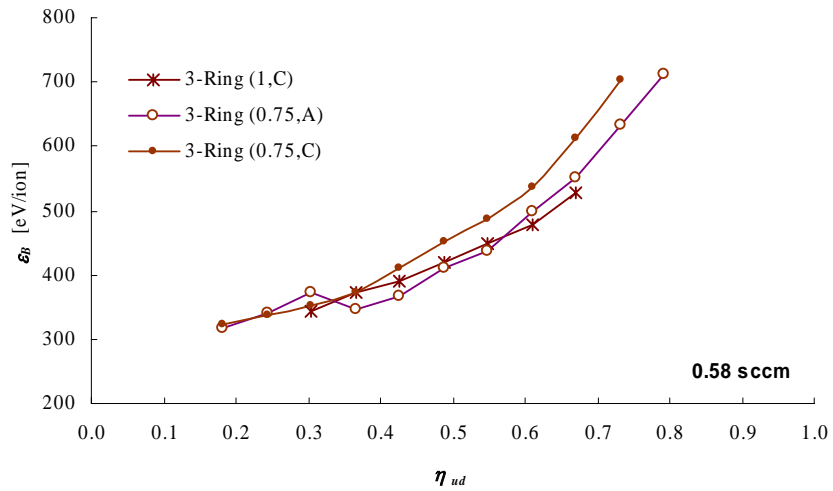Figure C-3b. 3-Ring Performance at 0.44 sccm Xenon Flow Rate

Figure C-3c. 3-Ring Performance at 0.58 sccm Xenon Flow Rate
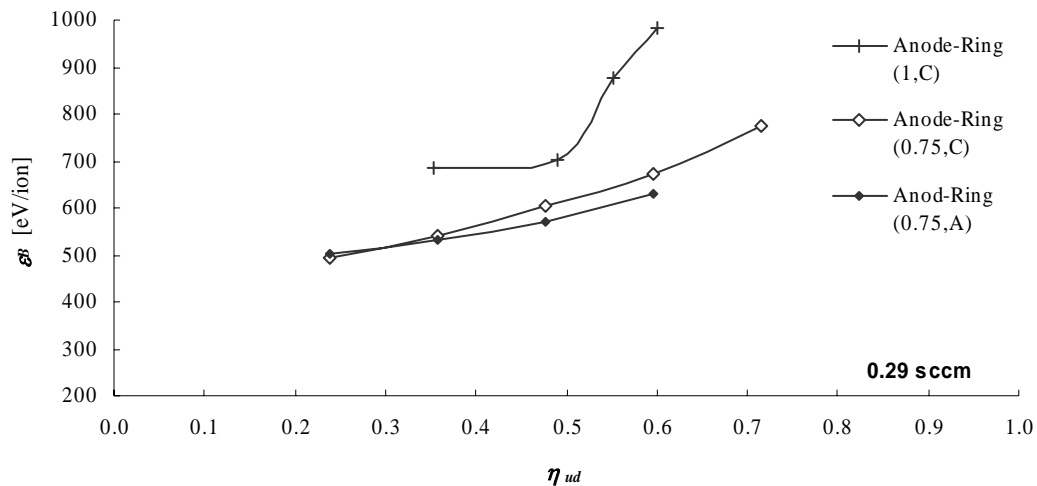
C-3

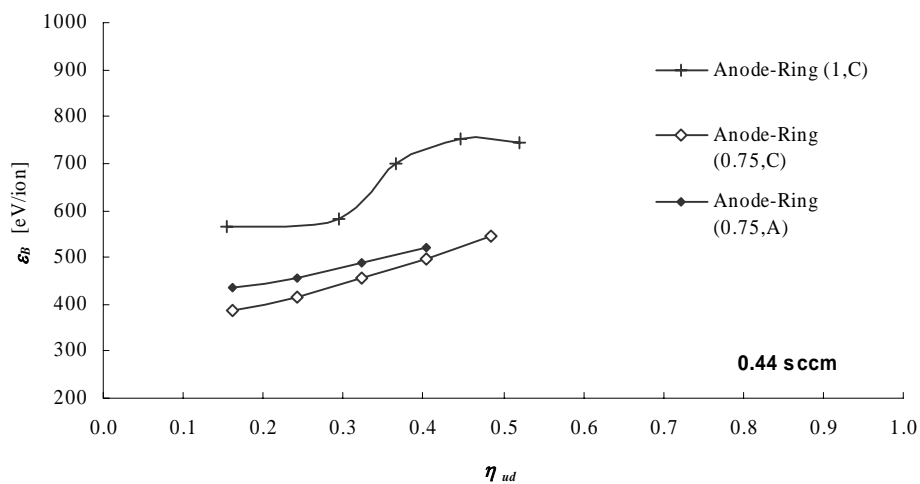Figure C-4a. Anode-Ring Performance at 0.29sccm Xenon Flow Rate

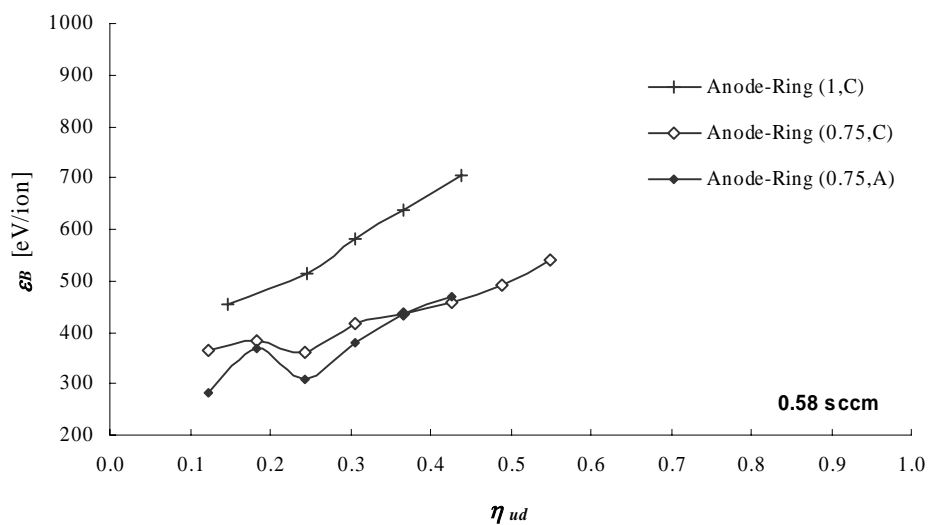Figure C-4b. Anode-Ring Performance at 0.44 sccm Xenon Flow Rate

Figure C-4c. Anode-Ring Performance at 0.58 sccm Xenon Flow Rate
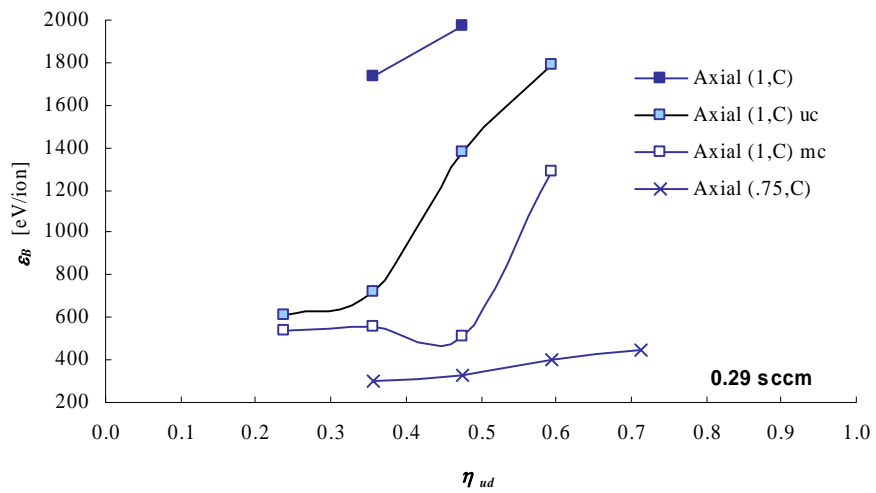
C-4

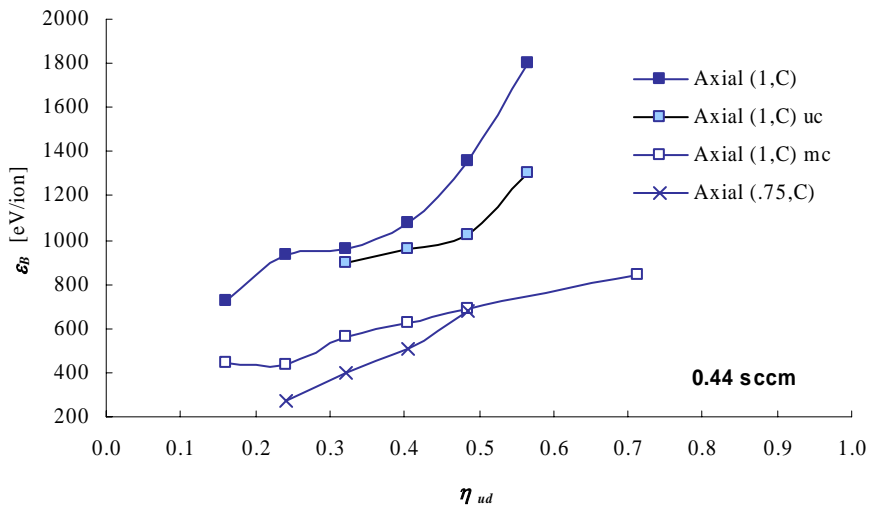Figure C-5a. Axial Performance at 0.29sccm Xenon Flow Rate

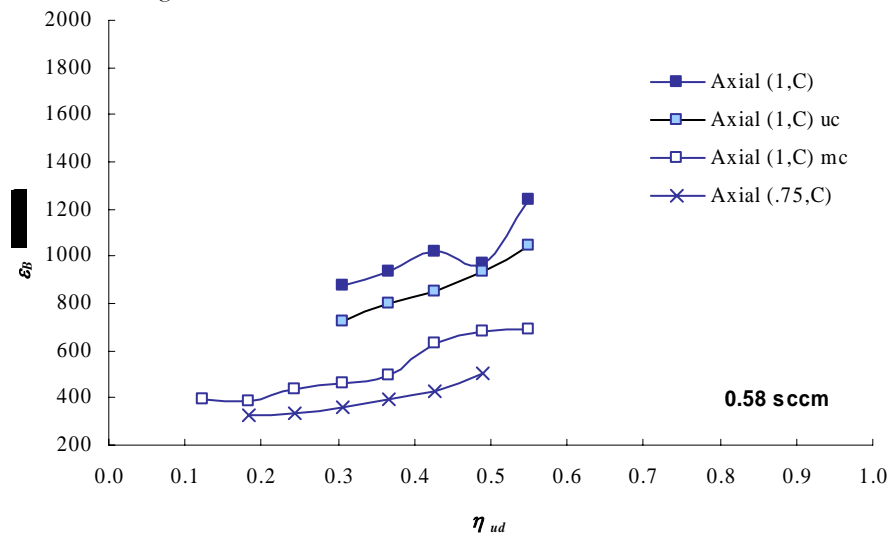Figure C-5b. Axial Performance at 0.44 sccm Xenon Flow Rate

Figure C-5c. Axial Performance at 0.58 sccm Xenon Flow Rate

C-5

Magnet Strength Sensitivity

Preliminary tests were used to determine magnetic field strengths that yielded favorable performance for the configurations from Table 5.2-1. Stronger magnetic fields for the 3-Ring and Anode Ring configurations, Figure C-6, resulted in low propellant efficiencies since the maximum J_B was limited relative to the nominal configurations. In tests conducted with a high magnetic field version of the Axial configuration, Figure C-6, a plasma discharge could not be initiated within the limits of the discharge and cathode heater power supplies. The 2-Ring configuration exhibited similar, but slightly lower, performance for lower magnet strength (one magnet deep) at the anode magnet ring.
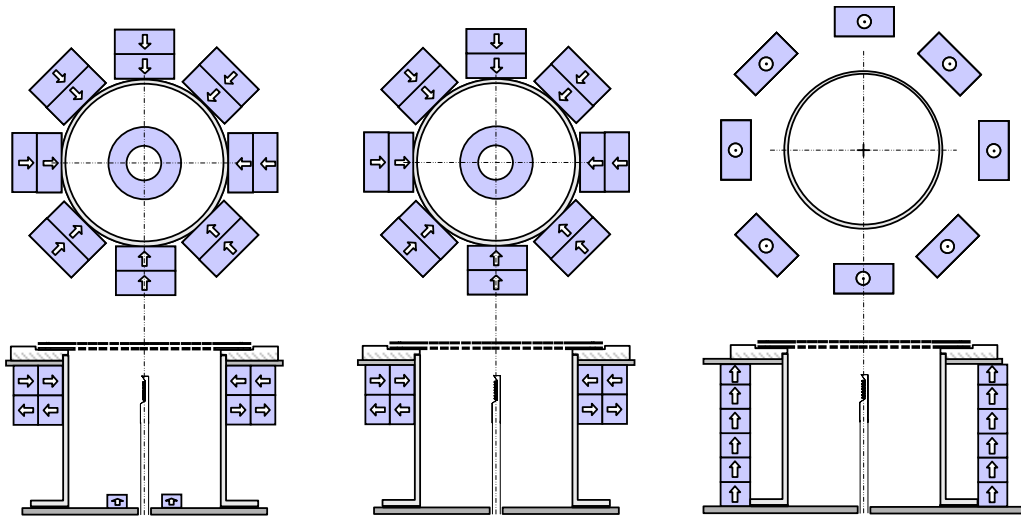

Figure C-6. Strong Magnetic Field Configuration for 3-Ring, Anode-Ring, and Axial

- Appendix D -

Non-Intrusive Discharge Diagnostics and Grid Performance Analysis

EXPERIMENTAL AND COMPUTATIONAL INVESTIGATION OF THE PERFORMANCE OF A MICRO-ION THRUSTER

Richard Wirz[*], James Polk[†], Colleen Marrese[†], Juergen Mueller[‡]

[*]California Institute of Technology, Pasadena, CA 91106, USA
[†]Jet Propulsion Laboratory, California Institute of Technology, 4800 Oak Grove Drive, Pasadena, CA 91109, USA

A micro-ion thruster with a characteristic diameter of 3-cm has been developed at JPL to study the scalability of ion engine technologies. The ability of the magnetic field in a small discharge chamber to create a uniform plasma profile that fully utilizes the capabilities of the ion extraction grids is investigated in this paper. Experimentally obtained beam profiles are used to determine the ion density profile just inside the chamber. A method is presented for determining the beam profile at the accelerator grid exit from beam profiles measured at two different distances downstream of the grids. The experimental and computational results show that the micro-ion thruster design discussed herein yields favorable beam and ion density profiles. The calculated values of ion and neutral density in the chamber, along with preliminary computational and experimental results, show that considerable increases to thruster performance may be attained with relatively minor design and operational modifications.

Nomenclature

Variables
F = flatness parameter [See Equation (8)]
I_{sp} = specific impulse
j = current density
J = current
k = Boltzmann's constant
m = mass
$\dot{m}$ = mass flow rate
n = particle density
$\dot{n}$ = particle flow rate [equivalent Amperes]
p = electron pressure = $n_e kT_e$
P = pressure
q = electric charge
Q = collision cross-section
r = distance from thruster axis
R = beam radius
t = time
T = temperature
v = velocity
V = voltage
z = axial distance

ε_B = beam ion energy cost
δ = open area fraction
ϕ = electric potential
η = efficiency
λ = mean free path

Subscripts
B = beam
CEX = charge exchange
ch = vacuum chamber
D = discharge
e = electron
i = ion
$prop$ = propellant
o = neutral atom
∞ = ambient

[*]Doctoral Student, Aeronautics. Member AIAA.
[†]Staff Engineer, Advanced Propulsion Technology Group. Member AIAA.
[‡]Presented at the 38th AIAA Joint Propulsion Conference, Indianapolis, IN, July 2002.

Introduction

Background and Motivation

Micro-ion thrusters offer the potential for a unique combination of high efficiency, high specific impulse (I_{sp}), benign propellants, and low thrust with the capability for continuous operation for a variety of future space missions[1]. Recent results have shown that attractive performance is possible for micro-ion thrusters if low power field emission array (FEA) or hollow cathodes can be incorporated[2]. Engine efficiency as high as 43%, neglecting cathode power, was achieved in initial tests using filament cathodes to simulate the FEA or hollow cathodes. Recent

results in the development of FEA cathodes for electric propulsion applications are reported in Reference [3]. It was shown in Reference [2] that for a micro-ion thruster with a 3cm diameter discharge chamber, the shape of the discharge magnetic field and the discharge chamber geometry greatly affect the performance of the thruster. However, the performance related to the micro-machined grids and the chamber ion and neutral densities has not been investigated.

The beam profiles in the thruster plume allow many characteristics of a thruster to be determined, including: beam divergence, grid utilization, nonuniform grid wear, and overall thruster performance. Statistical and qualitative correlations have been shown to exist between the beam profile at the grid exit plane and the discharge chamber ion density profile near the grids[4,5]. Consequently, the effectiveness of the ion thruster design is strongly dependent on the discharge ion density profile near the grids, which is reflected in the beam profiles measured downstream of the thruster.

Objective

This paper presents a method for determining the discharge chamber ion density of a micro-ion thruster just inside the grids by considering the beam profile at the exit plane and grid deflection due to thermal and electrostatic loads. At the micro-ion thruster scale, the beam measurements cannot be taken sufficiently close to the grid exit plane without electrical shorting of the probe to the grids. Consequently, a technique for projecting downstream beam profile data back to the grid exit plane is discussed. With this information the micro-ion thruster discharge chamber performance, grid utilization, beam divergence, and efficiencies can be more thoroughly understood.

Experimental Setup

The micro-ion thruster and testing facility used in this investigation are discussed in Reference [2]. The thruster faces vertically upward and a small faraday probe oriented parallel to the thruster axis was used to make linear sweeps across the thruster plume at various heights. The thruster configuration tested herein is a double ring cusp design with a length-to-diameter ratio of 1, as shown in Reference [2]. Flat micro-machined molybdenum grids with circular holes were used for the ion accelerator system.

Theory and Analysis

Beam Divergence and Charge Exchange

The following section discusses the relationships used to determine the effects of beam divergence and charge exchange collisions in the thruster plume.

The beam divergence for an ion thruster is primarily due to the ion-optical properties of the exit grids. Additional divergence is caused by the variations of plasma density and potential in the thruster plume. Quasi-neutral beams, such as those used in this investigation, may be considered isothermal and the spatial variation of the potential follows the barometric law[6].

$$n(\vec{r}) = n_o \, exp\left[\frac{q\phi(\vec{r})}{kT}\right] \qquad (1)$$

The motion of the beam ions is governed by the ion momentum equation.

$$m_i \frac{d\vec{v}_i}{dt} = -q\nabla\phi \qquad (2)$$

The barometric law, Equation (1), is derived from the momentum balance equation for a stationary electron gas

$$m_e \frac{d\vec{v}_e}{dt} = q\nabla\phi - \nabla p = 0 \qquad (3)$$

for constant T where the electron pressure is $p = nkT$. By combining Equations (2) and (3), and assuming a quasi-neutral beam plasma, we can determine the effect of the radial variation in plasma density on the motion of the beam ions by

$$m_i \frac{d\vec{v}_i}{dt} = -kT \frac{\nabla n}{n} \qquad (4)$$

The beam divergence is then governed by Equation (4) and the radial distribution of the ion optics.

It is important to determine the beam current that is lost due to charge exchange (CEX) interactions of the beam ions with the ambient xenon neutrals. The charge exchange losses in the beam will increase with distance from the thruster and will affect the accuracy of beam profile measurements at increasing distances from the grid exit plane. The loss of beam current J_B directed perpendicular to a region of xenon neutrals with density n_o and thickness dz may be expressed as

$$dJ_B = -J_B n_o Q_{CEX} dz \qquad (5)$$

Since the mean free path for CEX collisions is $\lambda_{CEX} = 1/(n_o Q_{CEX})$, the beam current at an axial location z from the exit plane of the thruster is

$$J_B(z) = J_B(0)exp\left[\frac{-z}{\lambda_{CEX}}\right] \qquad (6)$$

After correcting for CEX attenuation, the total beam current may be approximated from a measured beam profile by integrating the beam current densities over the radial extent of the profile such that,

$$J_B = \int_0^R j_B(r)2\pi r dr \qquad (7)$$

Chamber Ion Density

A 2-D ion optics code developed at JPL, CEX2D, can evaluate the performance of a given grid geometry over a wide range of discharge chamber densities[7]. By using this code, the ion density profile just inside the chamber can be determined if the beam profile near the grid exit plane is known.

Significant variations in the spacing between the flat grids used in this investigation can occur due to the large potential gradient between the grids and thermal expansion of the grid material during thruster operation. An analytical model is used to determine the deflection of the plates as a function of radius due to thermal buckling and electrostatic attraction between the grids[8,9]. The results of these deflections are used to more accurately specify the grid spacing in the ion optics code.

Grid Performance

The primary purpose of the grids is to prevent the loss of propellant neutrals while allowing a sufficient ion beam to be extracted. Therefore, grid performance can be determined by comparing the beam and neutral loss profiles at the grid exit plane. The neutral loss is usually considered to occur uniformly over the grids; however, the beam current density profile may have drastic variations. One way to quantitatively describe these variations is to use the flatness parameter, F, which is given by[10]

$$F = \frac{\int_0^R j_B(r)2\pi r dr}{\pi R^2 j_{B\max}} \qquad (8)$$

As discussed in Beattie [ref], a low flatness parameter value reveals the potential for localized grid wear and poor grid performance.

The rate of neutral loss through the grids may be calculated by the relation

$$\dot{n}_o = \dot{m}_{prop} - J_B \qquad (9)$$

where $\dot{n}_o$ and $\dot{m}_{prop}$ are expressed in equivalent amperes. Using the neutral loss rate and grid dimensions, neutral density inside the discharge chamber is approximated using free molecular flow through a sharp-edged orifice[11]

$$n_o = \frac{4\dot{n}_o}{ev_o A_g \delta_o} \qquad (10)$$

The neutral densities calculated by Equation (10) were used in the 2-D ion optics code for the calculation of CEX ion production rates.

Results

Experimental Results

The faraday probe was used to take beam profiles at distances of 8 and 23mm from the exit plane of the thruster. Profiles were taken at multiple thruster operating conditions within the ranges shown in Table 1. The calculated performance does not include cathode and neutralizer power since low power cathodes, such as field emitter arrays (FEAs) and hollow cathodes, will be used for future designs[2,3,11]. The primary upper limitation to the ranges in Table 1 is the 350°C maximum operating temperature of the samarium cobalt magnets.

Table 1. Thruster Operation Ranges

Parameter	Range*
V_B	700 – 1126 V
V_D	23.5 – 29 V
J_B	7 – 28 mA
J_D	70 - 500 mA
$\dot{m}_{prop}$	0.017 – 0.057 mg/s
Power	14 – 43 W
P_{ch}	6.3E-6 – 2.0E-5 Torr
T	180 – 330°C
Thrust	0.4 – 1.5 mN
I_{sp}	1764 – 3184 s
ε_B	450 – 743 eV/ion
η_u	0.48 – 0.82
η_{tot}	0.31 – 0.56

*Values ignore doubly-charged ions and cathode
input power as discussed in Reference 2.

An example of beam profiles obtained using probe measurements is shown in Figure 1. The measured beam current agrees within 6% of the total beam current obtained by integrating over the beam profiles with Equation (7).
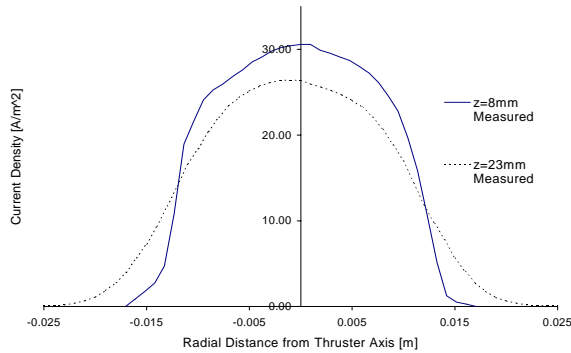

Figure 1. Measured Beam Profiles

The axial attenuation of the beam current due to charge exchange was calculated at a distance of 23mm from the thruster exit plane using Equation (6). At the highest measured ambient neutral gas pressure and operating voltage, the change in beam current for both singly- and doubly-charged ions due to charge exchange was only 0.6% and 0.4% respectively. Therefore, for the probe distances used, it is reasonable to ignore the effect of charge exchange collisions.

Exit Plane Beam Profiles

A simple finite-difference model was developed that uses beam profiles measured at two axial locations downstream of the thruster exit to predict the profile at the thruster exit plane. The model uses Equation (4) to describe the beam divergence due to the downstream plasma and uses the measured downstream density profiles to determine the radial distribution of ion optical properties of the exit grids.
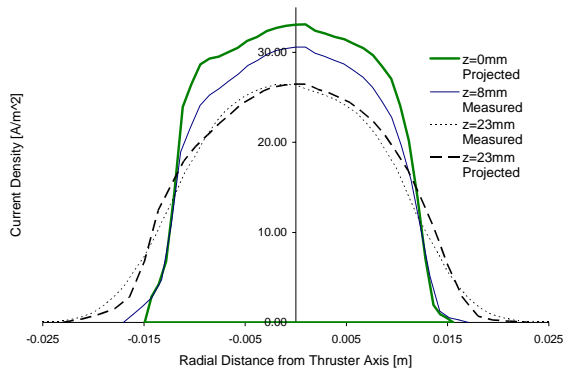

Figure 2. Projected Exit Plane Beam Profile

The predicted exit plane profile for the data presented in Figure 1 is shown in Figure 2. The model is matched exactly with the measured profile at 8mm. Divergence due to the ion optics is approximated such that, along with the self-consistent calculation of the radial potential distribution, the downstream profile predicted by the model matches the experimentally measured downstream profile at the same axial location within 5% of the beam flatness as calculated by Equation (8). The electron temperature of the downstream plasma was measured to be approximately 2.7eV for most operating conditions[12].

Grid Deflection

An analytical model that treats the grids as clamped circular plates was created. For a given change in temperature and electrostatic loading, the model generates an equivalent transverse loading that is used to determine the grid deflection as a function of radius. The model uses effective material properties for perforated molybdenum based on the open area fraction of the grids[13]. The accelerator and screen grids were assumed to have uniform temperature distributions at 24°C and 100°C above the temperature measured at the exterior of the anode wall, respectively[14]. Predictions by the analytical grid deflection model correspond well with preliminary results from a finite element model (FEM) for the screen grid.

The results of the analytical model show that the accelerator and screen grids deflect in the same direction. It was originally thought that the grids would deflect towards one another due to electrostatic attraction; however, the model predicts that this force contributes less than 0.4% of the total equivalent transverse load. This reveals that the deflections due to thermal loads dominate the total deflection of the grids used in this investigation. It is likely that a preloading associated with the grid mounting or some other force determines the direction of deflection such that both the grids overcome their electrostatic attraction and buckle in the same direction. Analysis of the measured beam profiles shows that some grid sets, where each grid set has its own grid mount, experience buckling towards the discharge chamber while others buckle away. This may be due to difference in the grid mounts, grid geometry, or a combination of both.

Since the accelerator and screen grids experience different temperatures during thruster operation and have different effective material properties, the extent of their deflections varies in magnitude relative to each other. Consequently, the model predicted a radial variation in the grid spacing.

For most cases, this variation gives a maximum decrease in grid spacing of over 50% at the center of the grids. Figure 3 shows the grid deflections and variation in the grid spacing predicted by the model at the conditions used in Figure 1 for grids originally spaced 300μm apart.
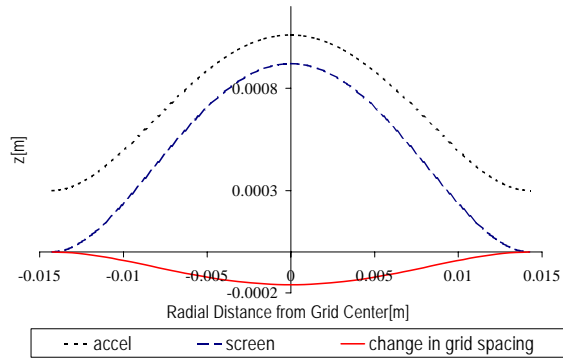

Figure 3. Grid Deflection and Grid Spacing Variation due to Thermal and Electrostatic Loading

Chamber Ion Density Profiles

Using the beam profile at the grid exit plane and the grid deflection results, the ion density profile just inside the chamber was approximated with the 2-D ion optics code, CEX2D[6]. Each run of the code gives beamlet currents at a range of chamber densities for a given grid geometry. Runs at multiple grid spacing values were performed to allow the effects of grid deflection to be investigated. The relationship of ion density to beam current generated by the code for a range of micro-ion grid spacing, and at the operating conditions used to generate the data in Figure 1, is shown in Figure 4.
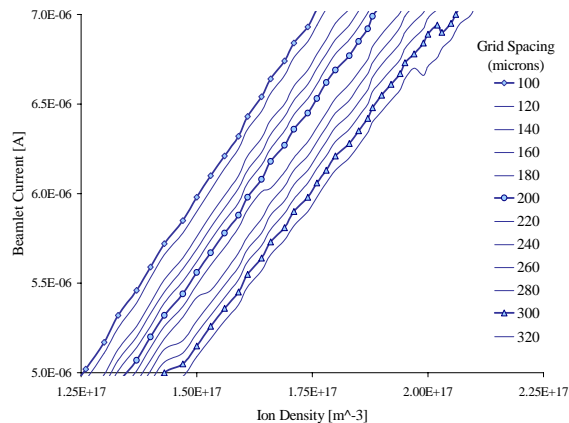

Figure 4. Chamber Ion Density vs. Beamlet Current for 100μm to 320μm Grid Spacing

The results shown in Figure 4 were used to generate multiple linear relationships between ion density and beamlet current. The slopes of these relationships were then determined to be a function of grid spacing so that the ion density was expressed as a function of grid spacing and beamlet current. The resulting expression was used to generate ion density profiles from the exit plane beam profiles and the grid deflection data.

Using this technique, the ion density profile corresponding to the exit beam profile (Fig. 2) and the grid deflection (Fig. 3) was determined as shown in Figure 5. Both profiles are normalized to show the degree of correlation. The variation in the normalized profiles is primarily due to the radial variation in grid spacing
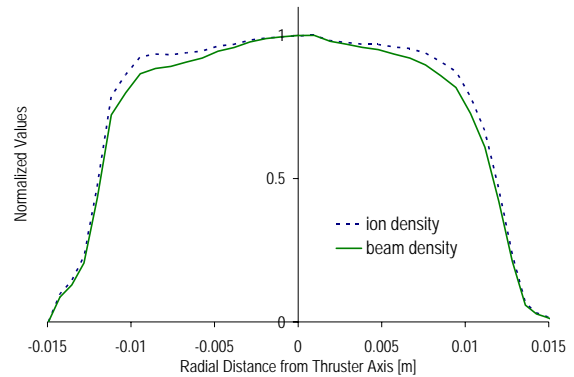
.

Figure 5. Normalized Ion Density Profile and Exit Plane Beam Density Profile

Ion Trajectories

CEX2D also calculates typical ion trajectories and the potential profile at the highest ion density for a given run. This information can be used to determine the ion optical properties of for a given grid geometry. For example, if large accelerator grid current is predicted by the code then the trajectories and potential profiles will reveal whether this current is due to crossover or direct impingement current to the accelerator grid. Since low accelerator grid currents were experimentally measured, the beamlets for this investigation were considered to be sufficiently focused to avoid crossover or direct impingement currents.

Figure 6 shows trajectory profiles for a micro-ion beamlet at grid spacing values of 300μm and 160μm. These trajectory plots show that the beamlet is far from intersecting the accelerator grid for the range of grid spacing predicted by the grid deflection model. Consequently, greater ion densities may be used before direct impingement on the accelerator grid will occur. This will result in greater

beamlet current and greater overall efficiency, but is limited by the maximum operating temperature of the magnets and may result in greater accelerator grid hole wall erosion[6]. On the other hand, for these operating conditions Small Hole Accelerator Grids (SHAG) optics will improve overall performance by reducing neutral losses[1]. This option is discussed later in this paper. As expected, Figures 4 and 6 show that closer spacing typically results in greater beamlet current but can yield greater beamlet divergence.
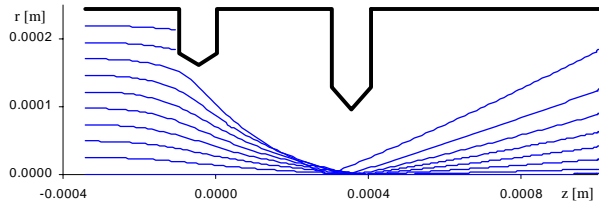

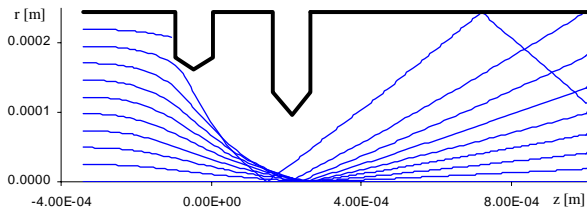Figure 6a. Ion Trajectories for 300μm Grid Spacing

Figure 6b. Ion Trajectories for 160μm Grid Spacing

Grid Performance

The flatness parameters for the exit beam and ion profiles in Figure 5 are 0.67 and 0.70, respectively. Similar values were obtained for other operating conditions. These data show that the chamber design used for the micro-ion thruster produces desirable ion and beam profiles for the operation ranges investigated in this paper.

The projected ion densities were typically on the order of 2.0×10^{17} m^{-3}, while the neutral densities were calculated using Equation (10) to be approximately 2.0×10^{19} m^{-3}. The neutral loss rate, in equivalent amperes, was typically over half the beam current. These data and the trajectories shown in Figure 6 show that increasing chamber ion density and decreasing the neutral loss rate will improve thruster efficiency without causing direct ion impingement on the accelerator grid.

For a given propellant flow rate and operating conditions, SHAG optics will reduce the neutral loses and increase the neutral density in the chamber. For properly sized SHAG optics, increasing the neutral density will increase ion density and beam current and result in greater overall efficiency. Preliminary runs of CEX2D indicate that

a decrease in the accelerator hole size to half of that used in Figure 6, will yield favorable results. Ion trajectories for SHAG optics and increased ion density are shown in Figure 7. By Equation (10), reducing the accelerator grid holes by a factor of 2 will reduce the neutral loss rate by 75% for a given neutral density.

A preliminary experimental investigation of SHAG optics was conducted. The results show that the use of SHAG optics increases the highest attainable propellant efficiency from 68% to 82% and total efficiency from 44% to at least 56%. As expected, SHAG optics increased the maximum attainable beam current for a given propellant flow rate.
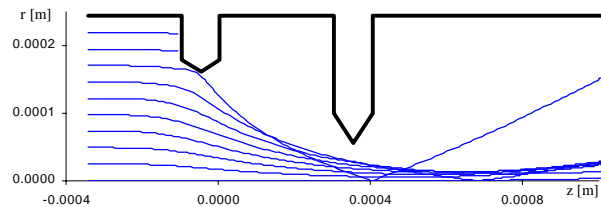
Figure 7. Ion Trajectories for 300μm Grid Spacing Using SHAG Optics and Increased Ion Density

Conclusions

Proper calculation of divergence and charge exchange in the beam of an ion thruster allows the beam profile at the exit plane of the thruster to be approximated using measured beam profiles from at least two different downstream locations. Assuming adequate beamlet focusing, the ion density inside the chamber may be expressed as a simple function of beam density at the exit plane and grid spacing. If crossover and direct impingement current to the accelerator grid are encountered, then the correlation is much less clear. A more accurate correlation of ion and beam density may be achieved if the angular deflection of the grids in the z-direction can be incorporated into CEX2D.

The micro-ion thruster design investigated herein yields favorable beam and ion profiles that show the magnetic field within the chamber helps create an ion density profile that efficiently uses the full radial extent of the grids.

The relatively high values for neutral loss and neutral density found in the initial data reveal possibilities for improvement to the current design. Preliminary results show that substantial increases in thruster efficiency are possible with SHAG optics.

Future Work

Modifications to the existing thruster design, such as smaller accelerator grid holes and stronger magnetic fields, will be investigated further. Due to the large grid deflections calculated herein, dished molybdenum or flat Carbon/Carbon grids are being considered to stand off greater grid voltage differentials and to allow optimal spacing through the radial extent of the grids. Low energy, flight-worthy cathode designs such as hollow and field emitter array (FEA) cathodes will be used in future test.

A computer model of the discharge chamber is being developed to help determine what modifications to the existing design will yield the best performance.

Acknowledgements

References

[1] – Mueller J., et al., "An Overview of MEMS- Based Micropropulsion Developments at JPL," IAA Paper B3-1004, 3rd International Symposium on Small Satellites for Earth Observation, International Academy of Astronautics (IAA), Berlin, Germany, April 2001

[2] – Wirz R., et al., "Development and Testing of a 3cm Electron Bombardment Micro-Ion Thruster," IEPC Paper 01-343, 27th IEPC, Pasadena, CA, Oct 2001

[3] - Marrese-Reading C., Polk J., Mackie B., Dandeneau D., Koel B., Quinlan M., "Field Emission Array Cathode Material Selection For Compatibility With Electric Propulsion Applications," 100th Electrochemical Society Conference, 2002

[4] – Wilbur P.J., "Correlation of Ion and Beam Current Densities in Kaufman Thrusters," Journal of Spacecraft and Rockets, Vol. 10, No. 9, Sept. 1973, pp 623-624

[5] – Knauer W., et al., "Radial Field Kaufman Thruster," Journal of Spacecraft and Rockets, Vol. 7, No. 3, March 1970, pp. 248-251

[6] – Parks D.E., Katz I., "Preliminary Model of Ion Beam Neutralization," Electric Propulsion and Its Applications to Space Missions, Finke R.C. editor, Progress in Astronautics and Aeronautics Vol. 79, AIAA 1981

[7] - Brophy J.R. Katz I., Polk J., Anderson J., "Numerical Simulations of Ion Thruster Accelerator Grid Erosion," AIAA-2002-4261, to be presented at the 38th AIAA/ASME/SAE/ASEE Joint Propulsion Conference & Exhibit, Indianapolis, IN, July 2002

[8] – Ugural A.C., "Stresses in Plates and Shells," McGraw-Hill, 1981

[9] – Lih M.S., "Parametric Study of the Structural Response of Carbon/Carbon Ion Grids," JPL Internal Document, May 2, 2001

[10] – Beattie J.R., "Cusped Magnetic Field Mercury Ion Thruster," NASA-CR – 135047, July 1976

[11] – Brophy, J.R., "Ion Thruster Performance Model," NASA-CR-174810, December, 1984

[12] – Schott L., "Electric Probes," Plasma Diagnostics, Lochte-Holtgreven W. editor, North-Holland, 1968, APS 1995

[13] – S. A. Meguid et al., "Analytical, Numerical and Experimental Studies of Effective Elastic Properties of Periodically Perforated Materials," Journal of Engineering Materials and Technology, P. 48 Vol. 118 Jan 1996.

[14] – Bond T.A., Christensen J.A., "NSTAR Ion Thrusters and Power Processors," NASA/CR-1999-209162

- Appendix E -

Development of Miniature Ion Thruster Cathode Technologies

Development of Cathode Technologies for a Miniature Ion Thruster

Richard Wirz[‡]
California Institute of Technology
Pasadena, CA

Dan Goebel[*], Colleen Marrese[†], Juergen Mueller[†]
Jet Propulsion Laboratory
4800 Oak Grove Drive
Pasadena, CA

Abstract – Ion thrusters have traditionally been thought to be infeasible at smaller sizes; however, recent investigations at JPL using a 3cm Miniature Xenon Ion (MiXI) thruster have shown that a potential exists for an efficient miniature ion thruster that is capable of providing thrust from 0.1 to >1.5 mN, Isp in excess of 3000 seconds, and propellant utilization efficiency greater than 80%. MiXI, thruster tests have thus far used filament cathodes as placeholders for low-power cathodes. This paper discusses the cathode technologies that are candidates for the MiXI thruster. A discussion about RF/microwave sources for MiXI is also given. Comparison of the interrelationship of thruster and cathode performance show the need for cathodes that do not require propellant beyond what is required for the discharge. In an effort to avoid the issue of excess propellant flow, and due to the low discharge current requirements of the MiXI discharge, direct emission cathodes are considered. Initial results demonstrated that direct emission cathodes are possible candidates for the MiXI discharge but vacuum facility and cathode assembly issues must be resolved before an accurate comparison of cathode technologies can be completed.

Nomenclature

Variables
B = magnetic flux density
I_{sp} = specific impulse
j = current density
J = current
k = Boltzmann's constant
m = mass
$\dot{m}$ = mass flow rate
n = particle density
P = pressure
T = temperature
v = velocity
V = voltage
ε_B = beam ion energy cost
ε_o = permittivity of free space
η = efficiency
ϕ = work function

Subscripts
B = beam
ch = vacuum chamber
D = discharge
e = electron
i = ion
$prop$ = propellant
o = neutral atom
u = propellant utilization

Introduction

Background and Motivation

The Miniature Xenon Ion (MiXI) thruster offers the potential for a unique combination of characteristics that are well suited for a variety of future space missions [1]. These characteristics include high efficiency, high specific impulse (I_{sp}), benign propellants, and high resolution of thrust. Notably, by using a benign propellant such as xenon, the MiXI thruster does not pose a contamination risk to sensitive spacecraft equipment when compared with other thruster options in the milli-Newton thrust range [2]. This characteristic is especially attractive to missions that will use sensitive optical lenses and equipment. Since the miniature ion thruster uses the same propellant and similar voltages as larger ion thrusters it may also be considered as secondary propulsion for spacecraft that use larger ion thrusters.

It was shown in Reference [3] that for a miniature ion thruster with a 3cm diameter discharge chamber, the shape of the discharge magnetic field and the discharge chamber geometry greatly affects the performance of the thruster. The work in Reference [4] showed that, at this scale, micro-machined ion extraction grids with low transparency to neutrals resulted in the possibility of very attractive performance, most notably propellant utilization in excess of 80%. Neglecting cathode

[‡]Doctoral Student, Aeronautics. Member AIAA.
[*]Section Staff, Advanced Propulsion Technology Group, Member AIAA
[†]Staff Engineer, Advanced Propulsion Technology Group. Member AIAA

power, engine efficiency as high as 56% was achieved in initial tests using filament cathodes as placeholders for future low-power cathodes. These results show that attractive performance is possible for MiXI-ion thrusters if low-power electron sources can be incorporated. Very low power field emission cathodes are being considered for the neutralizer. The use of low-power, low-temperature discharge cathodes allows for higher plasma densities within the discharge chamber and therefore higher thrust levels, in comparison to the high-temperature filament cathodes used in previous investigations. Many electron sources for the MiXI discharge exist, including: thermionic and field emission cathodes, radio frequency sources (RF), helicon sources, and microwave electron resonance (ECR) sources. Thermionic cathodes may be used in either a hollow or direct emission configuration. The advantages and disadvantages of MiXI discharge electron source options are discussed in this paper; however, much of this paper will focus on the use of direct emission cathodes.

Objective

This study investigates the use of thermionic emitting cathode technology for the MiXI discharge. In particular, directly emitting cathode materials and assemblies are evaluated. Hollow cathodes and other cathode options, as well as the potential for other discharge plasma sources, are discussed.

Experimental Setup

Equipment

The testing facility used to conduct the experiment is comprised of four primary systems: thruster assembly, vacuum chamber, power conditioning and diagnostics, and xenon propellant feed system. The MiXI thruster assembly includes the thruster, a plasma screen, and a neutralizer cathode. The thruster is comprised of a 3cm diameter discharge chamber, two molybdenum accelerator grids, a propellant inlet diffusion plate, and discharge and neutralizer cathode filaments. A plasma screen in the form of an aluminum box is used to prevent ambient electrons from impinging on the thruster's exterior components. This plasma screen surrounds the entire thruster assembly except for a small opening to allow for beam extraction. A stand, located near the opening, is used to hold a simple filament neutralizer cathode, as shown in Figure 1. The propellant feed line and electrical leads to the thruster are located on the opposite side of the box. The box may be opened to allow access to the thruster, Figure 2. The thruster faces vertically

upward and a small faraday probe, oriented parallel to the thruster axis, is used for diagnostics of the thruster plume (see Figure 1).
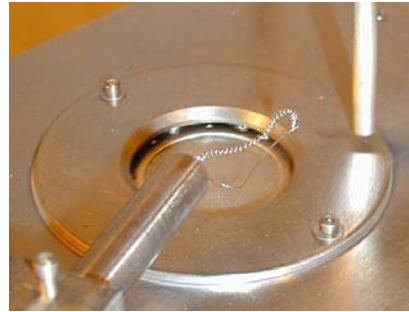
Figure 1. Isolation Box Opening, Filament Neutralizer and Stand, and Faraday Probe

Figure 2. MiXI Thruster inside open Plasma Screen

A mechanical and oil diffusion pump tandem assembly is used to produce the $\approx 1 \times 10^{-6}$ Torr base pressure vacuum environment used for testing. The vacuum is maintained within a ~1.2 m tall / 0.6m diameter bell jar vacuum chamber. The interfaces for the vacuum pumps, electrical power supply, and diagnostics are located at the base of the chamber. A simplified schematic of the electrical system and associated diagnostics is shown in Figure 3.

Thruster Configuration

The thruster configuration tested herein is a double ring cusp design with a length-to-diameter ratio of 1, as shown in Figure 4. This configuration was chosen after an extensive investigation of multiple thruster configurations [3]. Permanent samarium cobalt (SmCo) magnets are used for the discharge chamber magnetic field due to their high field strength density and high maximum operating condition. As will be discussed in the following sections, much of this investigation used an extended

American Institute of Aeronautics and Astronautics

anode configuration and the grids were often removed to allow greater visual and diagnostic access to the cathodes.

Figure 3. Electrical Diagram of the Thruster, Power Supplies, and Digital Diagnostic

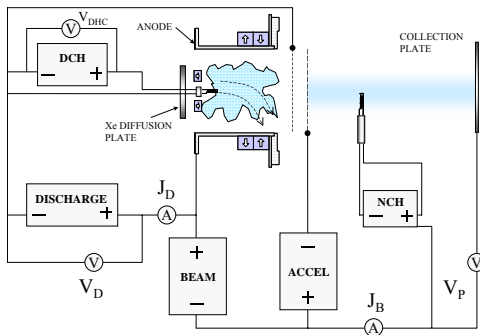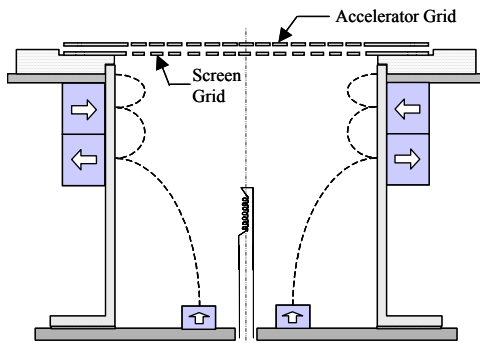Figure 4. Miniature ion thruster (not to scale)

Flow Calibration

Calibration for the propellant flow control and meter tandem is performed using a JPL-built four-channel propellant feed calibration system. The flow and flow valve voltage response was determined three separate times at every 0.300 sccm (cm^3/min) from 0.300 to 1.500 sccm. The propellant line response time was 60 minutes to accommodate the low flow rates. The flow meter display was then calibrated by comparing the voltage response of the flow control valve with a range of flow meter display values. The voltages from both calibration efforts were then used to determine the actual flow rate in sccm corresponding to given display values. The digital multimeters used for the power system diagnostics possess 0.1% DC voltage accuracy and a 0.05% DC current accuracy and are regularly calibrated on-site.

Electron Sources for the MiXI Thruster

Options

Although many different types of ion generators exist and a significant number are in development as plasma sources for ion thrusters, only four have the required performance characteristics and are sufficiently mature to be considered for the MiXI Thruster: cathodes, Radio frequency (RF) sources [5], Helicon sources [6,7], and microwave electron cyclotron resonance (ECR) sources [8,9]. Of these choices, use of a cathode source has potential for the greatest overall efficiency; and is therefore the first of the possible discharge technologies investigated for the MiXI thruster. Also, the thruster has thus far been developed using a tungsten-filament cathode discharge and the incorporation of a more robust and a lower-power cathode is a logical step in the design process.

Cathode Electron Sources

Choosing cathode materials and assemblies for the MiXI thruster requires consideration of many issues that are specific to each cathode type. In general, cathode power and propellant flow (if required to run the cathode, such as with hollow cathodes) should be low if high thruster efficiency is desired. Cathode technologies must have potential to be used in a flight-worthy design with lifetimes on the order of tens of thousands of hours and be resistant to poisoning from the discharge environment. Also, cathodes that generate a lower overall discharge chamber temperature will increase thruster performance. Specifically, a lower discharge temperature will reduce the speed, and hence, loss rate of propellant neutrals through the ion extraction grids. Also, for a magnetized discharge, lower temperature operation reduces the potential for permanent or temporary loss of magnet field strength. Low-power cathode technologies being considered for the MiXI thruster include: field emission arrays (FEA), hollow cathodes, and directly emitting thermionic cathodes.

Field Emission Array Cathodes

Low power field emitter array (FEA) cathodes have been considered an attractive candidate for the MiXI thruster [10] because of their high efficiency, < 8 μW/mA. Recent investigations have shown that this technology is well suited for neutralizing the charge build-up in small thrusters [11] if the appropriate materials and configurations are employed. Proposed advanced FEA cathode configurations such as ClaiR [12], should protect the field emission tips from being sputtered by the beam ions, but have not yet been demonstrated. Recently,

American Institute of Aeronautics and Astronautics

IrO$_2$ and NbC FEA cathodes were fabricated in an effort to demonstrate desirable performance stability in thruster environments; however, these cathodes have not yet been tested.

The ability of FEA cathodes to neutralize small thruster plumes is being investigated in a parallel effort. The current MiXI test facilities are unable to run FEA cathodes with the thruster due to the requirements for a high and extremely clean vacuum environment. However, a new ultra-high vacuum facility is being built that will allow the thruster to be run with neutralizer candidates, such as FEA cathodes, in the near future. This facility will also allow more complete characterization of thruster performance.

Hollow Cathodes

Hollow cathodes with Ba-W inserts have enjoyed much success in ion thruster applications but have not been effectively scaled to MiXI thruster capacity. The primary concern with hollow cathodes is that they need a designated propellant feed to operate. If the required flow approaches the total flow for the thruster then the efficiency of the thruster will significantly degrade. Investigations into small hollow cathodes with a 1.22mm insert ID have thus far shown that scaling down to the discharge currents and propellant flow rates of the MiXI thruster (0.2-1.1A and 0.2-1.0sccm, respectively) is difficult if the cathode is to run in self-heated mode [13,14,15]. For a hollow cathode to run self-heated at the low discharge current MiXI conditions it may need to be scaled down further and have a better thermal design than previous, low-current hollow cathodes. At this time discharge hollow cathodes are being designed for the MiXI thruster in collaboration with Semicon Corporation. These hollow cathodes will likely require some heater power to run at propellant flow rates $\leq$ 1.0sccm and currents $\leq$ 1.1A, but, as will be shown later in this paper, additional power is far less of a concern for performance than additional propellant flow. For a hollow cathode in the MiXI discharge chamber it is likely that most, if not all, of the propellant will be run through the cathode.

Directly Emitting Thermionic Cathodes

The primary advantage of the directly emitting thermionic cathodes is that they do not require a designated propellant feed and they are very simple to operate at lower discharge currents. Direct emission cathodes posses a more omni-directional electron emission when compared to hollow cathodes, and will likely require a shorter anode, and hence, less anode surface area. Since an omni-directional filament was used in the optimization of the thruster design and magnetic field thus far, a properly designed direct cathode should incorporate well with the existing thruster design. The directly emitting cathode materials considered herein are barium-calcium aluminate impregnated porous tungsten (Ba-W), lanthanum hexaboride (LaB$_6$), and cerium hexaboride (CeB$_6$).

The primary trade-off for a direct cathode is to design the emission surface to be small enough to prevent excessive radiative power losses and possible over-heating of the magnets while large enough to provide ample electron emission. The current density from a thermionic emitting surface as a function of temperature can be approximated by free electron theory using the Richardson-Dushman equation [16]

$$j = AT^2 \exp(-e\phi/kT)$$

where the emission coefficient A and the work function ϕ are specific to the emitting material, and given in Table 1 for the materials discussed in this paper. The current from the Richardson-Dushman equation is further enhanced by the presence of an applied field. This enhancement is known as the Schottky effect and results in a modified expression for the current density

$$j = AT^2 \exp(-e\phi/kT)$$
$$\left[\exp[(e/kT)\sqrt{Ee/4\pi\varepsilon_o}] \right]$$

where E is the field intensity at the cathode surface. The electron emission from a given cathode surface can be limited by the cathode's maximum thermionic emission current density at a given temperature (see Table 2) or by space-charge limiting effects. The space charge limit depends on the plasma parameters; specifically on the ion density and the electron temperature near the cathode by the relation

$$j_e = \frac{\kappa}{2} n_i e \sqrt{\frac{kT_e}{m_e}}$$

where n is the plasma density and κ is a constant usually about 1/2.

The cathode is heated to emission temperatures either directly by ohmic heating or indirectly by a heater. The heat is primarily lost by radiation from the exposed surface areas and by conduction through the supports and heater leads. The cathode also experiences electron evaporative cooling $J_e\phi$ and, in the presence of a plasma at potential V, ionic heating J_iV.

Another consideration for direct cathodes is their resistance to poisoning. According to Reference [17], the critical poisoning gas pressure for oxygen,

carbon dioxide, air, hydrogen, nitrogen, and argon are several orders of magnitude higher for LaB_6 than for Ba-W. This comparison was made at temperatures of about 94% of T_{max} for the respective cathodes.

Candidate Cathode Materials

The properties of the directly emitting cathode materials used in this investigation are shown in Table 1. The work function for the materials will increase with temperature, however, the nominal values given characterize the relative emission performance. A tungsten filament was used for the discharge in previous investigations of MiXI thruster performance [3,4] and is currently being used as a placeholder for the neutralizer cathode. Tungsten is not being considered for the final discharge cathode design due to the lower operating temperatures and work functions of the other cathodes. Ba-W

possesses the lowest operating temperature and work function but has lower j_{max}, a higher evaporation rate, and greater poisoning potential than the hexaborides. From these values we see that, for an equally sized cathode, the Ba-W will operate at lower temperatures, and likely power. If the space-charge limit for higher MiXI discharge currents is in excess of 10 A/cm^2 then a hexaboride cathode, due to higher j_{max}, may be sized smaller than a Ba-W for a similar discharge.

Table 2 is a summary of the discharge cathodes being considered for the MiXI thruster. In this table, both the hollow and dispenser cathodes use Ba-W, however the dispenser configuration is exposed directly to the discharge plasma environment and is therefore more susceptible to contamination.

Table 1. Properties of several candidate cathode materials.

Cathode Material	A, Emission Constant (A/cm^2/K^2)	ϕ, Work Function (eV)	j_{max}, Max Emission Density (A/cm^2)	T_{max}, Max Operating Temperature (°C)
Ba-W	120	2.14	10	1190
LaB$_6$	29 (120)	2.66 (2.8)	30	1675
CeB$_6$	29	2.43	~30	~1675
W	70	4.5	1	2350

Table 2. Thermionic cathode relative comparison.

Thermionic Cathode Option	Hollow (Ba-W)	Dispenser (Ba-W)	Hexaborides (LaB$_6$, CeB$_6$)
Advantages	- Lower temperature (~1100°C) - Possibly very low power due to self-heating	- Lower temperature (~1100°C) - Low heater power	- High current density - Higher critical poisoning pressure
Disadvantages	- Typically high current (2-35A, MiXI range 0.2 – 1.1 A) - High propellant flow required for low current (typically >2sccm, MiXI range: 0.2 –1.0sccm)	- Lower current density - Low critical poisoning pressure	- Higher temperature (~1400°C)
Work Function	2.14	2.14	LaB$_6 \approx 2.6$ CeB$_6 \approx 2.43$

Summary of Discharge Cathode Options

Field Emission Array (FEA) cathodes are currently not being considered for the discharge due to the additional development work required but are a lead candidate for the neutralizer cathode.

Ba-W hollow cathodes are used for ion thrusters because the configuration allows for greater emission densities for a given size and minimizes the exposure of the insert to the plasma environment to avoid insert erosion and contamination. However, making a hollow

American Institute of Aeronautics and Astronautics

cathode operate stably in the self-heating mode at the very low MiXI discharge currents is challenging and will be left for a future effort.

Directly emitting Ba-W dispenser cathodes are commonly used as the electron source in microwave tubes, in gas lasers, and in some CRT (cathode-ray-tube) displays and other vacuum devices, but are typically not used in heavy ion plasma discharges like the MiXI-type discharge plasma environment due to rapid sputtering and erosion of the emission surface by the ion bombardment.

LaB_6 is used in both hollow cathode configurations and directly emitting applications including hollow cathodes for Hall thrusters, discharge cathodes in industrial "ion plating" plasma coaters, and field emitter cathodes for scanning electron microscopes (SEM). At the temperatures required by the LaB_6 for significant emission, typical hollow cathode configurations run at much higher currents than that required for the MiXI thruster. LaB_6 is sufficiently robust to handle the ion bombardment from the medium density MiXI-type plasma, and is capable of a very high current density so that it may simply be used in a directly emitting cathode configuration.

CeB_6 is believed to be essentially interchangeable with LaB_6 for many applications. Vendor data [18] shows that CeB_6 has a lower work function and comparable resistance to contamination. CeB_6 also has a lower evaporation rate below 1600°C for good vacuum conditions. However, published information on CeB_6 performance is relatively scarce, so additional efforts will have to be taken to assess its potential as a MiXI discharge source.

Additional Plasma Sources

The most likely "cathodeless" electron plasma-source candidates for the MiXI discharge are RF, helicon, and microwave sources. These sources are potentially attractive because they do not use thermionic cathodes, which in principle can limit the life of thrusters with DC electron discharges.

RF sources operate in the radio frequency band, and efficient sources have been reported in the range of 1 to 100 MHz. In practice, RF sources tend to be designed around existing RF hardware where low cost RF generators and tuning networks exist at 1 MHz, 13.5 MHz, and 26 MHz. RF sources typically utilize an inductively coupled antenna isolated from the plasma by an insulator (quartz). The antenna produces an electric field that decreases away from the antenna and that is varying slowly compared to the local electron transient times. Electrons passing through this region are accelerated in this electric field and collisional processes result in net heating of the electron population in the plasma. RF plasma source can be very efficient, and RF ion thrusters have been under development in Europe and Japan for some time. An RF discharge source may result in a reduction of weight when compared to other sources that require permanent magnets. While this has not been pursued to date at JPL, this plasma generator is considered a good future candidate as a MiXI discharge source.

Helicon sources also operate in the RF band, but utilize a more complex antenna compared to RF sources and a relatively strong axial magnetic field to couple energy into the electron distribution via decay of an excited plasma wave. Helicon sources also have an insulator between the antenna and the plasma, and sufficient magnetic field can be produced by permanent magnets to make a small diameter, highly efficient plasma source. Unfortunately, helicon sources tend to be relatively long in the axial dimension (some finite fraction of a wavelength), and therefore have not been considered sufficiently compact for MiXI use.

Microwave plasma sources typically operate in the 1 to 10 GHz regime, and couple energy to the electron distribution by electron cyclotron resonance (ECR) heating. The required microwave frequency is just the cyclotron frequency $\omega_c = eB/m_e$, which corresponds to a frequency, f_c, of 2.8 GHz/kGauss, and higher frequency operation requires higher magnetic field strengths for the resonance conditions to be achieved. This can be an issue in ion thruster applications because the cutoff frequency for the microwaves in the plasma is just the plasma frequency $\omega_p = (ne^2/\varepsilon_o m)^{1/2}$, which corresponds to a frequency $f \approx 9000n^{1/2}$ for a density in cm^{-3}. To produce sufficiently high plasma densities to generate the ion current density required by the optics system, the plasma frequency can be in the GHz range. This density requirement then forces the use of several kilogauss magnetic fields to reach the electron cyclotron frequency that is not below cutoff.

There are two common configurations for ECR sources. First, a solenoidal magnetic field of sufficient strength is generated throughout the plasma volume, and the ECR resonance occurs everywhere the thruster body. Alternatively, strong cusp magnetic fields are used where the

American Institute of Aeronautics and Astronautics

ECR resonance occurs in a layer within the cusp region near the wall. The microwaves are then coupled to the resonance layer in the cusp, where trapped electrons are heated and produce ions. Due to this lossy configuration of electron heating and ion production close to the wall, the discharge efficiency of microwave source is typically lower than other types of discharge sources. In addition, the complexity of generating the microwaves using traveling wave tubes (TWTs) or magnetron sources and coupling the sources to the relatively small MiXI thruster makes this a less attractive plasma source option.

At this time, all of these RF/microwave plasma source approaches were rejected because of poor scalability to the very small discharge chamber, poor SOA efficiency, high specific mass, and low efficiency of the power supplies. In addition, there is some concern about the potential for new thruster failure modes associated with the antenna and coupling structure.

Results

Thruster Performance vs. Cathode Performance

To determine the best cathode for the MiXI thruster we should first consider the effect of cathode performance on the efficiency of the thruster. Table 3 shows the performance range of the thruster as reported in Reference [4], and actual and projected thruster operating conditions, OC1 and OC2. OC2 is a prediction of the highest throttle level of the thruster allowable with the small hole accelerator grid (SHAG) optics described in [4]. The maximum beam current for OC2 was determined using the optics code CEX2D, from Reference [19], and assuming a beam flatness parameter of 0.6. The mass flow rate and discharge current predicted for OC2 were determined by using a linear fit to data for a range of beam currents obtained using SHAG optics. These data are shown in Figures 5 and 6. The relationships used to calculate the performance are in Reference [3].

Using OC1 and OC2 from Table 3 and curve fits of thruster data, we can make predictions of thruster efficiency based on cathode performance. Figure 7 shows the effect of excess propellant flow, beyond what is needed for the discharge, on propellant efficiency. For example, if a hollow cathode that requires designated propellant flow is used for the neutralizer, this curve reflects the effect of that propellant flow on efficiency. If we assume the operating conditions shown in Table 3, these values may also be used to predict the effect of a discharge hollow cathode that requires more flow for a given discharge condition than is needed with a cathode that does not require a designated propellant flow.

Table 3. MiXI Performance

Parameter	Range*	Operating Condition 1* (OC1) (Actual)	Operating Condition 2* (OC2) (Projected)
V_B	700 – 1126 V	1089 V	1100 V
V_D	23.5 – 29 V	25 V	25 V
J_B	7 – 28 mA	28.3 mA	54.5 mA
J_D	70 - 500 mA	503 mA	1098.7 mA
$\dot{m}_{prop}$	0.17 – 0.57 sccm	0.51 sccm	0.81 sccm
Power	14 – 43 W	43.4 W	87.4 W
$P_{chamber}$	6.3E-6 – 2.0E-5 Torr	1.3E-5 Torr	
T	180 – 300°C	280 °C	
Thrust	0.4 – 1.5 mN	1.553 mN	3.0 mN
I_{sp}	1764 – 3184 s	3184 s	3864 s
ε_B	450 – 743 eV/ion	444 eV/ion	504 eV/ion
η_u	0.48 – 0.82	0.79 0.40 (w/ 0.5sccm excess flow)♠	0.95 0.59 (w/ 0.5sccm excess flow) ♠
η_{tot}	0.31 – 0.56	0.56 0.42 (w/ 15 W total cathode pwr) ♠ 0.21 (w/ 15 W and 0.5sccm excess flow) ♠	0.65 0.51 (w/ 25 W total cathode pwr) ♠ 0.31 (w/ 25 W and 0.5sccm excess flow) ♠

*Values ignore doubly-charged ions, beam divergence, and cathode input power (unless specified).
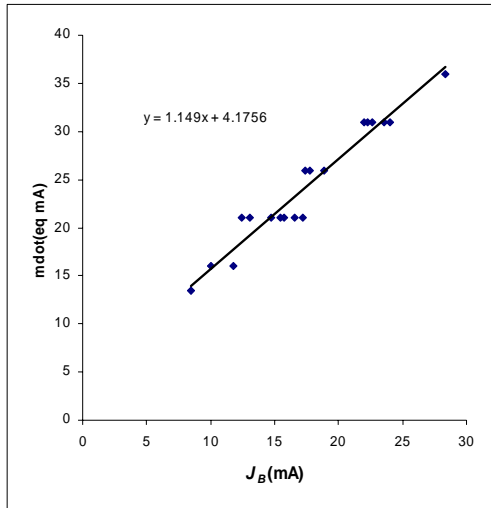♠Values obtained using parametric analysis (see below).
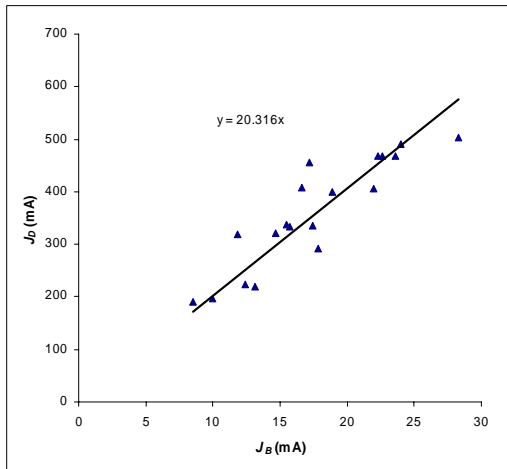
Figure 5. $\dot{m}$ vs. J_B

$y = 1.149x + 4.1756$
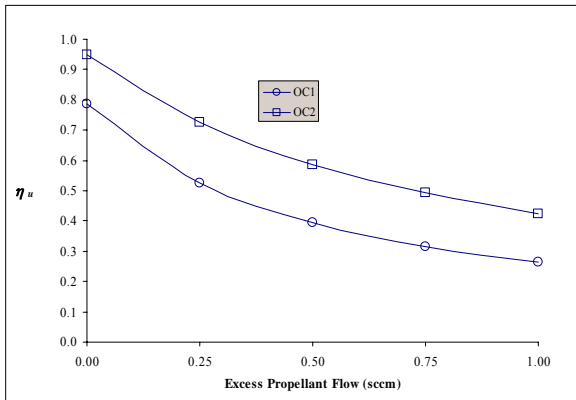

Figure 6. J_D vs. J_B

$y = 20.316x$

Figure 7. Effect of Excess Propellant Flow on Propellant Efficiency

Similarly, Figures 8 & 9 show the effect of cathode input power and excess propellant on the total efficiency of the thruster. From these figures it appears that adding 0.25sccm of excess propellant flow with no cathode power reduces thruster efficiency as much as adding 20-25W of cathode power with no excess flow. According to these results, it is important that the cathode not require excess propellant flow if at all possible. However, as discussed earlier, it is important to keep the cathode power low enough so as to not overheat the permanent magnets.
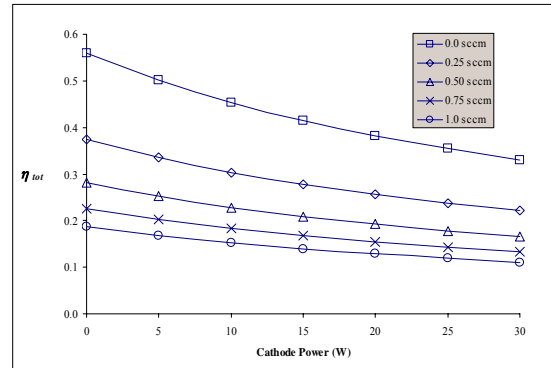
Figure 8. Total Efficiency vs. Cathode Power and Excess Propellant Flow for OC1
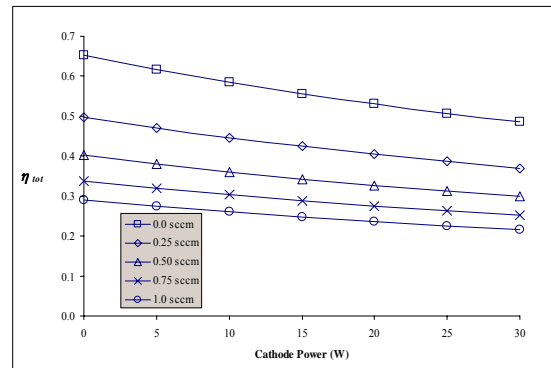
Figure 9. Total Efficiency vs. Cathode Power and Excess Propellant Flow for OC2

Direct Emission Cathode Performance

Direct emission cathode assemblies using LaB_6, CeB_6, and Ba-W were tested in the MiXI vacuum facilities. The focus of these tests was to determine the potential for these materials to be used in a direct emission configuration for the MiXI thruster. The 1/8" Ba-W dispenser cathode is shown mounted to base of the thruster in Figure 10. This assembly uses a tantalum heat

American Institute of Aeronautics and Astronautics

shield to reduce heat radiation from the potted heater located directly behind the Ba-W disk.

Figure 10. Ba-W Dispenser Cathode

The LaB6 and CeB6 were used in a Vogel-mounted configuration where the cathode material is sandwiched between to pyrolytic graphite blocks as shown in Figure 11. The graphite blocks and cathode are held together by two molybdenum-rhenium arms that are braised to an alumina disk. The blocks, due to high cross-plane resistance, serve as the cathode heaters. These cathodes were not outfitted with a heat shield.

Figure 11. Vogel-Mounted Cathodes
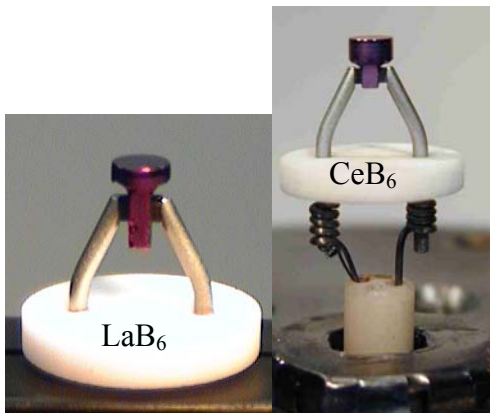
During initial testing, the cathodes were mounted such that the upstream most end of the cathode was ~1.2cm from the ion extraction grids, similar to the placement of the tungsten filament cathodes in previous tests. This configuration was well-suited for the Vogel-mounted cathodes since, like the filament cathodes, there is considerable emissive surface oriented in the radial direction. Both the CeB6 and LaB6 achieved very high currents at relatively low temperatures when they were first run. For example, the CeB_6 achieved a total emission of over 160mA at ~1150°C, which

required only 7.5W of heater power. The LaB_6 achieved a discharge current of 850mA with the extended anode at 28V discharge and ~4.7e18 neutral density. The current density for the LaB6 at this condition is 3.2A/cm^2.

Initial tests and Faraday probe data for the Ba-W cathode showed that most of the electron current was directed axially and was unable to be collected by the 3cm anode configuration. Consequently, a 2cm extension was added to the base of the anode to accommodate the Ba-W cathode. To mimic the 3cm anodes magnetic field an additional cathode magnet was added to the thruster when the 5cm anode was used. This additional magnet added about 0.3cm to the height of the cathode in the chamber such that with the 5cm anode the cathodes were ~2.9cm from the grids. Using the extended anode configuration at a 0.85sccm propellant flow, the Ba-W exhibited a current density of 8A/cm^2 at an approximate neutral density of 8e18m^{-3}, a discharge voltage of 32V, and a discharge current of 634mA. This performance was obtained with under 10 W of heater power to the Ba-W cathode. The surface are of the Ba-W was ~1/3 that of the hexaborides.

The data thus far mentioned represent operating points for the cathodes, however, cathode performance was not fully assessed due to cathode material poisoning. The primary culprit for poisoning of the cathodes was found to be oxygen. Residual Gas Analyzer (RGA) traces of the background chamber pressures found that oxygen levels, due to high water content, were sufficient to explain the poisoning of Ba-W cathode but not to explain the level of poisoning for the hexaboride cathodes[Ref Gallagher]. This was further demonstrated by the fact that the hexaboride cathodes would regain high emission currents after bake-out, while the Ba-W got progressively worse after each bake-out.

The CeB_6 was the first cathode to be run in the thruster and was therefore the cathode most thoroughly analyzed for poisoning mechanisms. A scanning electron microscope (SEM) was used to take before and after images of the CeB6 surface as shown in Figure 12. Auger analysis of the CeB_6 surface shows that contamination is caused primarily by oxygen and partly by carbon. The Auger results also show that heavy metals, such as molybdenum from the grids, were not responsible for CeB_6 cathode poisoning. Consequently, for the 10s of hours the cathode was run in the presence of the

molybdenum grids, no noticeable condensation of heavy metals was noticed on the cathode. In addition, over 75% of the CeB_6 tests were performed with the cathode only 1.2cm from the grids. From a thruster integration standpoint these are very important results since the vaporization temperature of most heavy metals, including molybdenum, is above the operating temperature of the cathode and therefore can constitute a contaminant that cannot be baked off.
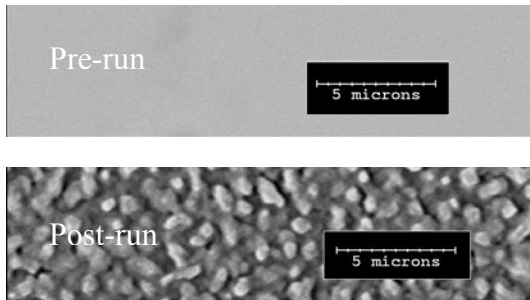

Figure 12. Pre-run and Post-run SEM images for CeB6

By running a cathode at higher temperatures, the effects of poisoning can be reduced or eliminated [15]. However, it was found that emission reduction for the hexaboride cathodes was still quite substantial at higher temperatures when in discharge mode. Since the hexaboride cathodes' emission could be recaptured after high temperature bake-out, the cathode poisoning for the hexaborides appeared to be related to the discharge and not the background pressure. RGA traces of the propellant showed flow showed that no appreciable cathode poisoning gases are introduced in the propellant flow. By comparing the results of cathode tests with and without the grids, and inspecting the surface of the MACOR structure used to mount the grids, it is apparent that some oxygen poisoning may arise from the presence of the MACOR. MACOR is composed of 96% oxide compounds [20] and sputtering of these compounds in a discharge condition could result in a high presence of oxygen on the cathode surfaces. Similarly, the alumina disk used for the Vogel-mounted cathode may also increase the potential for oxygen poisoning of the cathode surface. To see if the alumina disk was contributing to the emission reduction of the cathode, nickel foil was wrapped around the alumina disk to reduce the alumina surface exposed to the plasma. With nickel foil in place the stable emission current of

the LaB_6 cathode was increased by over 10%. However, more investigation is required to fully explain the poisoning mechanisms.

Conclusions

Predictions of the interrelationship of cathode and thruster performance show that it is desirable to use cathodes that do not require propellant flow beyond what is needed for the discharge. Consequently, the use of a hollow cathode neutralizer will likely result in poor overall thruster efficiency. The cathode tests show that the space-charge limit at the discharge cathode is greater than $8.0A/cm^2$ for 0.85sccm of propellant flow. Consequently, the predicted discharge current for OC2 should be easily obtainable with a direct emission cathode. Also, for the discharge current desired, the hexaboride cathode size can be smaller, which will result in lower cathode power due to the reduction of radiative losses. The hexaboride cathodes would also benefit from a better thermal design. The Ba-W cathode will likely perform well with 3cm anode if the emitting surface was shaped in a more omni-directional fashion.

The current MiXI diffusion pump vacuum facilities are inadequate for the use of Ba-W cathodes and will be upgraded before future cathode tests are conducted. Since Ba-W hollow cathode testing and additional direct emission cathode testing must be performed, the upgrades to the current facilities are required. Also, for future tests materials comprised of oxide compounds should not be exposed to the plasma discharge to avoid cathode contamination. Contamination of the cathodes from the thruster grids has not been shown to be an issue.

Future Work

To optimize the direct emission cathode design it would be helpful to find the space-charge limit at the cathode for the full range of MiXI discharge operating conditions. Also, a better thermal design of the hexaboride cathodes and a more omni-directional design for the Ba-W cathode are necessary to make an accurate comparison of the relative performance of these cathode materials in the MiXI discharge. Once improvements to the MiXI vacuum facilities are made, comparative test of direct emission cathodes and hollow cathodes will be performed for the MiXI discharge. The use of an

RF/microwave discharge and FEA neutralizers will also be investigated further.

Beyond the cathode work discussed herein, possible improvements to the existing magnetic field and grid design are being investigated. In particular, a parametric and computational investigation of the grid optics is currently underway. Also, analytical and experimental investigations will be used to look at the possible benefits of modifications to the exiting magnetic field design.

Acknowledgements

References

[1] – Mueller J., et al., "An Overview of MEMS- Based Micropropulsion Developments at JPL," IAA Paper B3-1004, 3rd International Symposium on Small Satellites for Earth Observation, International Academy of Astronautics (IAA), Berlin, Germany, April 2001

[2] – Mueller J., "Thruster Options for Microspacecraft" from "Micropropulsion for Small Spacecraft" Volume 187 Progress in Astronautics and Aeronautics © 2000

[3] – Wirz R., et al., "Development and Testing of a 3cm Electron Bombardment Micro-Ion Thruster," IEPC Paper 01-343, 27th IEPC, Pasadena, CA, Oct 2001

[4] – Wirz R., et al., "Experimental and Computational Investigation of the Performance of a Micro-Ion Thruster," AIAA-2002-3835, 38th JPC, Indianapolis, IN, July 2002

[5] - H. Leiter, R. Killinger, H. Bassner, J.Müller, R. Kukies, T. Frøohlich, "Evaluation of the Performance of the Advanced 200 mN Radio Frequency Ion Thruster RIT_XT", 38th JPC, AIAA 2002-3836

[6] - Boswell RW, Chen FF, "Helicons - The early years", IEEE T PLASMA SCI 25 (6): 1229-1244 DEC 1997

[7] - Chen FF, Boswell RW, "Helicons - The past decade", IEEE T PLASMA SCI 25 (6): 1245-1257 DEC 1997

[8] - Toki, K., et al., "Technological Readiness of Microwave Ion Engine System for MUSES-C Mission," IEPC-01-174, 27th International Electric Propulsion Conference, Pasadena, CA, 15-19 October, 2001

[9] - S.Tamaya, I.Funake, M.Murakami, H. Kuninaka, "Plasma Production processes in an ECR Ion Thruster", 33rd AIAA Plasma Dynamics and Lasers Conference, AIAA 2002-2196, 2002

[10] - Marrese-Reading C., Polk J., Mackie B., Dandeneau D., Koel B., Quinlan M., "Field Emission Array Cathode Material Selection For Compatibility With Electric Propulsion Applications," 100th Electrochemical Society Conference, 2002

[11] - Marrese, C.M., Polk, J., Mueller, J., Owens, A., Tajmar, M., Spindt, C., Fink, R., "In-FEEP Thruster Ion Beam Neutralization with Thermionic and Field Emission Cathodes," IEPC Paper No. 01-290, 27th IEPC, October 2001, Pasadena, CA

[12] - Marrese, C. M., Mackie, W.A., Evans, D., and Gallimore, A. D., "The Design of a Cathode to Operate in an Oxygen-Rich Environment," STAIF Paper No. 97-224, Space Technology and Applications International Forum, January 26-30, 1997, Albuquerque, NM

[13] – Domonkos M., "Evaluation of Low-Current Orificed Hollow Cathodes," Ph.D. Thesis, University of Michigan, 1999

[14] – Domonkos M., "An Evaluation of Hollow Cathode Scaling to Very Low Power and Flow Rate," IEPC-97-189

[15] – Domonkos M., "Low-Current Hollow Cathode Evaluation," AIAA-99-2575

[16] – Forrester A., "Large Ion Beams," ©1988

[17] – Gallagher H., "Poisoning of LaB$_6$ Cathodes" Journal of Applied Physics, 40, 44 (1969)

[18] – FEI Company, Beam Technology Division correspondence

[19] - Brophy J.R. Katz I., Polk J., Anderson J., "Numerical Simulations of Ion Thruster Accelerator Grid Erosion," AIAA-2002-4261, 38th AIAA/ASME/SAE/ASEE Joint Propulsion Conference & Exhibit, Indianapolis, IN, July 2002

[20] - Corning Incorporated "Lighting and Materials" 2003 Catalogue

- Appendix F -

Magnetostatic Theory and Results

The Discharge Model requires magnetic field solutions for the Electron Collision, Ion Diffusion, and Electron Thermal sub-models. The Ion Diffusion and Electron Thermal models require the magnetic field only at the centers of the elements and edges of the Internal Mesh. The Electron Collision model requires much greater resolution since the primary electron particle algorithm requires the magnetic field at any location in the chamber. The following discussion presents a magnetic dipole approximation that is sufficiently fast to allow the magnetic field to be calculated at every step in the primary tracking algorithm. A simple magnetic dipole approximation yields significant errors in the near field so a simple method for approximating the permanent magnet near-field is used.

Magnetostatic Solution

The magnetic rings for ion thrusters are typically composed of many rectangular magnets. The field due to the individual permanent magnets is approximated by discrete magnetic dipole moments whose orientation and strength are determined by entering the magnet properties, sizes, number per ring, 2-D location of the ring, magnet orientation, and temperature. With this information the magnetic flux density vectors, B (Tesla), and the magnetic vector potential, A (Tesla·meters), are determined at any point by summing the effects of all magnets. The NSTAR thruster has ~200 magnets, but even for this number of magnets the simple method presented below yields very short runs times in comparison to other aspects of the code.

The magnetic field due to a permanent magnet can be approximated from the "magnetic scalar potential" Φ_M, which is defined by

$$\vec{B} \equiv -\nabla \Phi_m \qquad\qquad \text{[F-1]}$$

Since $\nabla \cdot \vec{B} = 0$, the magnetic scalar potential satisfies Laplace's equation

$$\nabla^2 \Phi_m = 0 \qquad\qquad \text{[F-2]}$$

Assuming the field for the magnet is azimuthally symmetric and approaches zero as $r \to \infty$, the solution for the harmonic function Φ_M can be expressed using Legendre polynomials, P_k, by

$$\Phi_m(r,\theta) = \sum_{k=0}^{\infty} \frac{m_k}{r^{k+1}} P_k(\cos\theta) \qquad\qquad \text{[F-3]}$$

The series coefficients, m_k, represent the strength of the magnetic moments of the multipole expansion. For this Fourier-type expansion of Legendre polynomials it can be shown that even indexed coefficients are zero for magnetostatic solutions. Combining Equation F-1 and the first nontrivial term from Equation F-3 yields the dipole approximation of the magnetic flux density, $\vec{B}$, as

$$\vec{B}(r,\theta) = \frac{m_1}{r^3}\left[2\cos(\theta)\hat{r} + \sin(\theta)\hat{\theta}\right] \qquad \text{[F-4]}$$

For permanent magnets the dipole magnetic moment, m_1, is determined from the magnet perveance specification, B_R, and volume, V_m, by the relation

$$m_1 = \frac{B_R V_m}{4\pi} \qquad \text{[F-5]}$$

The analytical solution for the magnetic field along the axis of permanent magnet is

[F-6]
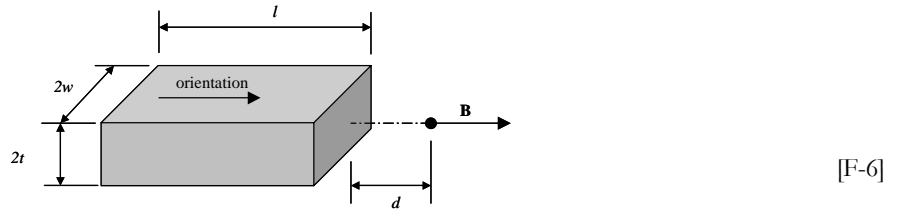
$$B(r,\theta=0) = \frac{B_R}{\pi}\left[\tan^{-1}\left(\frac{d+l}{tw}\sqrt{t^2+w^2+(d+l)^2}\right) - \tan^{-1}\left(\frac{d}{tw}\sqrt{t^2+w^2+d^2}\right)\right]$$

For the magnet sizes used in the NSTAR and Micro-Ion thrusters, the dipole approximation from equations F-4 and F-5 is within 20% of the on-axis permanent magnet values beyond $d = 1$ cm from the magnet face but the error is >50% at $d = 0.5$ cm. Initially, the higher-order terms of the multipole expansion were employed in an attempt to increase the accuracy of the magnetostatic solution near the magnets. This approach yielded mixed results, so a different approach was used. By assuming the near magnet field contours to be spherical, the on-axis permanent magnet analytical solution could be used to correct the field magnitude from the dipole approximation. Therefore, in the near magnet region (r<2cm) the dipole field was used to calculate the B-field unit vector and the permanent magnet solution was used to correct the magnitude. In regions within d_{max} of the magnet the magnetic field magnitude was approximated by

$$\left|B(r,\theta)\right| \approx \frac{d_{max}-r}{d_{max}}\left|B_p(r)\right| + \frac{r}{d_{max}}\left|B_d(r,\theta)\right| \qquad \text{[F-7]}$$

where B_p is the permanent magnet solution from Equation F-6 and B_d is the dipole solution from Equation F-4. For the magnets sizes used herein, $d_{max} = 2$cm gave a maximum error of <40% on-axis and yielded reasonable off-axis agreement as shown later in the Micro-Ion B-field comparison.

The cylindrical (r, z) coordinate system of the dipole approximation was transformed so that arbitrary magnetization directions could be used. In a Cartesian $\bar{x} = (x, y, z)$ reference frame, the magnetic field contribution at location $\bar{x}_o$, from a magnetic

multipole centered at $\bar{x}_m$ oriented in the $\hat{m}$-direction, may be determined using Equation F-7 and simple vector analysis. The vector between the magnetic multipole and $\bar{x}_o$ is simply

$$\bar{r} = \bar{x}_o - \bar{x}_m \qquad\qquad\text{[F-8]}$$

where, from Equation F-7 $r \equiv |\bar{r}|$. The $\hat{\theta}$-direction is defined by first crossing the $\hat{m}$- and $\hat{r}$-directions, then crossing that result again with the $\hat{r}$-direction resulting in the expression

$$\hat{\theta} = (\hat{m} \times \hat{r}) \times \hat{r} \qquad\qquad\text{[F-9]}$$

where $\hat{r} \equiv \bar{r}/|\bar{r}|$ is the unit vector in the $\hat{r}$-direction in Cartesian coordinates. The trigonometric functions from Equation F-7 are then

$$\cos\theta = \hat{m} \cdot \hat{r}$$
$$\sin\theta = -\hat{m} \cdot \hat{\theta} \qquad\qquad\text{[F-10]}$$

The B-field in the $\hat{r}$- and $\hat{\theta}$-directions is defined by

$$\bar{B}(r,\theta) \equiv B_r \hat{r} + B_\theta \hat{\theta} \qquad\qquad\text{[F-11]}$$

The B-field from Equation F-7 can presented in the Cartesian coordinate frame of the multipole using the relations

$$B_x = B_r \hat{r} \cdot \hat{x} + B_\theta \hat{\theta} \cdot \hat{x}$$
$$B_y = B_r \hat{r} \cdot \hat{y} + B_\theta \hat{\theta} \cdot \hat{y} \qquad\qquad\text{[F-12]}$$
$$B_z = B_r \hat{r} \cdot \hat{z} + B_\theta \hat{\theta} \cdot \hat{z}$$

where

$$\bar{B}(\bar{x}) \equiv B_x \hat{x} + B_y \hat{y} + B_z \hat{z} \qquad\qquad\text{[F-13]}$$

and $\hat{x}, \hat{y}, \hat{z}$ are unit vectors.

For a simple dipole analysis these equations reduce to an expression for the magnetic flux density, as a function of $\bar{r}$, as

$$\bar{B}_{dipole}(\bar{r}) = \frac{m_1 \left(3(\hat{r} \cdot \hat{m})\hat{r} - \hat{m}\right)}{r^3} \qquad\qquad\text{[F-14]}$$

In Jackson [75] this expression was derived by taking the curl of the magnetic *vector* potential, A_m, for a simple magnetic dipole

$$\bar{A}_{m,dipole}(\bar{r}) = \frac{m_1 (\hat{m} \times \bar{r})}{r^3} \qquad\qquad\text{[F-15]}$$

since, by definition

$$\bar{B} \equiv \nabla \times \bar{A}_m \qquad\qquad\text{[F-16]}$$

Returning to Equation F-3, the dipole approximation of the magnetic *scalar* potential, Φ_m, is simply

$$\Phi_{m,dipole}\left(r,\theta\right) = \frac{m_1 \cos\theta}{r^2} \qquad\qquad [\text{F-17}]$$

Combining this with Equation F-10 gives the result

$$\Phi_{m,dipole}\left(\vec{r}\right) = \frac{m_1\left(\hat{m}\cdot\vec{r}\right)}{r^3} \qquad\qquad [\text{F-18}]$$

Comparison of Magnetostatic Field Solution with Measurements

NSTAR Thruster

Figures F-1 and F-2 show the results of the magnetostatic model versus data of experimental measurements of four thrusters (NKO, NSTAR, NSTAROct02, and CBT) that all use the exact NSTAR magnetic field design. These comparisons are indicative of the very good agreement that was found with all the NSTAR magnetic field data (Figure F-3)

Figure F-1. Comparison of magnetostatic B_z solution with NSTAR magnetic field measurements on thruster axis (r=0cm)
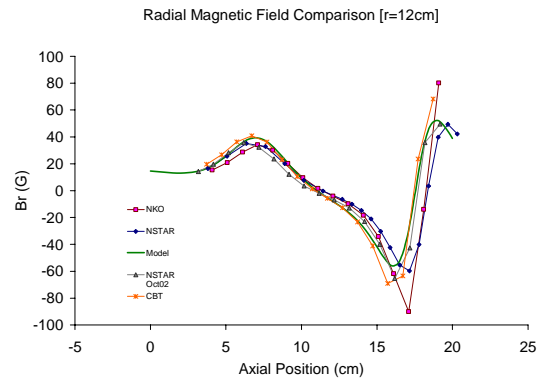
Figure F-2. Comparison of magnetostatic B_r solution with NSTAR magnetic field measurements near the anode surface (r=12cm)
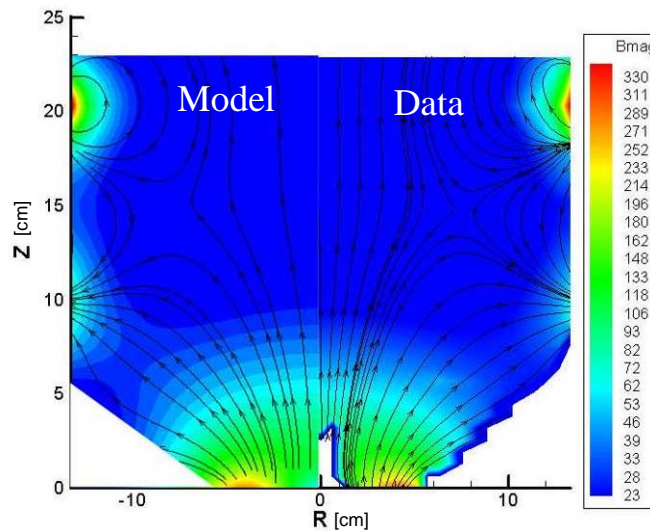
Figure F-3 Comparison of magnetostatic |B| solution with NSTAR magnetic field data [Gauss]

Micro-Ion Thruster

The magnetic field comparisons in figures F-4 and F-5 show that the agreement of the magnetostatic solution is not nearly as good at the small Micro-Ion thruster scale; however, the contour plots in Figure F-6 show that the general shape and strength of the magnetic field is approximated.

Figure F-4. Comparison of magnetostatic |B| solution with Micro-Ion magnetic field measurements on thruster axis (r=0)
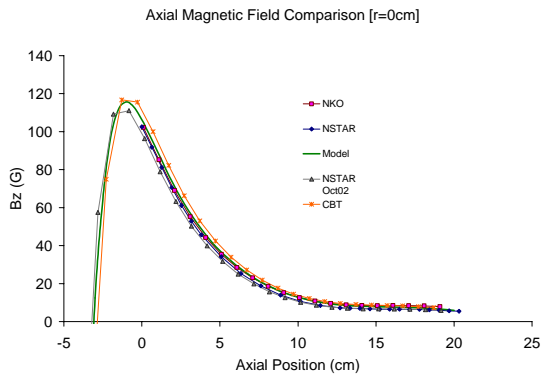

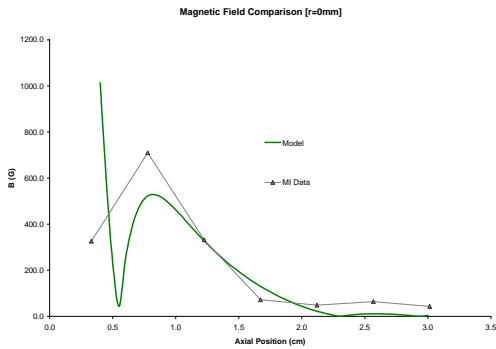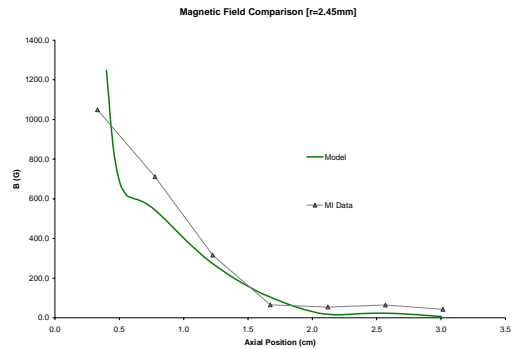Figure F-5. Comparison of magnetostatic |B| solution with NSTAR magnetic field measurements off thruster axis (r=2.46mm)
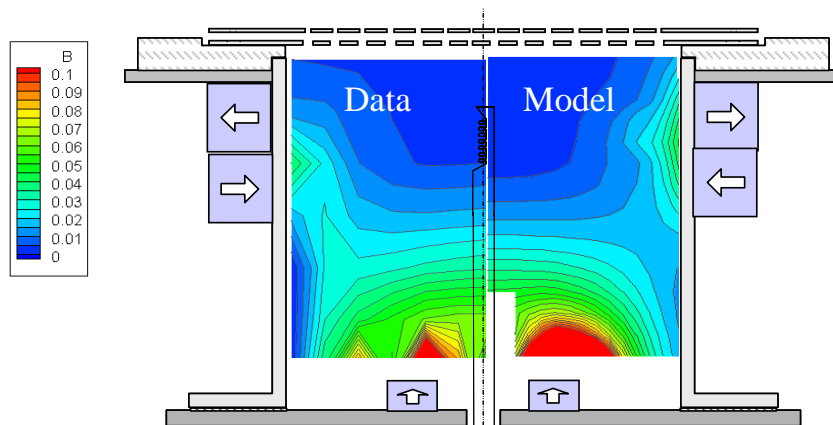
Figure F-6. Comparison of magnetostatic |B| solution with Micro-Ion magnetic field contours [Tesla]

- Appendix G -

Plasma and Computational Formulations

Electron Collisions

The rate constants for electron collision with heavy species (neutral atoms and ions) is found by assuming that the heavy species velocity is negligible compared to the electron velocity, such that

$$K = \int_0^\infty w f(w) \sigma(w) dw \qquad \text{[G-1]}$$

where, $f(w)$ is the velocity distribution of the electrons and $\sigma(w)$ is the collision cross-section as a function of velocity.

Electron Velocity Distributions

The velocity distribution for the secondary electrons is assumed Maxwellian by

$$f_M(w) = 4\pi w^2 \left(\frac{m}{2\pi k T_s} \right)^{3/2} \exp\left(-\frac{mw^2}{2kT_s} \right) \qquad \text{[G-2]}$$

where T_s is the temperature of the secondary electron population. The velocity distribution of the primary electrons is assumed to depend on the type of cathode used. For a hollow cathode the electrons are assumed to thermalize in the cathode insert plasma before being introduced [73]. As discussed in Medicus [76], the acceleration of this thermalized population of electrons by the discharge voltage results in an accelerated half-Maxwellian distribution function for the primaries. The distribution is half-Maxwellian since all of the velocity components directed into the cathode are missing from the full-Maxwellian. Following Medicus [76], the half-Maxwellian velocity distribution for electrons at temperature Tp, that are accelerated through a potential Vp, is described by

$$f_{HM}(\alpha) = \frac{2}{E(\alpha_o)}\alpha(\alpha - \alpha_o)\exp(-\alpha^2)$$

[G-3]

where

$$\alpha = \sqrt{\frac{V_p + 3T_p}{T_p}}$$

$$\alpha_o = \sqrt{V_p/T_p}$$

[G-4]

$$E(\alpha_o) = \int_{x=\alpha_o}^{\infty} \exp(-x^2)dx$$

For this model, the accelerating potential, V_p, is assumed to manifest entirely at the cathode exit and is approximated by summing the potentials seen by the primary electron as it leaves the cathode. The electrons emitted from the cathode are assumed to start at the cathode operating voltage, V_c, and accelerate through the remaining discharge voltage and average plasma potential with respect to anode, ϕ, such that

$$V_p = V_D + \phi - V_c$$

[G-4]

For the primary particle-tracking algorithm in Chapter 3, it is useful to use the average velocity of the primary. The average velocity for a velocity distribution, $f(w)$, is

$$\langle w \rangle = \int_0^{\infty} wf(w)\,dw$$

[G-5]

This velocity is used to determine the average energy of the primaries to determine the source terms for the Electron Thermal Sub-Model by $\langle \varepsilon_p \rangle = \frac{1}{2}m\langle w \rangle^2/k$. This average velocity is also used to find the primary-secondary collision rate constant as discussed below.

For thermionic direct emission cathodes, the electrons are emitted directly from the cathode surface into the discharge. The Micro-Ion discharge filament power supply was connected so that the filament drop was positive with respect to cathode potential. For this arrangement, the average cathode potential can be approximated as half of the voltage drop,

V_{drop} , across the filament, such that $V_c \cong V_{drop}/2$. The primary electron voltage, V_p , is then approximated as

$$V_p = V_D + \phi - V_{drop}/2 \qquad \text{[G-6]}$$

Primaries from direct emission cathodes, such as a filament or the IC cathode, can be simply treated as single-energy electrons since the thermal distribution of the electron population leaving such surfaces is only ~0.2eV, which is negligible compared to the cathode sheath voltage. For a single-energy primary electron the rate constant, K_{se}, is simply

$$K_{se} = \sigma(w)w \qquad \text{[G-7]}$$

where the velocity of the primary is $w = \sqrt{2kV_p/m}$.

Collision Cross-Sections

The total xenon atom inelastic collision cross-sections versus electron energies are given by the empirical curve fits [77,78] shown in Figure G-1. The double ionization cross-sections for xenon ions and neutrals [58] are shown in Figure G-2. These cross-sections were used in Equation G-1, along with the appropriate velocity distribution, to determine the rate constants (i.e., K_{iz}^o, K_{ex}^o, K_{iz}^+) for the Discharge Model.
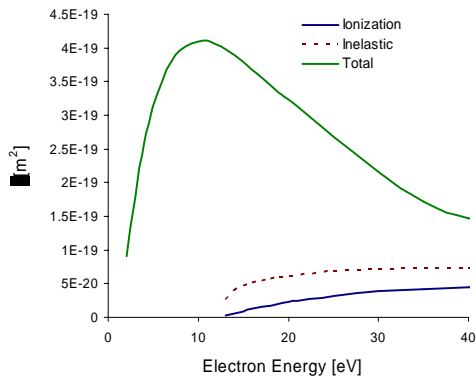
Figure G-1. Electron/Neutral Collision Cross-sections
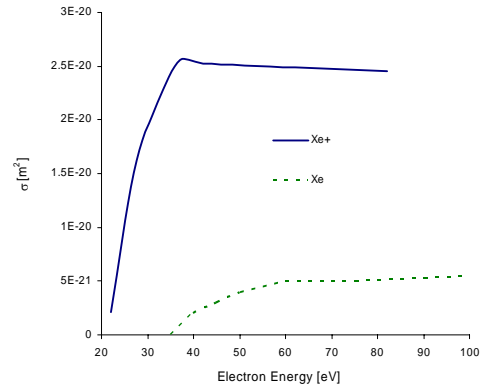
Figure G-2. Electron Double Ionization Collision Cross-sections

Primary-Secondary Electron Collision Rate Constant

The relaxation time for a primary at speed, w, in the presence of a field of secondary electrons of density, n_s, and temperature, T_s, is determined by the Spitzer slowing (relaxation) time (in CGS units):

$$t_{slow} = \frac{w^3}{4A_D G\left(w\sqrt{\frac{m}{2kT_s}}\right)}$$

[G-8]

where the diffusion constant, A_D, is defined using the Coulomb logarithm, $\ln\Lambda$, by

$$A_D = \frac{8\pi e^4 n_s \ln\Lambda}{m_e^2}$$

[G-9]

The function G is defined by

$$G(x) = \frac{\Phi(x) - x\Phi'(x)}{2x^2}$$

[G-10]

where

$$\Phi(x) = \tfrac{2}{\sqrt{\pi}} \int_0^x \exp\left(-y^2\right) dy$$

[G-11]

Using these equations, the primary slowing rate constant is defined as

$$K_{slow}^s = \frac{1}{n_s t_{slow}}$$

[G-12]

Secondary Electron-Ion Collisions

The secondary electron-ion collision frequency, assuming a Maxwellian distribution of electrons, is defined as [79]

$$v_{ei} = 2.91 \cdot 10^{-12} n_e \ln\Lambda T_e^{-3/2}$$

[G-13]

Ion Collisions

The charge-exchange collision frequency for xenon ions with xenon neutrals is defined by

$$v_{CEX} = \sigma_{CEX} n_o \sqrt{\frac{8kT_i}{\pi m_i}}$$

[G-14]

where [53]

$$\sigma_{CEX} = 87.3 - 13.6 \log_{10}(T_i) \cdot 10^{-20}$$

[G-15]

The ion-neutral collision frequency is defined using kinetic theory for hard sphere collisions [54] by

$$v_{io} = \sqrt{2} \sigma_{io} n_o \sqrt{\frac{8kT_i}{\pi m_i}}$$

[G-16]

where, using the diameter of a xenon atom, d_{Xe}, gives the cross-section

$$\sigma_{in} = \pi d_{Xe}^2$$

[G-17]

Classical Ambipolar Mobilities

The following ambipolar mobilities were derived in Koch [22] for weakly ionized plasma. To reduce unnecessary clutter in the equation, the "‖" notation is not used for the parallel mobilities.

$$\mu_i = \frac{e}{m_e \nu_{ei}\left(1 + \nu_i^* + \nu_i^*/\nu_e^*\right)}$$

$$\mu_e = \frac{e}{m_e \nu_{ei}\left(1 + \nu_e^* + \nu_e^*/\nu_i^*\right)}$$

$$\mu_{ie} = \frac{k}{m_e \nu_{ei}\left(\nu_e^* + \nu_i^* + \nu_i^*\nu_e^*\right)}$$

$$\mu_{ii} = \mu_{ie}\left(1 + \nu_e^*\right) \;,\; \mu_{ei} = \mu_{ie} \;,\; \mu_{ee} = \mu_{ei}\left(1 + \nu_i^*\right)$$

[G-18]

$$\mu_i^\perp = \frac{e}{\Delta m_e \nu_{ei}}\left[\nu_i^*\Omega^2 + \nu_e^*\left(\nu_e^* + \nu_i^* + \nu_e^*\nu_i^*\right)\right]$$

$$\mu_e^\perp = \frac{e}{\Delta m_e \nu_{ei}}\left[\nu_e^*\Omega^2 + \nu_i^*\left(\nu_e^* + \nu_i^* + \nu_e^*\nu_i^*\right)\right]$$

$$\mu_{ie}^\perp = \frac{k}{\Delta m_e \nu_{ei}}\left[\Omega^2 + \nu_e^* + \nu_i^* + \nu_e^*\nu_i^*\right]$$

$$\mu_{ei}^\perp = \mu_{ie}^\perp$$

[G-19]

$$\mu_{ii}^\perp = \frac{k}{\Delta m_e \nu_{ei}}\left[\left(1 + \nu_i^*\right)\Omega^2 + \left(1 + \nu_e^*\right)\left(\nu_e^* + \nu_i^* + \nu_e^*\nu_i^*\right)\right]$$

$$\mu_{ee}^\perp = \frac{k}{\Delta m_e \nu_{ei}}\left[\left(1 + \nu_e^*\right)\Omega^2 + \left(1 + \nu_i^*\right)\left(\nu_e^* + \nu_i^* + \nu_e^*\nu_i^*\right)\right]$$

where

$$\nu_e^* = \frac{\nu_{e-o}}{\nu_{ei}} \;,\; \nu_i^* = \frac{m_i \nu_{i-o}}{m_e \nu_{ei}} \;,\; \Omega = \frac{eB}{m_e \nu_{ei}}$$

$$\Delta = \left[\Omega^2 + \nu_e^* + \nu_i^* + \nu_e^*\nu_i^*\right]^2 + \Omega^2\left[\nu_i^* - \nu_e^*\right]^2$$

[G-20]

Double Ion Formulation

The double ion motion density is determined using a simple upwind time-step control volume formulation. This method uses the results of the single ion motion equation for the drift velocities as shown in Equation 3.5-50, which is repeated here for convenience:

$$\frac{\partial n_{++}}{\partial t} + \nabla \cdot \left(n_{++} u_+ \sqrt{2} \right) = \dot{n}_{++}$$

Integrating over the volume of the cell and assuming constant volume properties yields

$$\frac{\partial n_{++}}{\partial t} V_{cell} = \dot{n}_{++} V_{cell} - \sqrt{2} \int \left(n_{++} u_i \right) dA$$

[G-21]

For the upwind time-step formulation the flux across the cell boundaries is decomposed into components into the cell at the beginning of the time-step and out of the cell at the end of the time-step $(t+1)$ by

$$\sqrt{2} \int \left(n_{++} u_i \right) dA = \sqrt{2} \sum \left(n_{++}^{t+1} u_{out} A_{out} \right) - \sqrt{2} \sum \left(n_{++}^{t} u_{in} A_{in} \right)$$

[G-22]

For a differential time-step, Δt, Equation G-21 can now be written as

$$V_{cell} \frac{n_{++}^{t+1} - n_{++}^{t}}{\Delta t} = V_{cell} \dot{n}_{++} + \sqrt{2} \sum \left(n_{++}^{t} u_{[in]} A_{[in]} \right) - \sqrt{2} \sum \left(n_{++}^{t+1} u_{[out]} A_{[out]} \right)$$

[G-23]

For an initial double ion density n_{++}^{t} the density at the end of the time step is approximated by

$$n_{++}^{t+1} \left(V_{cell} + \Delta t \sqrt{2} \sum \left(u_{[out]} A_{[out]} \right) \right) = V_{cell} n_{++}^{t} + \Delta t \left[V_{cell} \dot{n}_{++} + \sqrt{2} \sum \left(n_{++}^{t} u_{[in]} A_{[in]} \right) \right]$$

[G-24]

For $t=0$ the initial guess for double ion density is

$$n_{++}^{t=0} = \frac{n_i^{tot} R_{++}}{\sqrt{2}}$$

[G-25]

The time step, Δt, is chosen to satisfy the Courant condition.

Control Volume Formulation / Diffusion Formulation

This section describes the formulation for a simplified diffusion equation, $\dot{n} = -\nabla \cdot D\nabla n$. The following control volume formulation technique was used for the ion, electron, and thermal diffusion equations from Chapter 3.

1. Control Volume Analysis

The conservation equations are satisfied at each cell of the Internal Mesh using a flux definition of the continuity equation. Integrating over the differential volume, dV, and all differential surface areas, dA, yields

$$\int \nabla \cdot \Gamma \, dV = \int \dot{\Gamma} \cdot d\mathbf{A} = \int \dot{n} \, dV \qquad \text{[G-26]}$$

For a quadrilateral cell, E, with its neighboring four cells denoted by m, this becomes

$$\sum_{m}^{4} \Gamma_m \cdot \hat{n}_m A_m = \underbrace{\dot{n} V_E}_{RHS} \qquad \text{[G-27]}$$

To determine the flux for cells that are not aligned with the B-field it is useful to define a B-field coordinate system (z^B, r^B) where the z^B-axis is aligned parallel to the tangent of the B-field such that $B_{\parallel} = \mathbf{B} \cdot \hat{z}^B$ and $B_{\perp} = \mathbf{B} \cdot \hat{r}^B$. To demonstrate this methodology we define a flux aligned with the B-field coordinate system as the product of an arbitrary tensor $\mathbf{D}$ (such as an anisotropic diffusion or mobility tensor) and the gradient, also aligned with the B-field, of an arbitrary scalar, x, (such as $\nabla(nT)$ or $\nabla \psi$). Thus, our arbitrary flux definition is

$$\Gamma^B = -\underline{\underline{\mathbf{D}}} \nabla^B x \qquad \text{[G-28]}$$

Defining θ as the angle between the B-field (z^B, r^B) and standard cylindrical (z,r) coordinates we can use a rotation matrix, $\underline{\underline{R}}$, to align the flux and gradient to the standard axes:

$$\Gamma^B = \underline{\underline{R}}\Gamma \quad ; \quad \nabla^B x = \underline{\underline{R}}\nabla x$$

$$\text{where, } \underline{\underline{R}} \equiv \begin{bmatrix} \cos\theta & \sin\theta \\ -\sin\theta & \cos\theta \end{bmatrix} \qquad \text{[G-29]}$$

G-8

This allows the diffusion tensor, and consequently the flux, to be defined in the (z,r) coordinate system by

$$\Gamma = -\underline{\underline{R}}^{-1}\underline{\underline{D}}\underline{\underline{R}}\nabla x = -\underline{\underline{\mathbf{D}}}^{z,r}\nabla x$$

[G-30]

$$\underline{\underline{\mathbf{D}}}^{z,r} = \begin{bmatrix} D_{\parallel}\cos^2\theta + D_{\perp}\sin^2\theta & \left(D_{\parallel}-D_{\perp}\right)\sin\theta\cos\theta \\ \left(D_{\parallel}-D_{\perp}\right)\sin\theta\cos\theta & D_{\parallel}\sin^2\theta + D_{\perp}\cos^2\theta \end{bmatrix} \equiv \begin{bmatrix} D_A & D_B \\ D_B & D_C \end{bmatrix}$$

[G-31]

$$\begin{bmatrix} \Gamma_z \\ \Gamma_r \end{bmatrix} = \begin{bmatrix} D^A & D^B \\ D^B & D^C \end{bmatrix}\begin{bmatrix} \nabla_z x \\ \nabla_r x \end{bmatrix}$$

[G-32]

Using this formulation we see that the flux in a given direction for standard (z,r) is influenced by the gradients in both the parallel and perpendicular directions. A control volume analysis was chosen to achieve explicit conservation across flux surfaces. To generalize the formulation we define Equation G-29 for the direction normal to the flux surface, the "n-direction," as

$$\Gamma_k = -D^{A,C}\nabla_k x - D^B\nabla_j x$$

[G-33]

where,

$k \equiv$ direction normal to the flux surface

$j \equiv$ direction along flux surface

$$D^{A,C} \equiv \begin{cases} D^A, \; k = z-\text{direction} \\ D^C, \; k = r-\text{direction} \end{cases}$$

Referring to Figure G-3, we define the k-direction as the vector between the subject element, E, and a flush neighboring element, m. By this definition, the gradient of x in the k-direction can be simply expressed as

$$\nabla_k x = \frac{x_m - x_E}{d_{m,E}}\hat{n}_k$$

[G-34]

where $\hat{n}_k$ is the unit vector for the outwardly facing normal of the surface. The density gradient in the j-direction, (or "cross-gradient") is defined by the difference of scalar x between nodes 1 and 2 from Figure 3. The x-values at these nodes, x_1 and x_2, are defined using bilinear interpolation of the cell-centered values of the surrounding elements. In this way the cross-gradient, using the nomenclature from Figure G-3, may be defined by

$$\nabla_j x = \frac{x_2 - x_1}{d_{1,2}} \tag{G-35}$$

$$x_1 = \sum_q x_q W_{1,q} = x_a W_{1,a} + x_b W_{1,b} + x_m W_{1,m} + x_E W_{1,E} \tag{G-36}$$

$$x_2 = \sum_q x_q W_{2,q} = x_E W_{2,E} + x_m W_{2,m} + x_c W_{2,c} + x_d W_{2,d} \tag{G-37}$$

where the bilinear weights, w, are determined using volumetric weighting of the x-values, and $d_{1,2}$ is the distance between the nodes.
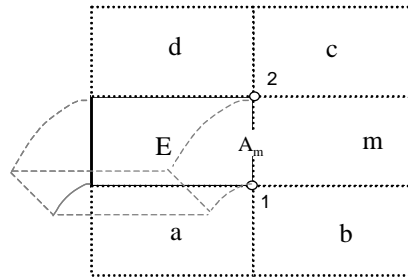
Figure G-3. Schematic of cells contributing to the flux
across a surface, A_m, in the computational domain

From the above equations we can develop an expression for the flux with respect to the element center, Γ, as a function of the scalar properties, x, of the surrounding elements. Following the nomenclature for nearby elements and nodes in Figure G-3, the flux from element-E to element-m, across surface A_m with normal $\hat{n}_m$, can be written as

$$\Gamma_k A_m \hat{n}_m = \left[-D^{A,C} \nabla_k x - D^B \nabla_j x \right] A_m \hat{n}_m$$

$$= x_E \left[C_{E,m}^1 D^{A,C} + C_{E,m}^2 D^B \right] + x_m \left[C_{m,m}^1 D^{A,C} + C_{m,m}^2 D^B \right]$$
$$+ x_a \left[C_{a,m} D^B \right] + x_b \left[C_{b,m} D^B \right] + x_c \left[C_{c,m} D^B \right] + x_d \left[C_{d,m} D^B \right]$$

[G-38]

$$C_{E,m}^1 \equiv \frac{A_m}{d_{E,m}} \quad ; \quad C_{E,m}^2 \equiv \frac{\left(w_{1,E} - w_{2,E} \right) A_m \hat{n}_m}{d_{1,2}}$$

$$C_{m,m}^1 \equiv \frac{-A_m}{d_{E,m}} \quad ; \quad C_{m,m}^2 \equiv \frac{\left(w_{1,m} - w_{2,m} \right) A_m \hat{n}_m}{d_{1,2}}$$

$$C_{a,m} \equiv \frac{w_{1,a}}{d_{1,2}} A_m \hat{n}_m \quad ; \quad C_{b,m} \equiv \frac{w_{1,b}}{d_{1,2}} A_m \hat{n}_m$$

$$C_{c,m} \equiv \frac{-w_{2,c}}{d_{1,2}} A_m \hat{n}_m \quad ; \quad C_{d,m} \equiv \frac{-w_{2,d}}{d_{1,2}} A_m \hat{n}_m$$

where geometric coefficients, *C*, are used and the direction of positive flux is "out" of the element. The definition of nodes *1* and *2* must be chosen carefully to assure that the cross-gradient flux is in the proper direction. Using the surrounding node and element definition for element "**E**" and node "*n*":

Elements surrounding Element "E"	Nodes surrounding Element "E"	Elements surrounding Node "*n*"

`8|4|7`
`-+-+-`
`1|E|3`
`-+-+-`
`5|2|6`
	4-3
	`|E|`
	1-2
		`4|3`
		-n-
		`1|2`

and following Figure 3 nomenclature, we identify proximate elements *a, b, c,* and *d*; and proximate nodes *1* and *2* for flush element "*m*" by the following definitions:

Flush Element	Element-a	Element-b	Element-c	Element-d	Node-1	Node-2	$D^{A,C}$
1	2	5	8	4	1	4	D^A
2	1	5	6	3	1	2	D^C
3	2	6	7	4	2	3	D^A
4	1	8	7	3	4	3	D^C

Similarly, for the bilinear weighting coefficients in Equation G-38 it is necessary to identify the positions of the elements relative to nodes *1* and *2* by:

Flush Element	Element Positions Relative to Node-1				Element Positions Relative to Node-2			
	$w_{1,a}$	$w_{1,b}$	$w_{1,E}$	$w_{1,m}$	$w_{2,c}$	$w_{2,d}$	$w_{2,E}$	$w_{2,m}$
1	2	1	3	4	4	3	2	1
2	4	1	3	2	2	3	4	1
3	1	2	4	3	3	4	1	2
4	1	4	2	3	3	2	1	4

- Appendix H -

Additional Discharge Model Results

The Discharge Model was used to simulate NSTAR at throttle point (TH12) from Table 4.1-1. The hollow cathode insert plasma electron temperature, T_p, is assumed higher (3eV) since the relatively lean cathode flow should result in higher insert plasma temperatures [73].

<div align="center">
(Repeated)
Table 4.1-1. NSTAR Throttle Points [Beginning of Life]
</div>

Throttle Points	Main Flow [sccm]	Cathode Flow [sccm]	J_B [A]	J_D [A]	V_D [V]	V_B [V]	V_{accel} [V]	Model Specific Inputs	
								Vp [V]	Tp [eV]
TH12	19.85	2.92	1.59	10.87	25.4	1100	-249	21	3
TH15	23.42	3.73	1.76	13.13	25.1	1100	-249	20	2.5

The beam and neutral density profiles in Figure H-1 show good agreement with the experimentally measured profile. The profiles are similar to those given for TH15 in Chapter 4, including similar inconsistency with the experimental data in the near-axis and extreme radial locations. The values in Table H-1 show that the Discharge Model predicts low, but similar, double ion content in the beam.

<div align="center">
Table H-1. Discharge Performance Parameters at TH12
</div>

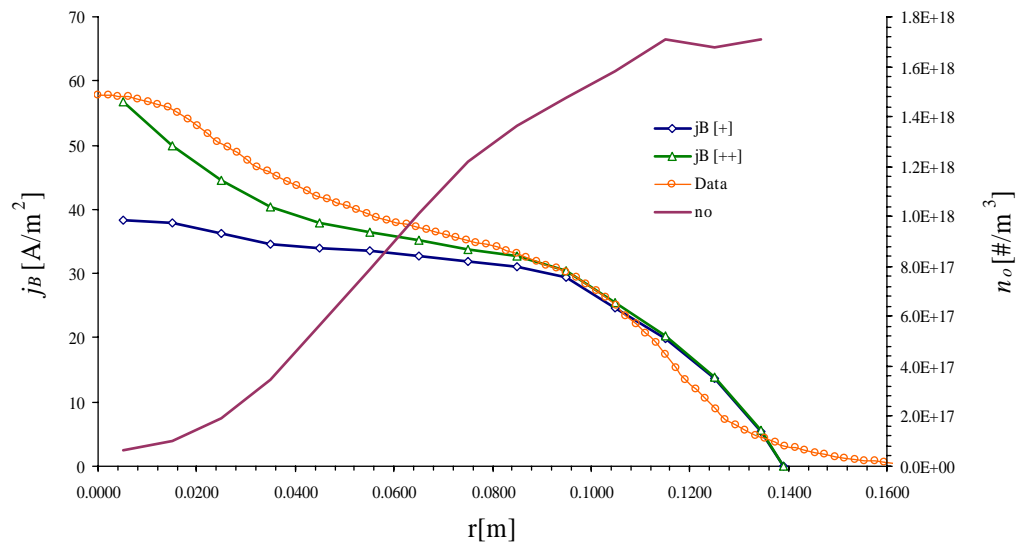| Discharge Parameters	$\eta_{ud[*]}$	$\eta_{ud[act]}$	ε_B	J_{B++}/J_{B+}	J_i	J_{ip}	n_i	n_p	n_o	f_A	f_B	f_C	F_B	F_{B*}
Units	%	%	eV/ion	-	A	A	m^{-3}	m^{-3}	m^{-3}	-	-	-	-	-
Model Results	97.7	91.0	173	0.159	5.16	3.32	1.48 $*10^{17}$	1.09 $*10^{16}$	2.82 $*10^{18}$	0.65	0.31	0.04	0.46	0.63
Data	97.3	89.2-90.3	173	0.168-0.20									0.46	

Figure H-1. Beam and Neutral Density Profiles at Grids for TH12